THE UNIVERSITY OF CHICAGO

METAL COMPLEXES SUPPORTED BY NOVEL LIGANDS

A DISSERTATION SUBMITTED TO

THE FACULTY OF THE DIVISION OF THE PHYSICAL SCIENCES

IN CANDIDACY FOR THE DEGREE OF

DOCTOR OF PHILOSOPHY

DEPARTMENT OF CHEMISTRY

BY

ERIK DOUGLAS REINHART

CHICAGO, ILLINOIS

JUNE 2019

TABLE OF CONTENTS

LIST OF TABLES

CHAPTER TWO

CHAPTER THREE

LIST OF FIGURES

CHAPTER TWO

CHAPTER THREE

LIST OF SCHEMES

LIST OF CHARTS

LIST OF EQUATIONS

CHAPTER TWO

ACKNOWLEDGEMENTS

First, I thank my advisor, Professor Richard Jordan, for his help, guidance, thoroughness and criticism. I also thank the other members of my thesis committee, Professors Michael Hopkins and John Anderson, whom also served on my candidacy committee, for their helpful advice and discussions throughout my time at the University of Chicago.

As the last Ph. D. student from the Jordan group, I would like to thank former group members who made for a fun and helpful working environment, including Dr. Rebecca Black, Dr. Alison Johnson Wilders, Dr. Frank Olechnowicz, Dr. Feng Zhai, Dr. Ge (David) Feng, Dr. Jia Wei, Dr Tabbetha Bohac, Max Weinberg, Joseph Solomon, and James Earl. I would specifically like to thank my undergraduates Amanda Waterbury and Isabel Jensen for their hard work. I would also like to thank the entire Anderson group for adopting me into their group this last year as the Jordan group as dwindled in size.

The research described in this thesis relied heavi ly on departmental facilities, and I thank Dr. Antoni Jurkiewicz for his assistance with NMR Spectroscopy, Dr. Chang-Jin Qin for his assistance with mass spectrometry, and Dr. Alexander Filatov and Andrew McNecee for their assistance with X-ray crystallography.

Finally, I thank my family who have provided tremendous support throughout graduate school: my parents Tod and Kristin Reinhart, my siblings Zachary and Katie, and my grandparents Donald and Norma Holm, and Arnold and Paulette Reinhart. I thank Marek Piechowicz and Maggie Hudson for being fantastic friends starting when we were TA'ing Organic Chemistry together and throughout graduate school. I thank my friends Jason Normand and Anna Duell for supporting me through my time at Willamette University and the University of Chicago. Lastly, I thank my friends that I have played League of Legends with for over half a decade, some of which I have known since high school: Nicolas Evans, Franky Robles, Andy Alvarez, Mondo Moreno, Tony Quinn, Jesse Martinez, Trevor Ryals and Evan Bartlett.

ABSTRACT

Chapter One introduces two classes of late-transition metal ethylene polymerization catalysts. The first class are Pd(II)-alkyl complexes supported by phosphine-arenesulfonate (PO) ligands. (PO)PdRL catalysts are unique in their ability to copolymerize ethylene and a wide variety of polar vinyl monomers to highly linear functionalized polyethylene. The ability to produce new types of functionalized polymers with enhanced properties motivates the development of new PO-type Pd catalysts and new strategies for enhancing the catalytic performance of these catalysts. The second class are the pyridine-diimine (PDI) Co and Fe catalysts which produce highly linear polyethylene with high activity. (PDI)Co and (PDI)Fe complexes have also been shown to versatile catalysts for a wide variety of organic transformations such as CO_2/ethylene coupling, hydroboration, hydrosilylation, and [2+2] cycloaddition.

Chapter Two describes the ethylene polymerization behavior of new PO-type zwitterionic electronically-unsymmetrical Pd(II)-Me complexes supported by phosphino-perchloro-*closo*-decaborane ligands ($PR_2CB_9Cl_9$). The κ^2-*P*,*Cl*-($PR_2CB_9Cl_9$)PdMe(THF) (R = ^{i}Pr, Ph) complexes and the κ^2-*P*,*O*-(P(*o*-OMe-Ph)$_2$$CB_9Cl_9$)PdMe(THF) complex were synthesized and characterized in solution and solid state. Reaction of κ^2-*P*,*O*-(P(*o*-OMe-Ph)$_2$$CB_9Cl_9$)PdMe(THF) with excess ethylene *in situ* generates the κ^2-*P*,*O*-(P(*o*-OMe-Ph)$_2$$CB_9Cl_9$)PdMe(ethylene) adduct. Ethylene

insertion kinetics of the κ^2-*P*,*O*-(P(*o*-OMe-Ph)$_2$CB$_9$Cl$_9$)PdMe(ethylene) are described in addition to bulk polymerization studies for all three complexes.

Chapter Three describes the the template-free synthesis a bis-(pyridine-dieanamine) proligand, which was metalated to synthesize a variety of bis-(pyridine-diimine) (bis-PDI) and bis-(pyridine-dienamido) (bis-PDE) metal complexes, in the hopes of synthesizing dinuclear bis-PDI complexes to exploit metal-metal cooperativity effects to engender new reactivity. Three five-coordinate dinuclear (bis-PDI)M_2Cl_4 (M = Zn, Co, Fe) complexes were synthesized and characterized in solution and the solid state for M = Zn and Co. A four-coordinate square-planar dinculear [(bis-PDI)Pd_2Br_2][$BAr^F{}_4$]$_2$ was synthesized in solution and the solid state. The bis-(pyridine-dienamine) form of the proligand allowed for the facile synthesis of a (bis-PDE)$Zr_2(NMe_2)_4$ complex, which was subsequently alkylated to synthesize (bis-PDE)Zr_2Me_4 and (bis-PDE)$Zr_2(CH_2SiMe_3)_2(NMe_2)_2$ complexes, the latter of which was characterized in the solid state.

PREFACE

Each chapter has an independent numbering system for compounds. A given compound may have a different number in different chapters. For each chapter, the relevant experimental information, references and notes are provided at the end of the chapter.

Chapter One

Late-Transition Metal Ethylene Polymerization Catalysts

1.1 Introduction to Electronically-Unsymmetrical Pd Catalysts

In 2002, Pugh and Drent discovered that Pd(II) catalysts generated *in situ* from $Pd(dba)_2$ or $Pd(OAc)_2$ and 1-PH^+(2-OMe-Ph)$_2$-2-SO_3^--Ph (PO-H) copolymerize ethylene and alkyl acrylates to linear in-chain ester-functionalized polyethylene (Scheme 1.1 a).[1] In 1995, Brookhart showed that Pd(II) α-diimine catalysts are able to generate highly-branched functionalized polyethylene, however this system is only able to incorporate polar comonomers at the chain ends (Scheme 1.1 b).[2–5] This type of copolymerization with polar comonomers of ethylene is not possible with the highly-active Group IV metallocene or Ziegler-Natta catalysts due their high oxophilicity. Extensive work by Claverie,[6–12] Jordan,[13–27] Mecking,[28–43] Nozaki,[44–53] Rieger,[54–59] Sen,[60–63] Chen,[59,64–68] and others[58,69–73] has focused on ethylene homopolymerization and copolymerization with polar monomers with discrete (PO)PdR complexes (Scheme 1.1 c). As a result, new types of functionalized polyethylenes have been synthesized utilizing a wide array of polar comonomers.[17,52,53]

Scheme 1.1. Examples of Ethylene/polar Monomer Copolymerization with Pd(II) Catalysts.

a) Pugh and Drent's ethylene/alkyl acrylate copolymerization

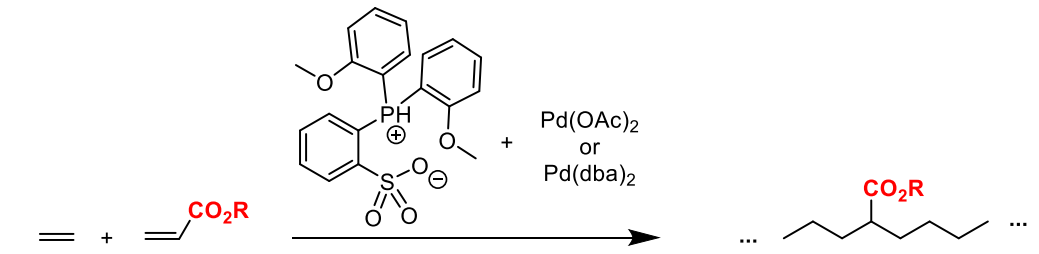

R = Me, ^{i}Pr, ^{n}Bu, ^{t}Bu

b) Brookhart-type catalysts

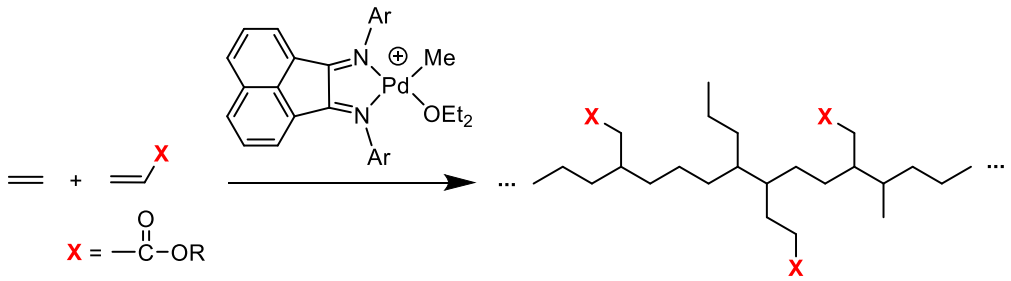

c) (PO)Pd catalysts

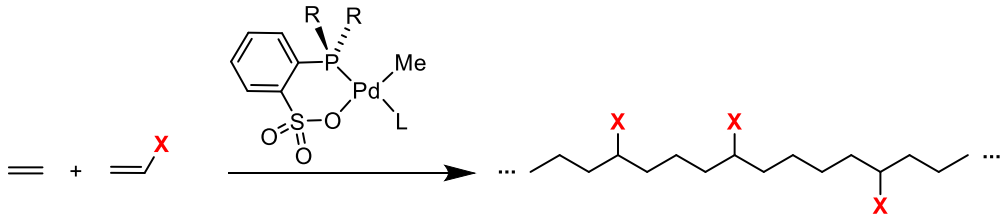

X = OR, OAr, F, CN, OAc, —C(=O)—OR , —C(=O)—OH , —C(=O)—R ,

—C(=O)—NHR , —N(C=O)— , —SO_2R , —P(=O)(OH)—OH , —CF_3

A simplified polymerization mechanism for (PO)PdMeL catalysts is shown in Scheme 1.2.[20,23,46] The first step is the displacement of the L ligand (py, lut, dmso, THF) by ethylene to form a (PO)PdR(ethylene) adduct which, with some exceptions, is the catalyst resting state. This equilibrium, especially for L = py and lut, has been shown to detrimental to catalyst activity and

for this reason the L ligand is often removed from the reaction mixture by the addition of a Lewis acid such as $B(C_6F_5)_3$. However, $B(C_6F_5)_3$ may bind to the sulfonate group of the catalyst, resulting in changes in the chain growth and chain transfer rates.[18,27] The (PO)PdR(ethylene) adduct can undergo migratory insertion to form a transient β-agostic species, growing the chain and opening up a coordination site for further ethylene binding. Insertion occurs from the *trans-R,P*-(PO)PdR(ethylene) complex, which is in equilibrium with the ground-state *R*,P-*cis* species. Chain transfer occurs *via* β-H elimination, followed by a ligand exchange reaction that releases the vinyl-capped polymer chain and forms a (PO)PdH(ethylene) species that inserts ethylene and re-enters the chain-growth cycle. The olefin exchange normally occurs by the classical associative mechanism that is commonly observed for square-planar Pd(II) complexes, Berry pseudorotation(s), and release of the vinyl-capped polymer chain releasing from the opposite axial site.

Scheme 1.2. Simplified Polymerization Mechanism for (PO)-type Pd Catalysts.

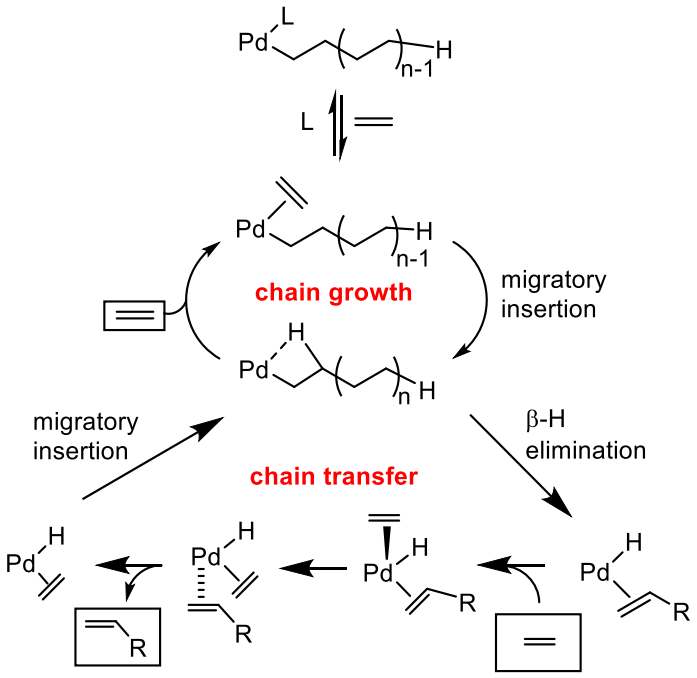

As mentioned above, the electronically-symmetrical α-diimine Pd system produces highly branched polyethylene, in contrast to the electronically-unsymmetrical (PO)Pd system which produces linear polyethylene. This difference can be rationalized by examining the relative trans influence of the ligands in the chain growing species (Scheme 1.3). In general, the most stable isomers of square-planar complexes have strong *trans*-influence ligands *trans* to weak *trans*-influence ligands. In the β-agostic (PO)PdR complex, the ground state is such that the strong *trans*-influence P and R groups are *trans* to the weak *trans*-influence O and β-agostic donors, respectively. β-H elimination would generate a species in which the strong phosphine and hydride ligands are *trans* and is therefore inhibited. Since β-H elimination is the first step in chain transfer and in the chain walking process that generates branches in the polymer chain, suppression of this process results in increased polymer MW and linear chains in ethylene homopolymerization. In copolymerization with polar comonomers, these same electronic effects inhibit catalyst deactivation *via* β-X elimination.

Scheme 1.3. Influence of Electronic Asymmetry on the Reactivity of (PO)PdR Olefin Polymerization Catalysts. Red letters refer to *trans*-influence (*vs* = very strong, *s* = strong, *m* = medium, *w* = weak, *vw* = very weak).

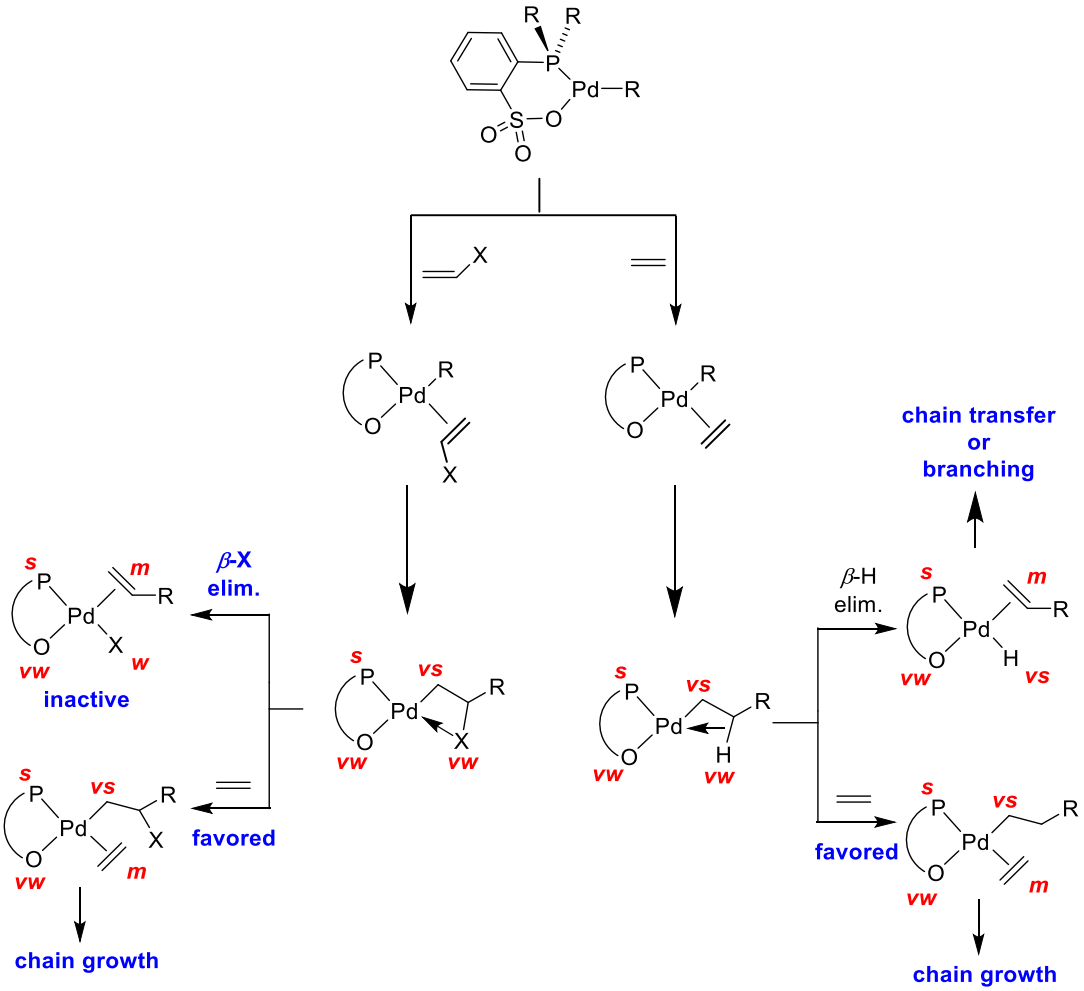

In general, the polar comonomers act as chain growth inhibitors and chain transfer accelerators, decreasing the catalyst activity and the MW of the polymer products. Modifications to the PO system were made by changing the electronic and/or steric nature of the phosphine substituents to combat these negative effects and improve catalyst performance. Recent work in this field by Jordan[13,18,74], Chen[66,67], Nozaki[44], and Carrow[47,75] has focused on studying how changing the weak donor group affects the polymerization reactivity profile. Representative examples of catalysts in

which the sulfonate group has been modified or replaced with an alternative weak donor group are shown in Chart 1.1. In ethylene homopolymerization the parent catalyst **A** (R = 2-Et-Ph) generates polyethylene with moderate molecular weight (M_n = 29,000 Da) with moderate activity (1,570 kg mol_{Pd}^{-1} h^{-1}).[26] Cationic phosphine-sulfonamide complex **B** (R = ^{i}Pr) produces C_2 – C_8 ethylene oligomers (primarily butene) with low activity (137 kg mol_{Pd}^{-1} h^{-1}).[66] Phosphine-di-*tert*-butylphosphine oxide complex **C** exhibits high activity (2,800 kg mol_{Pd}^{-1} h^{-1}) and produces polyethylene with moderate MW (M_n = 29,000).[44] Catalyst **D** (R = Ph), which is supported by a phosphine-phosphonamide ligand, is both very active (6,000 kg mol_{Pd}^{-1} h^{-1}) and produces high-MW polyethylene (M_n = 130,000 Da).[75] Phosphonic diamide-phosphine complex **E** (R^1 = ^{i}Pr, R^2 = 2, R^3 = *o*-OMe-Ph) is moderately active (2,200 kg mol_{Pd}^{-1} h^{-1}) and produces polyethylene with very high MW (M_n = 340,000 Da).[67] Catalyst **F** (R^1 = ^{i}Pr, R^2 = *o*-OMe-Ph) which contains a $B(C_6F_5)_3$-coordinated phosphine-phosphonate ligand produces polyethylene with low activity (10 kg mol_{Pd}^{-1} h^{-1}) and low-MW polyethylene (M_n = 9,030 Da). Addition of 8 equiv. of $B(C_6F_5)_3$ substantially increases the activity (5700 g $mmol_{Pd}^{-1}$ h^{-1}) and the MW of the formed polyethylene (99,200 Da).[18] This enhancement in catalyst performance results from the fact that excess $B(C_6F_5)_3$ sequesters the lutidine and inhibits dissociation of $B(C_6F_5)_3$ from the phosphonate group. Trifluoroborate-phosphine complex **G** dimerizes ethylene with very low activity (10 kg mol_{Pd}^{-1} h^{-1}). In this case, addition of $[H(OEt_2)][B(3,5\text{-}(CF_3)_2\text{-}Ph)_4]$ to trap the L ligand (collidine) increases the activity by a factor of 10.[13]

Chart 1.1: Examples of (PO)Pd-type Complexes With Weak-donor Group Modifications.

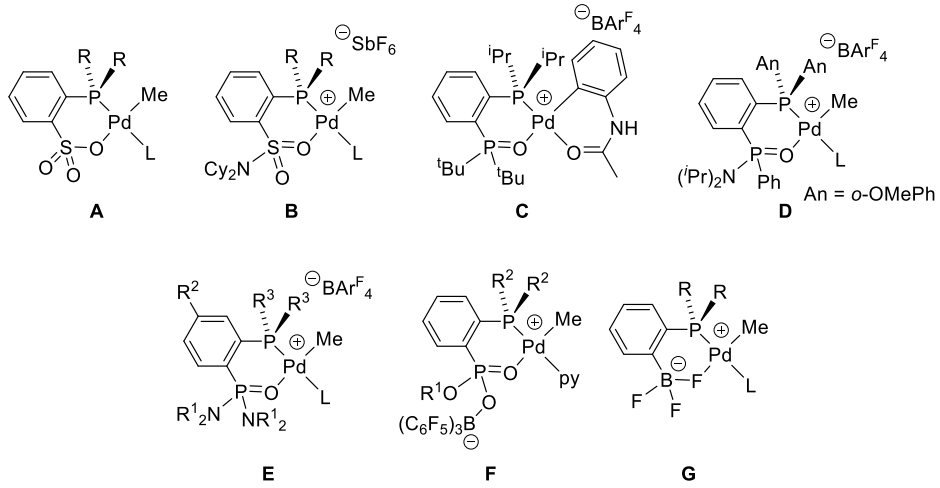

1.2 Introduction to (Pyridine-diimine)M (M = Fe, Co) Catalysts

In 1998, Brookhart and Gibson reported that Fe and Co complexes supported by pyridine-diimine (PDI) ligands (**H,** Chart 1.2) and activated with methylaluminoxane (MAO) or MMAO-12 displayed very high activity in ethylene homopolymerization.[76,77] The Fe complexes are typically an order of magnitude more active than the Co analogues and both produce linear polyethylene. The steric bulk of the aryl substituent significantly affects both activity and the M_n of the polyethylene that is formed. For example, for large 2,6-diisopropylphenyl substituents **H** (M = Fe), these catalysts show high activity (MAO activator, 53,000 kg mol_{Fe} h^{-1}), and produce polyethylene with moderate MW (M_n = 64,000; bimodal molecular distribution due to chain transfer to Al). However for smaller 2,6-dimethylphenyl substituents the activity drops by an order of magnitude (9,340 kg mol_{Fe} h^{-1}) and the MW decreases by a factor of 5 (M_n = 9,600).[77] The active species in olefin polymerization is the $(PDI)MR^+$ (M = Fe, Co) (**I**) species, which have been isolated and extensively characterized by Chirik.[78–81]

Schemes 1.4 and 1.5 show generalized ethylene polymerization mechanisms for (PDI)$FeCl_2$ and (PDI)$CoCl_2$ complexes activated with an aluminum activator. The initial reaction of **H** with MAO, MMAO-12, $AlMe_3$, or Al^iBu_3 generates a bridged-heterobimetallic alkyl species **J** (Scheme 1.4, M = Fe; Scheme 1.5, M = Co).[82–84] The capping Al (AlR_3) unit is displaced by ethylene to generate a (PDI)M(alkyl)(ethylene)$^+$ complex. This adduct undergoes migratory insertion to the (PDI)M-alkyl$^+$ bond, growing the polymer chain and forming a β-agostic species. For M = Fe, the β-agostic species is the resting state, as the activity of the Fe catalysts depends on ethylene pressure. For M = Co, the (PDI)Co(alkyl)(ethylene)$^+$ adduct is the resting state, consistent with the observation that the activity of the Co complexes is generally independent of ethylene pressure. Computational studies suggest that for M = Fe, the chain transfer process occurs through a concerted β-H transfer mechanism (β-H transfer to monomer), forming a (PDI)$FeEt^+$ complex which starts a new chain.[85–88] In contrast, experimental and computational studies show that for M = Co the chain transfer process occurs through the more typical β-H elimination pathway to form a (PDI)Co-H^+ which binds ethylene to start a new chain.[89]

Scheme 1.4. Simplified Ethylene Polymerization Mechanism for (PDI)FeR$^+$ catalysts.

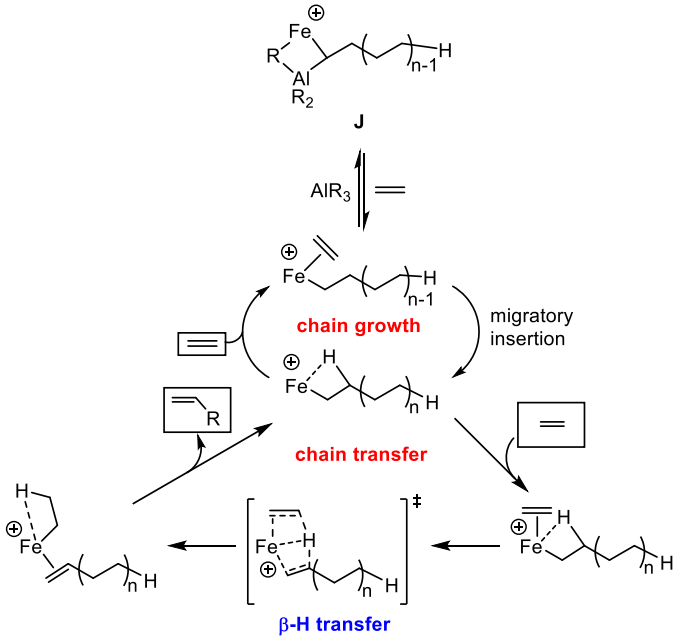

Scheme 1.5. Simplified Ethylene Polymerization Mechanism for (PDI)CoR$^+$ catalysts.

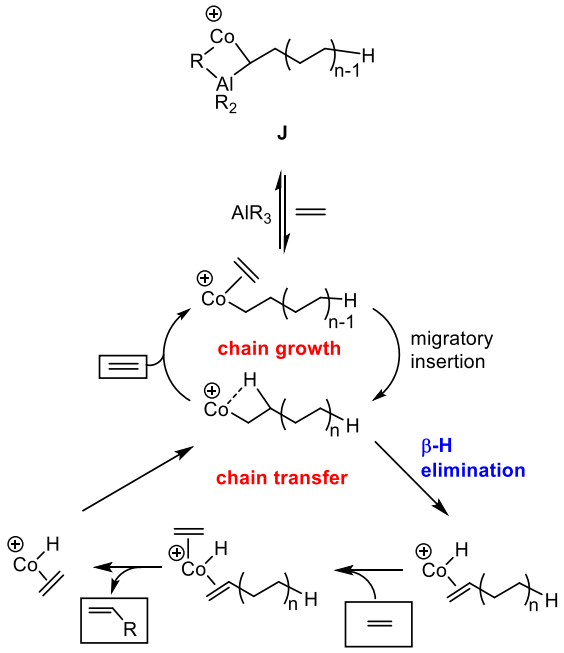

Work by Chirik,[80,81,90–118] Sun,[68,119–133] Groysman,[134–137], Budzelaar,[138–153] Gibson,[77,154–167] Byers,[168–174] and others[76,138,175–195] has demonstrated the versatility of the PDI complexes in olefin polymerization and other important small-molecule transformations. For example, discrete (PDI)M(N_2)$_x$ (M = Co, x = 1; M = Fe, x = 2) complexes (**K**, Chart 1.2) are very active for intra and intermolecular [2+2] cycloaddition reactions,[95,114,196,197] as well as hydrosilylation[105,106,198] and hydroboration.[110,117] Recently these complexes have been shown to be active in CO_2/ethylene coupling, being the first example of metallocyclolactones that insert ethylene to generate linear short-chain carboxylates.[199] Byers has shown that (PDI)Fe(OR)$_2$ complexes (**L**) are active for the ring-opening polymerization of lactide and epoxides.[168–171,173]

Chart 1.2. Examples of Co and Fe PDI complexes

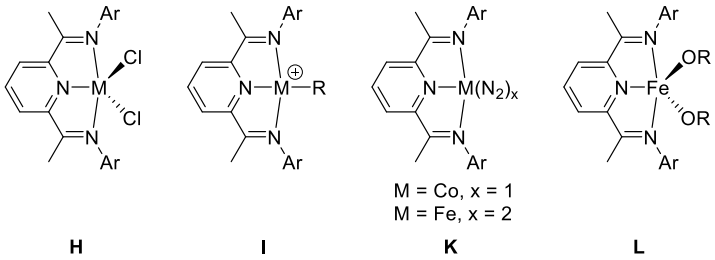

1.3 Thesis Objectives

As mentioned above, work in the (PO)Pd system is focused on utilizing new weak donor groups towards efforts to improve catalytic performance. Chapter Two The synthesis and ethylene reactivity of the zwitterionic Pd methyl complexes (κ^2-*P*,*Cl*-$PR_2CB_9Cl_9$)PdMe(THF) (**7**, R = ^{i}Pr; **8**, R = Ph) and (κ^2-*P*,*O*-P(*o*-OMe-Ph)$_2CB_9Cl_9$)PdMe(THF) (**9**), which contain the first phosphines appended with anionic 10-vertex perchlorinated *closo*-carboranes, are described. **7** and **8**

oligomerize ethylene (23 ºC, 2 atm) to a Schulz-Flory distribution of $C_4 - C_{10}$ olefins with TOFs of ca. 8000 and 1800 t.o./h respectively. **8** is ca. 4 times more active than the analogous (κ^2-*P,F*-*ortho*-$PPh_2C_6H_4BF_3$)PdMe(L) (L = pyridine or collidine) system reported by Jordan and Piers, which produces butenes. **9** reacts with ethylene to yield polyethylene wax (M_n ca. 1000, Đ ca. 1.5) that is similar to commercial Fisher-Tropsch waxes. The activities of these complexes are independent of ethylene pressure and the presence of $B(C_6F_5)_3$, suggesting that the catalyst resting state is the corresponding ($PR_2CB_9Cl_9$)PdR($H_2C=CH_2$) adduct. The molecular weights of the oligomer/polymer products are independent of ethylene pressure, which is consistent with an associative chain transfer mechanism. Reaction of **9** with ethylene generates the corresponding ethylene complex (κ^2-*P,O*-P(*o*-OMe-Ph)$_2CB_9Cl_9$)PdMe($H_2C=CH_2$), which inserts ethylene at -20 ºC with a barrier ($\Delta G^{\neq}_{\text{insertion}}$) of 18.1 kcal/mol.

Chart 1.3. The Complexes that are Described in Chapter 2.

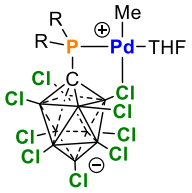

7: R = ^{i}Pr
8: R = Ph

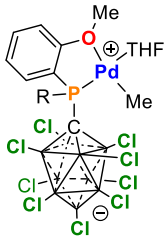

9: R = *o*-OMe-Ph

As discussed in Section 1.2, the PDI ligand system provides the basis for the design of versatile catalysts for a wide variety of chemical transformations. Multinuclear complexes based on bis- or multi-PDI ligands may exhibit new reactivity due to metal-metal cooperativity effects. Chapter Three describes the synthesis of a bis(pyridine-dienamine) proligand **2'** (Scheme 1.6)

synthesized via a non-templated method and its associated bis-PDI or bis-(pyridine-dienamido) (bis-PDE) metal complexes. Several (bis-PDI)M_2Cl_4 (M = Zn, Co, Fe) complexes were synthesized and characterized in solution and in the solid state. These complexes are fluxional at room temperature, and variable temperature NMR studies were conducted to probe the associated macrocyclic ring inversion process and determine activation parameters. A [(bis-PDI)PdBr][$BAr^F{}_4$]$_2$ complex was synthesized and characterized in the solution and solid state. The reaction of $Zr(NMe_2)_4$ with the bis(pyridine-dienamine) proligand generates the (bis-PDE)$Zr_2(NMe_2)_4$ *via* amine elimination. This complex was alkylated with $AlMe_3$ and $Al(CH_2SiMe_3)_3$ to form (bis-PDE)Zr_2Me_4 and (bis-PDE)$Zr_2(CH_2SiMe_3)_2(NMe_2)_2$ respectively, the latter of which was characterized in the solid state.

Scheme 1.6. Synthesis of the Dinuclear Bis-PDI and Bis-PDE Complexes Described in Chapter 3.

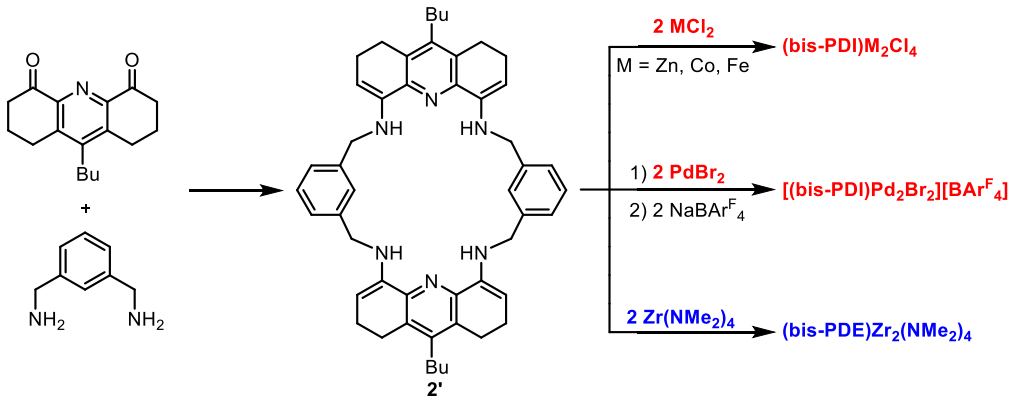

1.4 References

(1) Drent, E.; van Dijk, R.; van Ginkel, R.; van Oort, B.; Pugh, R. I. *Chem. Commun.* **2002**, 744–745.

(2) Johnson, L. K.; Killian, C. M.; Brookhart, M. *J. Am. Chem. Soc.* **1995**, *117*, 6414–6415.

(3) Johnson, L. K.; Mecking, S.; Brookhart, M. *J. Am. Chem. Soc.* **1996**, *118*, 267–268.

(4) DiRenzo, G. M.; White, P. S.; Brookhart, M. *J. Am. Chem. Soc.* **1996**, *118*, 6225–6234.

(5) Mecking, S.; Johnson, L. K.; Wang, L.; Brookhart, M. *J. Am. Chem. Soc.* **1998**, *120*, 888–899.

(6) Skupov, K. M.; Piche, L.; Claverie, J. P. *Macromolecules* **2008**, *41*, 2309–2310.

(7) Piche, L.; Daigle, J. C.; Rehse, G.; Claverie, J. P. *Chem. Eur. J.* **2012**, *18*, 3277–3285.

(8) Skupov, K. M.; Marella, P. R.; Hobbs, J. L.; McIntosh, L. H.; Goodall, B. L.; Claverie, J. P. *Macromolecules* **2006**, *39*, 4279–4281.

(9) Skupov, K. M.; Marella, P. R.; Simard, M.; Yap, G. P. A.; Allen, N.; Conner, D.; Goodall, B. L.; Claverie, J. P. *Macromol. Rapid Commun.* **2007**, *28*, 2033–2038.

(10) Daigle, J.-C.; Piche, L.; Claverie, J. P. *Macromolecules* **2011**, *44*, 1760–1762.

(11) Daigle, J.-C.; Piche, L.; Arnold, A.; Claverie, J. P. *ACS Macro Lett.* **2012**, *1*, 343–346.

(12) Piche, L.; Daigle, J.-C.; Poli, R.; Claverie, J. P. *Eur J Inorg Chem* **2010**, *2010*, 4595–4601.

(13) Kim, Y.; Jordan, R. F. *Organometallics* **2011**, *30*, 4250–4256.

(14) Zhou, X.; Bontemps, S.; Jordan, R. F. *Organometallics* **2008**, *27*, 4821–4824.

(15) Shen, Z.; Jordan, R. F. *Macromolecules* **2010**, *43*, 8706–8708.

(16) Shen, Z.; Jordan, R. F. *J. Am. Chem. Soc.* **2010**, *132*, 52–53.

(17) Nakamura, A.; Anselment, T. M. J.; Claverie, J.; Goodall, B.; Jordan, R. F.; Mecking, S.; Rieger, B.; Sen, A.; van Leeuwen, P. W. N. M.; Nozaki, K. *Acc. Chem. Res.* **2013**, *46*, 1438–1449.

(18) Johnson, A. M.; Contrella, N. D.; Sampson, J. R.; Zheng, M.; Jordan, R. F. *Organometallics* **2017**, *36*, 4990–5002.

(19) Contrella, N. D.; Sampson, J. R.; Jordan, R. F. *Organometallics* **2014**, *33*, 3546–3555.

(20) Conley, M. P.; Jordan, R. F. *Angew. Chem. Int. Ed. Engl.* **2011**, *50*, 3744–3746.

(21) Black, R. E.; Jordan, R. F. *Organometallics* **2017**, *36*, 3415–3428.

(22) Wei, J.; Shen, Z.; Filatov, A. S.; Liu, Q.; Jordan, R. F. *Organometallics* **2016**, *35*, 3557–3568.

(23) Zhou, X.; Lau, K.-C.; Petro, B. J.; Jordan, R. F. *Organometallics* **2014**, *33*, 7209–7214.

(24) Weng, W.; Shen, Z.; Jordan, R. F. *J. Am. Chem. Soc.* **2007**, *129*, 15450–15451.

(25) Luo, S.; Vela, J.; Lief, G. R.; Jordan, R. F. *J. Am. Chem. Soc.* **2007**, *129*, 8946–8947.

(26) Vela, J.; Lief, G. R.; Shen, Z.; Jordan, R. F. *Organometallics* **2007**, *26*, 6624–6635.

(27) Cai, Z.; Shen, Z.; Zhou, X.; Jordan, R. F. *ACS Catal.* **2012**, *2*, 1187–1195.

(28) Wucher, P.; Goldbach, V.; Mecking, S. *Organometallics* **2013**, *32*, 4516–4522.

(29) Wiedemann, T.; Voit, G.; Tchernook, A.; Roesle, P.; Göttker-Schnetmann, I.; Mecking, S. *J. Am. Chem. Soc.* **2014**, *136*, 2078–2085.

(30) Zhang, D.; Guironnet, D.; Göttker-Schnetmann, I.; Mecking, S. *Organometallics* **2009**, *28*, 4072–4078.

(31) Guironnet, D.; Roesle, P.; Rünzi, T.; Göttker-Schnetmann, I.; Mecking, S. *J. Am. Chem. Soc.* **2009**, *131*, 422–423.

(32) Guironnet, D.; Caporaso, L.; Neuwald, B.; Göttker-Schnetmann, I.; Cavallo, L.; Mecking, S. *J. Am. Chem. Soc.* **2010**, *132*, 4418–4426.

(33) Rünzi, T.; Guironnet, D.; Göttker-Schnetmann, I.; Mecking, S. *J. Am. Chem. Soc.* **2010**, *132*, 16623–16630.

(34) Rünzi, T.; Fröhlich, D.; Mecking, S. *J. Am. Chem. Soc.* **2010**, *132*, 17690–17691.

(35) Rünzi, T.; Tritschler, U.; Roesle, P.; Göttker-Schnetmann, I.; Möller, H. M.; Caporaso, L.; Poater, A.; Cavallo, L.; Mecking, S. *Organometallics* **2012**, *31*, 8388–8406.

(36) Neuwald, B.; Ölscher, F.; Göttker-Schnetmann, I.; Mecking, S. *Organometallics* **2012**, *31*, 3128–3137.

(37) Neuwald, B.; Caporaso, L.; Cavallo, L.; Mecking, S. *J. Am. Chem. Soc.* **2013**, *135*, 1026–1036.

(38) Neuwald, B.; Falivene, L.; Caporaso, L.; Cavallo, L.; Mecking, S. *Chem. Eur. J* **2013**, *19*, 17773–17788.

(39) Jian, Z.; Wucher, P.; Mecking, S. *Organometallics* **2014**, *33*, 2879–2888.

(40) Jian, Z.; Falivene, L.; Boffa, G.; Sánchez, S. O.; Caporaso, L.; Grassi, A.; Mecking, S. *Angew. Chem. Int. Ed. Engl.* **2016**, *55*, 14378–14383.

(41) Jian, Z.; Baier, M. C.; Mecking, S. *J. Am. Chem. Soc.* **2015**, *137*, 2836–2839.

(42) Wucher, P.; Schwaderer, J. B.; Mecking, S. *ACS Catal.* **2014**, *4*, 2672–2679.

(43) Jian, Z.; Falivene, L.; Wucher, P.; Roesle, P.; Caporaso, L.; Cavallo, L.; Göttker-Schnetmann, I.; Mecking, S. *Chem. Eur. J.* **2015**, *21*, 2062–2075.

(44) Carrow, B. P.; Nozaki, K. *J. Am. Chem. Soc.* **2012**, *134*, 8802–8805.

(45) Kanazawa, M.; Ito, S.; Nozaki, K. *Organometallics* **2011**, *30*, 6049–6052.

(46) Noda, S.; Nakamura, A.; Kochi, T.; Chung, L. W.; Morokuma, K.; Nozaki, K. *J. Am. Chem. Soc.* **2009**, *131*, 14088–14100.

(47) Mitsushige, Y.; Carrow, B. P.; Ito, S.; Nozaki, K. *Chem. Sci.* **2016**, *7*, 737–744.

(48) Ota, Y.; Ito, S.; Kuroda, J.; Okumura, Y.; Nozaki, K. *J. Am. Chem. Soc.* **2014**, *136*, 11898–11901.

(49) Mitsushige, Y.; Yasuda, H.; Carrow, B. P.; Ito, S.; Kobayashi, M.; Tayano, T.; Watanabe, Y.; Okuno, Y.; Hayashi, S.; Kuroda, J.; Okumura, Y.; Nozaki, K. *ACS Macro Lett.* **2018**, *7*, 305–311.

(50) Yasuda, H.; Nakano, R.; Ito, S.; Nozaki, K. *J. Am. Chem. Soc.* **2018**, *140*, 1876–1883.

(51) Nakano, R.; Chung, L. W.; Watanabe, Y.; Okuno, Y.; Okumura, Y.; Ito, S.; Morokuma, K.; Nozaki, K. *ACS Catal.* **2016**, *6*, 6101–6113.

(52) Nakamura, A.; Ito, S.; Nozaki, K. *Chem. Rev.* **2009**, *109*, 5215–5244.

(53) Ito, S.; Nozaki, K. *Chem. Rec.* **2010**, *10*, 315–325.

(54) Kissling, S.; Lehenmeier, M. W.; Altenbuchner, P. T.; Kronast, A.; Reiter, M.; Deglmann, P.; Seemann, U. B.; Rieger, B. *Chem. Commun.* **2015**, *51*, 4579–4582.

(55) Anselment, T. M. J.; Wichmann, C.; Anderson, C. E.; Herdtweck, E.; Rieger, B. *Organometallics* **2011**, *30*, 6602–6611.

(56) Hearley, A. K.; Nowack, R. J.; Rieger, B. *Organometallics* **2005**, *24*, 2755–2763.

(57) Reisinger, C. M.; Nowack, R. J.; Volkmer, D.; Rieger, B. *Dalton Trans.* **2007**, 272–278.

(58) Haras, A.; Michalak, A.; Rieger, B.; Ziegler, T. *Organometallics* **2006**, *25*, 946–953.

(59) Chen, C.; Anselment, T. M. J.; Fröhlich, R.; Rieger, B.; Kehr, G.; Erker, G. *Organometallics* **2011**, *30*, 5248–5257.

(60) Newsham, D. K.; Borkar, S.; Sen, A.; Conner, D. M.; Goodall, B. L. *Organometallics* **2007**, *26*, 3636–3638.

(61) Liu, S.; Borkar, S.; Newsham, D.; Yennawar, H.; Sen, A. *Organometallics* **2007**, *26*, 210–216.

(62) Borkar, S.; Newsham, D. K.; Sen, A. *Organometallics* **2008**, *27*, 3331–3334.

(63) Luo, R.; Newsham, D. K.; Sen, A. *Organometallics* **2009**, *28*, 6994–7000.

(64) Chen, M.; Yang, B.; Chen, C. *Angew. Chem. Int. Ed. Engl.* **2015**, *54*, 15520–15524.

(65) Tan, C.; Chen, C. *Angew. Chem. Int. Ed. Engl.* **2019**.

(66) Zhang, Y.; Cao, Y.; Leng, X.; Chen, C.; Huang, Z. *Organometallics* **2014**, *33*, 3738–3745.

(67) Sui, X.; Dai, S.; Chen, C. *ACS Catal.* **2015**, *5*, 5932–5937.

(68) Chen, Q.; Zhang, W.; Solan, G. A.; Liang, T.; Sun, W.-H. *Dalton Trans.* **2018**, *47*, 6124–6133.

(69) Ravasio, A.; Boggioni, L.; Tritto, I. *Macromolecules* **2011**, *44*, 4180–4186.

(70) Rezabal, E.; Ugalde, J. M.; Frenking, G. *J. Phys. Chem. A* **2017**, *121*, 7709–7716.

(71) Haras, A.; Anderson, G. D. W.; Michalak, A.; Rieger, B.; Ziegler, T. *Organometallics* **2006**, *25*, 4491–4497.

(72) Friedberger, T.; Ziller, J. W.; Guan, Z. *Organometallics* **2014**, *33*, 1913–1916.

(73) Perrotin, P.; McCahill, J. S. J.; Wu, G.; Scott, S. L. *Chem. Commun.* **2011**, *47*, 6948–6950.

(74) Gott, A. L.; Piers, W. E.; Dutton, J. L.; McDonald, R.; Parvez, M. *Organometallics* **2011**, *30*, 4236–4249.

(75) Zhang, W.; Waddell, P. M.; Tiedemann, M. A.; Padilla, C. E.; Mei, J.; Chen, L.; Carrow, B. P. *J. Am. Chem. Soc.* **2018**, *140*, 8841–8850.

(76) Small, B. L.; Brookhart, M.; Bennett, A. M. A. *J. Am. Chem. Soc.* **1998**, *120*, 4049–4050.

(77) Britovsek, G. J. P.; Bruce, M.; Gibson, V. C.; Kimberley, B. S.; Maddox, P. J.; Mastroianni, S.; McTavish, S. J.; Redshaw, C.; Solan, G. A.; Strömberg, S.; White, A. J. P.; Williams, D. J. *J. Am. Chem. Soc.* **1999**, *121*, 8728–8740.

(78) Bouwkamp, M. W.; Lobkovsky, E.; Chirik, P. J. *J. Am. Chem. Soc.* **2005**, *127*, 9660–9661.

(79) Tondreau, A. M.; Milsmann, C.; Patrick, A. D.; Hoyt, H. M.; Lobkovsky, E.; Wieghardt, K.; Chirik, P. J. *J. Am. Chem. Soc.* **2010**, *132*, 15046–15059.

(80) Bouwkamp, M. W.; Bart, S. C.; Hawrelak, E. J.; Trovitch, R. J.; Lobkovsky, E.; Chirik, P. J. *Chem. Commun.* **2005**, 3406–3408.

(81) Hojilla Atienza, C. C.; Milsmann, C.; Lobkovsky, E.; Chirik, P. J. *Angew. Chem. Int. Ed. Engl.* **2011**, *50*, 8143–8147.

(82) Bryliakov, K. P.; Talsi, E. P.; Semikolenova, N. V.; Zakharov, V. A. *Organometallics* **2009**, *28*, 3225–3232.

(83) Bryliakov, K. P.; Semikolenova, N. V.; Zudin, V. N.; Zakharov, V. A.; Talsi, E. P. *Catal Commun* **2004**, *5*, 45–48.

(84) Bryliakov, K. P.; Semikolenova, N. V.; Zakharov, V. A.; Talsi, E. P. *Organometallics* **2004**, *23*, 5375–5378.

(85) Deng, L.; Margl, P.; Ziegler, T. *J. Am. Chem. Soc.* **1999**, *121*, 6479–6487.

(86) Khoroshun, D. V.; Musaev, D. G.; Vreven, T.; Morokuma, K. *Organometallics* **2001**, *20*, 2007–2026.

(87) Minaev, B.; Baryshnikova, A.; Sun, W.-H. *J Organomet Chem* **2016**, *811*, 48–65.

(88) Cruz, V. L.; Ramos, J.; Martínez-Salazar, J.; Gutiérrez-Oliva, S.; Toro-Labbé, A. *Organometallics* **2009**, *28*, 5889–5895.

(89) Tellmann, K. P.; Humphries, M. J.; Rzepa, H. S.; Gibson, V. C. *Organometallics* **2004**, *23*, 5503–5513.

(90) Trovitch, R. J.; Lobkovsky, E.; Chirik, P. J. *J. Am. Chem. Soc.* **2008**, *130*, 11631–11640.

(91) Bart, S. C.; Chłopek, K.; Bill, E.; Bouwkamp, M. W.; Lobkovsky, E.; Neese, F.; Wieghardt, K.; Chirik, P. J. *J. Am. Chem. Soc.* **2006**, *128*, 13901–13912.

(92) Stieber, S. C. E.; Milsmann, C.; Hoyt, J. M.; Turner, Z. R.; Finkelstein, K. D.; Wieghardt, K.; DeBeer, S.; Chirik, P. J. *Inorg. Chem.* **2012**, *51*, 3770–3785.

(93) Schaefer, B. A.; Margulieux, G. W.; Tiedemann, M. A.; Small, B. L.; Chirik, P. J. *Organometallics* **2015**, *34*, 5615–5623.

(94) Bouwkamp, M. W.; Lobkovsky, E.; Chirik, P. J. *Inorg. Chem.* **2006**, *45*, 2–4.

(95) Bouwkamp, M. W.; Bowman, A. C.; Lobkovsky, E.; Chirik, P. J. *J. Am. Chem. Soc.* **2006**, *128*, 13340–13341.

(96) Rummelt, S. M.; Zhong, H.; Léonard, N. G.; Semproni, S. P.; Chirik, P. J. *Organometallics* **2019**.

(97) Archer, A. M.; Bouwkamp, M. W.; Cortez, M.-P.; Lobkovsky, E.; Chirik, P. J. *Organometallics* **2006**, *25*, 4269–4278.

(98) Fernández, I.; Trovitch, R. J.; Lobkovsky, E.; Chirik, P. J. *Organometallics* **2008**, *27*, 109–118.

(99) Bowman, A. C.; Milsmann, C.; Atienza, C. C. H.; Lobkovsky, E.; Wieghardt, K.; Chirik, P. J. *J. Am. Chem. Soc.* **2010**, *132*, 1676–1684.

(100) Russell, S. K.; Darmon, J. M.; Lobkovsky, E.; Chirik, P. J. *Inorg. Chem.* **2010**, *49*, 2782–2792.

(101) Sylvester, K. T.; Chirik, P. J. *J. Am. Chem. Soc.* **2009**, *131*, 8772–8774.

(102) Bowman, A. C.; Milsmann, C.; Bill, E.; Lobkovsky, E.; Weyhermüller, T.; Wieghardt, K.; Chirik, P. J. *Inorg. Chem.* **2010**, *49*, 6110–6123.

(103) Russell, S. K.; Milsmann, C.; Lobkovsky, E.; Weyhermüller, T.; Chirik, P. J. *Inorg. Chem.* **2011**, *50*, 3159–3169.

(104) Russell, S. K.; Bowman, A. C.; Lobkovsky, E.; Wieghardt, K.; Chirik, P. J. *Eur J Inorg Chem* **2012**, *2012*, 535–545.

(105) Tondreau, A. M.; Atienza, C. C. H.; Weller, K. J.; Nye, S. A.; Lewis, K. M.; Delis, J. G. P.; Chirik, P. J. *Science* **2012**, *335*, 567–570.

(106) Hojilla Atienza, C. C.; Tondreau, A. M.; Weller, K. J.; Lewis, K. M.; Cruse, R. W.; Nye, S. A.; Boyer, J. L.; Delis, J. G. P.; Chirik, P. J. *ACS Catal.* **2012**, *2*, 2169–2172.

(107) Yu, R. P.; Darmon, J. M.; Hoyt, J. M.; Margulieux, G. W.; Turner, Z. R.; Chirik, P. J. *ACS Catal.* **2012**, *2*, 1760–1764.

(108) Atienza, C. C. H.; Milsmann, C.; Semproni, S. P.; Turner, Z. R.; Chirik, P. J. *Inorg. Chem.* **2013**, *52*, 5403–5417.

(109) Darmon, J. M.; Stieber, S. C. E.; Sylvester, K. T.; Fernández, I.; Lobkovsky, E.; Semproni, S. P.; Bill, E.; Wieghardt, K.; DeBeer, S.; Chirik, P. J. *J. Am. Chem. Soc.* **2012**, *134*, 17125–17137.

(110) Obligacion, J. V.; Chirik, P. J. *Org. Lett.* **2013**, *15*, 2680–2683.

(111) Milsmann, C.; Semproni, S. P.; Chirik, P. J. *J. Am. Chem. Soc.* **2014**, *136*, 12099–12107.

(112) Trovitch, R. J.; Lobkovsky, E.; Bill, E.; Chirik, P. J. *Organometallics* **2008**, *27*, 1470–1478.

(113) Joannou, M. V.; Bezdek, M. J.; Al-Bahily, K.; Korobkov, I.; Chirik, P. J. *Organometallics* **2017**, *36*, 4215–4223.

(114) Hoyt, J. M.; Sylvester, K. T.; Semproni, S. P.; Chirik, P. J. *J. Am. Chem. Soc.* **2013**, *135*, 4862–4877.

(115) Obligacion, J. V.; Chirik, P. J. *Nat. Rev. Chem.* **2018**, *2*, 15–34.

(116) Joannou, M. V.; Bezdek, M. J.; Chirik, P. J. *ACS Catal.* **2018**, *8*, 5276–5285.

(117) Obligacion, J. V.; Chirik, P. J. *J. Am. Chem. Soc.* **2013**, *135*, 19107–19110.

(118) E Stieber, S. C.; Milsmann, C.; Hoyt, J. M.; Turner, Z. R.; Finkelstein, K. D.; Wieghardt, K.; Debeer, S.; Chirik, P. J. *Organometallics* **2012**, *31*, 2275–2285.

(119) Mahmood, Q.; Guo, J.; Zhang, W.; Ma, Y.; Liang, T.; Sun, W.-H. *Organometallics* **2018**, *37*, 957–970.

(120) Huang, F.; Xing, Q.; Liang, T.; Flisak, Z.; Ye, B.; Hu, X.; Yang, W.; Sun, W.-H. *Dalton Trans.* **2014**, *43*, 16818–16829.

(121) Wang, L.; Sun, J. *Inorg. Chim. Acta* **2008**, *361*, 1843–1849.

(122) Suo, H.; Solan, G. A.; Ma, Y.; Sun, W.-H. *Coord Chem Rev* **2018**, *372*, 101–116.

(123) Flisak, Z.; Sun, W.-H. *ACS Catal.* **2015**, *5*, 4713–4724.

(124) Xing, Q.; Zhao, T.; Qiao, Y.; Wang, L.; Redshaw, C.; Sun, W.-H. *RSC Adv.* **2013**, *3*, 26184.

(125) Xing, Q.; Zhao, T.; Du, S.; Yang, W.; Liang, T.; Redshaw, C.; Sun, W.-H. *Organometallics* **2014**, *33*, 1382–1388.

(126) Antonov, A. A.; Semikolenova, N. V.; Zakharov, V. A.; Zhang, W.; Wang, Y.; Sun, W.-H.; Talsi, E. P.; Bryliakov, K. P. *Organometallics* **2012**, *31*, 1143–1149.

(127) Semikolenova, N. V.; Sun, W.-H.; Soshnikov, I. E.; Matsko, M. A.; Kolesova, O. V.; Zakharov, V. A.; Bryliakov, K. P. *ACS Catal.* **2017**, *7*, 2868–2877.

(128) Du, S.; Zhang, W.; Yue, E.; Huang, F.; Liang, T.; Sun, W.-H. *Eur J Inorg Chem* **2016**, *2016*, 1748–1755.

(129) Wang, Z.; Solan, G. A.; Mahmood, Q.; Liu, Q.; Ma, Y.; Hao, X.; Sun, W.-H. *Organometallics* **2018**, *37*, 380–389.

(130) Guo, L.; Zada, M.; Zhang, W.; Vignesh, A.; Zhu, D.; Ma, Y.; Liang, T.; Sun, W.-H. *Dalton Trans.* **2019**.

(131) Wang, Z.; Ma, Y.; Guo, J.; Liu, Q.; Solan, G. A.; Liang, T.; Sun, W.-H. *Dalton Trans.* **2019**, *48*, 2582–2591.

(132) Bariashir, C.; Wang, Z.; Solan, G. A.; Huang, C.; Hao, X.; Sun, W.-H. *Polymer* **2019**, *171*, 87–95.

(133) Chen, Q.; Zhang, W.; Solan, G. A.; Zhang, R.; Guo, L.; Hao, X.; Sun, W.-H. *Organometallics* **2018**, *37*, 4002–4014.

(134) Hollingsworth, R. L.; Beattie, J. W.; Grass, A.; Martin, P. D.; Groysman, S.; Lord, R. L. *Dalton Trans.* **2018**, *47*, 15353–15363.

(135) Reed, B. R.; Stoian, S. A.; Lord, R. L.; Groysman, S. *Chem. Commun.* **2015**, *51*, 6496–6499.

(136) Beattie, J. W.; SantaLucia, D. J.; White, D. S.; Groysman, S. *Inorg. Chim. Acta* **2017**, *460*, 8–16.

(137) Reed, B. R.; Yousif, M.; Lord, R. L.; McKinnon, M.; Rochford, J.; Groysman, S. *Organometallics* **2017**, *36*, 582–593.

(138) Groen, J. H.; Annemieke, de Z.; Vlaar, Mark J. M.; Ernsting, J. M.; van Leeuwen, Piet W. N. M.; Vrieze, K.; Kooijman, H.; Smeets, Wilberth J. J.; Spek, A. L.; Budzelaar, Peter H. M.; Xiang, Q.; Thummel, R. P. *European Journal of Inorganic Chemistry* **1998**.

(139) Talarico, G.; Budzelaar, P. H. M. *Organometallics* **2008**, *27*, 4098–4107.

(140) Rahimi, N.; Herbert, D. E.; Budzelaar, P. H. M. *Eur J Inorg Chem* **2018**, *2018*, 4856–4866.

(141) Sugiyama, H.; Korobkov, I.; Gambarotta, S.; Möller, A.; Budzelaar, P. H. M. *Inorg. Chem.* **2004**, *43*, 5771–5779.

(142) Rahimi, N.; de Bruin, B.; Budzelaar, P. H. M. *Organometallics* **2017**, *36*, 3189–3198.

(143) Knijnenburg, Q.; Smits, J. M. M.; Budzelaar, P. H. M. *Organometallics* **2006**, *25*, 1036–1046.

(144) Sugiyama, H.; Aharonian, G.; Gambarotta, S.; Yap, G. P. A.; Budzelaar, P. H. M. *J. Am. Chem. Soc.* **2002**, *124*, 12268–12274.

(145) Khorobkov, I.; Gambarotta, S.; Yap, G. P. A.; Budzelaar, P. H. M. *Organometallics* **2002**, *21*, 3088–3090.

(146) Scott, J.; Vidyaratne, I.; Korobkov, I.; Gambarotta, S.; Budzelaar, P. H. M. *Inorg. Chem.* **2008**, *47*, 896–911.

(147) Scott, J.; Gambarotta, S.; Korobkov, I.; Budzelaar, P. H. M. *J. Am. Chem. Soc.* **2005**, *127*, 13019–13029.

(148) Vidyaratne, I.; Gambarotta, S.; Korobkov, I.; Budzelaar, P. H. M. *Inorg. Chem.* **2005**, *44*, 1187–1189.

(149) Scott, J.; Gambarotta, S.; Korobkov, I.; Knijnenburg, Q.; de Bruin, B.; Budzelaar, P. H. M. *J. Am. Chem. Soc.* **2005**, *127*, 17204–17206.

(150) Zhu, D.; Budzelaar, P. H. M. *Organometallics* **2008**, *27*, 2699–2705.

(151) Vidyaratne, I.; Scott, J.; Gambarotta, S.; Budzelaar, P. H. M. *Inorg. Chem.* **2007**, *46*, 7040–7049.

(152) Scott, J.; Gambarotta, S.; Korobkov, I.; Budzelaar, P. H. M. *Organometallics* **2005**, *24*, 6298–6300.

(153) Zhu, D.; Korobkov, I.; Budzelaar, P. H. M. *Organometallics* **2012**, *31*, 3958–3971.

(154) Gibson, V. C.; Redshaw, C.; Solan, G. A. *Chem. Rev.* **2007**, *107*, 1745–1776.

(155) Gibson, V. C.; Long, N. J.; Oxford, P. J.; White, A. J. P.; Williams, D. J. *Organometallics* **2006**, *25*, 1932–1939.

(156) Tellmann, K. P.; Gibson, V. C.; White, A. J. P.; Williams, D. J. *Organometallics* **2005**, *24*, 280–286.

(157) Humphries, M. J.; Tellmann, K. P.; Gibson, V. C.; White, A. J. P.; Williams, D. J. *Organometallics* **2005**, *24*, 2039–2050.

(158) McTavish, S.; Britovsek, G. J. P.; Smit, T. M.; Gibson, V. C.; White, A. J. P.; Williams, D. J. *J. Mol. Catal. A: Chem* **2007**, *261*, 293–300.

(159) Britovsek, G. J.; Mastroianni, S.; Solan, G. A.; Baugh, Simon P. D.; Redshaw, C.; Gibson, V. C.; White, Andrew J. P.; Williams, D. J.; Elsegood, Mark R. J. *Chemistry - A European Journal* **2000**.

(160) Gibson, V. C.; McTavish, S.; Redshaw, C.; Solan, G. A.; White, A. J. P.; Williams, D. J. *Dalton Trans.* **2003**, 221–226.

(161) Britovsek, G. J. P.; Cohen, S. A.; Gibson, V. C.; Van Meurs, M. *J. Am. Chem. Soc.* **2004**, *126*, 10701–10712.

(162) Blackmore, I. J.; Gibson, V. C.; Hitchcock, P. B.; Rees, C. W.; Williams, D. J.; White, A. J. P. *J. Am. Chem. Soc.* **2005**, *127*, 6012–6020.

(163) Smit, T. M.; Tomov, A. K.; Gibson, V. C.; White, A. J. P.; Williams, D. J. *Inorg. Chem.* **2004**, *43*, 6511–6512.

(164) Britovsek, G. J. P.; Gibson, V. C.; Spitzmesser, S. K.; Tellmann, K. P.; White, A. J. P.; Williams, D. J. *J. Chem. Soc., Dalton Trans.* **2002**, 1159.

(165) Gibson, V. C.; Tellmann, K. P.; Humphries, M. J.; Wass, D. F. *Chem. Commun.* **2002**, 2316–2317.

(166) Smit, T. M.; Tomov, A. K.; Britovsek, G. J. P.; Gibson, V. C.; White, A. J. P.; Williams, D. J. *Catal. Sci. Technol.* **2012**, *2*, 643.

(167) Britovsek, G. .; Gibson, V.; Mastroianni, S.; Oakes, D. .; Redshaw, C.; Solan, G.; White, A. .; Williams, D. *European Journal of Inorganic Chemistry* **2001**.

(168) Biernesser, A. B.; Li, B.; Byers, J. A. *J. Am. Chem. Soc.* **2013**, *135*, 16553–16560.

(169) Qi, M.; Dong, Q.; Wang, D.; Byers, J. A. *J. Am. Chem. Soc.* **2018**, *140*, 5686–5690.

(170) Delle Chiaie, K. R.; Biernesser, A. B.; Ortuño, M. A.; Dereli, B.; Iovan, D. A.; Wilding, M. J. T.; Li, B.; Cramer, C. J.; Byers, J. A. *Dalton Trans.* **2017**, *46*, 12971–12980.

(171) Ortuño, M. A.; Dereli, B.; Chiaie, K. R. D.; Biernesser, A. B.; Qi, M.; Byers, J. A.; Cramer, C. J. *Inorg. Chem.* **2018**, *57*, 2064–2071.

(172) Delle Chiaie, K. R.; Yablon, L. M.; Biernesser, A. B.; Michalowski, G. R.; Sudyn, A. W.; Byers, J. A. *Polym. Chem.* **2016**, *7*, 4675–4681.

(173) Biernesser, A. B.; Delle Chiaie, K. R.; Curley, J. B.; Byers, J. A. *Angew. Chem. Int. Ed. Engl.* **2016**, *55*, 5251–5254.

(174) Manna, C. M.; Kaur, A.; Yablon, L. M.; Haeffner, F.; Li, B.; Byers, J. A. *J. Am. Chem. Soc.* **2015**, *137*, 14232–14235.

(175) Small, B. L. *Acc. Chem. Res.* **2015**, *48*, 2599–2611.

(176) Small, B. L.; Brookhart, M. *J. Am. Chem. Soc.* **1998**, *120*, 7143–7144.

(177) Small, B. L.; Marcucci, A. J. *Organometallics* **2001**, *20*, 5738–5744.

(178) Small, B. L. *Organometallics* **2003**, *22*, 3178–3183.

(179) Li, W.; Lyu, Y.; Zhang, H.; Zhu, M.; Tang, H. *Dalton Trans.* **2016**, *46*, 106–115.

(180) Sherbow, T. J.; Carr, C. R.; Saisu, T.; Fettinger, J. C.; Berben, L. A. *Organometallics* **2016**, *35*, 9–14.

(181) Myers, T. W.; Sherbow, T. J.; Fettinger, J. C.; Berben, L. A. *Dalton Trans.* **2016**, *45*, 5989–5998.

(182) Myers, T. W.; Berben, L. A. *J. Am. Chem. Soc.* **2013**, *135*, 9988–9990.

(183) Dammann, W.; Buban, T.; Schiller, C.; Burger, P. *Dalton Trans.* **2018**, *47*, 12105–12117.

(184) Nückel, S.; Burger, P. *Organometallics* **2001**, *20*, 4345–4359.

(185) Sieh, D.; Schlimm, M.; Andernach, L.; Angersbach, F.; Nückel, S.; Schöffel, J.; Šušnjar, N.; Burger, P. *Eur J Inorg Chem* **2012**, *2012*, 444–462.

(186) Liu, P.; Zhang, W.; He, R. *Appl Organomet Chem* **2009**, *23*, 135–139.

(187) *Synthesis and Reactivity in Inorganic, Metal-Organic, and Nano-Metal Chemistry*.

(188) Appukuttan, V. K.; Liu, Y.; Son, B. C.; Ha, C.-S.; Suh, H.; Kim, I. *Organometallics* **2011**, *30*, 2285–2294.

(189) Kim, I.; Ha, Y. S.; Ha, C.-S. *Macromol. Rapid Commun.* **2004**, *25*, 1069–1072.

(190) Hanton, M. J.; Tenza, K. *Organometallics* **2008**, *27*, 5712–5716.

(191) Ben-Daat, H.; Hall, G. B.; Groy, T. L.; Trovitch, R. J. *Eur J Inorg Chem* **2013**, *2013*, 4430–4442.

(192) Thammavongsy, Z.; LeDoux, M. E.; Breuhaus-Alvarez, A. G.; Seda, T.; Zakharov, L. N.; Gilbertson, J. D. *Eur J Inorg Chem* **2013**, *2013*, 4008–4015.

(193) Widger, L. R.; Jiang, Y.; Siegler, M. A.; Kumar, D.; Latifi, R.; de Visser, S. P.; Jameson, G. N. L.; Goldberg, D. P. *Inorg. Chem.* **2013**, *52*, 10467–10480.

(194) Liu, H.; Wang, F.; Han, C.; Zhang, H.; Bai, C.; Hu, Y.; Zhang, X. *Inorg. Chim. Acta* **2015**, *434*, 135–142.

(195) Esteruelas, M. A.; López, A. M.; Méndez, L.; Oliván, M.; Oñate, E. *Organometallics* **2003**, *22*, 395–406.

(196) Hoyt, J. M.; Schmidt, V. A.; Tondreau, A. M.; Chirik, P. J. *Science* **2015**, *349*, 960–963.

(197) Schmidt, V. A.; Hoyt, J. M.; Margulieux, G. W.; Chirik, P. J. *J. Am. Chem. Soc.* **2015**, *137*, 7903–7914.

(198) Bart, S. C.; Lobkovsky, E.; Chirik, P. J. *J. Am. Chem. Soc.* **2004**, *126*, 13794–13807.

(199) Rummelt, S. M.; Zhong, H.; Korobkov, I.; Chirik, P. J. *J. Am. Chem. Soc.* **2018**, *140*, 11589–11593.

Chapter Two

Ethylene Oligomerization and Polymerization by Palladium(II) Methyl Complexes Supported by Phosphines Bearing a Perchlorinated 10-Vertex *closo*-Carborane Anion Substituent

2.1 Introduction

Square planar palladium(II) alkyl complexes that contain unsymmetrical chelating phosphine-arenesulfonate ligands (**A**, Chart 2.1) have been studied extensively because of their ability to polymerize ethylene to linear polyethylene and copolymerize ethylene with polar monomers.[1–3] However, the performance of these catalysts is generally inferior compared to that of other classes of olefin polymerization catalysts, which has motivated studies of related catalysts with other unsymmetrical ligands.[4–12] One interesting analog of **A**, studied independently by the Jordan and Piers groups, is the zwitterionic phosphine-trifluoroborate system **B**, in which the sulfonate unit of **A** is replaced by a weakly-coordinating trifluoroborate group.[9,11] In the presence of ([$H(OEt_2)_2$][$B(3,5\text{-}(CF_3)_2\text{-}C_6H_3)_4$]) to sequester the collidine ligand as [collidinium][$B(3,5\text{-}(CF_3)_2\text{-}C_6H_3)_4$], **B** (L = collidine) catalytically dimerizes ethylene to butene with a turnover frequency (TOF) of 385 t.o./h at 23 °C (CD_2Cl_2 solvent, 150 psi ethylene). Under these conditions, the catalyst resting state is the (κ^2-*P*,*F*-*o*-$PPh_2C_6H_4BF_3$)$PdEt(H_2C{=}CH_2)$ complex and the primary product 1-butene is isomerized to *cis* and *trans* 2-butene.

Carborane clusters offer interesting possibilities as frameworks or components for ligands for organometallic catalysts due to their structural rigidity, steric and electronic tunability[13–17] and synthetic availability. [18–30] In particular, halogenated *closo*-carborane anions are exceptionally

stable[31,32] and may engage in weak dative BX→M interactions that may influence catalyst performance.[33]

Chart 2.1. Pd(II) Alkyl Complexes with Unsymmetrical Chelating Ligands. B atoms in the Carboranes are Represented as Unlabeled Vertices.

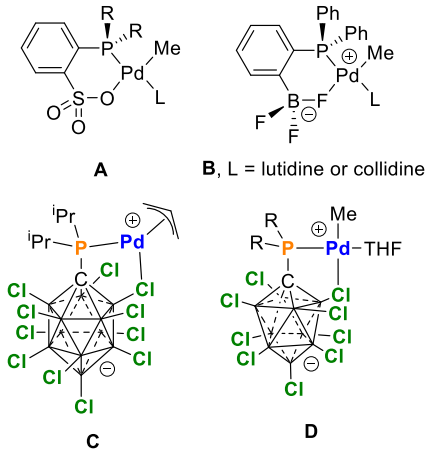

Lavallo and coworkers recently reported the synthesis and characterization of zwitterionic ($P^iPr_2CB_{11}Cl_{11}$)Pd(allyl) (**C**, Chart 2.1), bearing a diisopropyl phosphine ligand with a 12-vertex perchloro-*closo*-carborane anion substituent.[34] In the solid-state the $P^iPr_2CB_{11}Cl_{11}^-$ ligand in **C** is bound in an κ^2-*P,Cl* mode, and thus **C** may be viewed as a structural analogue of **B**. Complex **C** reacts with norbornene to give organic-soluble polynorbornene but does not react with ethylene.

Here we describe the synthesis and reactivity with ethylene of ($PR_2CB_9Cl_9$)PdMe(THF) complexes of type **D**, bearing a 10-vertex perchloro-*closo*-carborane anion substituent bearing a 10-vertex perchloro-*closo*-carborane anion substituent. Based on studies of the parent $P^iPr_2CB_9H_9^-$ and $P^iPr_2CB_{11}H_{11}^-$ ligands, a $PR_2CB_9Cl_9^-$ ligand is expected to be a stronger donor and to exhibit a slightly smaller cone angle compared to an analogous $PR_2CB_{11}Cl_{11}^-$ ligand.[14] The objective of

the present work was to explore how these differences influence the reactivity of complexes of type **D** with ethylene. The steric and electronic properties of the phosphine-arenesulfonate ligands in **A** strongly influence the ethylene polymerization performance.[35] We report the synthesis of a new family of $PR_2CB_9Cl_9^-$ ligands (**1**, R = ^{i}Pr; **2**, R = Ph; **3**, R = *o*-OMe-Ph) and the corresponding zwitterionic $(PR_2CB_9Cl_9)PdMe(THF)$ complexes (**7**–**9**). Complexes **7** and **8**, which contain diisopropyl- and diphenyl-phosphino units respectively, are structurally analogous to **B**, with the $PR_2CB_9Cl_9^-$ ligands bound to Pd in a κ^2-*P*,*Cl* mode. In contrast, **9**, which contains a di-*o*-anisolyl phosphine unit, adopts a κ^2-*P*,*O* bonding mode in which one *o*-anisolyl methoxy group is bound to Pd.

2.2 Results and Discussion

Synthesis and Characterization of $(PR_2CB_9Cl_9)PdMe(THF)$ Complexes. The $PR_2CB_9Cl_9^-$ ligands **1**–**3** were synthesized as the $Li(THF)_x$ salts (x = 2–4) following the procedure developed earlier for the 12-vertex analogue $[Li(THF)_3][P^iPr_2CB_{11}Cl_{11}]$ (Scheme 2.1).[19,34] C-Lithiation of $HCB_9Cl_9^-$ followed by addition of the appropriate R_2PCl electrophile affords $[Li(THF)_x][$**1**–**3**] in >90 % yield.

The reaction of $[Li(THF)_x][$**1**–**3**] with (COD)PdMeCl yields the chloro-bridged dinuclear complexes $[Li(THF)_3][\{(PR_2CB_9Cl_9)PdMe\}_2(\mu\text{-}Cl)]$ ($[Li(THF)_3][$**4**]–$[Li(THF)_3][$**6**]). Reaction of $[Li(THF)_3][$**4**]–$[Li(THF)_3][$**6**] with 0.5 equiv of $AgBF_4$ yields the corresponding $(PR_2CB_9Cl_9)PdMe(THF)$ complexes **7**–**9** in > 80% yield.

Scheme 2.1. Synthesis of Ligands and Complexes.

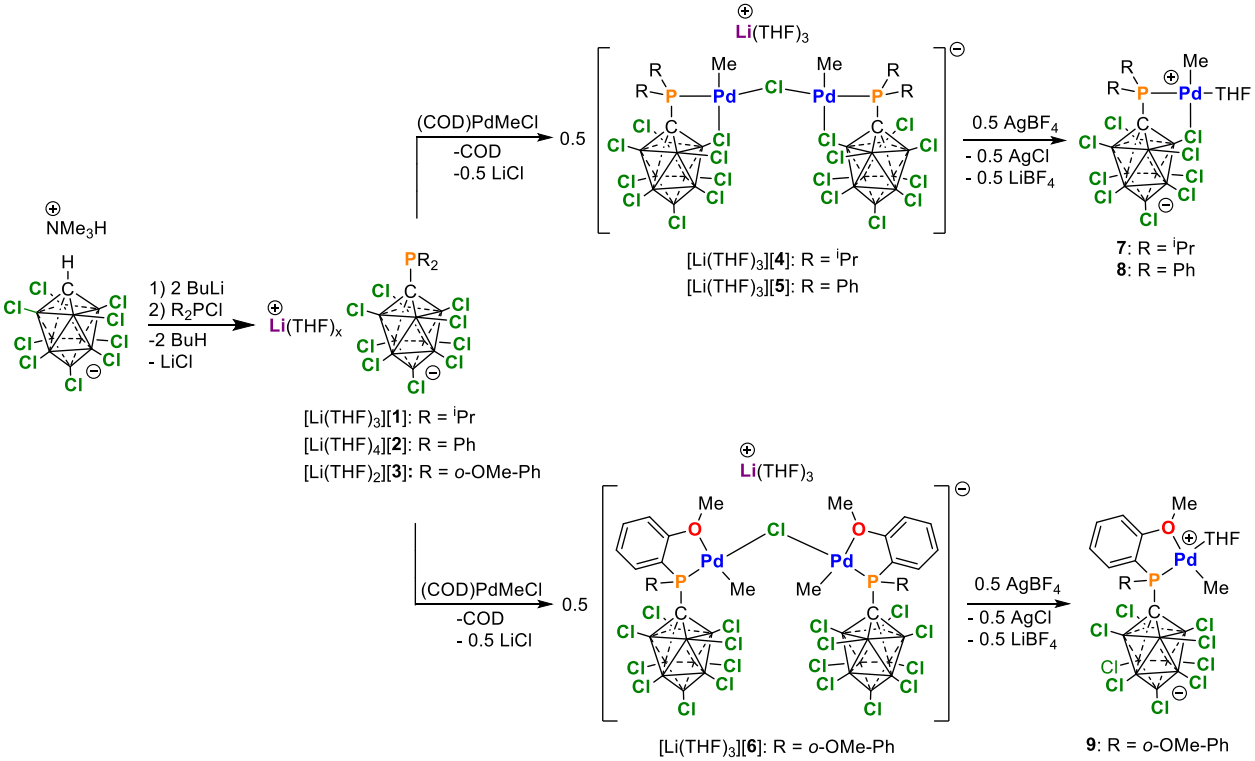

X-ray quality crystals of [Li(THF)$_3$][**5**] were grown from THF/pentane. Crystallization of **7** from CH$_3$CN/PhF gave X-ray quality crystals of the corresponding CH$_3$CN adduct ($P^iPr_2CB_9Cl_9$)PdMe(CH$_3$CN)•(PhF)$_{0.89}$ (**7**–**CH$_3$CN**•(PhF)$_{0.89}$). X-ray quality crystals of **8** were grown from PhF/hexanes. X-ray structural analyses of [Li(THF)$_3$][**5**], **7**–**CH$_3$CN**, and **8** (Figures 2.1 – 2.3) show that the $PR_2CB_9Cl_9^-$ ligands are bound in a κ^2-*P*,*Cl* mode in these complexes. The B–Cl bond lengths for the bound B–Cl units ([Li(THF)$_3$][**5**]: 1.790(2) Å, **7**–**CH$_3$CN**: 1.795(2) Å; **8**: 1.800(2) Å) are ca. 0.03 Å longer than average lengths of the terminal B–Cl bonds in the *ortho* layer of the carboranyl unit ([Li(THF)$_3$][**5**]: 1.761[1] Å, **7**–**CH$_3$CN**: 1.768[1] Å; **8**: 1.764[4] Å), similar to what is observed for **C**.[34] The 5-membered Pd–P–C–B–Cl chelate ring adopts an

envelope conformation in **7** and a planar conformation in [Li(THF)$_3$][**5**] and **8**. The Pd-Me group is *cis* to phosphine in all three complexes as expected due to the stronger *trans* influence of the phosphine versus the weakly-coordinating B-Cl unit. In the solid-state structure of [Li(THF)$_3$][**5**], the positively charged Li(THF)$_3^+$ unit is in close contact with the sterically accessible *p*-Cl of one of the $CB_9Cl_9^-$ units, indicative of negative charge density on the these clusters.

Figure 2.1. Solid state structure of [Li(THF)$_3$][**5**]: H atoms are omitted. Thermal ellipsoids are drawn at the 50% probability level. Key bond lengths (Å): Li1-Cl4 2.575(4) Pd1-C1 2.024(2), Pd1-P1 2.2255(6), Pd1-Cl1 2.4950(5), Pd1-Cl2 2.3847(6), B1-Cl1 1.790(2), Pd2-C2 2.024(2), Pd2-P2 2.2137(8), Pd2-Cl3 2.5600(5), Pd2-Cl2 2.3963(8), B2-Cl3 1.789(2). Key bond angles (°): C1-Pd1-P2 89.62(6), C1-Pd1-Cl2 84.70(2), P1-Pd1-Cl1 89.62(6), Cl2-Pd1-Cl 84.70(2), Pd1-Cl2-Pd2 103.34(2). Color code: C, gray; B, pink; Cl, green; P, orange; Pd, blue; O, red; Li, violet.

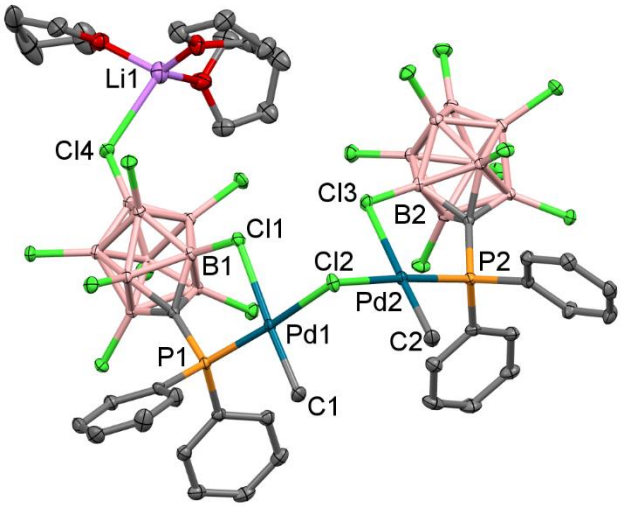

Figure 2.2. Solid state structure of **7–CH_3CN•**$(PhF)_{0.89}$. H atoms and PhF molecules are omitted and only one orientation of the disordered ^{i}Pr unit is shown. Thermal ellipsoids are drawn at the 50% probability level. Key bond lengths (Å): Pd1-C1 2.029(3), Pd1-P1 2.2329(6), Pd1-N1 2.088(2), Pd1-Cl1 2.5876(7), B1-Cl1 1.795(2). Key bond angles (º): C1-Pd1-P1 91.79(8), C1-Pd1-N1B 88.4(1), P1-Pd1-Cl1 87.36(2), N1-Pd1-Cl 92.78(6). Color code: C, gray; B, pink; Cl, green; P, orange; Pd, blue; O, red; N, light blue.

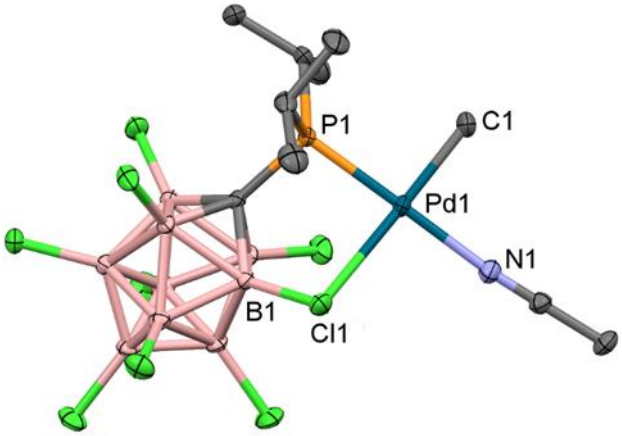

Figure 2.3. Solid state structure of **8**. H atoms are omitted. One orientation is shown. Thermal ellipsoids are drawn at the 50% probability level. Key bond lengths (Å): Pd1-C1 2.021(2), Pd1-O1 2.1362(15), Pd1-P1 2.2070(7), Pd1-Cl1 2.5135(6), B2-Cl1 1.800(2). Key bond angles (º): C1-Pd1-O1 90.05(8), C1-Pd1-P1 88.18(7), O1-Pd1-Cl1 88.71(5), Cl1-Pd1-P1 93.20(2). Color code: C, gray; B, pink; Cl, green; P, orange; Pd, blue; O, red.

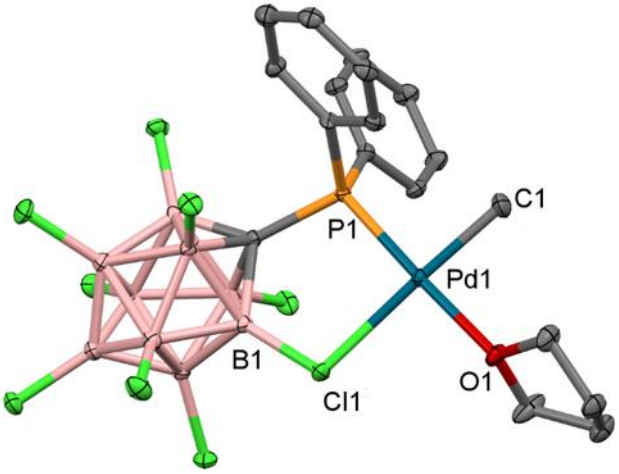

X-ray quality crystals of **9•**$(CH_2Cl_2)_{1.037}$(pentane)$_{0.5}$ were grown from CH_2Cl_2/pentane. In contrast to the κ^2-*P,Cl* bonding mode observed for the $PR_2CB_9Cl_9^-$ ligands in [Li(THF)$_3$][**5**], **7–CH$_3$CN** and **8**, X-ray analysis shows that the P(*o*-OMe-Ph)$_2CB_9Cl_9^-$ ligand in **9** is bound in a κ^2-*P,O* mode through one of the *o*-anisolyl methoxy groups (Figure 2.4). The difference in structure between **8** and **9** may be driven by steric effects. Analysis of a space-filling model of **8** (Figure 2.5) reveals that the P*Ph$_2$* rings are pinned by the bulky perchlorocarboranyl unit in sterically crowded positions that would be inaccessible for the larger P*(o-OMe-Ph)$_2$* groups of **9**. Additionally, the ether functionality in **9** is a stronger donor compared to the weakly-coordinating B–Cl moiety of the $CB_9Cl_9^-$ unit. The Pd–P–C–C–O chelate ring in **9** adopts an envelope conformation. The non-Pd-bound –OMe group is positioned above the Pd square plane and is in close contact with the Pd center (Pd–O3 = 3.063 Å; sum of O and Pd van der Waals radii = 3.15 Å).

Figure 2.4. Solid state structure of **9**•$(CH_2Cl_2)_{1.037}(C_5H_{12})_{0.5}$. H atoms and CH_2Cl_2 and pentane solvent molecules are omitted. Thermal ellipsoids are drawn at the 50% probability level. Only one orientation of the disordered THF ligand is shown. Bond lengths (Å): Pd1-O1 2.127(1), Pd1-C1 2.019(1), Pd1-P1 2.1855(7), Pd1-O2 2.225(1). Key bond angles (º): O1-Pd1-C1 92.75(5), O1-Pd1-O2 89.98(4), C1-Pd1-P1 94.33(4), P1-Pd1-O1 82.53(3). Color code: C, gray; B, pink; Cl, green; P, orange; Pd, blue; O, red.

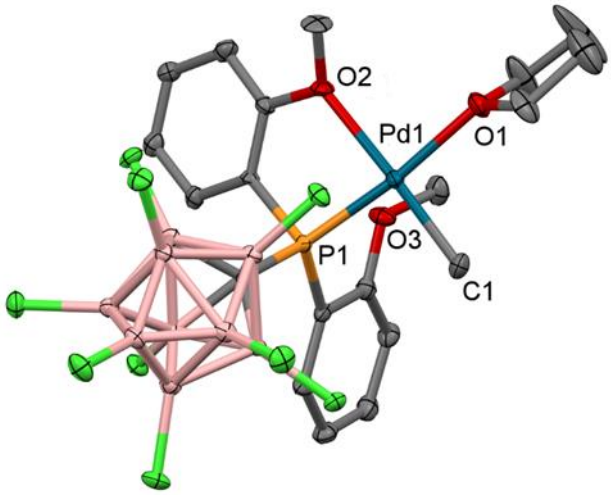

The $^{11}B\{^1H\}$ NMR spectra of [Li(THF)$_3$][**5**], **7**, and **8** contain three resonances in a 1:4:4 intensity ratio, indicative of effective C_{4v} symmetry of the $CB_9Cl_9^-$ cluster. This is consistent with the $CB_9Cl_9^-$ unit rotating rapidly around the C–P bond with concomitant exchange of the Pd-bound and non-Pd-bound B-Cl units on the *ortho*-ring of the carborane clusters in these compounds, as observed previously for **C**.[34]

Figure 2.5. Left: view of the space-filling model of **8** looking down the P-Pd bond. Right, view of the space-filling model of **8** looking down unto the Pd square plane.

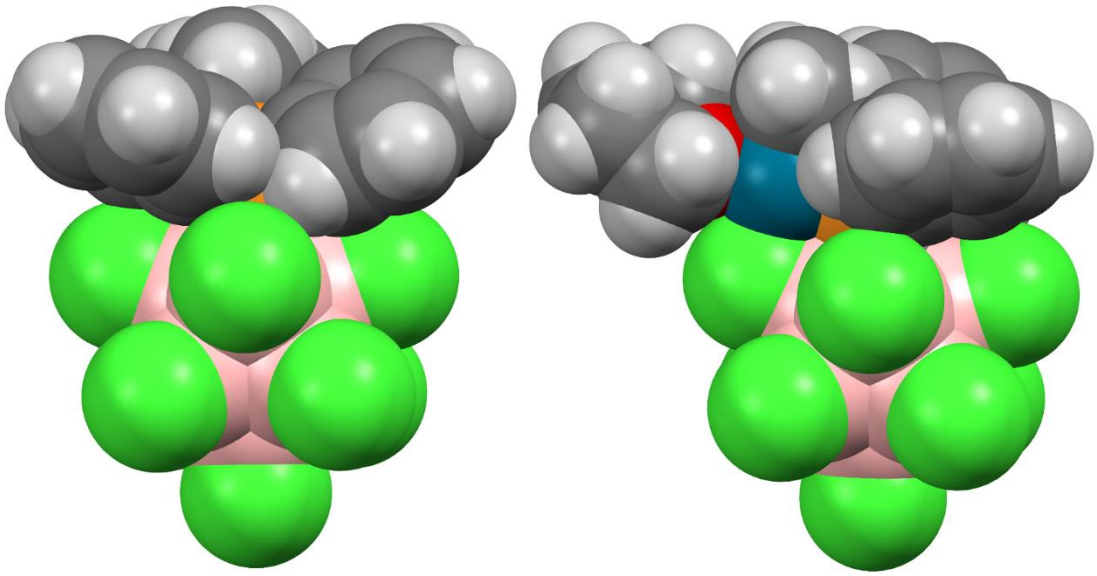

The low temperature (-60 °C) ^{1}H NMR and ^{13}C{^{1}H} NMR spectra in CD_2Cl_2 of **9** contain two sets of *o*-anisolyl resonances (Figure 2.6). The difference in the chemical shifts of the –OMe resonances (^{1}H: $\Delta\delta = 0.32$; ^{13}C: $\Delta\delta(^{13}C) = 3.7$) is close to the coordination shift for the THF α-H resonances (^{1}H: $\delta_{bound} - \delta_{free} = 0.47$; ^{13}C: $\delta_{bound} - \delta_{free} = 4.6$), which is consistent with the coordination of one –OMe group to Pd, as observed in the solid-state structure. The ^{1}H NMR and ^{13}C{^{1}H} spectra of **9** in CD_2Cl_2 at room temperature contain one set of *o*-anisolyl resonances, indicating that the *o*-anisolyl groups exchange rapidly on the NMR timescale at this temperature. The barrier to anisolyl group exchange, $\Delta G^{\neq} = 12.3$ kcal/mol, was determined from the coalescence of the –OMe ^{1}H NMR resonances ($T_{coalescence}$ = -5 °C, 500 MHz). The ^{11}B{^{1}H} NMR spectrum of **9** is similar to those of [Li(THF)$_3$][**5**], **7**, and **8**, indicating that the $CB_9Cl_9^-$ unit rotates rapidly around the C–P bond, regardless of the phosphine-carborane bonding mode, κ^2-*P*,*Cl* or κ^2-*P*,*O*.

Figure 2.6. ^{1}H NMR spectra of **9** at 23 ºC (top) and -60 ºC (bottom) illustrating the exchange of the anisolyl rings. The aromatic and –OMe regions of the spectra are shown. The –OMe resonances appear at δ 4.05 and 3.73 at -60 ºC and are coalesced at 23 ºC (CD_2Cl_2).

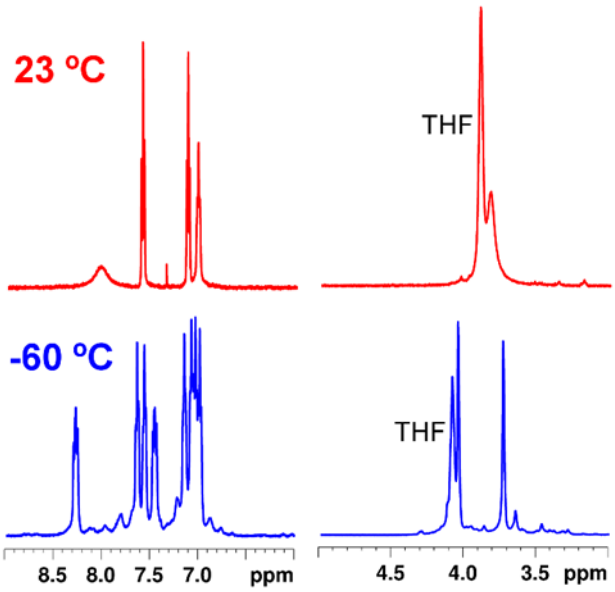

The ^{1}H and ^{31}P{^{1}H} NMR spectra of [Li(THF)$_3$][**6**] at -60 ºC in CD_2Cl_2 show that this species exists as a 1.6/1 mixture of two isomers, each of which exhibits two sets of anisolyl resonances in the ^{1}H spectrum. The isomers are assigned as diastereomers that differ in the relative configuration of the phosphorous atoms, which are stereogenic centers due to the κ^2-*P,O* bonding mode of the P(*o*-OMe-Ph)$_2$CB$_9$Cl$_9^-$ ligand. In contrast, only one species is observed at room temperature and -60 ºC in the ^{1}H and ^{31}P{^{1}H} NMR spectra of κ^2-*P,Cl*-[Li(THF)$_3$][**5**]. The difference in the ^{1}H chemical shifts for the Pd-bound and non-Pd-bound –OMe groups of [Li(THF)$_3$][**6**] ($\Delta\delta_{\text{major isomer}}$ = 0.52, $\Delta\delta_{\text{minor isomer}}$ = 0.80) of [Li(THF)$_3$][**6**] are similar to that for **9**. Isomer exchange is fast on the NMR time scale at 23 ºC due to fast exchange of the Pd-bound and non-Pd-bound methoxy groups.

Ethylene Reactivity. Complexes **7** and **8** oligomerize ethylene to a Schulz-Flory distribution of C_4 – C_{10} olefins at 23 ºC and 2 atm ethylene pressure in mixed toluene/fluorobenzene solvent (Table 2.1). GC-MS analysis of the oligomers shows that **7** produces predominately α-olefins while **8** produces an approximately 1/1 mixture of α-olefins and internal olefins. Catalyst **7** is 5 times more active than **8**. In both cases, the catalytic activity and molecular weight distribution of the oligomers (as assessed by the Schulz-Flory propagation probability α)[36] are independent of ethylene pressure and are unaffected by the addition of $B(C_6F_5)_3$.

Complex **9** reacts with ethylene at 23 ºC and 2 atm ethylene pressure to produce polyethylene (PE) wax with a narrow molecular weight distribution characteristic of a single-site catalyst (Table 2.2). At 50 ºC the activity is increased by a factor of 4 while the M_n value of the product is decreased by a factor of 3. As observed for **7** and **8**, the catalyst activity and M_n of the polymer are independent of ethylene pressure (up to 54 atm) and are unaffected by the presence of $B(C_6F_5)_3$.

The observation that the ethylene oligomerization/polymerization activity of **7**–**9** is independent of ethylene pressure and unaffected by the presence of $B(C_6F_5)_3$ suggests that the resting state for these catalysts is the corresponding $(PR_2CB_9Cl_9)PdR'(CH_2{=}CH_2)$ ethylene complex (R' = growing chain). The observation that the molecular weight of the oligomer/polymer product is independent of ethylene pressure is consistent with an associative chain transfer mechanism, which is typical for square planar ethylene polymerization catalysts.[37]

Table 2.1. Ethylene Oligomerization Data for Catalysts 7 and 8.[a]

Entry[b]	Cat.	P (atm)	Ethylene Consumed (mg)[d]	Activity (kg mol_{Pd}^{-1} h^{-1})	TOF (h^{-1})	α[e]	% α-olefin[f]
1	7[c]	2	420	210	7500	0.15	85
2	7[c]	6	470	240	8400	0.16	91
3[g]	7[c]	6	450	220	8000	0.17	83
4	8[h]	2	450	45	1600	0.22	47
5	8[h]	6	513	51	1800	0.17	46
6[g]	8[h]	6	540	54	1900	0.16	48

[a]Conditions: 49 mL toluene, 1 mL fluorobenzene, 23 ºC, 2 h. [b]Average of two identical runs. [c]1 μmol Pd. [d]Determined by mass flow. [e]Schulz-Flory propagation probability. [f]Percentage of olefins that are α-olefins, determined by GC-MS. [g]1 equiv of $B(C_6F_5)_3$ added. [h]5 μmol Pd.

Table 2.2. Ethylene Polymerization Data for Catalyst 9.[a]

Entry[b]	P (atm)	Yield (mg)	Activity (kg mol_{Pd}^{-1} h^{-1})	TOF (h^{-1})	M_n (Da)[c]	M_n (Da)[d]	Đ[d]	Branches /1000 C[c]	T_m (ºC)[g]
1	2	103	10.3	370	1080	810	1.6	14	82.5, 92.3, 104.5
2[e]	2	345	34.5	1240	720	460	1.4	15	73.2, 89.2, 97.4
3	6	135	13.5	480	950	710	1.6	12	77.9,87.0, 103.0
4[f]	6	132	13.2	470	980	710	1.6	13	76.6, 86.6,102.6
5	54	100	10.0	360	810	580	1.5	14	71.0, 101.5

[a]Conditions: 49 mL toluene, 1 mL fluorobenzene, 23 ºC, 2 h, 5 μmol Pd. [b]Average of two identical runs. [c]Determined by ^{1}H NMR. [d]Determined by GPC. [e]50 ºC. [f]1 equiv of $B(C_6F_5)_3$ added. [g]Determined by DSC

Characterization of Polyethylene Produced by 9. The PE formed by **9** was characterized by ^{1}H and $^{13}C\{^1H\}$ NMR and representative spectra shown in Figure 2.7 and Figure 2.8 respectively. Peak assignments were made based on literature data and 2D NMR experiments.[38–48] The PE produced by **9** at 23 ºC contains one olefin unit per chain, of which >95% are internal olefins. The internal olefins comprise primarily 2-olefins (42%), followed by 3-olefins (21%), 4-olefins (10%) and 5+-olefins (27%), with 70 % of the total olefins in the *trans* configuration. The triplet at δ 1.05 in ^{1}H NMR was assigned as the homoallylic methyl group of the 3-olefin chain-

ends on the basis of an HMBC spectrum. The broad resonance at δ 1.2 in ^{1}H NMR was assigned as the αB_1 hydrogens by HSQC spectroscopy. The PE produced at 50 ºC contains 90% internal olefins (Table 2, entry 2) in a 1/1 *cis*/*trans* ratio. The PEs produced at both 23 and 50 ºC contain ca. 13 branches per 1000 C (i.e. ca. one branch per chain) as determined by ^{1}H NMR. ^{13}C{^{1}H} NMR analysis shows that methyl, ethyl and *sec*-butyl branches are present in a 3/1/1 ratio. The PE microstructure is independent of ethylene pressure and is unaffected by the presence of $B(C_6F_5)_3$.

Figure 2.7. ^{1}H NMR spectrum of polyethylene formed by **9** (Table 2.2, entry 1). NMR Conditions: $CDCl_2CDCl_2$, 500 MHz, 100 ºC

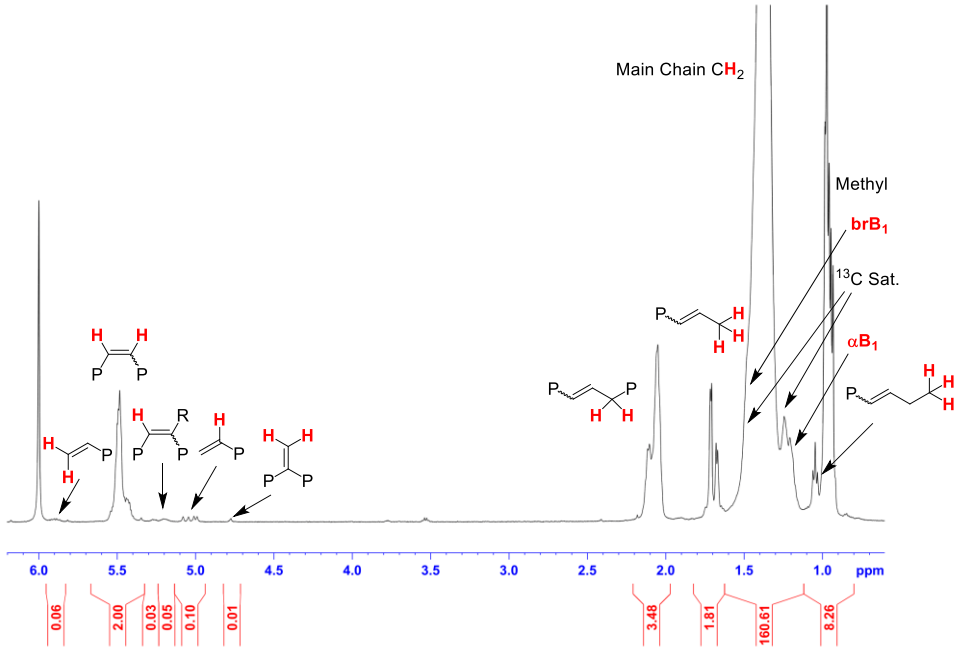

Figure 2.8. Olefin region of the $^{13}C\{^{1}H\}$ NMR spectrum of polyethylene formed by **9** (Table 2.2, entry 1). NMR Conditions: $CDCl_2CDCl_2$, 126 MHz, 100 ºC.

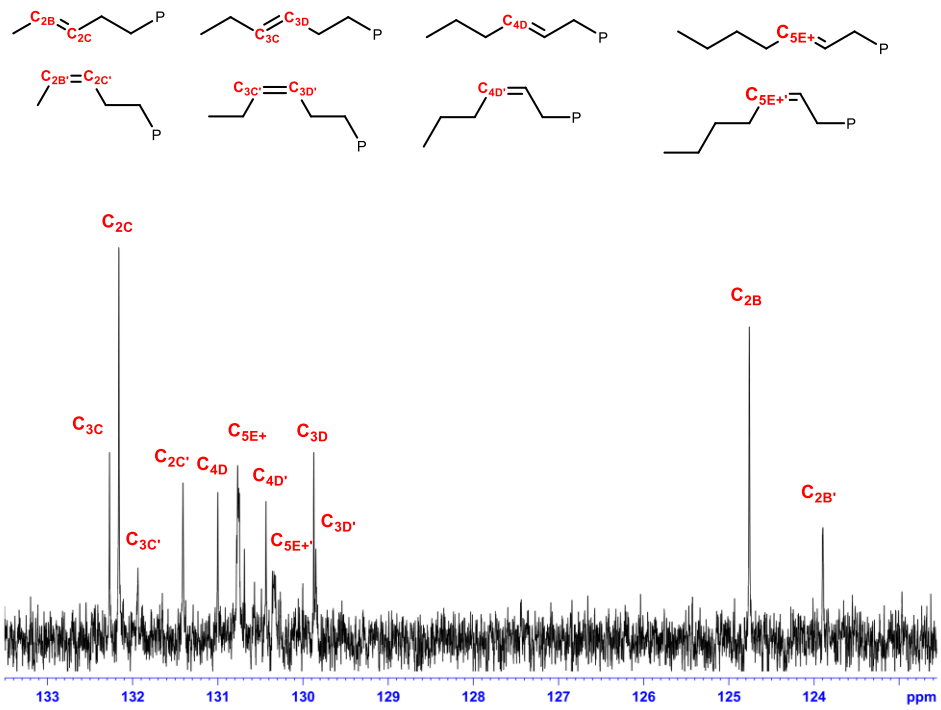

DSC analysis shows that the PE produced by **9** melts over a broad temperature range (Figure 2.9, left) with apparent T_m values at ca. 80, 90, and 103 ºC (Table 2.2). Similar results have been observed for other low-molecular-weight PE waxes.[49–54] For example, saturated linear Fisher-Tropsch waxes, such as SasolWax H1 (M_n = 800, Đ = 1.4, 1.6 branches/1000 C), exhibit multiple melt transitions in DSC that are very similar to those observed for the PE formed by **9** (Figure 2.9, right). This behavior has been ascribed to the melting of crystallites consisting mainly of short chains at lower temperature and the progressive melting of crystallites composed primarily of longer and longer chains as the temperature is raised.[49,55–57]

Figure 2.9. Left: DSC of SasolWax H1. Right: representative DSC of the polyethylene produced by **9** (Table 2, Entry 1).

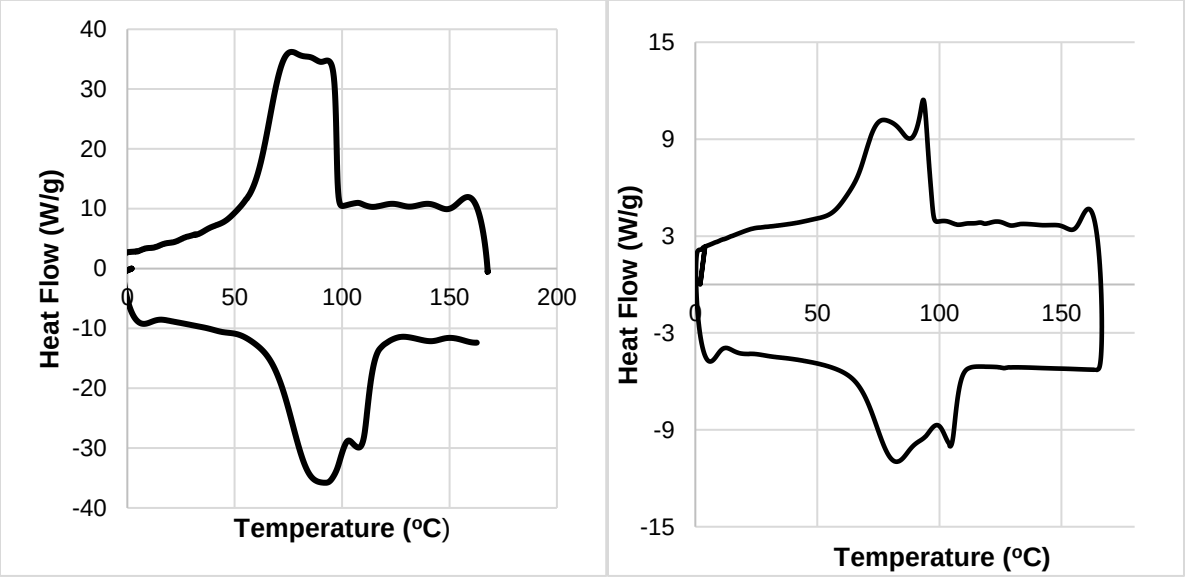

Generation of a ($PR_2CB_9Cl_9$)PdMe($H_2C=CH_2$) Ethylene Complex and Kinetics of PE Chain Growth. The reaction of **9** with ethylene was studied by NMR at low temperature in order to probe ethylene binding and monitor the chain growth process. The reaction of **9** with excess ethylene at -78 °C in CD_2Cl_2 generates the ethylene adduct (κ^2-*P,O*-P(*o*-OMe-Ph)$_2CB_9Cl_9$)PdMe($H_2C=CH_2$) (**10**, Scheme 2.2). The bound ethylene in **10** gives rise to an AA'BB' pattern at δ 5.42 and 5.30 in the ^{1}H NMR spectrum and a singlet at δ 101.5 in the $^{13}C\{^1H\}$ NMR spectrum at -78 °C, consistent with rapid rotation of the bound ethylene around the Pd-ethylene centroid bond (Figure 2.23).[58] The ^{1}H and $^{13}C\{^1H\}$ spectra of **10** at -78 °C contain two –OMe resonances, the chemical shift differences of which are similar to those observed for **9** and consistent with a κ^2-*P,O* bonding mode for the phosphine-carborane ligand. The Pd-Me group gives rise to a doublet in the ^{1}H NMR spectrum with a small $^3J_{PH}$ value (3 Hz) and a singlet in the $^{13}C\{^1H\}$ spectrum, indicating that the Me group is *cis* to the phosphine. The ^{1}H-^{1}H NOESY spectrum of **10** (-78 °C) contains strong correlations between the bound ethylene resonance and

the Pd- Me resonance and one –OMe resonance (δ 4.03, Pd-bound), as well as a weak correlation with the other –OMe resonance at (δ 3.71, non-Pd-bound). The bound ethylene ^{1}H NMR resonances are coalesced with the free ethylene resonance at -30 ºC. The –OMe ^{1}H NMR resonances are coalesced at -20 ºC, indicating that **10** undergoes an anisolyl group exchange process, as observed for **9**.

Scheme 2.2. Generation of Ethylene Complex **10** and Subsequent Reaction with Ethylene to Generate **11**.

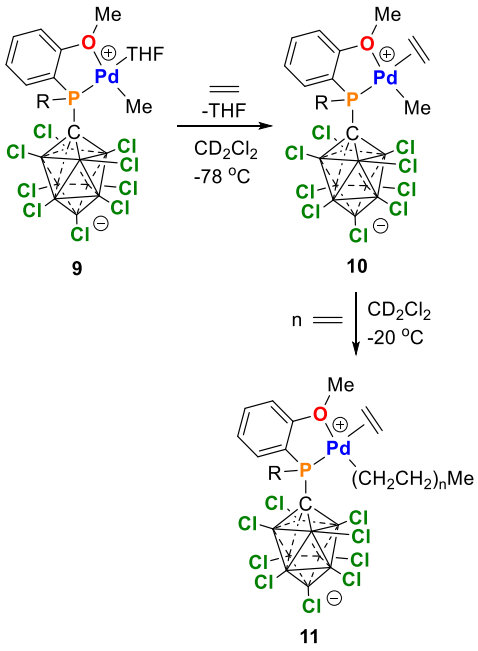

Figure 2.10. NMR Spectra of **10**

(a) ^{1}H NMR of **10** generated by the reaction of **9** with 3.5 equiv. of ethylene (CD_2Cl_2, 500 MHz, -78 ºC) (* denotes acetone and water on the outside of the NMR tube)

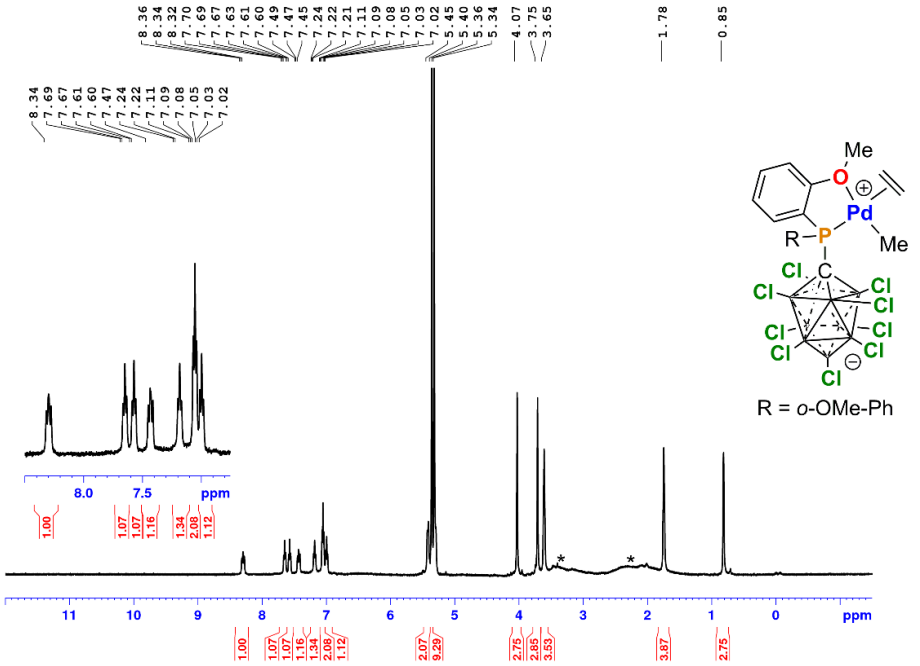

(b) ^{13}C{^{1}H} NMR of **10** given by the reaction of **9** with 3.5 equiv. of ethylene (CD_2Cl_2, 126 MHz, -78 ºC)

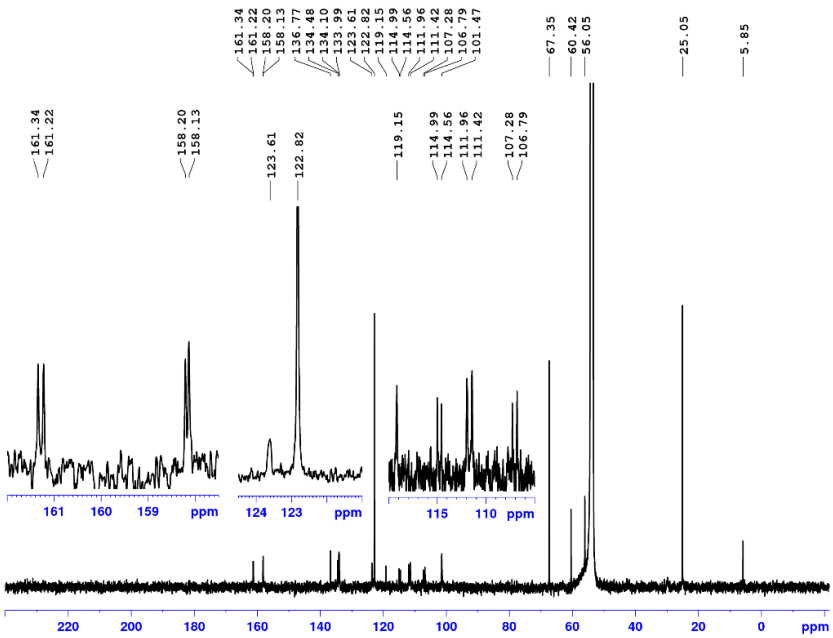

Complex **10** undergoes repetitive ethylene insertion at -20 °C to generate a mixture of (κ^2-*P*,*O*-P(*o*-OMe-Ph)$_2$CB$_9$Cl$_9$)PdR'($H_2C{=}CH_2$) alkyl species (**11**, R' = growing chain). β–H elimination and olefin formation do not occur at this temperature and therefore the polymerization is living. The chain growth process was monitored by ^{1}H NMR. As 1 molecule of THF is released per equivalent of **9** in the formation of **10**, the total concentration of Pd species during chain growth is $[Pd]_{total}$ = [**10**] + [**11**] = [THF]. Therefore, the average number of ethylene units inserted per Pd-*R'* chain, X_n, is equal to the ratio (total integral of the Pd-*R'* resonances)/(integral of the THF β-H resonance).[59] Plots of X_n versus time are linear with a slope that is independent of ethylene concentration (Figure 2.10), indicating that the growth rate is zero-order in ethylene, which is consistent with the polymerization results. The composite insertion rate constant (for Pd-Me and Pd-R'), $k_{insertion}$ (eq 1), was determined to be 1.05(6) x 10^{-3} s^{-1} (-20 °C), which corresponds to an apparent insertion barrier $\Delta G^{\neq}_{\text{insertion}}$ of 18.1(1) kcal/mol.

$$\frac{\mathrm{d}(\boldsymbol{X_n})}{\mathrm{dt}} = k_{insertion} \qquad (1)$$

Figure 2.11. Representative plots of X_n versus time for the reaction of *in situ*-generated **10** with ethylene at -20 °C. Blue data and curve: $[Pd]_{total}$ = 9.3 mM, $[ethylene]_{initial}$ = 0.15 M (16 equiv). Red data and curve: $[Pd]_{total}$ = 9.1 mM, $[ethylene]_{initial}$ = 0.32 M (35 equiv). The two curves do not overlap because the extent of chain growth at the beginning of data collection was different for the two runs. This difference affects the y intercept but not the slope of the line.

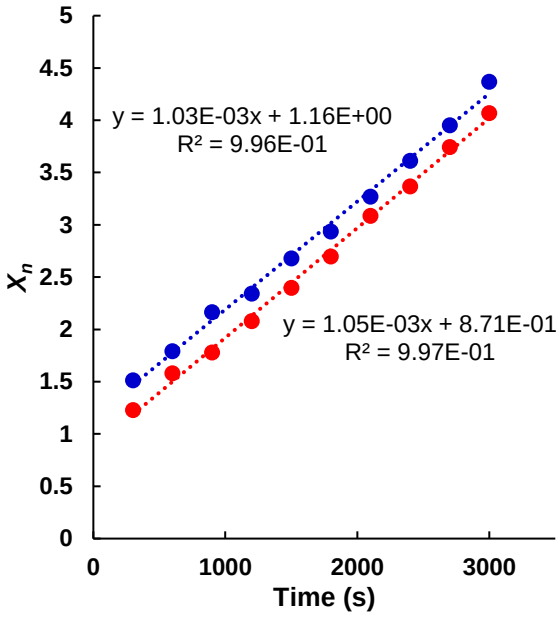

2.3 Conclusion

In conclusion, we have described the synthesis and characterization of **7**–**9**, which contain phosphino-perchlorocarba-*closo*-decaborate ligands. Compounds **7** and **8**, which contain κ^2-*P*,*Cl*-$PR_2CB_9Cl_9^-$ ligands, oligomerize ethylene to C_4-C_{10} olefins, while **9**, which contains a κ^2-*P*,*O*-P(*o*-OMe-Ph)$_2CB_9Cl_9^-$ ligand, polymerizes ethylene to PE wax. These results contrast with the lack of reactivity with ethylene observed for $PR_2CB_{11}Cl_{11}^-$ complex **C**.[34] Catalyst **7**, which contains a strong donor P^iPr_2 unit, is significantly more active than **8** or **9**, which contain P(aryl)$_2$ units. A similar trend was observed for analogous phosphine-arenesulfonate palladium alkyl catalysts **A**.[35] It is notable that **8** is ca. 4 times more reactive than the trifluoroborate analogue **B**/[H(OEt$_2$)$_2$][B(3,5-(CF$_3$)$_2$C$_6$H$_3$)$_4$], as assessed by the TOFs for ethylene oligomerization/dimerization.[9,11] As the catalyst resting state in both cases is the corresponding

PdR($H_2C=CH_2$) species, this reactivity trend is due to a difference in the ethylene insertion rate. The steric bulk of the perchlorocarborane backbone may contribute to the enhanced reactivity of **8**. The combination of the low molecular weight, low branch density, predominance of short branches, and preponderance of internal olefins in the polyethylene formed by **9** indicates that the secondary alkyl-metal species formed by chain walking undergo preferential chain transfer rather than chain growth.

2.4 Experimental Section

General Considerations. The majority of the synthetic work, explicitly shown in Scheme 1.1, was done by our collaborators from the Lavallo group at UC Riverside and is included for completion. The X-ray structures of **7-CH_3CN**, **8**, and **9** were determined at UC Riverside while the X-ray structure of [$Li(THF)_3$][**5**] was determined at the University of Chicago.

All manipulations were carried out using standard Schlenk or glovebox techniques under a nitrogen or argon atmosphere at room temperature unless otherwise stated. PhF was dried over and distilled from P_2O_5 or CaH_2. THF was dried and distilled from K metal. CH_2Cl_2, pentane, and toluene were purified by passage through BASF R3−11 oxygen scavenger and activated alumina. CD_2Cl_2 was dried over P_2O_5 or 3 Å molecular sieves and degassed. $CDCl_2CDCl_2$ and CD_3CN were dried over 3 Å molecular sieves and degassed. Unless specifically stated, reagents were purchased from commercial vendors and used without further purification. NMR spectra were recorded using Bruker Avance 300 MHz, Avance 400 MHz, Avance 500 MHz, or Avance 600 MHz instruments or a Varian Inova 300 MHz spectrometer. ^{1}H and ^{13}C NMR chemical shifts are reported relative to $SiMe_4$ and are internally referenced to the residual solvent resonance. ^{31}P NMR chemical shifts are externally referenced to H_3PO_4. ^{11}B NMR chemical shifts were externally referenced to BF_3Et_2O and the baseline of the spectra corrected using a multipoint spline. For all compounds,

the carboranyl carbon resonance was not observed in $^{13}C\{^{1}H\}$ NMR spectra. NMR assignments for $[Li(THF)_3][\mathbf{1}]$**–8** were made based on peak multiplicities and integrations. NMR assignments for **9** and **10** were made using 2D NMR experiments. High-resolution mass spectrometry (HRMS) was performed on an Agilent Technologies 6210 (TOF LC/MS) ESI/APCI instrument. $[Me_3NH][HCB_9Cl_9]$ was synthesized according to literature procedures.[60] (COD)PdMeCl was synthesized according to literature procedures.[61] The purity of all isolated compounds was established by multinuclear NMR (see Supporting Information) and high resolution mass spectrometry.

$[Li(THF)_3][P^iPr_2CB_9Cl_9]$ ($[Li(THF)_3][\mathbf{1}]$). $[Me_3NH][HCB_9Cl_9]$ (0.500 g, 1.02 mmol) was dissolved in THF (3 mL) in a 20 mL scintillation vial equipped with a stir bar. *n*-BuLi (2.1 equiv, 2.0 M in hexanes) was added and the mixture was stirred for 30 min. This mixture was added to pentane (15 mL) that was being stirred and a white solid precipitated. The solid was collected by filtration, washed twice with pentane, and dried under vacuum. The resulting white powder was dissolved in THF (3 mL), $^{i}Pr_2PCl$ (171 mg, 1.12 mmol) was added, and the mixture was stirred for 1 h. The volatiles were removed under vacuum. The resulting oil was washed with pentane, taken up in PhF, and the insoluble LiCl was removed by filtration. The filtrate was evaporated to dryness to yield $[Li(THF)_3][\mathbf{1}]$ as a white solid. Yield: 720 mg, 92%. ^{1}H NMR (400 MHz, CD_2Cl_2, 23 ºC): δ 3.79 (m, 12H, THF), 2.94 (d of septets, $^{3}J_{HH}$ = 7 Hz; $^{2}J_{PH}$ = 1.5 Hz, 2H), –C*H*$(CH_3)_2$), 1.98 (m, 12H, THF), 1.34 (two overlapping dds, $^{3}J_{PH}$ = 19 Hz, $^{3}J_{PH}$ = 11 Hz, $^{3}J_{HH}$ = 7.4 Hz, $^{3}J_{HH}$ = 6.9 Hz, 12H, –CH(C*H*$_3)_2$). $^{13}C\{^{1}H\}$ NMR (101 MHz, CD_2Cl_2, 23 ºC): δ 69.1 (THF), 25.9 (THF), 24.4 (d, $^{2}J_{PC}$ = 36 Hz, –CH(*C*$H_3)_2$), 22.2 (d, $^{2}J_{PC}$ = 26 Hz, –CH(*C*$H_3)_2$), 21.2 (d, $^{1}J_{PC}$ = 12 Hz, –*C*H$(CH_3)_2$). $^{11}B\{^{1}H\}$ NMR (96 MHz, CD_2Cl_2, 23 ºC): δ 23.6 (1B), -0.8 (4B), -2.4 (4B).

$^{31}P\{^{1}H\}$ NMR (162 MHz, CD_2Cl_2, 23 ºC): δ 45.2. ESI/APCI HRMS (m/z): $[M]^-$ calculated for $C_7H_{14}B_9PCl_9$: 544.9044; found: 544.9044. MP: 100.0 – 106.7 ºC.

Figure 2.12. NMR Spectra of $[Li(THF)_3][\mathbf{1}]$.

(a) ^{1}H NMR **(**CD_2Cl_2, 400 MHz, 23 ºC)

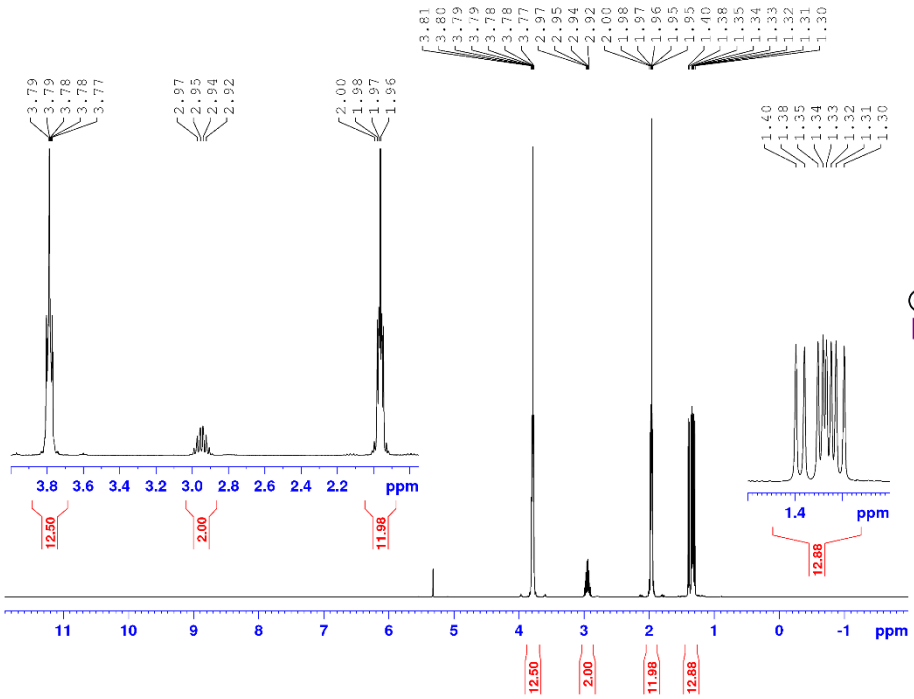

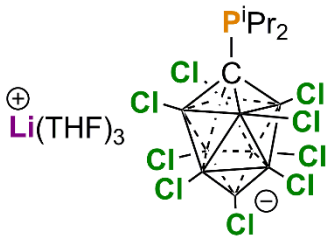

Figure 2.12, continued.

(b) $^{13}C\{^{1}H\}$ NMR (CD_2Cl_2, 101 MHz, 23 ºC)

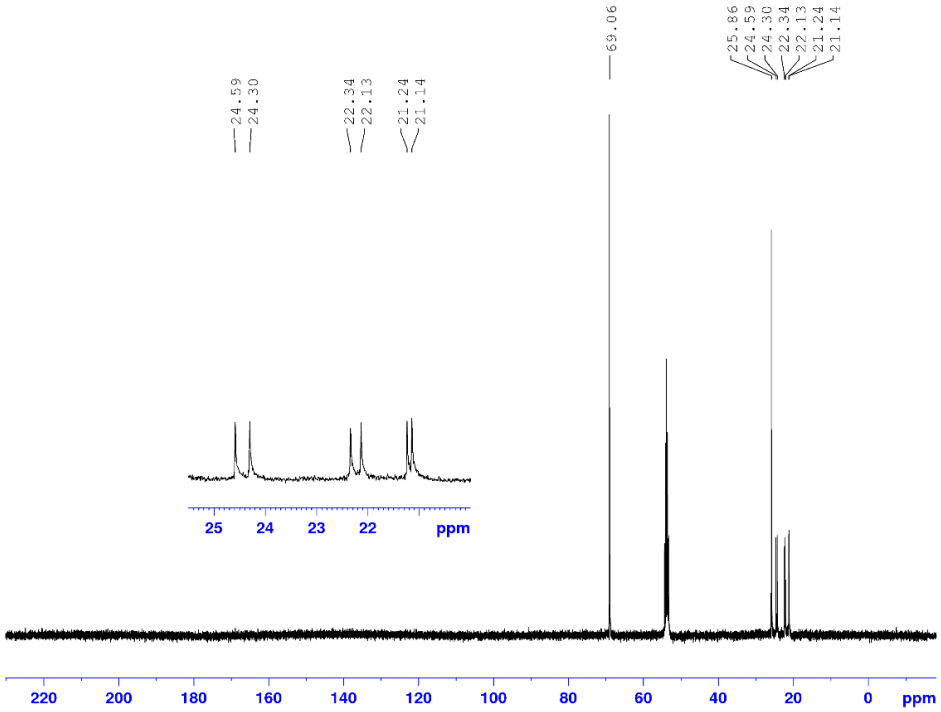

(c) $^{11}B\{^{1}H\}$ NMR (CD_2Cl_2, 128 MHz, 23 ºC)

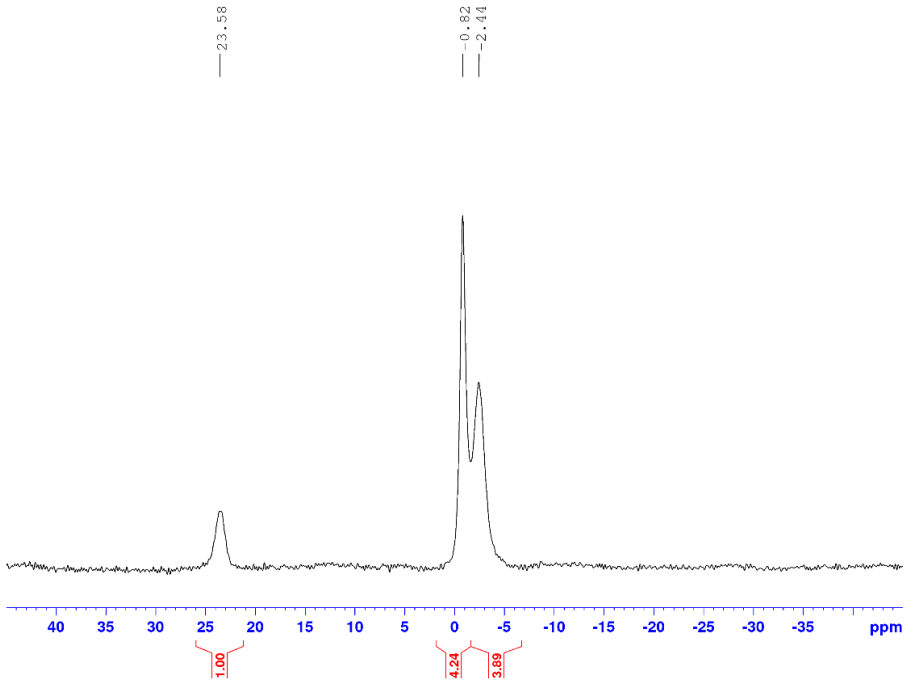

Figure 2.12, continued.

(d) $^{31}P\{^{1}H\}$ NMR (CD_2Cl_2, 162 MHz, 23 ºC)

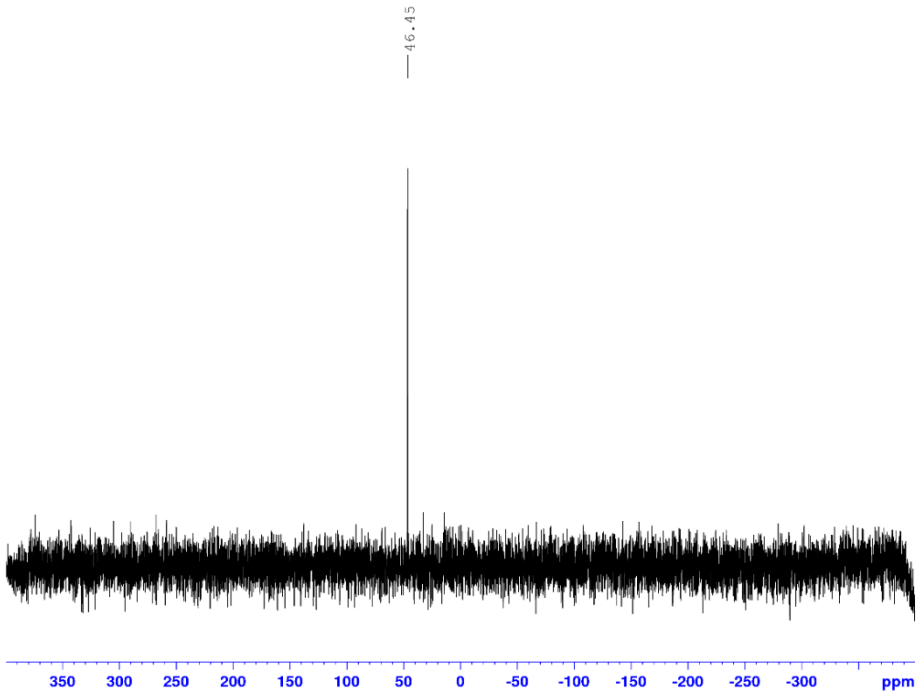

[Li(THF)$_4$][PPh$_2$CB$_9$Cl$_9$] ([Li(THF)$_4$][2]). [Li(THF)$_4$][**2**] was prepared from [Me$_3$NH][HCB$_9$Cl$_9$] (0.500 g, 1.02 mmol), *n*-BuLi (2.1 equiv, 2.0 M in hexanes) and Ph$_2$PCl (247 mg, 1.12 mmol) using the procedure described above for [Li(THF)$_3$][**1**]. Yield: white solid, 880 mg, 95%. ^{1}H NMR (300 MHz, CD_2Cl_2, 23 ºC): δ 8.07 (m, 4H, Ar), 7.37 (m, 6H, Ar), 3.78 (m, 16H, THF), 1.96 (m, 16H, THF). $^{13}C\{^{1}H\}$ NMR (101 MHz, CD_2Cl_2, 23 ºC): δ 137.5 (d, $^{2}J_{PC}$ = 29 Hz, *o*–Ph), 133.1 (d, $^{1}J_{PC}$ = 16 Hz, *ispo*–Ph), 130.1 (*p*–Ph), 128.0 (d, $^{3}J_{PC}$ = 10 Hz, *m*–Ph), 69.1 (THF), 25.9 (THF). $^{11}B\{^{1}H\}$ NMR (96 MHz, CD_2Cl_2, 23 ºC): δ 20.5 (1B), -4.3 (4B), -6.3 (4B). $^{31}P\{^{1}H\}$ NMR (162 MHz, CD_2Cl_2, 23 ºC): δ 11.5. ESI/APCI HRMS (m/z): $[M]^-$ calculated for $C_{13}H_{10}B_9PCl_9$: 612.8744; found: 612.8714. MP: 143.2 – 145.5 ºC.

Figure 2.13. NMR spectra of $[Li(THF)_2][\mathbf{2}]$.
(a) ^{1}H NMR (CD_2Cl_2, 400 MHz, 23 ºC)

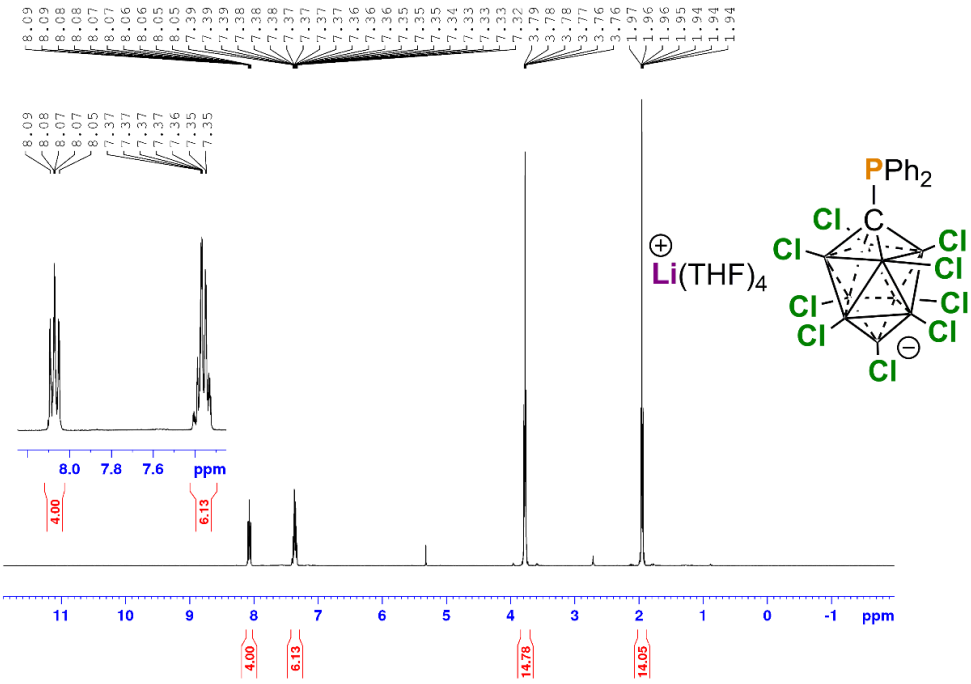

(b) $^{13}C\{^{1}H\}$ NMR (CD_2Cl_2, 101 MHz, 23 ºC).

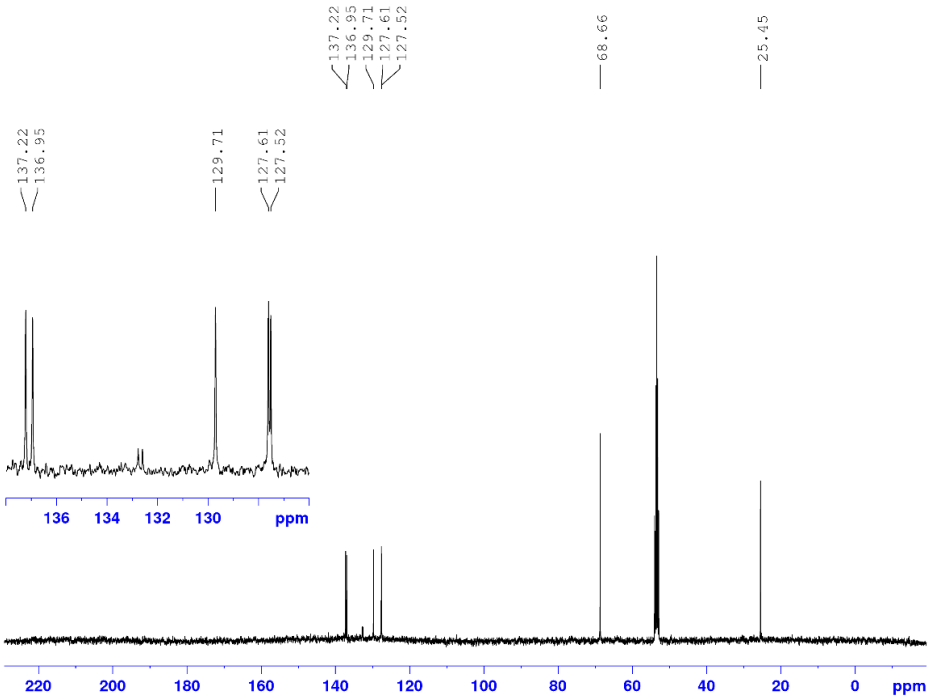

Figure 2.13, continued.

(c) $^{11}B\{^{1}H\}$ NMR (CD_2Cl_2, 128 MHz, 23 ºC)

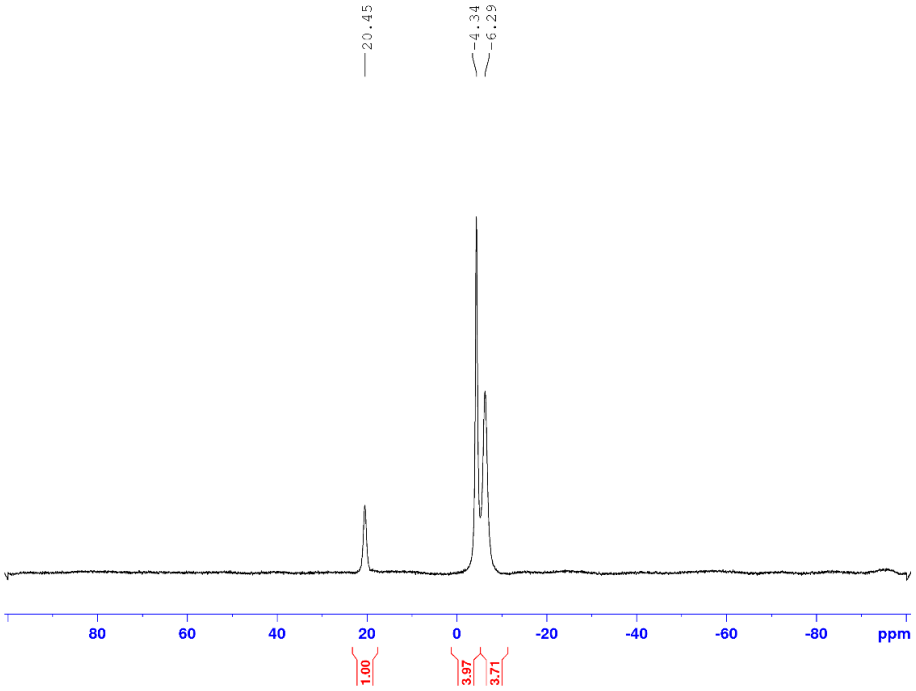

(d) $^{31}P\{^{1}H\}$ NMR (CD_2Cl_2, 162 MHz, 23 ºC)

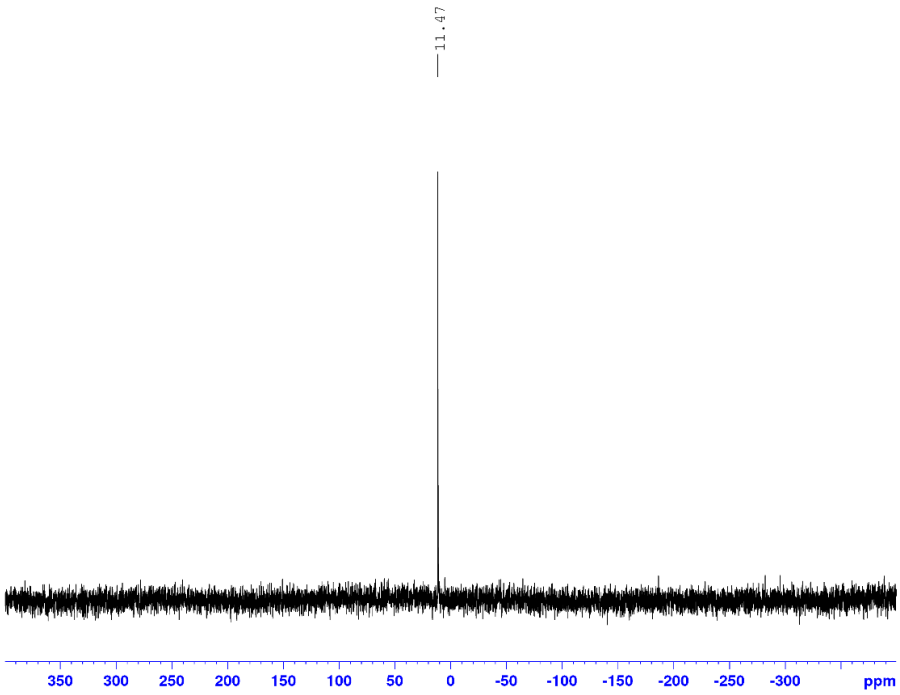

[Li(THF)$_2$][P(*o*-Me-Ph)$_2$CB$_9$Cl$_9$] ([Li(THF)$_2$[3]). [Li(THF)$_2$[**3**] was prepared from [Me$_3$NH][HCB$_9$Cl$_9$] (0.500 g, 1.02 mmol), *n*-BuLi (2.1 equiv, 2.0 M in hexanes) and (*o*-OMe-Ph)$_2$PCl (315mg, 1.12 mmol) using the procedure described above for [Li(THF)$_3$][**1**]. Yield: white solid, 760 mg, 90%. ^{1}H NMR (400 MHz, CD$_3$CN, 23 ºC): δ 7.93 (m, 2H, Ar), 7.36 (m, 2H, Ar), 6.90 (m, 4H, Ar), 3.69 (s, 6H, -OC*H*$_3$), 3.65 (m, 8H, THF), 1.81 (m, 8H, THF). ^{13}C{^{1}H} NMR (101 MHz, CD$_3$CN, 23 ºC): δ 163.0 (d, $^2J_{PC}$ = 22 Hz, *C*–OCH$_3$), 137.7 (Ar), 131.9 (Ar), 123.2 (d, $^1J_{PC}$ = 29 Hz, C_{ipso}-P), 120.5 (Ar), 111.9 (Ar), 68.3 (THF), 56.4 (–O*C*H$_3$), 26.2 (THF). ^{11}B{^{1}H} NMR (96 MHz, CD$_3$CN, 23 ºC): δ 20.4 (1B), -4.4 (4B), -6.3 (4B). ^{31}P{^{1}H} NMR (162 MHz, CD$_3$CN, 23 ºC): δ -9.8. ESI/APCI HRMS (m/z): [M]$^-$ calculated for C$_{15}$H$_{14}$B$_9$O$_2$PCl$_9$: 672.9211; found: 672.9199. MP: 240.1 – 243.3 ºC.

Figure 2.14. NMR spectra of [Li(THF)$_4$][**3**].

(a) ^{1}H NMR (CD$_3$CN, 400 MHz, 23 ºC)

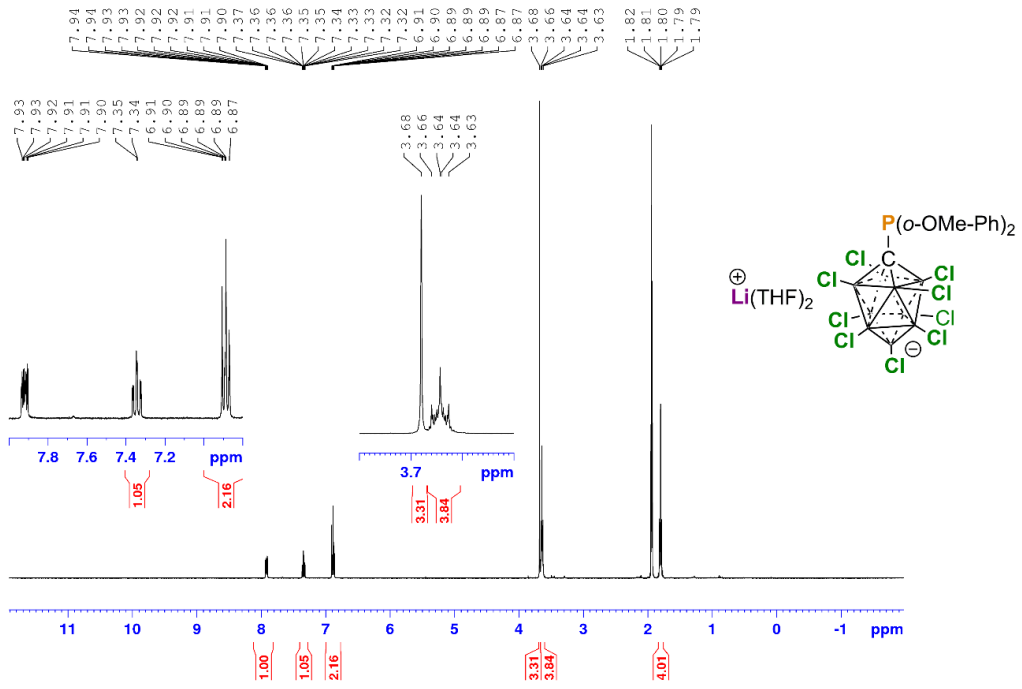

Figure 2.14, continued.

(b) $^{13}C\{^{1}H\}$ NMR (CD_3CN, 101 MHz, 23 ºC)

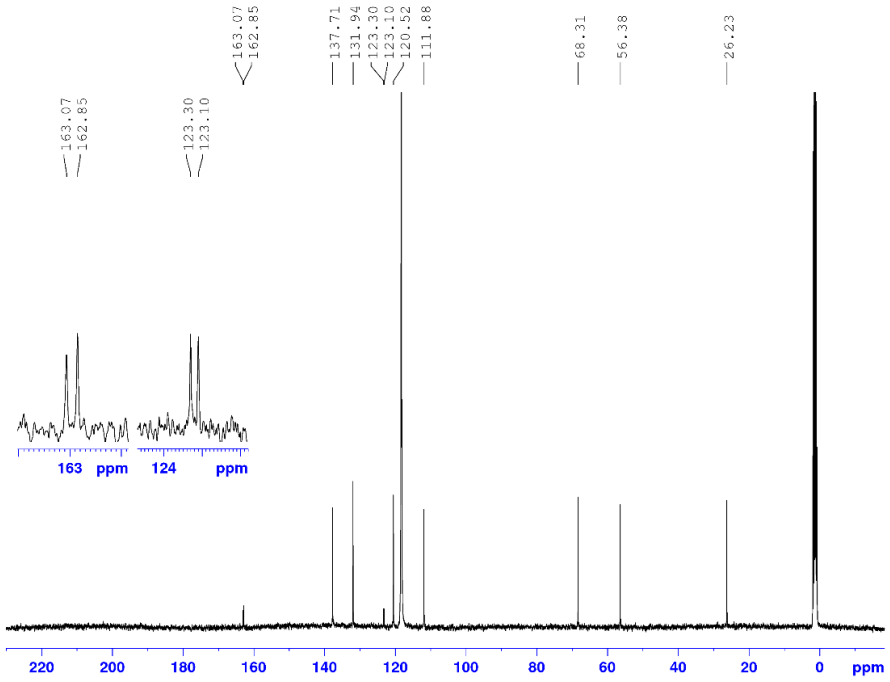

Figure 2.14, continued.

(c) $^{11}B\{^{1}H\}$ NMR (CD_3CN, 128 MHz, 23 ºC).

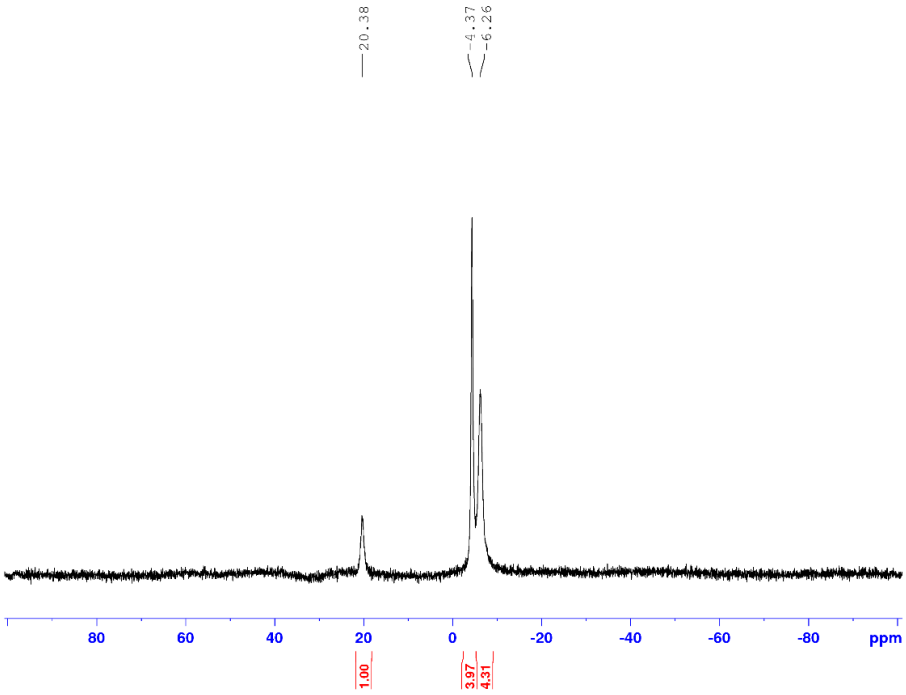

Figure 2.14, continued.

(d) $^{31}P\{^{1}H\}$ NMR (CD_3CN, 162 MHz, 23 ºC)

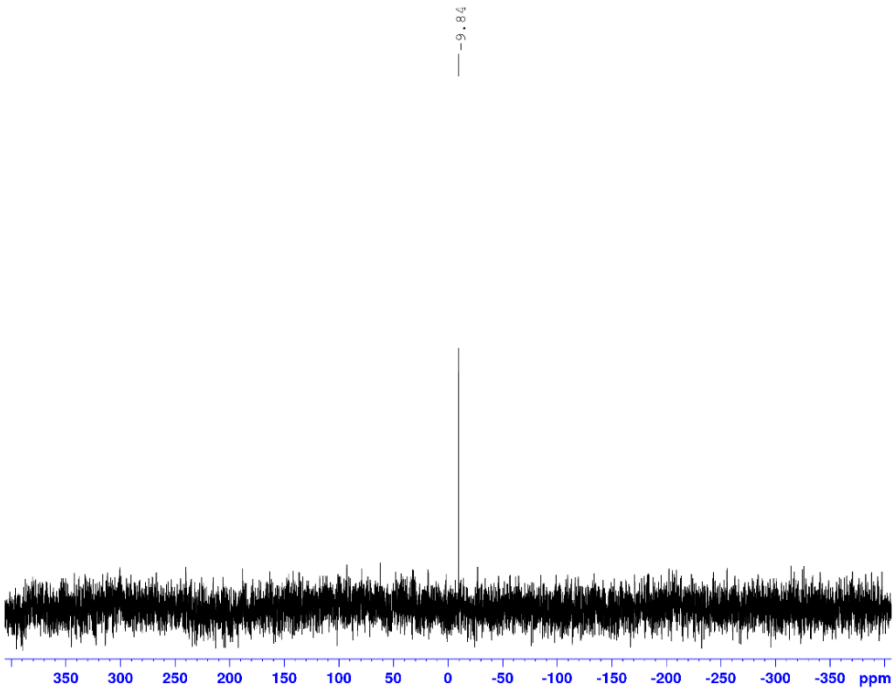

(κ^2-*P,Cl*-P^{i}Pr$_2$CB$_9$Cl$_9$)PdMe(THF) (7). **1** (100 mg, 0.12 mmol) and PhF (1 mL) were added to a 20 mL scintillation vial equipped with a stir bar. (COD)PdMeCl (31.5 mg, 0.120 mmol) was separately dissolved in PhF (1 mL) in a second vial. The (COD)PdMeCl solution was slowly added to the solution of **1**. The second vial was washed with PhF (1 mL) and the wash was added to the solution of **1**. The mixture was stirred for 30 min and concentrated under vacuum. Pentane was added and the resulting light brown precipitate was allowed to settle. The pentane supernatant was decanted off and the precipitate was washed twice with pentane and dried under vacuum to yield [Li(THF)$_3$][**4**] as a brown solid. ^{1}H NMR (500 MHz, CD_2Cl_2, 23 ºC): δ 3.08 (m, 12 H, THF), 3.27 (m, 4H, –C*H*(CH_3)$_2$), 1.95 (m, 12H, THF), 1.73 (dd, $^{3}J_{HH}$ = 7.2 Hz, $^{2}J_{PH}$ = 19.0 Hz), 12 H, –CH(C*H*$_3$)$_2$), 1.01 (overlapping dd and s, $^{3}J_{HH}$ = 7.0 Hz, $^{2}J_{PH}$ = 17.5 Hz, 18H, Pd –C*H*$_3$ and –

$CH(CH_3)_2$). $^{13}C\{^1H\}$ NMR (126 MHz, CD_2Cl_2, 23 ºC) δ 68.9 (THF), 27.0 ($^1J_{PC}$ = 20 Hz, -$CH(CH_3)_2$), 26.4 (THF), 23.0 (-$CH(CH_3)_2$), 19.9 (–$CH(CH_3)_2$), 0.3 (Pd –CH_3). $^{11}B\{^1H\}$ NMR (96 MHz, CD_3CN, 23 ºC): δ 24.0 (1B), -3.1 (4B), -5.6 (4B). $^{31}P\{^1H\}$ NMR (202 MHz, CD_2Cl_2, 23 ºC): δ 76.6. MP: 92.1 – 97.5 ºC (dec).

Figure 2.15. NMR spectra of $[Li(THF)_3][$**4**$]$.

(a) ^1H NMR (CD_2Cl_2, 500 MHz, 23 ºC)

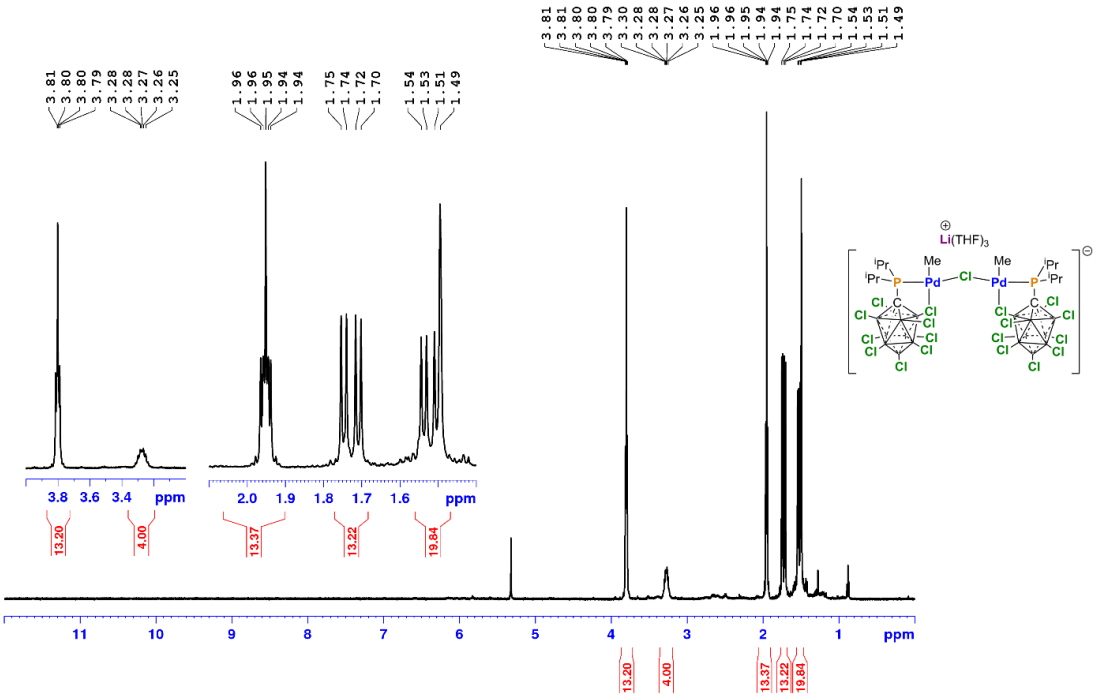

Figure 2.15, continued.

(b) $^{13}C\{^{1}H\}$ NMR (CD_2Cl_2, 126 MHz, 23 ºC)

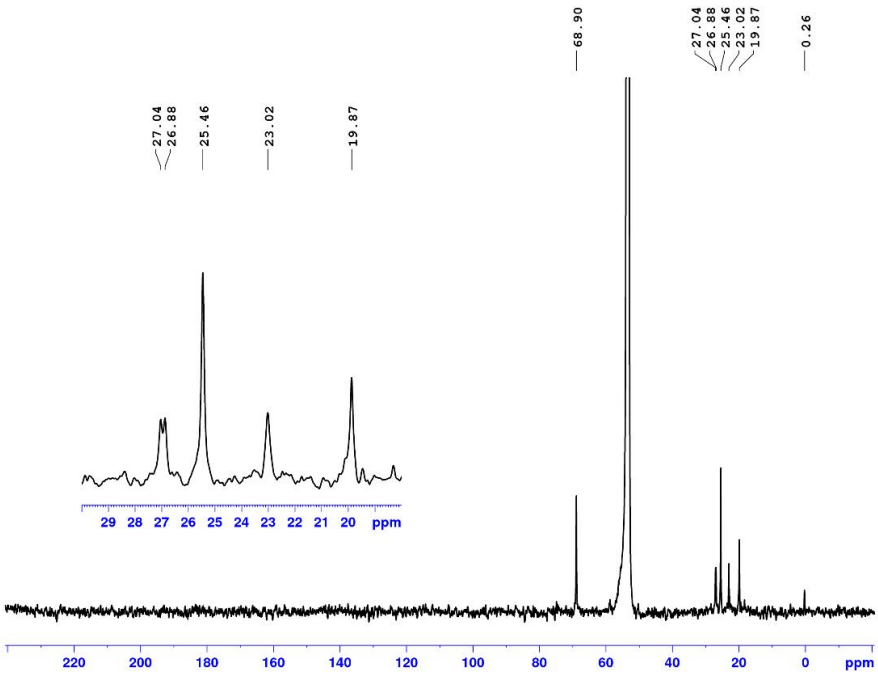

(c) $^{11}B\{^{1}H\}$ NMR (CD_2Cl_2, 128 MHz, 23 ºC)

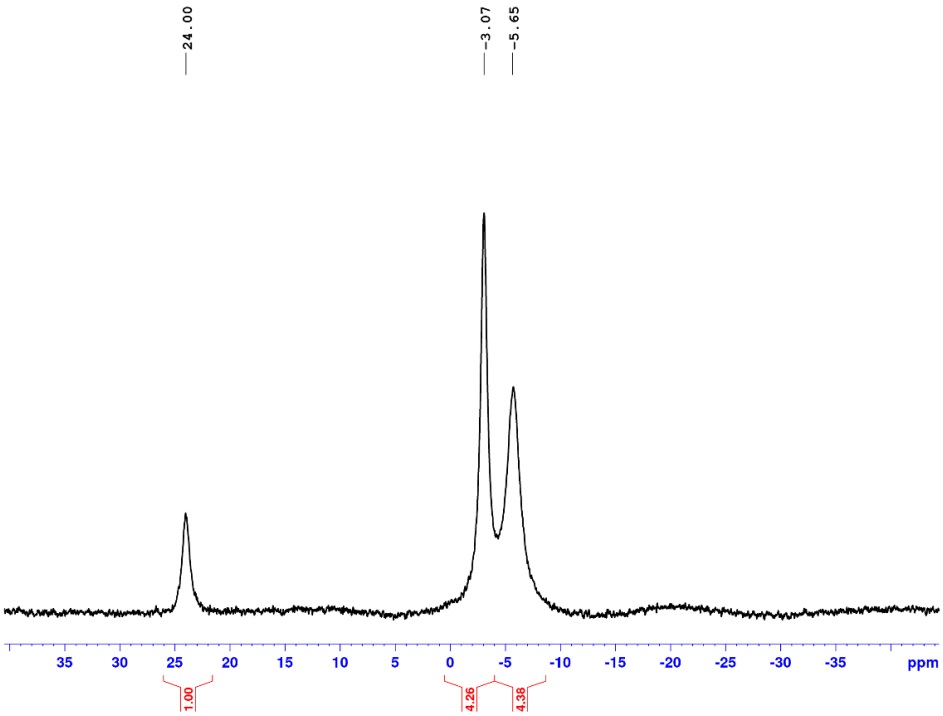

Figure 2.15, continued.

(d) $^{31}P\{^{1}H\}$ NMR (CD_2Cl_2, 202 MHz, 23 ºC)

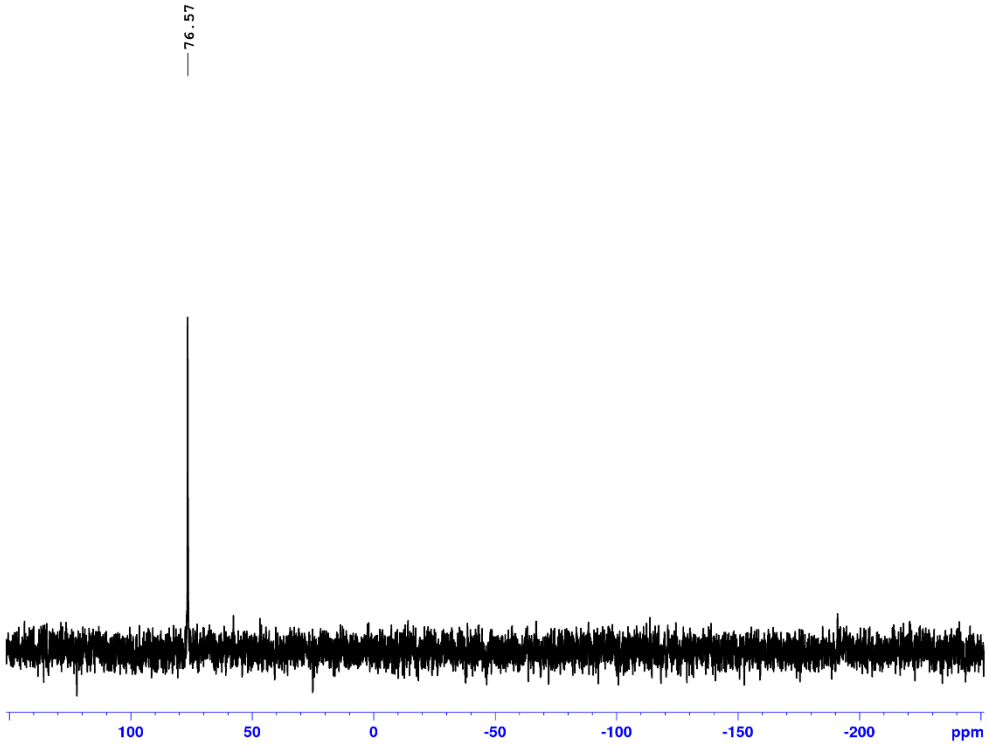

Without further purification, [Li(THF)$_3$][**4**] was dissolved in PhF (1mL) and $AgBF_4$ (11.0 mg, 0.0600 mmol) was added. The mixture was stirred for 30 min and filtered, and the collected solid was washed with CH_2Cl_2 (3 x 15 mL). The solvent was removed from the filtrate and washes under vacuum to afford **7** as a brown powder that contained a small amount of residual PhF. 80% pure by $^{31}P\{^{1}H\}$ NMR. Yield 77 mg, 87%. ^{1}H NMR (400 MHz, CD_2Cl_2, 23 ºC): δ 3.96 (m, 2H, THF), 3.28 (m, 2H, -C*H*$(CH_3)_2$), 1.97 (m, 2H, THF), 1.73 (dd, $^{2}J_{PH}$ = 20 Hz, $^{3}J_{HH}$ =7 Hz, 6H, –CH(C*H*$_3)_2$), 1.52 (dd, $^{2}J_{PH}$ = 20 Hz, $^{3}J_{HH}$ =7 Hz, 6H, –CH(C*H*$_3)_2$), 1.44 (s, 3H, Pd-C*H*$_3$). $^{13}C\{^{1}H\}$ NMR (101 MHz, CD_2Cl_2, 23 ºC): δ 72.9 (THF), 27.2 (d, $^{2}J_{PC}$ = 24 Hz, –CH(*C*H$_3)_2$), 25.6 (THF), 23.3 (br s, –CH(*C*H$_3)_2$), 20.0 (-*C*H$(CH_3)_2$), 1.2 (Pd-Me). $^{11}B\{^{1}H\}$ NMR (96 MHz, CD_2Cl_2, 23 ºC): δ 24.2 (1B), -3.4 (4B), -6.0 (4B). $^{31}P\{^{1}H\}$ NMR (162 MHz, CD_2Cl_2, 23 ºC): δ 77.5. ESI/APCI

HRMS (m/z): $[M - THF + CH_3CN]^-$ calculated for $C_{10}H_{20}B_9NPCl_9Pd$: 701.8363; found: 701.8352.

MP: 109.3 – 117.1 ºC (dec).

Figure 2.16. NMR spectra of **7**.

(a) ^1H NMR(CD_2Cl_2, 400 MHz, 23 ºC) (* denotes PhF impurity)

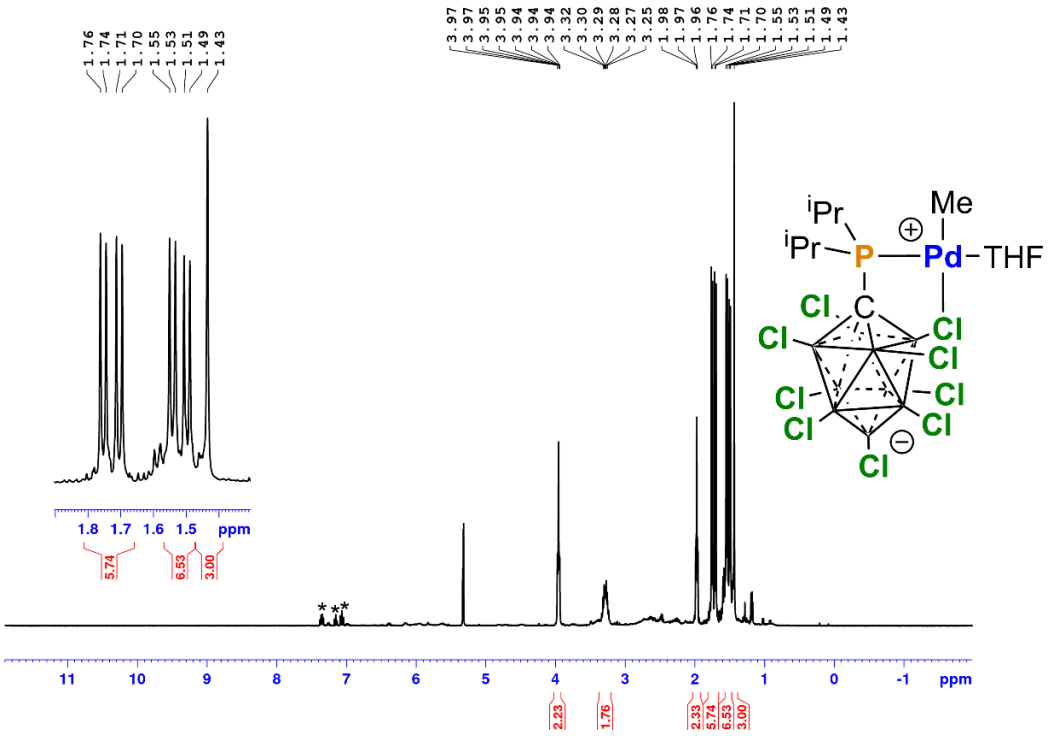

Figure 2.16, continued.

(b) $^{13}C\{^{1}H\}$ NMR (CD_2Cl_2, 101 MHz, 23 ºC)

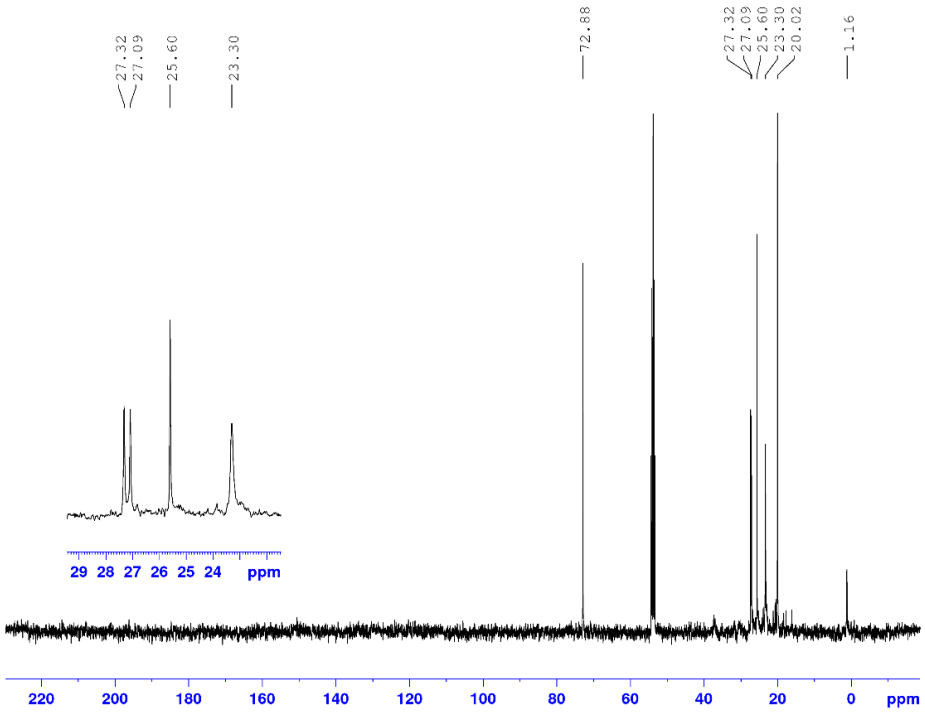

(c) $^{11}B\{^{1}H\}$ NMR (CD_2Cl_2, 128 MHz, 23 ºC)

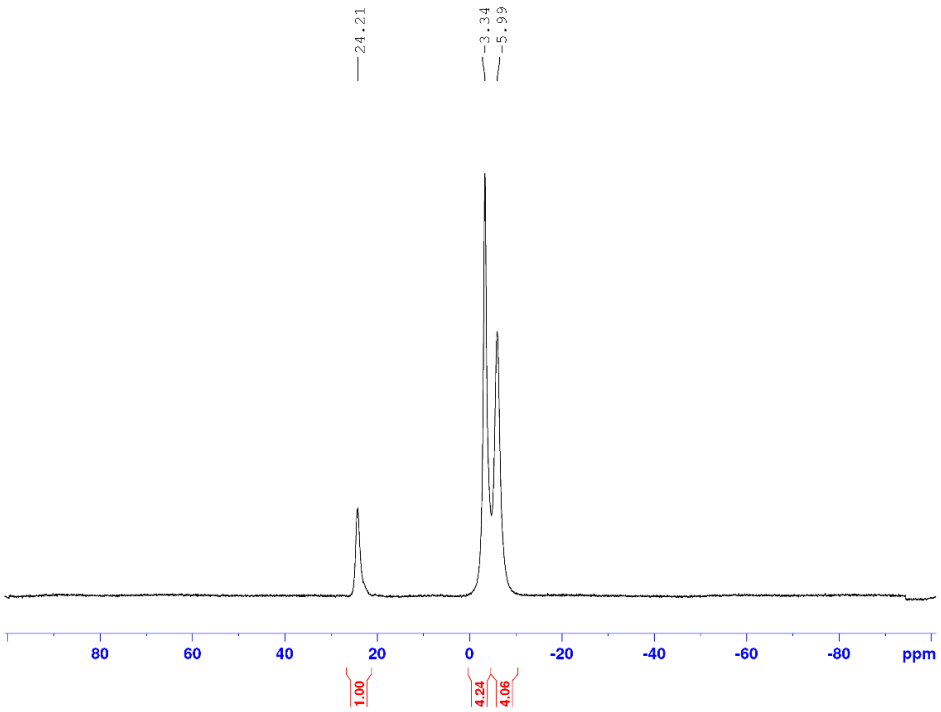

Figure 2.16, continued.

(d) $^{31}P\{^{1}H\}$ NMR (CD_2Cl_2, 162 MHz, 23 ºC) (* denotes unknown impurities)

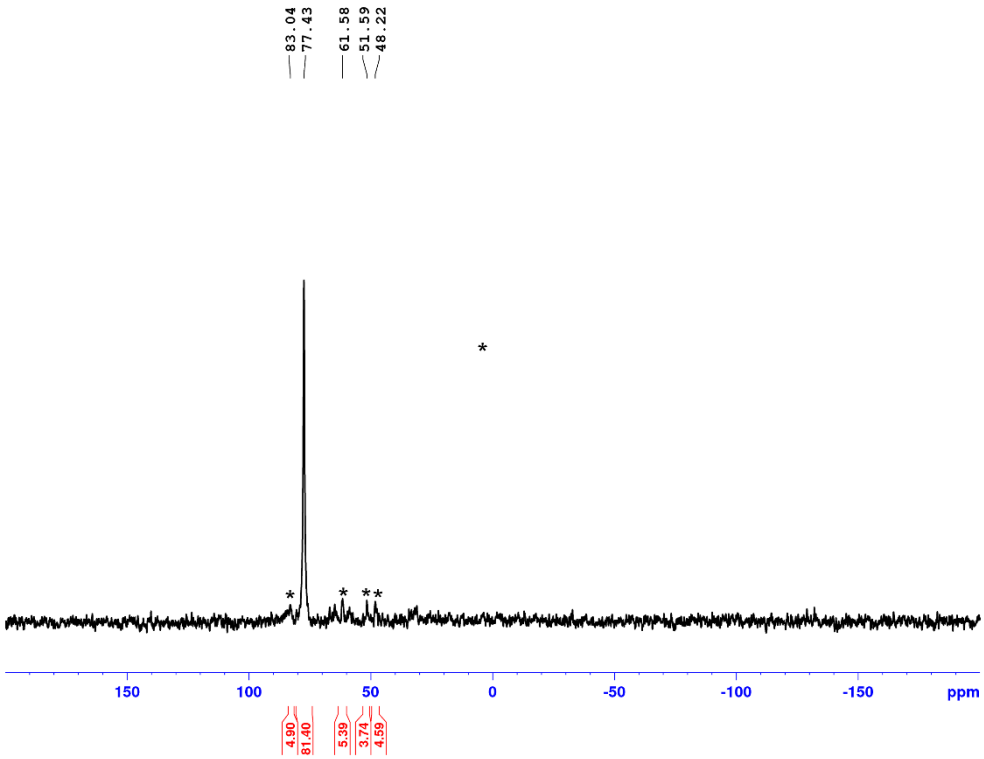

(κ^2-*P,Cl*-PPh$_2$CB$_9$Cl$_9$)PdMe(THF) (8). [Li(THF)$_3$][**5**] was generated as tan powder from **2** (100 mg, 0.110 mmol) and (COD)PdMeCl (28.9 mg, 0.110 mmol) using the procedure for [Li(THF)$_3$][**4**]. ^{1}H NMR (400 MHz, CD_2Cl_2, 23 ºC): δ 8.53 (dd, $^{2}J_{PH}$ = 12.5 Hz, $^{3}J_{HH}$ = 8.5 Hz, 8H, *o*–Ph), 7.60 (m, 12H, *m*–Ph and *p*–Ph), 3.78 (m, 12H, THF), 1.95 (m, 12H, THF), 1.38 (s, 6H, Pd–CH_3). $^{13}C\{^{1}H\}$ NMR: δ 138.5 (d, $^{2}J_{PC}$ = 16 Hz, *o*–Ph), 133.3 (d, $^{4}J_{PC}$ = 2 Hz, *p*–Ph), 128.8 (d, $^{3}J_{CP}$ = 12 Hz, *m*–Ph), 124.2 (d, $^{1}J_{CP}$ = 55 Hz, *ipso*–Ph), 69.2 (THF), 25.9 (THF), 12.6 (Pd–CH_3). $^{11}B\{^{1}H\}$ NMR (124 MHz, CD_2Cl_2, 23 ºC): δ 23.4 (1B), -3.16 (4B), -5.79 (4B). $^{31}P\{^{1}H\}$ NMR (162 MHz, CD_2Cl_2, 23 ºC): δ 56.6. Low temperature NMR data: ^{1}H NMR (500 MHz, CD_2Cl_2, -60 ºC): δ 8.48(dd, $^{2}J_{PH}$ = 12.5 Hz, $^{3}J_{HH}$ = 8.5 Hz, 8H, *o*-Ar), 7.59 (m, 12H, *m*-Ar and *p*-Ar), 3.66 (m, 16H,

THF), 1.84 (m, 16H, THF), 1.30 (s, 6H, Pd-CH_3). $^{31}P\{^1H\}$ NMR (162 MHz, CD_2Cl_2, -60 ºC): δ 57.8. MP: 91.4 – 104.7 ºC (dec).

Figure 2.17. NMR spectra of [Li(THF)$_3$][**5**].

(a) ^1H NMR (CD_2Cl_2, 400 MHz, 23 ºC)

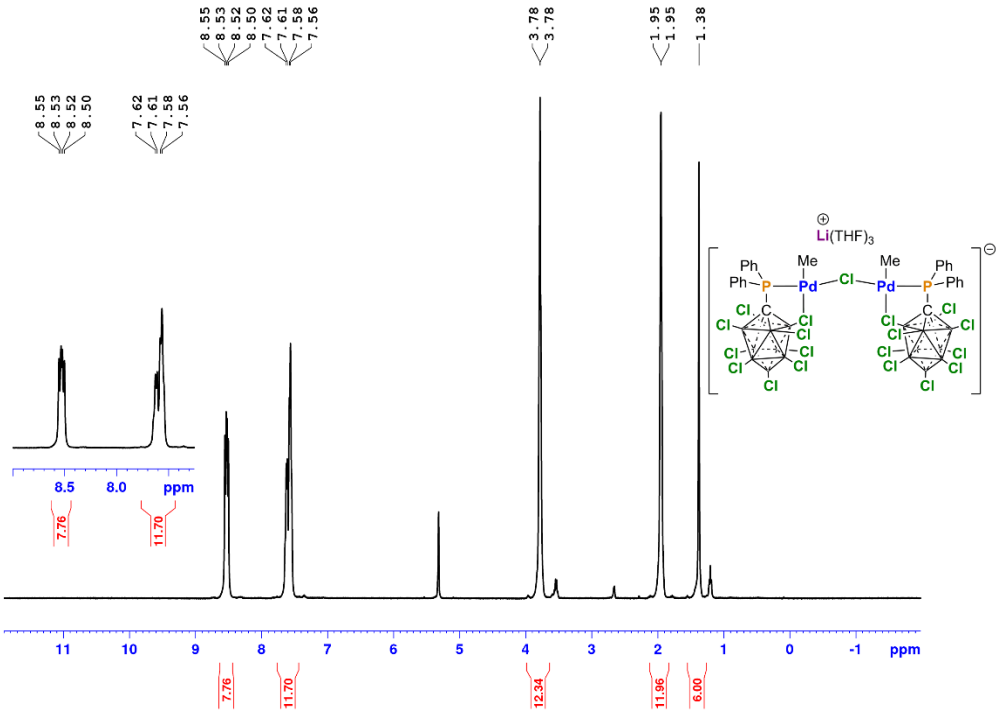

Figure 2.17, continued.

(b) $^{13}C\{^{1}H\}$ NMR (CD_2Cl_2, 101 MHz, 23 ºC)

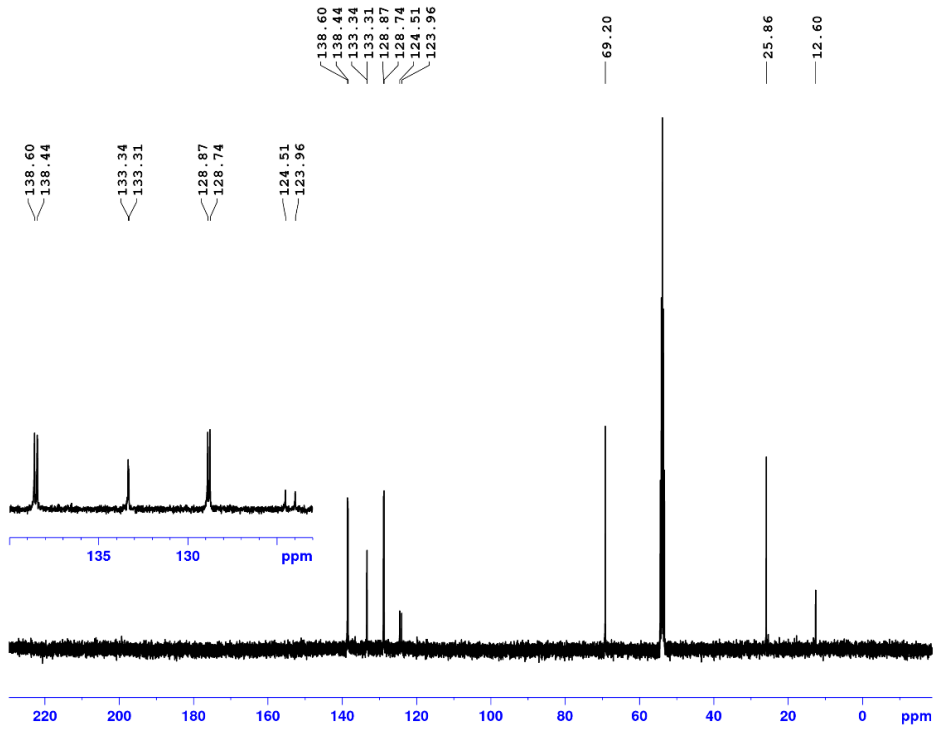

(c) $^{11}B\{^{1}H\}$ NMR (CD_2Cl_2, 128 MHz, 23 ºC)

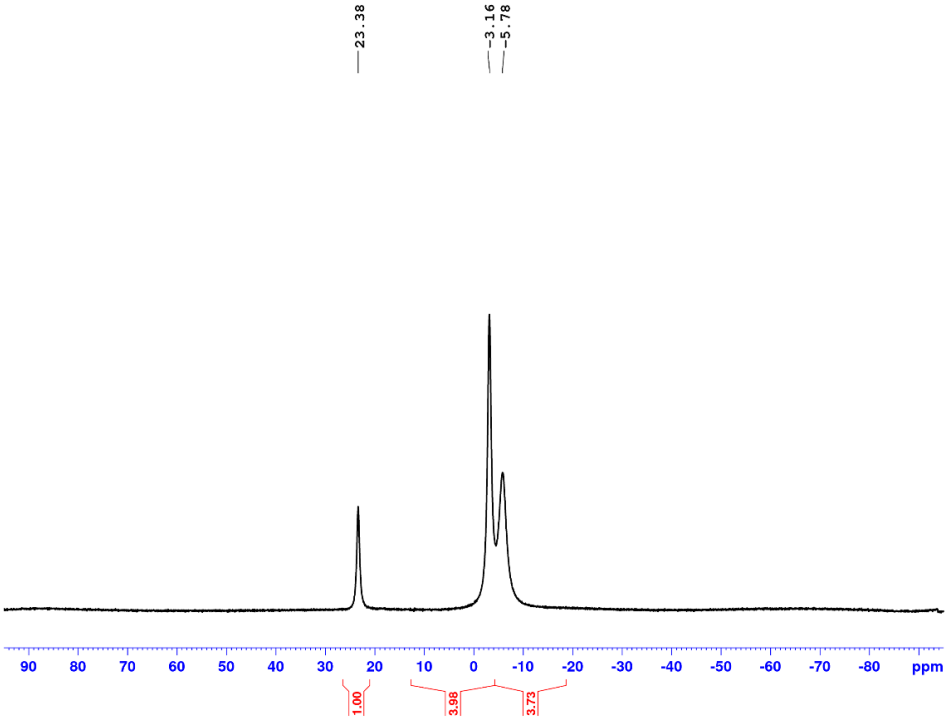

Figure 2.17, continued.

(d) $^{31}P\{^{1}H\}$ NMR (CD_2Cl_2, 162 MHz, 23 ºC)

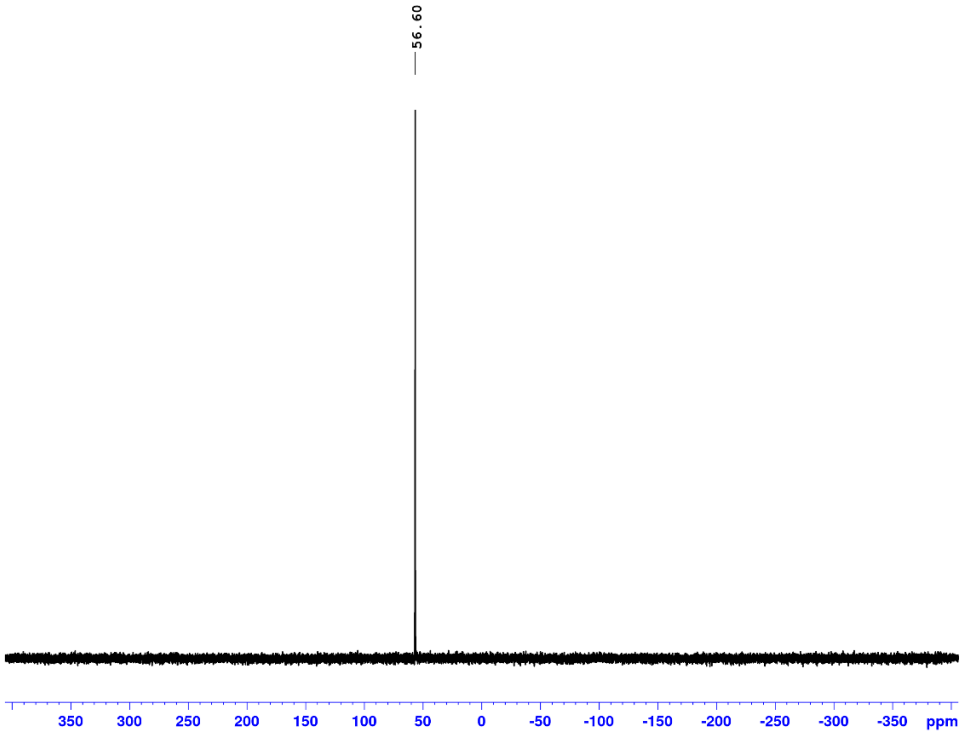

(e) ^{1}H NMR (CD_2Cl_2, 500 MHz, -60 ºC)

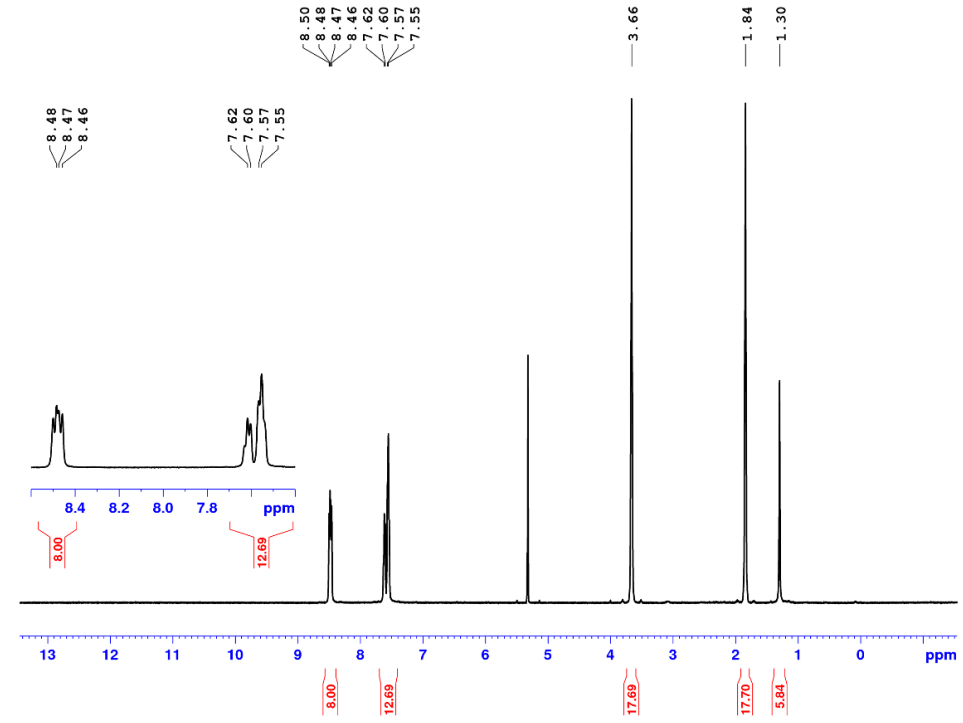

Figure 2.17, continued.

(f) $^{31}P\{^{1}H\}$ NMR (CD_2Cl_2, 202 MHz, -60 ºC)

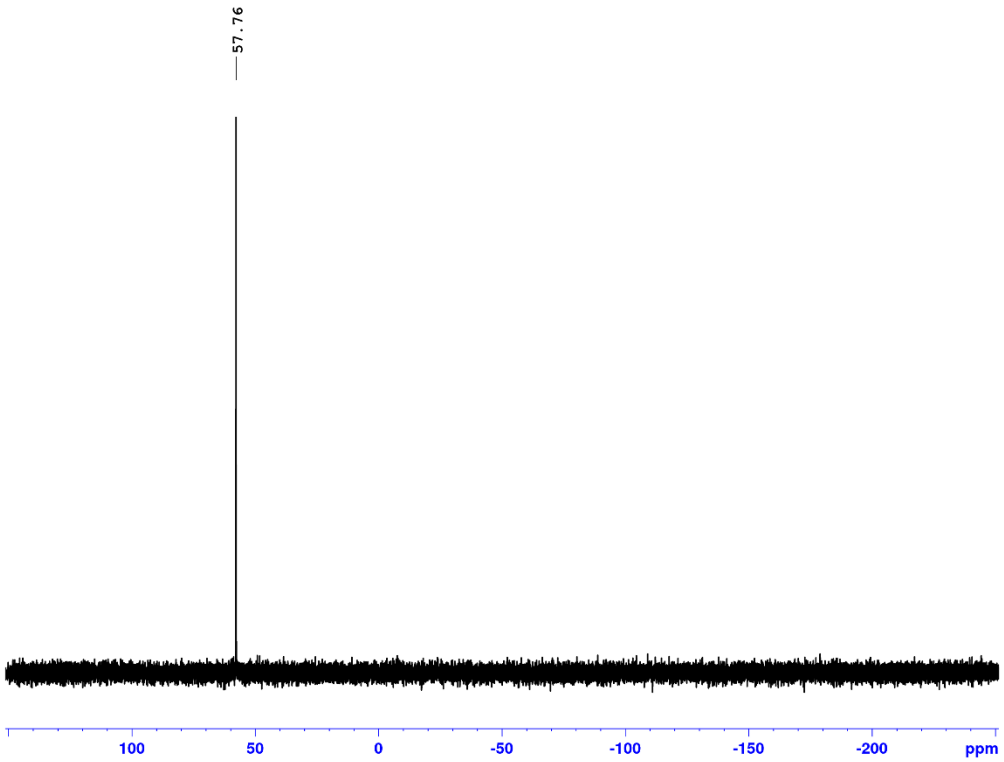

Without further purification, $[Li(THF)_3][\mathbf{5}]$ was reacted with $AgBF_4$ (10.7 mg, 0.06 mmol) using the procedure described above for **7** to yield **8** as a light brown powder. Yield: 78 mg, 88%. ^{1}H NMR (500 MHz, CD_2Cl_2, 23 ºC): δ 8.41 (dd, $^{2}J_{PH}$ = 12.5 Hz, $^{3}J_{HH}$ = 8.5 Hz, 4H, *o*–Ph), 7.63 (m, 6H, *m*–Ph and *p*–Ph), 4.09 (m, 4H, THF), 2.05 (m, 4H, THF), 1.18 (s, 3H, Pd–C*H*$_3$). $^{13}C\{^{1}H\}$ NMR (101 MHz, CD_2Cl_2, 23 ºC): δ 137.7 (d, $^{2}J_{PC}$ = 14 Hz, *o*-Ph), 133.7 (*p*-Ph), 129.0 (d, $^{3}J_{PC}$ = 13 Hz, *m*-Ph), 123.6 (d, $^{1}J_{PC}$ = 59 Hz, *ipso*-Ph), 71.2 (THF), 16.6 (THF), 14.6 (Pd-Me). $^{11}B\{^{1}H\}$ NMR (96 MHz, CD_2Cl_2, 23 ºC): δ 24.3 (1B), -3.2 (4B), -5.9 (4B). $^{31}P\{^{1}H\}$ NMR (162 MHz, CD_2Cl_2, 23 ºC): δ 56.6. ESI/APCI HRMS (m/z): $[M - THF + CH_3CN]^-$ calculated for $C_{16}H_{16}B_9NPCl_9Pd$: 779.8360; found: 779.8365. MP: 150.4 – 159.7 ºC (dec).

Figure 2.18. NMR Spectra of **8**.

(a) ^{1}H NMR of **8** (CD_2Cl_2, 400 MHz, 23 ºC)

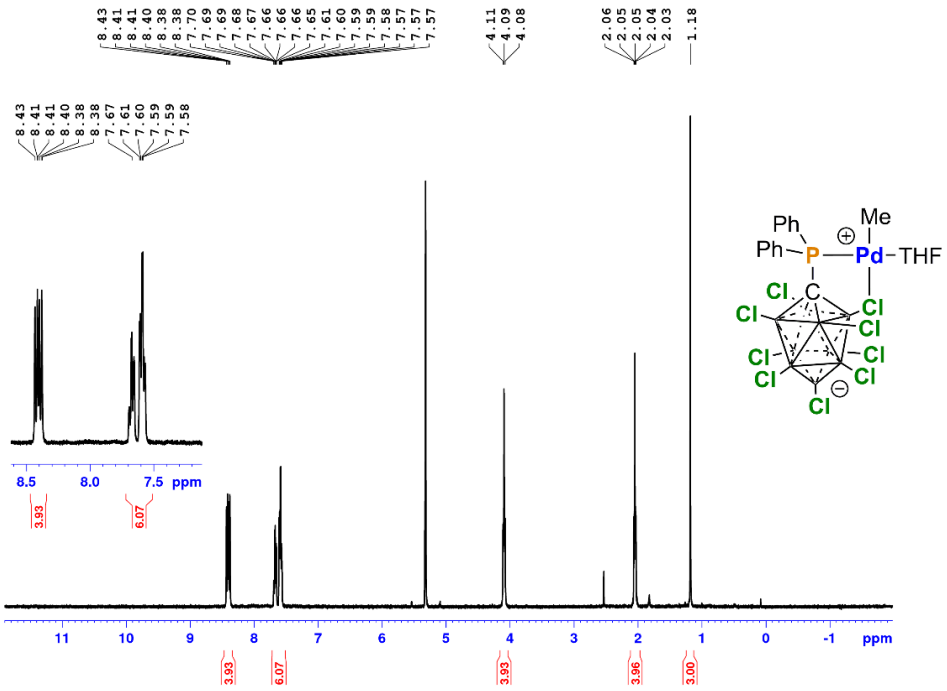

(b) $^{13}C\{^{1}H\}$ NMR (CD_2Cl_2, 101 MHz, 23 ºC)

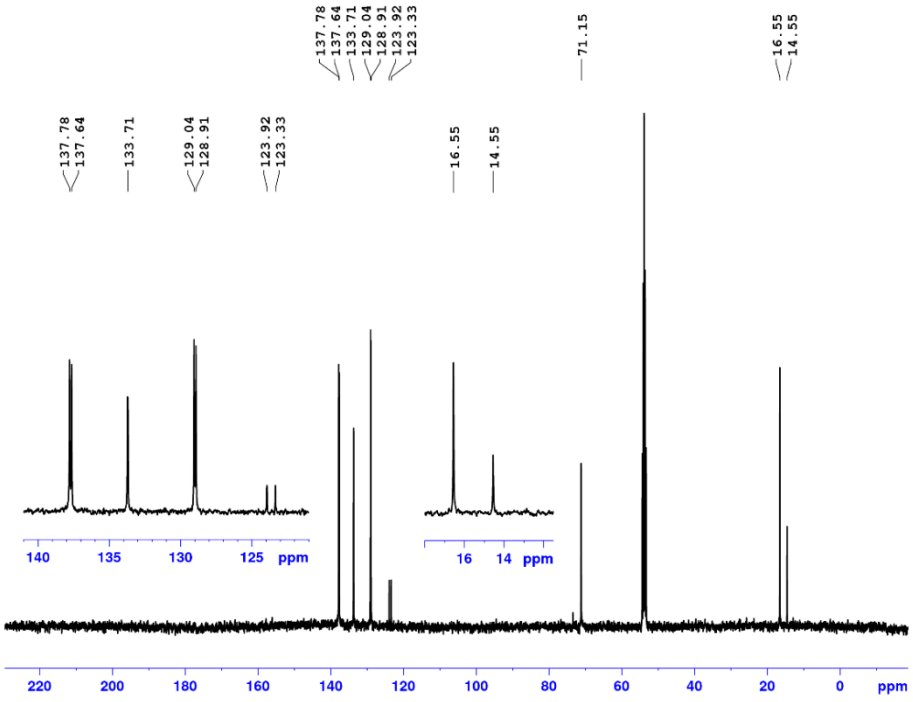

Figure 2.18, continued.

(c) $^{11}B\{^{1}H\}$ NMR (CD_2Cl_2, 128 MHz, 23 ºC)

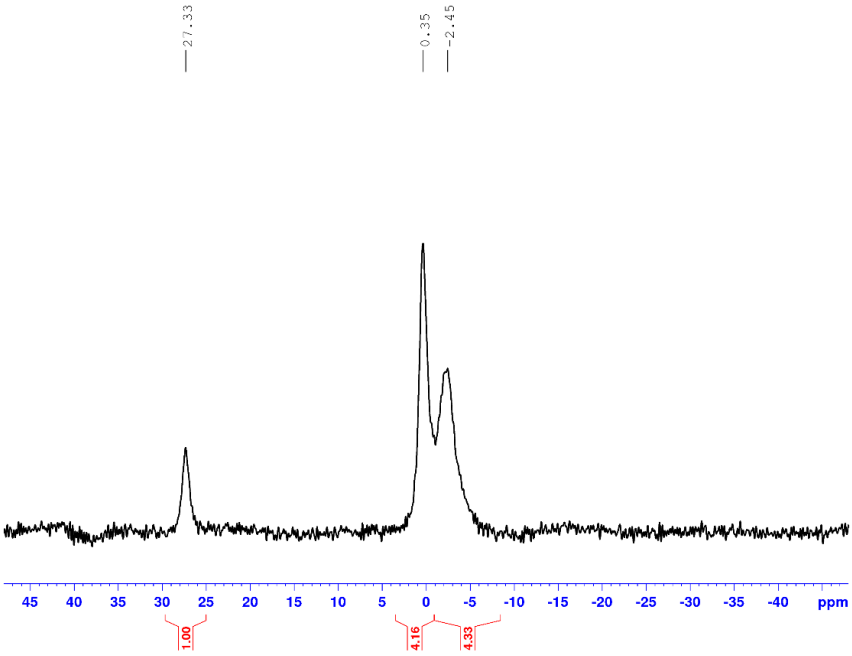

(d) $^{31}P\{^{1}H\}$ NMR of **8** (CD_2Cl_2, 162 MHz, 23 ºC)

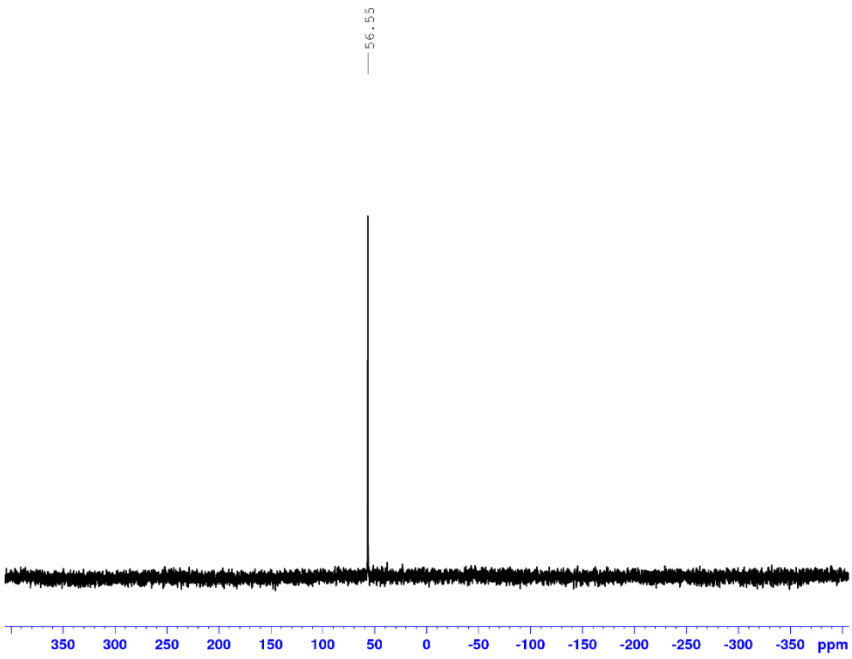

(κ^2-*P,O*-P(*o*-OMe-Ph)$_2$CB$_9$Cl$_9$)PdMe(THF) (9). [Li(THF)$_3$][**6**] was generated as a tan powder from **3** (100 mg, 0.10 mmol) and (COD)PdMeCl (27.3 mg, 0.100 mmol) using the procedure for [Li(THF)$_3$][**4**]. 94 % pure by inverse-gated ^{31}P{^{1}H} NMR. ^{1}H NMR (500 MHz, CD_2Cl_2, 23 ºC): δ 8.00 (br s, Ar, 3H, integration is lower than expected due to broadness), 7.54 (t, *J* = 7.7 Hz, 4H, Ar), 7.06 (t, *J* = 7.5 Hz, 4H, Ar), 6.99 (t, *J* = 7.1 Hz, 4H, Ar), 3.76 (overlapping m and br s, 24 H, –OC*H*$_3$ and THF), 1.94 (m, 12 H, THF), 1.13 (s, 6H, Pd-C*H*$_3$). ^{13}C{^{1}H} NMR (126 MHz, CD_2Cl_2, 23 ºC): δ 161.6 (br s, Ar), 136.1 (br s, Ar) 134.2 (Ar), 121.5 (br s, Ar), 112.6 (Ar), 69.0 (THF), 58.3 (br s, –O*C*H$_3$), 56.1 (br s, –O*C*H$_3$), 25.9 (THF), 0.7 (br s, Pd–*C*H$_3$). ^{11}B{^{1}H} NMR (96 MHz, CD_2Cl_2, 23 ºC): δ 24.2 (1B), -3.5 (4B), -6.0 (4B). Inverse-gated ^{31}P{^{1}H} NMR (162 MHz, CD_2Cl_2, 23 ºC): δ 21.2. Low temperature NMR data: Major isomer (62 %) ^{1}H NMR (500 MHz, CD_2Cl_2, -60 ºC): 4.08 (s, 6H –OC*H*$_3$,), 3.56 (s, 6H –OC*H*$_3$), 1.01 (s, 6H Pd–C*H*$_3$). ^{31}P{^{1}H} NMR (202 MHz, CD_2Cl_2, -60 ºC): 20.0. Minor isomer (38 %) ^{1}H NMR (500 MHz, CD_2Cl_2, -60 ºC): δ 4.18 (s, 6H, –OC*H*$_3$), 3.38 (s, 6H, –OC*H*$_3$), 0.97 (s, 6H, Pd–C*H*$_3$). Inverse-gated ^{31}P{^{1}H} NMR (202 MHz, CD_2Cl_2, -60 ºC): δ 20.4. The Ar resonances for these two species are overlapped. The ^{1}H NMR resonances for bound THF are observed at δ 3.66 and 1.83 in ^{1}H NMR. MP: 125.3 – 129.8 ºC (dec).

Figure 2.19. NMR Spectra of [Li(THF)$_3$][**6**]

(a) ^{1}H NMR (CD_2Cl_2, 500 MHz, 23 ºC)

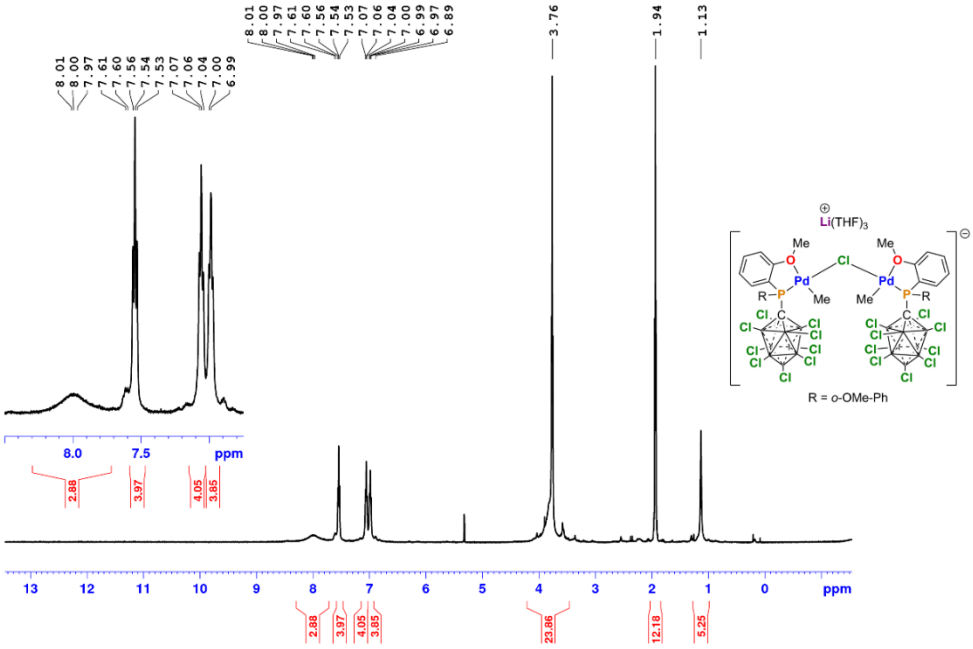

(b) ^{13}C{^{1}H} NMR of [Li(THF)$_3$][**6**] (CD_2Cl_2, 126 MHz, 23 ºC)

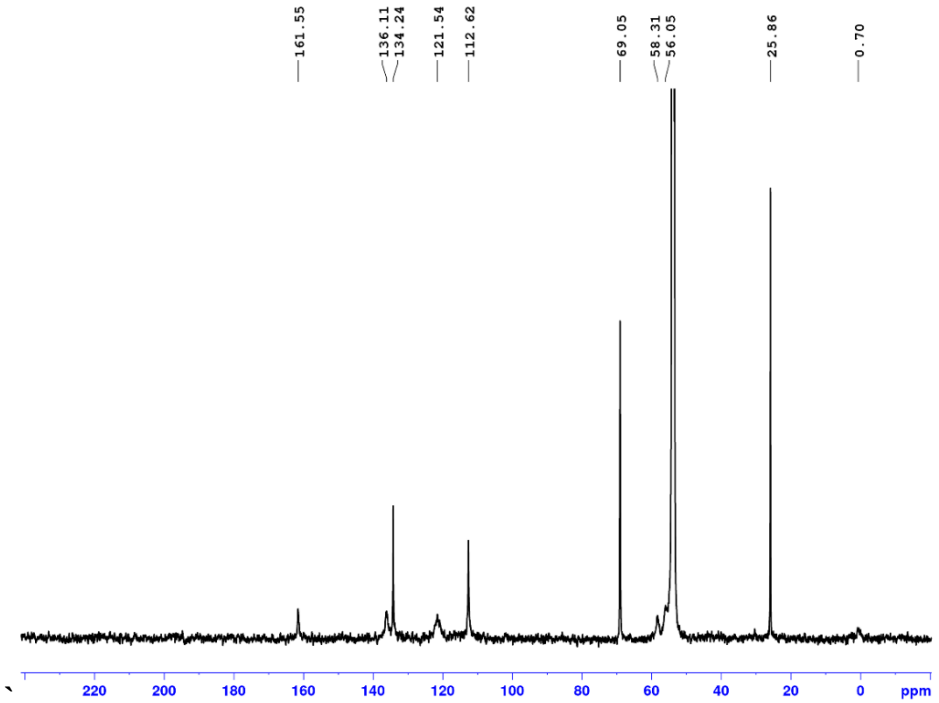

Figure 2.19, continued.

(c) $^{11}B\{^{1}H\}$ NMR (CD_2Cl_2, 128 MHz, 23 ºC)

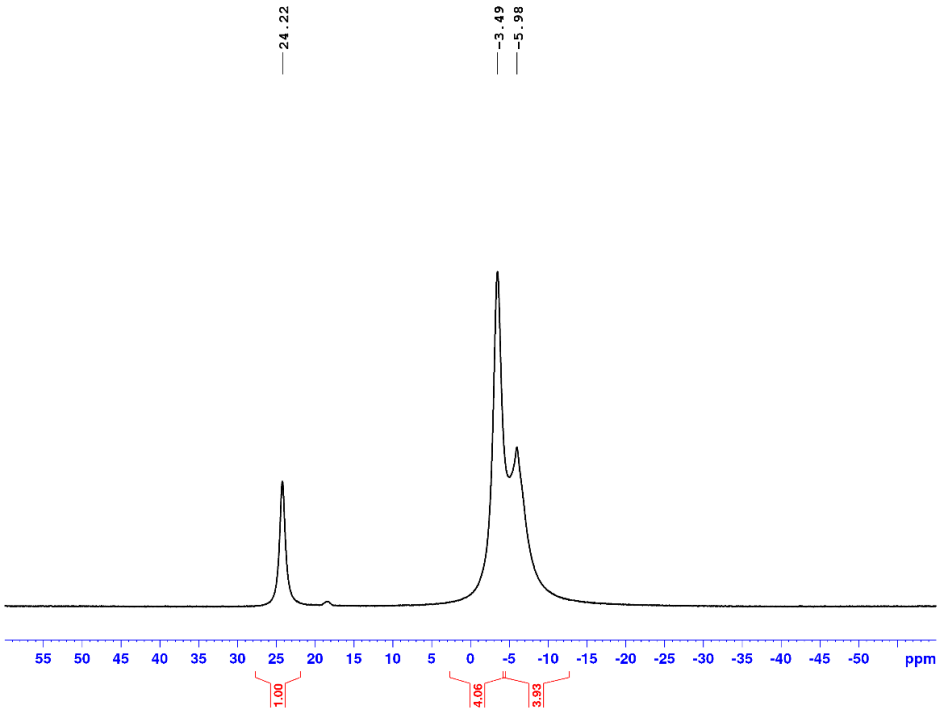

(d) Inverse-gated $^{31}P\{^{1}H\}$ NMR of $[Li(THF)_3][\mathbf{6}]$ (CD_2Cl_2, 162 MHz, 23 ºC) (* denotes unknown impurity)

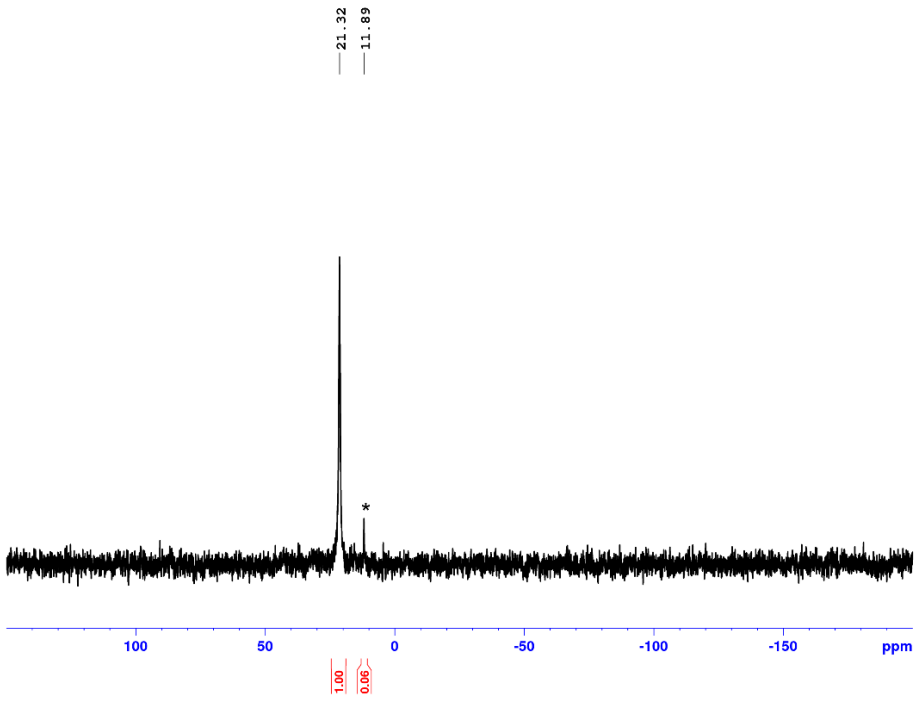

Figure 2.19, continued.

(e) ^{1}H NMR (CD_2Cl_2, 500 MHz, -60 ºC)

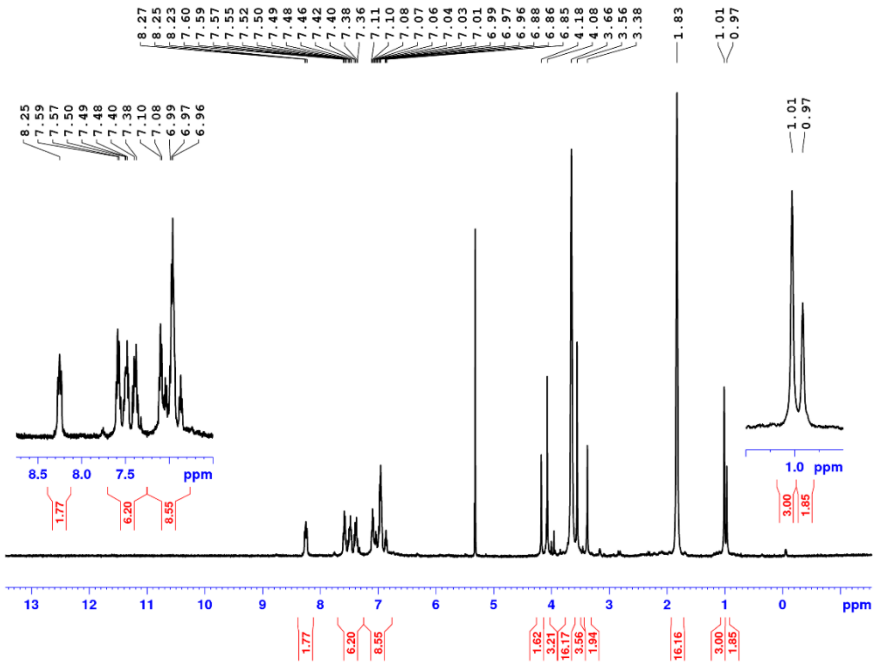

(f) Inverse-gated $^{31}P\{^{1}H\}$ NMR of [Li(THF)$_3$][**6**] (CD_2Cl_2, 202 MHz, -60 ºC) (* denotes unknown impurity)

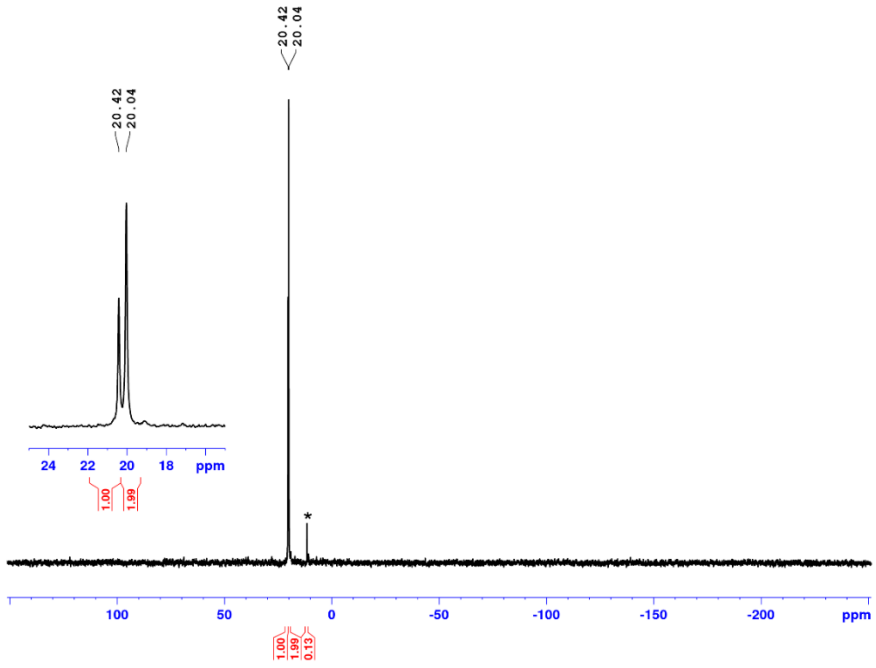

Without further purification [Li(THF)$_3$][**6**] was reacted with $AgBF_4$ (10.0 mg, 0.0500 mmol) using the procedure described for **7** to yield **9** as a tan powder. Yield: 81 mg, 94% yield. The labelling scheme for **9** is shown in Figure 2.20. ^{1}H NMR (500 MHz, CD_2Cl_2, 23 ºC): δ 8.0 (br s, 2H, Ar), 7.59 (m, 2H, Ar), 7.12 (m, 2H, Ar), 7.01 (m, 2H, Ar), 4.04 (m, 4H, THF), 3.82 (br s, 6H, –OC*H*$_3$), 2.02 (m, 4H, THF), 0.89 (s, 3H, Pd–C*H*$_3$). ^{13}C{^{1}H} NMR (151 MHz, CD_2Cl_2, 23 ºC): δ 160.8 (*C*–OMe), 135.9 (br, Ar), 134.3 (br, Ar), 121.6 (br, Ar), 112.1 (Ar), 69.6 (THF), 57.8 (br s, –O*C*H$_3$), 25.4 (THF), 2.6 (br s, Pd–*C*H$_3$). ^{11}B{^{1}H} NMR (96 MHz, CD_2Cl_2, 23 ºC): δ 24.6 (1B), -4.0 (4B), -6.5 (4B). Inverse-gated ^{31}P{^{1}H} NMR (162 MHz, CD_2Cl_2, 23 ºC): δ 21.2. Low temperature NMR data[62]: ^{1}H NMR (500 MHz, CD_2Cl_2, -60 ºC): δ 8.27 (dd, $^3J_{PH}$ = 12.5 Hz, J_{HH} = 8 Hz, 1H, H^{13}), 7.64 (t, J_{HH} = 7.5 Hz ,1H, H^{11}), 7.56 (t, J = 7.5 Hz, H^4,), 7.45 (dd, $^3J_{PH}$ = 12.5 Hz, J_{HH} = 8 Hz, 1H, H^6), 7.14 (t, J_{HH} = 7 Hz, 1H, H^{12}), 7.08 (t, J_{HH} = $^4J_{PH}$ = 7.5 Hz, 1H, H^{10}), 7.04 (t, J_{HH} = 7.5 Hz, 1H, H^5), 6.98 (t, J_{HH} = $^4J_{PH}$ = 8 Hz , 1H, H^3), 4.09 (br m, 4H, THF), 4.05 (s, 3H, H^7), 3.73 (s, 3H, H^{14}), 2.01 (br m, 4H, THF), 0.71 (s, 3H, Pd-C*H*$_3$). ^{13}C{^{1}H} NMR (126 MHz, CD_2Cl_2, -60 ºC): δ 160.8 (d, $^2J_{PC}$ = 13 Hz, C^2), 158.8 (d, $^2J_{PC}$ = 9 Hz, C^9), 136.4 (C^{13}), 134.3 (C^{11}) 134.2 (C^4) 133.5 (C^{16}), 123.2 (C^5), 118.8 (d, $^2J_{PC}$ = 10 Hz, C^{12}), 115.5 (d, $^1J_{PC}$ = 58 Hz, C^1) 111.8 (d, $^2J_{PC}$ = 6 Hz, C^3), 111.1 (d, $^2J_{PC}$ = 8 Hz, C^{10}), 108.3 (d, $^1J_{PC}$ = 71 Hz, C^8) , 72.8 (THF), 59.6 (C^7), 55.9 (C^{14}), 25.1 (THF), 1.2 (Pd-*C*H$_3$). Inverse-gated ^{31}P{^{1}H} NMR (202 MHz, CD_2Cl_2, -60ºC): δ 20.8. HRMS: ESI/APCI HRMS (m/z): [M – THF + CH_3CN]$^-$ calculated for $C_{18}H_{20}B_9NO_2PCl_9Pd$: 829.8318; found: 829.8320. MP: 123.5 – 135.2 ºC (dec).

Figure 2.20. Labelling scheme for **9**.

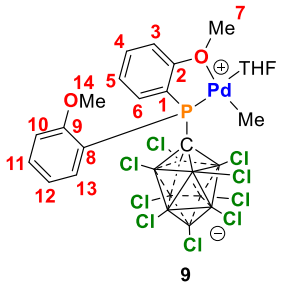

Figure 2.21. NMR Spectra of **9**.

(a) ^{1}H NMR (CD_2Cl_2, 500 MHz, 23 ºC)

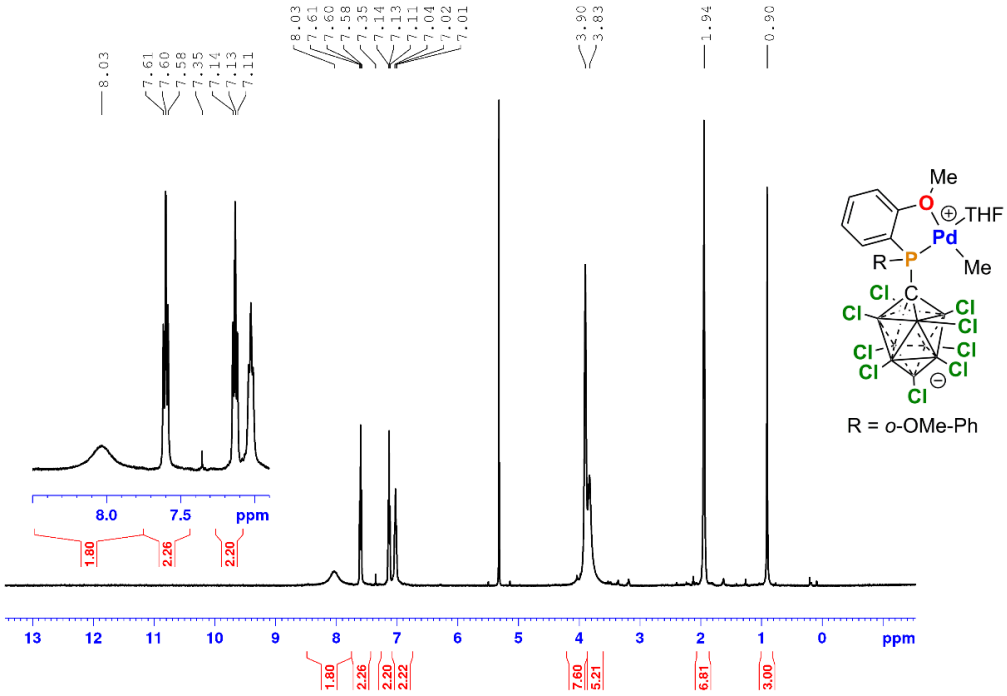

Figure 2.21, continued.

(b) $^{13}C\{^{1}H\}$ NMR (CD_2Cl_2, 151 MHz, 23 ºC)

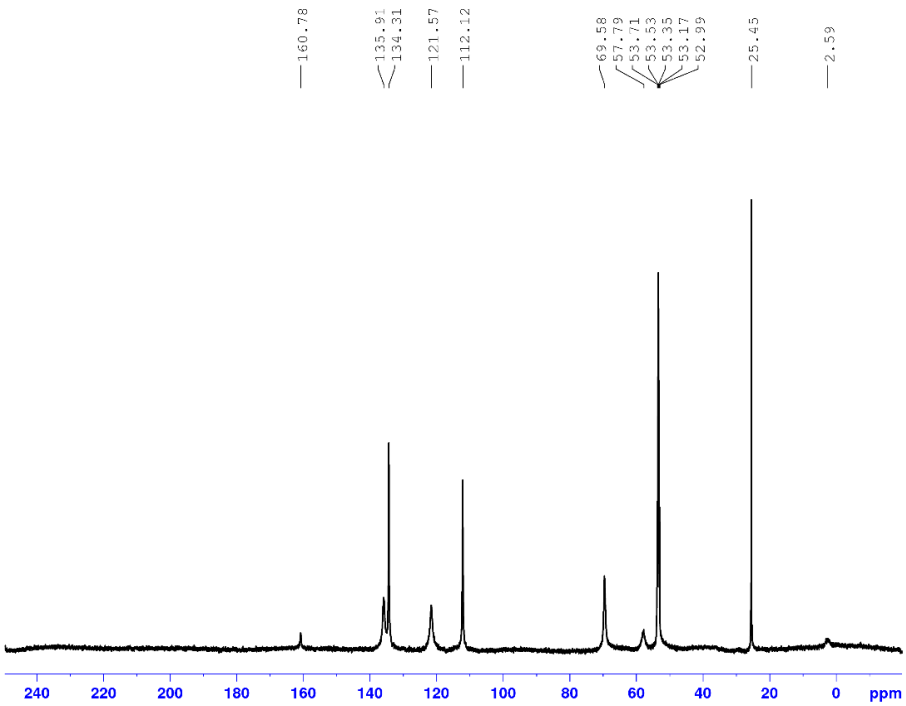

(c) $^{11}B\{^{1}H\}$ NMR (CD_2Cl_2, 128 MHz, 23 ºC)

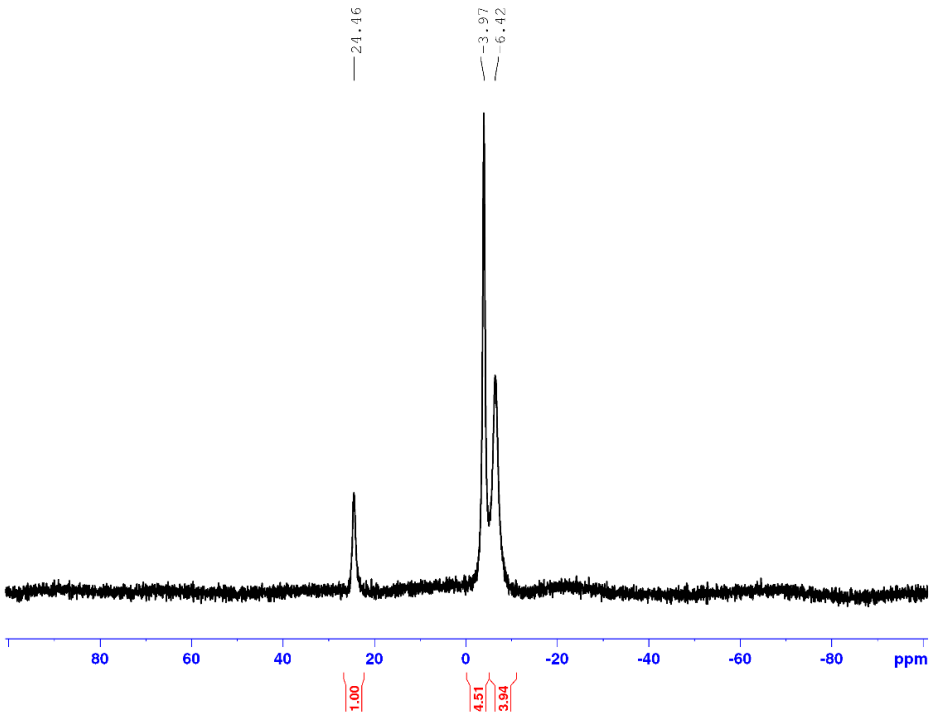

Figure 2.21, continued.

(d) $^{31}P\{^{1}H\}$ NMR (CD_2Cl_2, 162 MHz, 23 ºC)

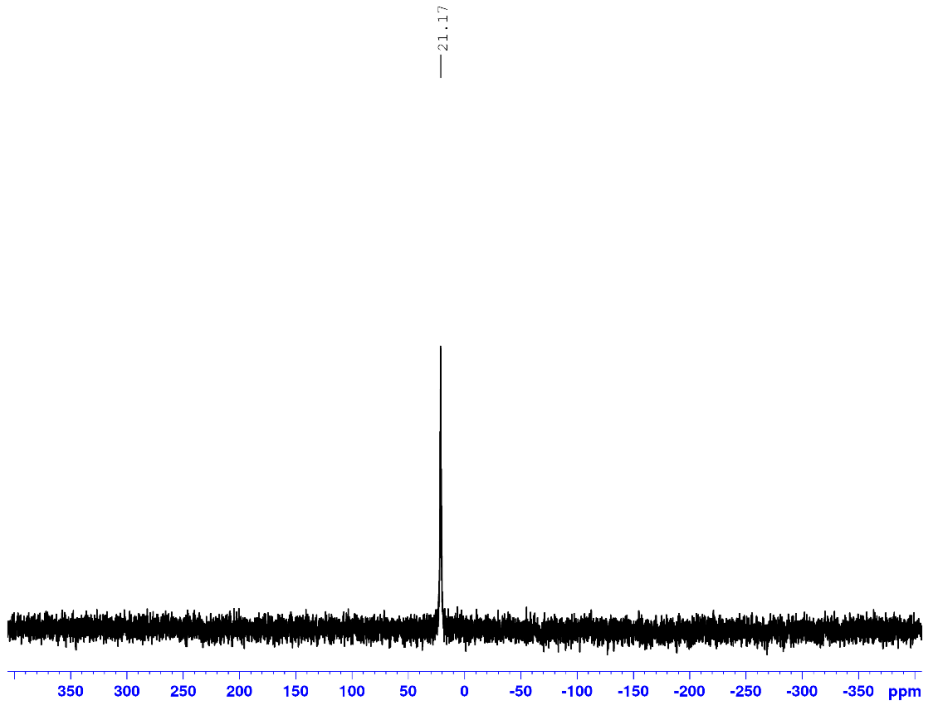

(e) ^{1}H NMR (CD_2Cl_2, 500 MHz, -60 ºC) (* denotes CH_3CN adduct impurity)

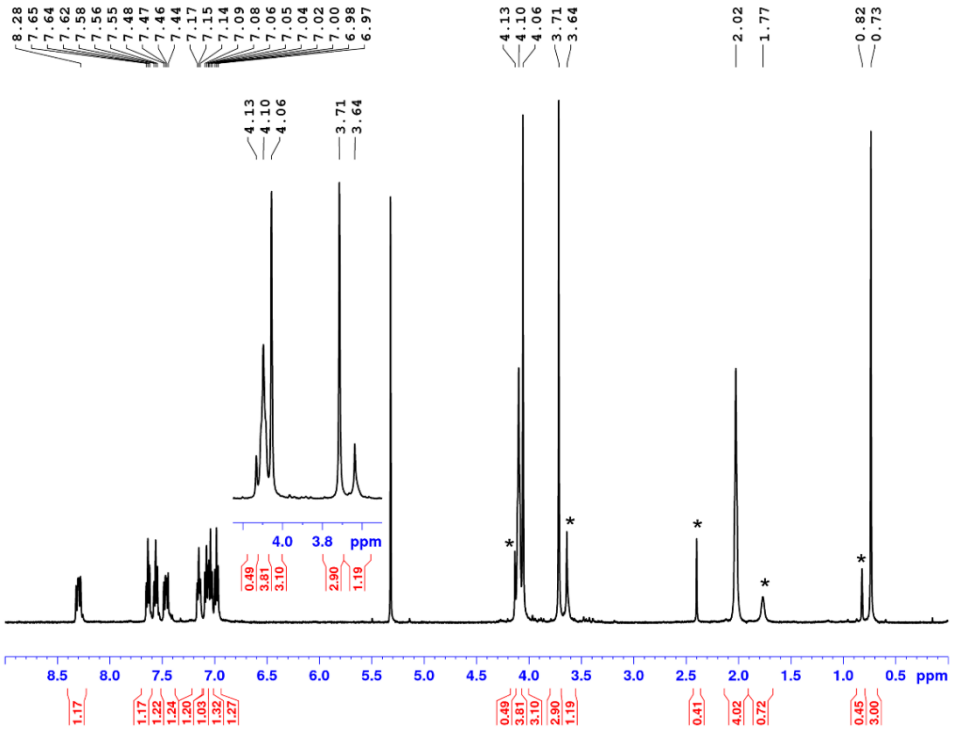

Figure 2.21, continued.

(f) $^{13}C\{^{1}H\}$ NMR (CD_2Cl_2, 126 MHz, -60 ºC)

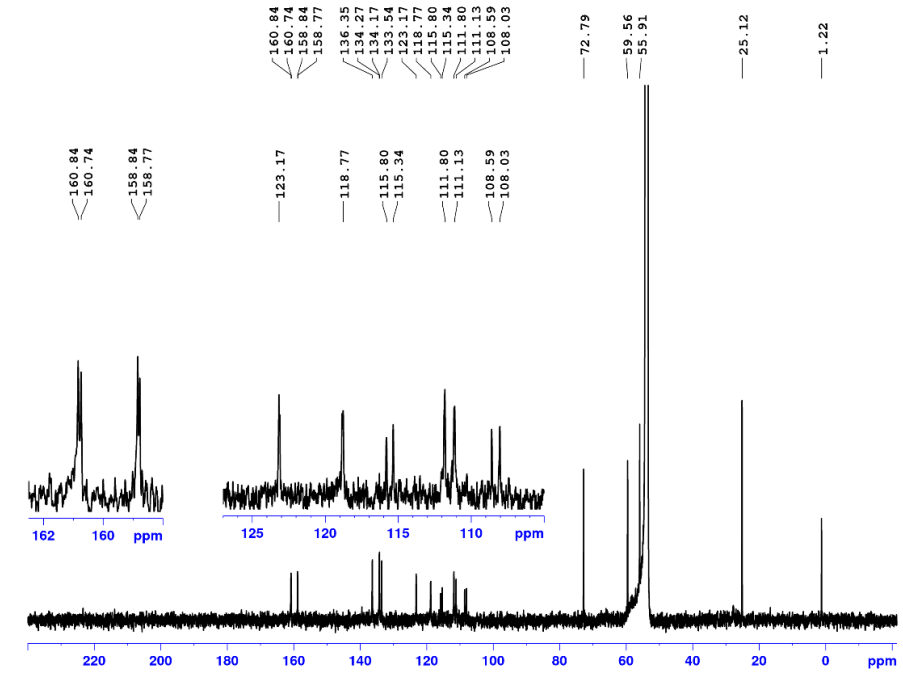

(g) Inverse-gated $^{31}P\{^{1}H\}$ NMR **9** (CD_2Cl_2, 202 MHz, -60 ºC) (* denotes CH_3CN adduct impurity)

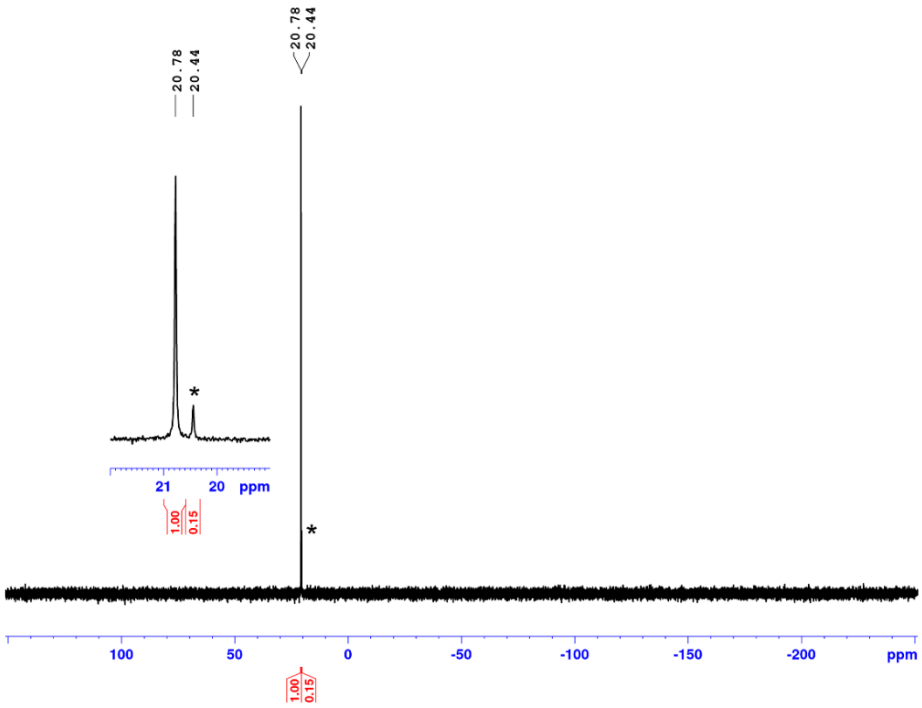

Figure 2.21, continued.

(h) HSQC of **9** (CD_2Cl_2, 500 MHz, -60 ºC)

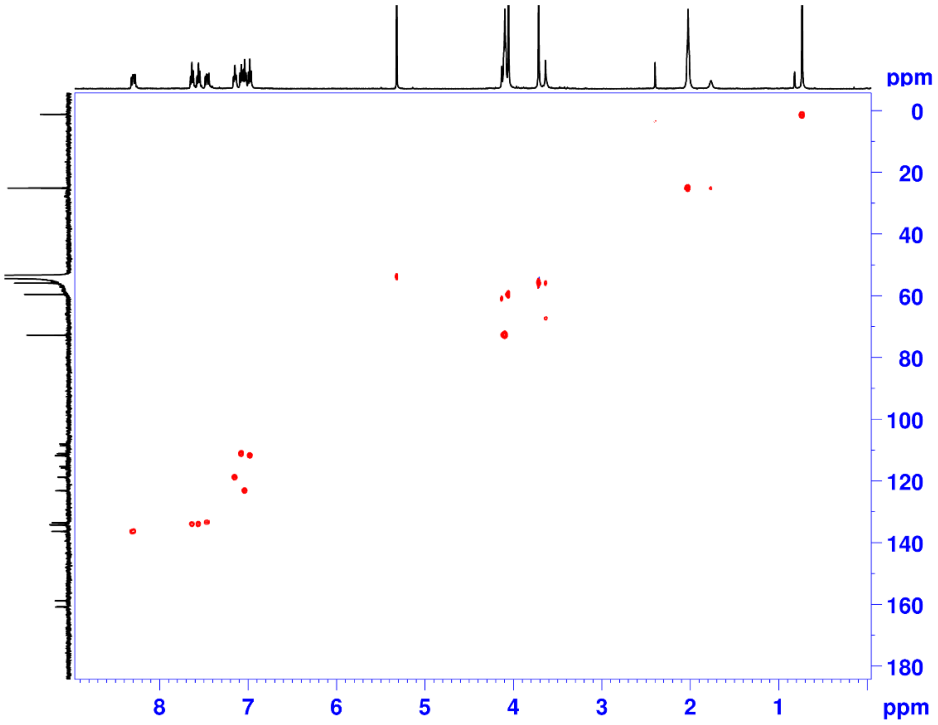

(i) Expansion of HSQC ((δ 8.9 – 6.5), (δ 145 – 100)) of **9** (CD_2Cl_2, 500 MHz, -60 ºC)

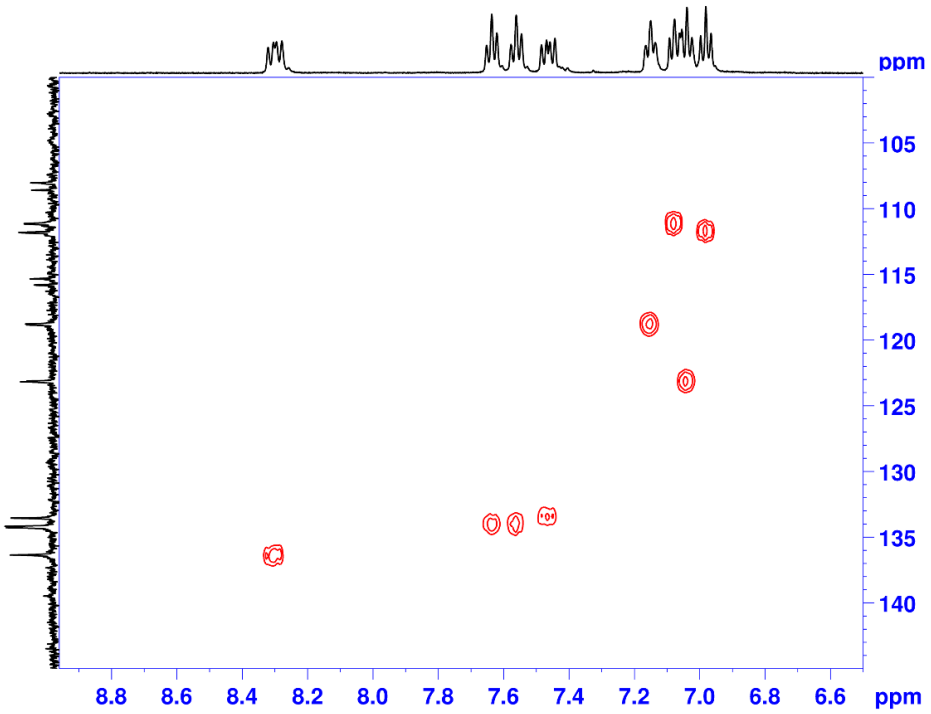

Figure 2.21, continued.

(j) VT ^{1}H NMR of **9** (CD_2Cl_2, 500 MHz)

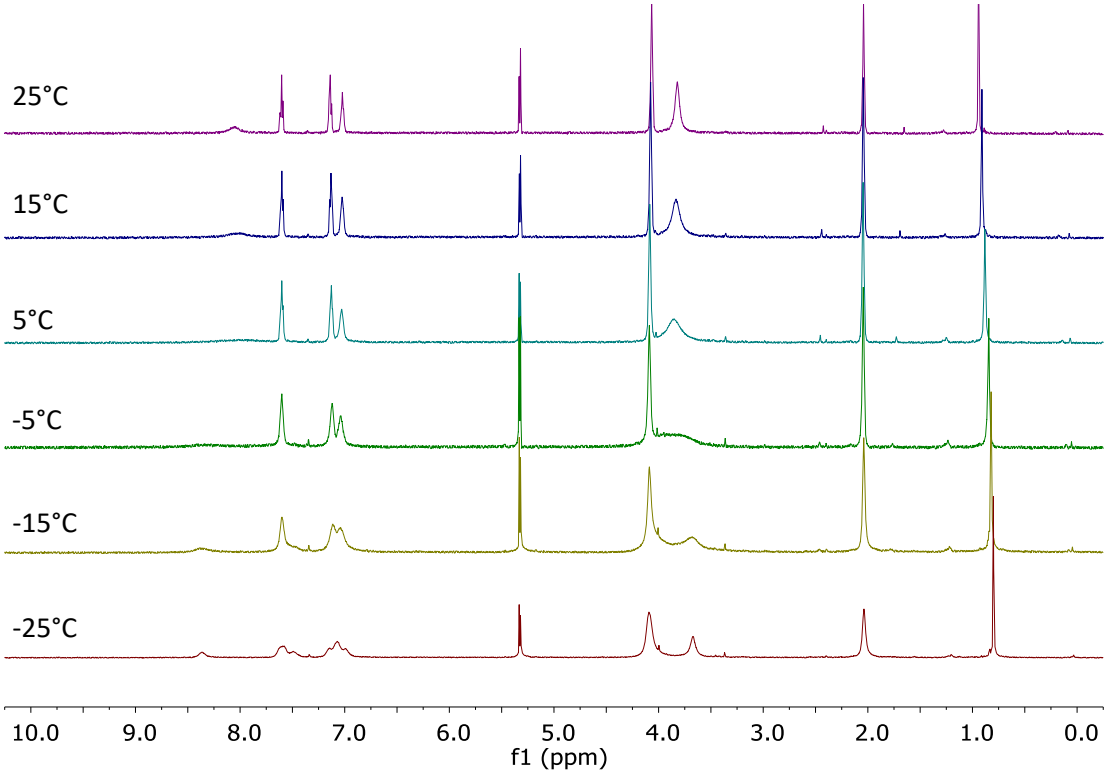

Generation of (κ^2-*P,O*-P(*o*-OMe-Ph)$_2$CB$_9$Cl$_9$)PdMe(CH$_2$=CH$_2$) (10). A solution of **9** (~5.0 mg) in CD_2Cl_2 was prepared in a J. Young NMR tube. The tube was cooled to -196 ^{o}C in a liquid nitrogen bath and the desired amount of ethylene was added by vacuum transfer. The tube was allowed to thaw and warm to -78 ^{o}C to afford a yellow-orange solution. The tube was shaken several times to ensure proper mixing of ethylene into the solvent and then was placed in an NMR probe that had been precooled to -78 $^{\circ}$C.[62] The labelling scheme for **10** is shown in Figure 2.22. ^{1}H NMR (CD_2Cl_2, 500 MHz, -78 ^{o}C): δ 8.30 (dd, J_{HH} =8 Hz, J_{PH} = 12 Hz, 1H, H^{13}), 7.66 (t, J = 8 Hz, 1H, H^{11}), 7.57 (t, J =7.5 Hz, 1H, H^{4}), 7.43 (dd, J_{HH} =8 Hz, J_{PH} = 12 Hz, 1H, H^{6}), 7.18 (t, J =7 Hz, 1H, H^{12}), 7.05 (t, J =7.5 Hz, 2H, H^{3} and H^{5}), 6.99 (dd, J_{HH} =8 Hz, J_{PH} = 8 Hz, H^{10}), 5.42 (br d, J = 9 Hz, 2H, bound ethylene AA'), 5.36 (s, free ethylene), 5.30 (br d, bound ethylene BB' (overlapped with solvent resonance)), 4.03 (s, 3H, H^{7}), 3.71 (s, 3H, H^{14}), 3.61 (m, 4H, free THF), 1.74 (m, 4H,

free THF), 0.82 (s, $^{3}J_{PH}$ = 3 Hz, 3H, Pd-CH_3). $^{13}C\{^{1}H\}$ NMR (CD_2Cl_2, 126 MHz, -78 ºC): δ 161.3 (d, $^{2}J_{PC}$ = 15 Hz, C^{9}), 158.2 (d, $^{2}J_{PC}$ = 10 Hz, C^{2}), 136.8 (C^{13}), 134.5 (C^{1}), 134.1 (C^{4}), 134.0 (C^{11}), 123.6 (C^{5}), 122.8 (s, free ethylene), 119.1 (C^{12}), 114.7 (d, $^{1}J_{PC}$ = 54 Hz, C^{1}), 112.0 (C^{3}), 111.4 (C^{10}), 107.0 (d, $^{1}J_{PC}$ = 61 Hz, C^{8}), 101.5 (s, bound ethylene), 67.3 (s, free THF), 60.4 (C^{7}), 56.0 (C^{14}), 25.0 (free THF), 5.9 (Pd-CH$_3$). Inverse-gated $^{31}P\{^{1}H\}$ NMR (202 MHz, CD_2Cl_2, -78 ºC): δ 9.8.

Figure 2.22. Labelling scheme for **10**.

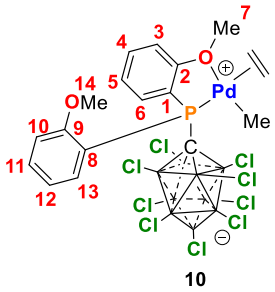

10

Figure 2.23. NMR Spectra of **10.**

(a) ^{1}H NMR of **10** generated by the reaction of **9** with 3.5 equiv. of ethylene (CD_2Cl_2, 500 MHz, -78 ºC) (* denotes acetone and water on the outside of the NMR tube)

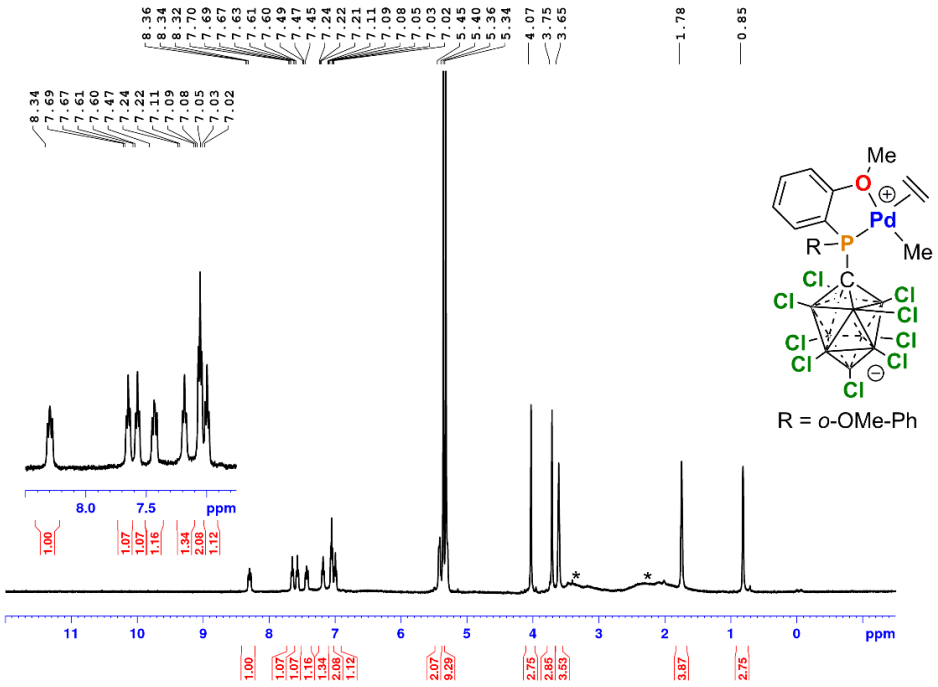

Figure 2.23, continued.

(b) Expansion of ^{1}H NMR (δ 5.75 – 5.00) of **10** given by the reaction of **9** with 3.5 equiv. of ethylene (CD_2Cl_2, 500 MHz, -78 ºC)

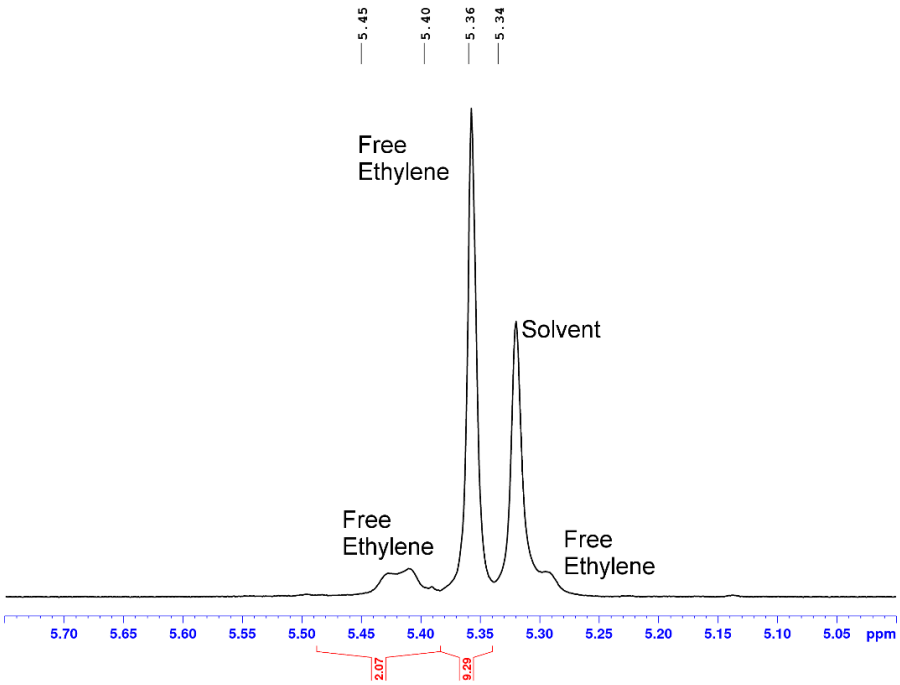

(c) $^{13}C\{^{1}H\}$ NMR of **10** given by the reaction of **9** with 3.5 equiv. of ethylene (CD_2Cl_2, 126 MHz, -78 ºC)

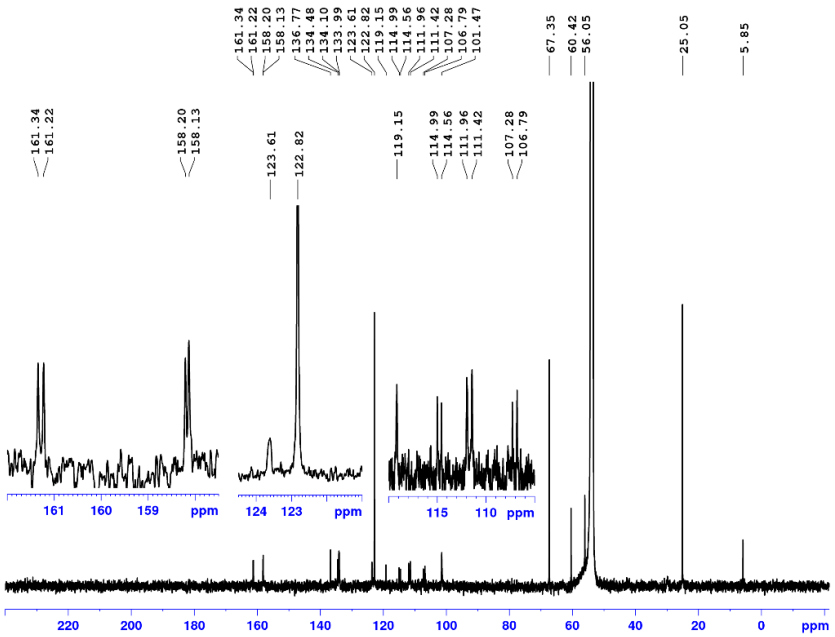

Figure 2.23, continued.

(d) ^{1}H-^{1}H COSY of **10** given by the reaction of **9** with 3.5 equiv. of ethylene (CD_2Cl_2, 500 MHz, -78 ºC)

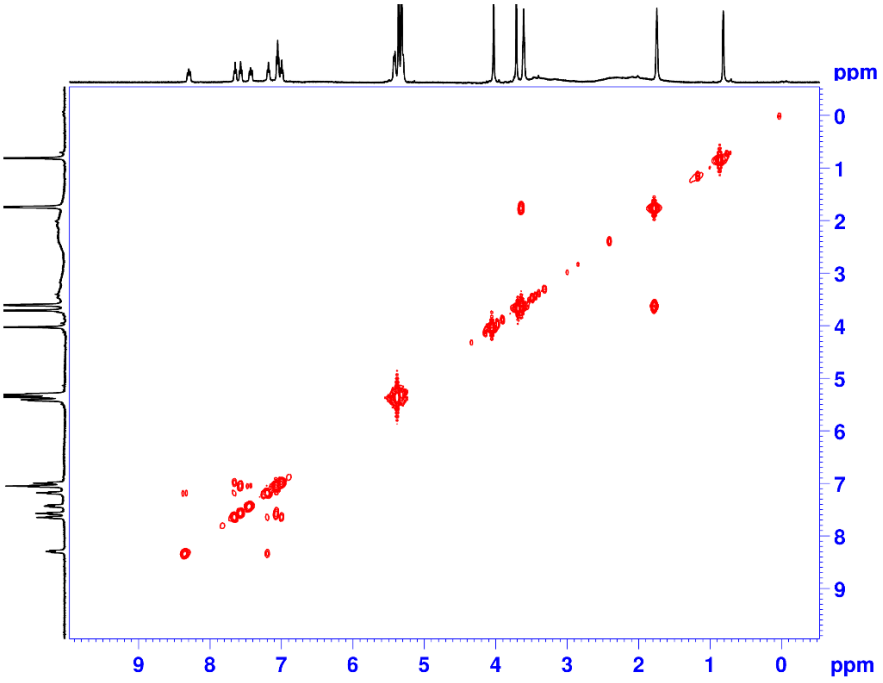

(e) Expansion of ^{1}H-^{1}H COSY ((δ 9.00 – 6.00), (δ 9.00 – 6.00)) of **10** given by the reaction of **9** with 3.5 equiv. of (CD_2Cl_2, 500 MHz, -78 ºC)

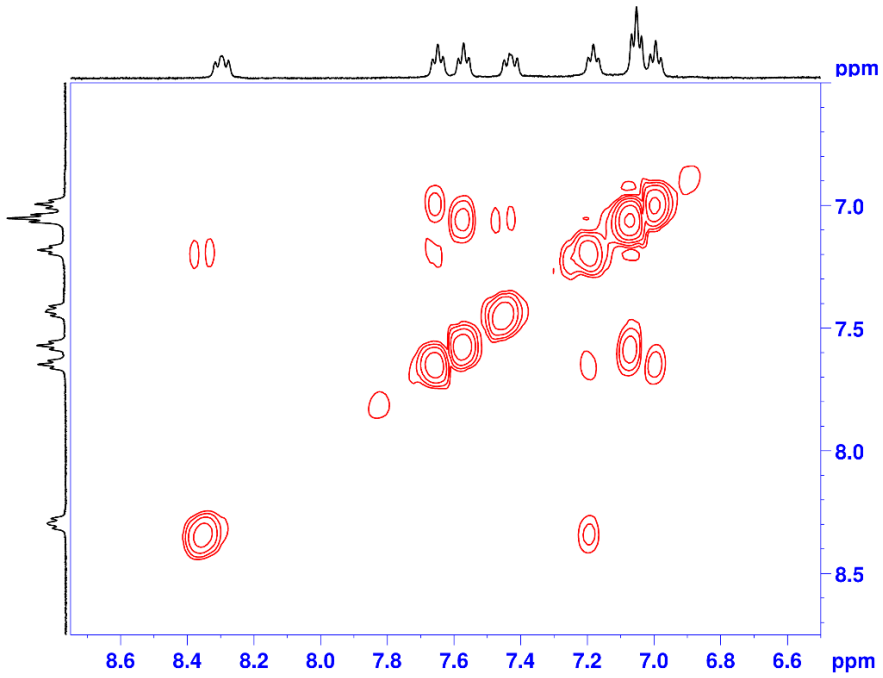

Figure 2.23, continued.

(f) ^{1}H NMR of **10** given by the reaction of **9** with 35 equiv. of ethylene (CD_2Cl_2, 500 MHz, -78 ºC) (* denotes CH_3CN adduct impurity)

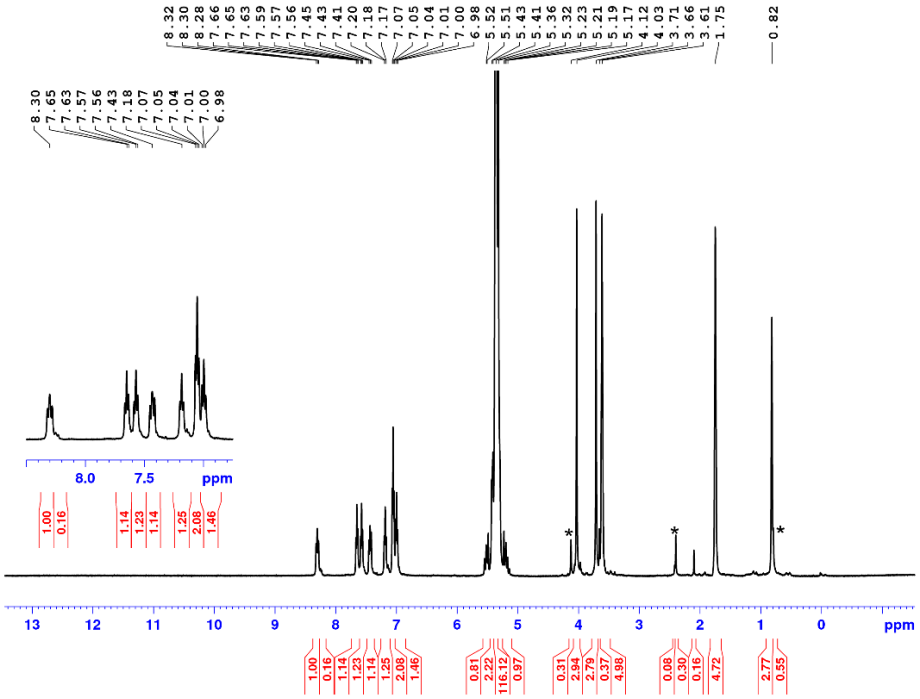

(g) Expansion of ^{1}H NMR (6.1 – 4.6 ppm) of of **10** given by the reaction of **9** with 35 equiv. of ethylene (CD_2Cl_2, 500 MHz, -78 ºC) (* denotes ^{13}C satellites of free ethylene[63])

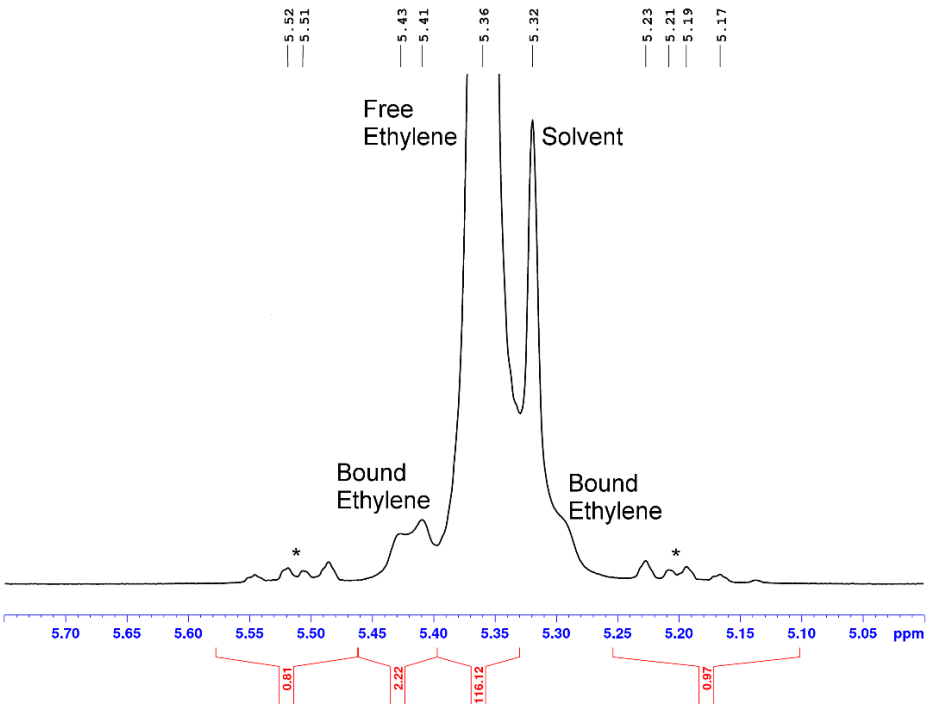

Figure 2.23, continued.

(h) HSQC of **10** given by the reaction of **9** with 35 equiv. of ethylene (CD_2Cl_2, 500 MHz, -78 ºC)

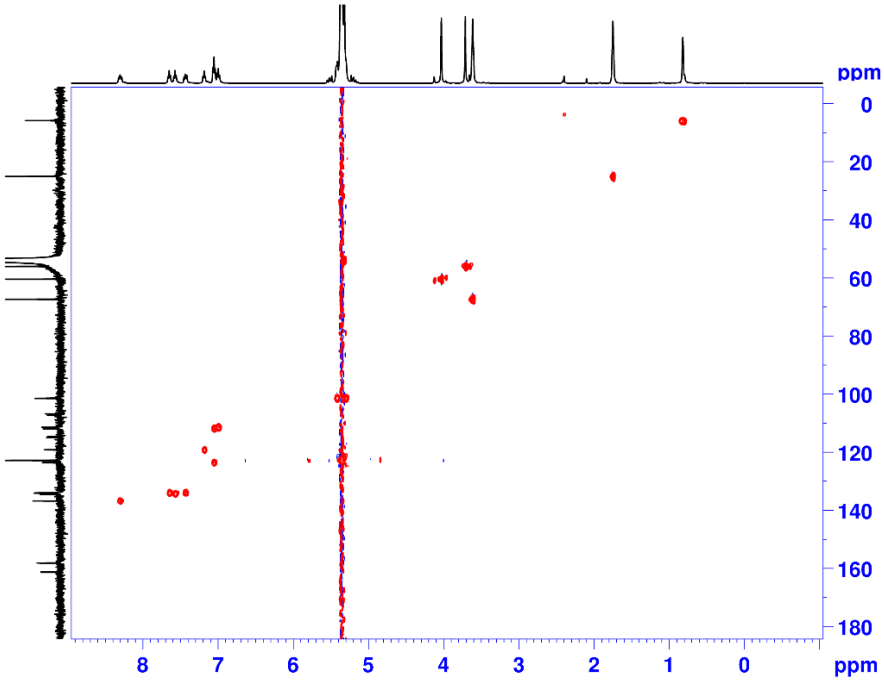

(i) Expansion of HSQC ((δ 6.0 – 5.0), (δ 120 – 90)) of **9** (CD_2Cl_2, 500 MHz, -60 ºC)

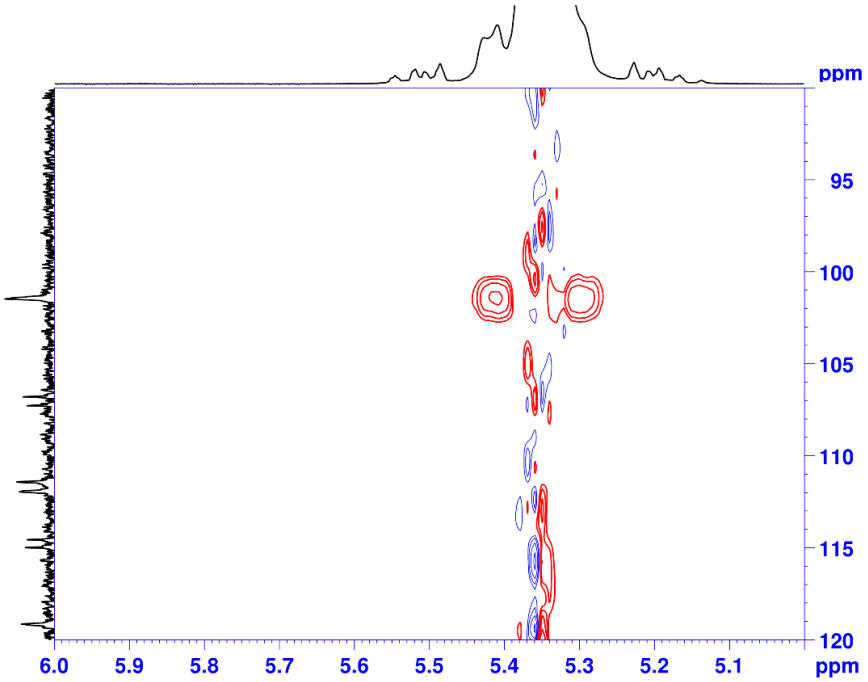

Figure 2.23, continued.

(j) ^{1}H-^{1}H NOESY of **10** given by the reaction of **9** with 35 equiv. of ethylene (CD_2Cl_2, 500 MHz, -78 ºC)

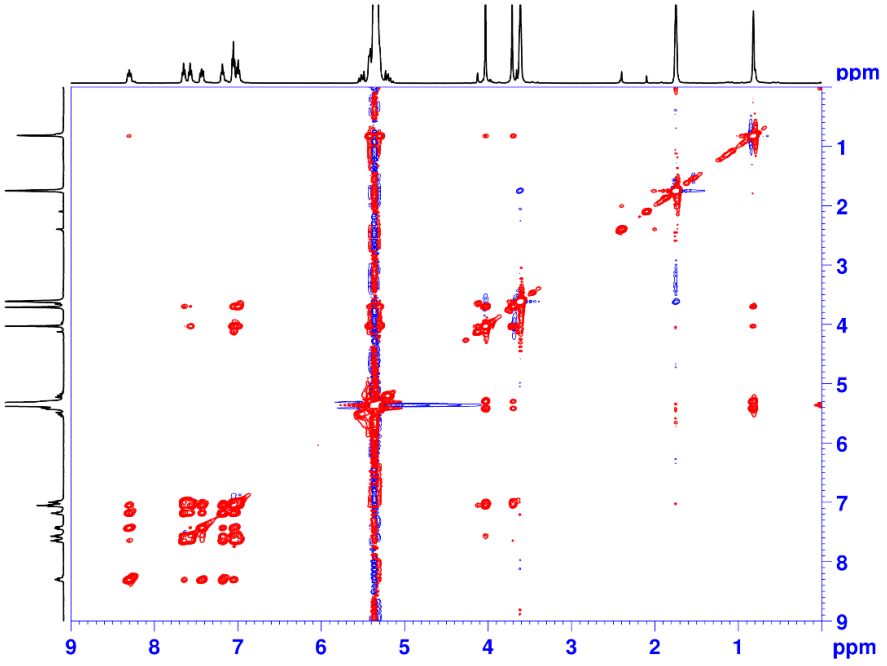

(k) Expansion of ^{1}H-^{1}H NOESY ((δ 5.0 – 0), (δ 5.8 – 5.0)) of **10** given by the reaction of **9** with 35 equiv. of ethylene (CD_2Cl_2, 500 MHz, -78 ºC)

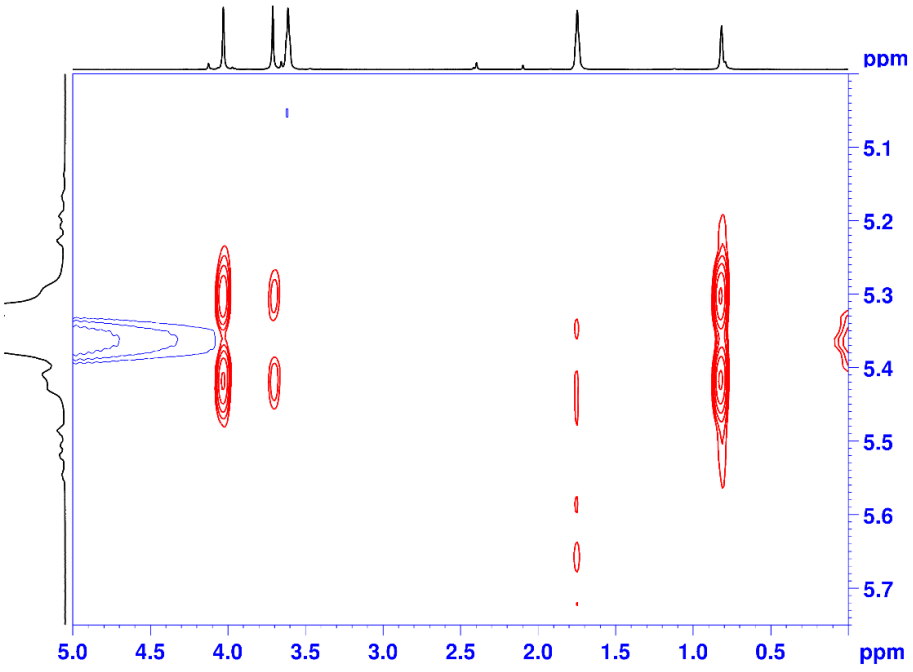

Figure 2.23, continued.

(l) Inverse-gated $^{31}P\{^{1}H\}$ NMR of **10** (35 equiv. of ethylene) (CD_2Cl_2, 202 MHz, -78 ºC) (* denotes CH_3CN adduct resonances)

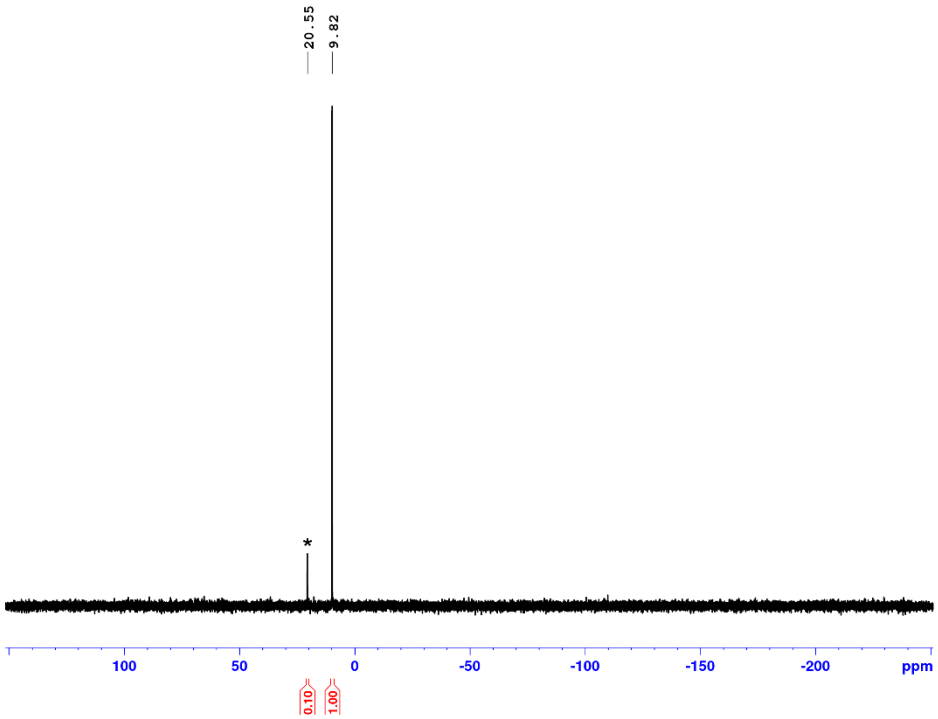

Chain Growth of 10 at -20 ºC. A solution of **10** in CD_2Cl_2 containing excess ethylene (16, 26, or 35 equiv) was generated in a J. Young NMR tube as described above. The tube was placed in the NMR probe that was prechilled to -25 ºC and equilibrated for 10 min. The probe was then warmed to -20 ˚C and the tube was monitored by ^{1}H NMR for ca. 1 h. The resonances for **10** disappeared and resonances assigned to **11** higher alkyl species grew in. Key ^{1}H NMR data for **11**: δ 4.02 (s, –OC*H*$_3$), 3.56 (s, –OC*H*$_3$), 2.40 (br s), 2.23 (br s), 1.99 (br s), 1.22 (s, –C*H*$_2$–), 1.16 (br m), 0.97 (br m), 0.83 (q, J_{HH} = 7 Hz), 0.78 (t, J_{HH} = 8 Hz, –C*H*$_3$), 0.65 (t, J_{HH} =7 Hz, –C*H*$_3$), 0.59 (t, J_{HH} = 8 Hz, –C*H*$_3$).

Figure 2.24. Representative stacked ^{1}H NMR spectra of the chain growth of **11** over 1 h in the presence of 35 equiv. of ethylene (CD_2Cl_2, 500 MHz, -20 ºC)

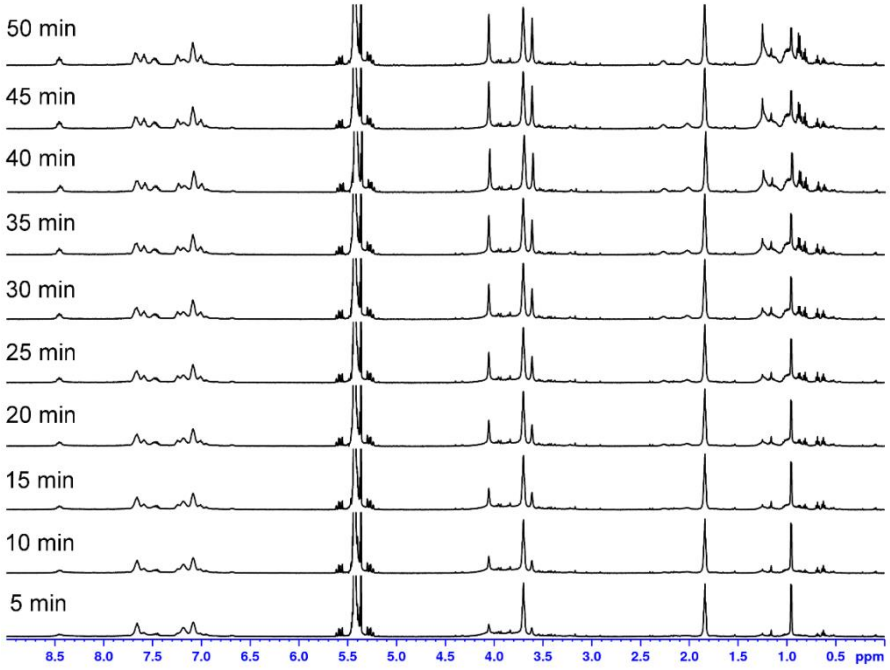

Figure 2.25. Plot of X_n versus time for the reaction of *in situ*-generated **10** in the presence of ethylene at -20 ºC. $[Pd]_{total}$ = 9.1 mM, $[ethylene]_{initial}$ = 0.24 M (26 equiv).

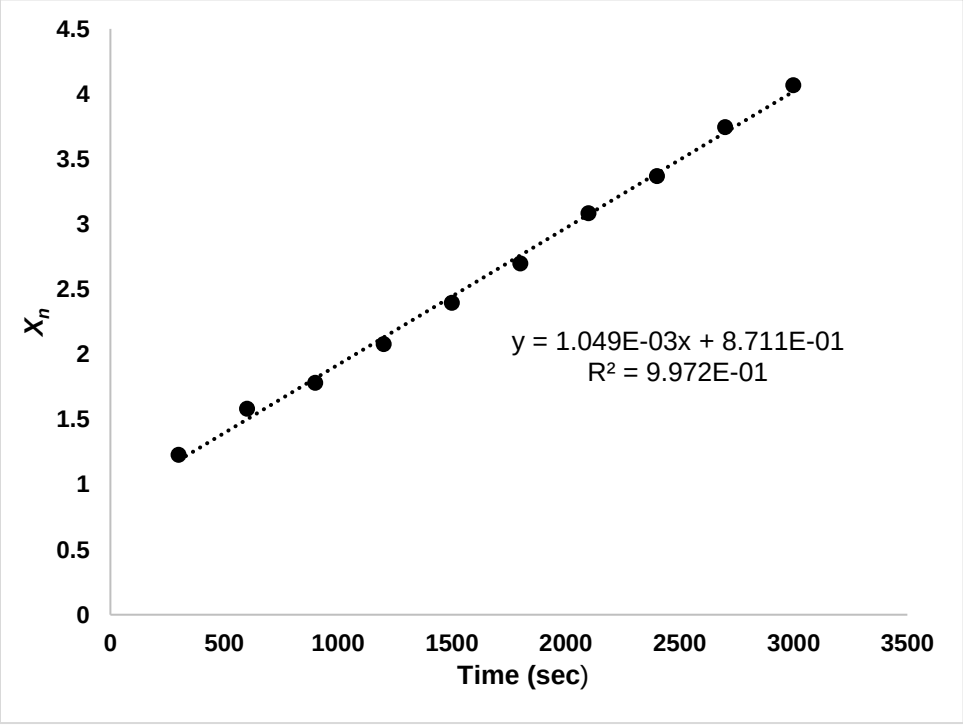

Figure 2.26. Plot of X_n versus time for the reaction of *in situ*-generated **10** in the presence of of ethylene at -20 ºC. $[Pd]_{total}$ = 8.1 mM, $[ethylene]_{initial}$ = 0.28 M (35 equiv)

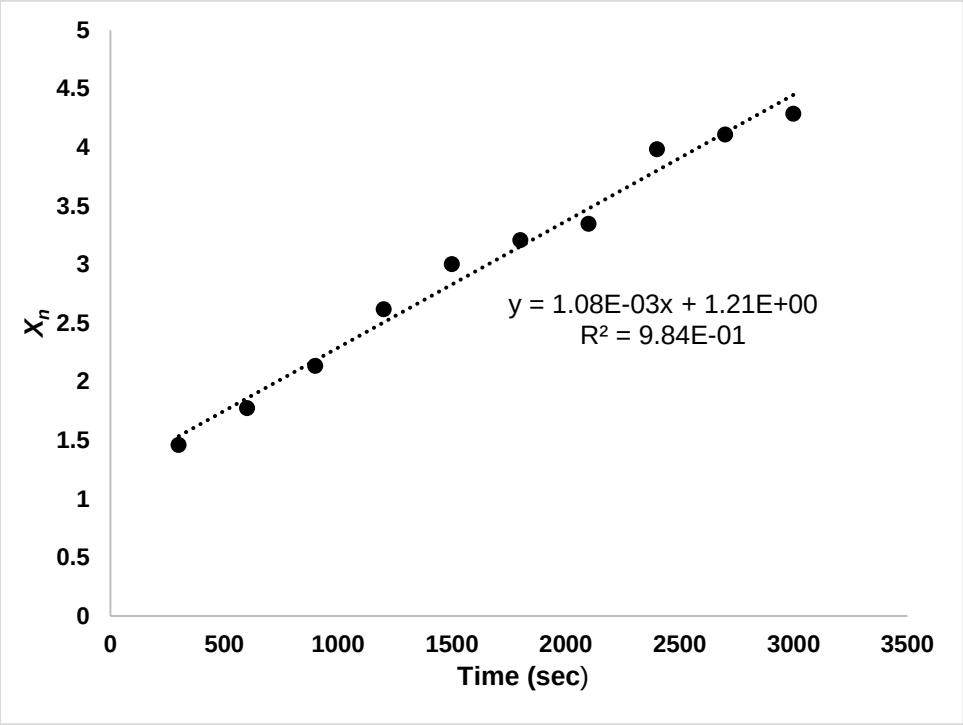

Low pressure ethylene oligomerization and polymerization reactions. Ethylene oligomerization/polymerization reactions at 2 and 6 atm were performed in a 200 mL Fischer-Porter bottle equipped with a 2-inch long Teflon-coated magnetic stir bar and a stainless-steel pressure head fitted with inlet and outlet needle valves, a septum-capped ball valve for injections, a safety check valve, and a pressure gauge. In a N_2-filled glovebox, the Fischer-Porter bottle was charged with toluene (49 mL). The apparatus was removed from the glovebox, connected to a stainless-steel double manifold vacuum/ethylene line, placed in a room temperature water bath or 50 ºC oil bath, and stirred at 370 rpm. The N_2 atmosphere was replaced with ethylene by three evacuation-refill cycles. The solution was equilibrated at either 2 or 6 atm of ethylene pressure for 15 min. For the 2 atm experiments, a freshly-prepared stock solution of catalyst in PhF (1 mL) was

added via gas-tight syringe. For the 6 bar experiments, the pressure was decreased to 1.4 atm, a stock solution of catalyst in PhF (1 mL) was added immediately via gas-tight syringe, and the pressure was immediately increased to 6 atm. The ethylene pressure was kept constant by feeding ethylene on demand.

For catalysts **7** and **8**, ethylene consumption was measured using a Brooks Instruments 5860i Mass Flow Sensor. The total ethylene consumption was determined by numerical integration of the mass flow curve using the LabView software package. Control experiments showed that equilibration of ethylene between the gas and solution phases at 6 atm ethylene pressure requires ca. 15 min under the reaction conditions (23 ºC, 370 rpm stirring), and therefore the activity for the 6 atm experiments was determined using the mass flow curve excluding the first 15 min. After 2 h, the ethylene line was closed, the Fischer-Porter bottle was vented, *o*-xylene (100 μL) was added as an internal standard, and the solution was analyzed by GC-MS using an Aglient 6890/5973N GC-MS instrument. The masses of hexene, octene, and decene were determined by GC-MS using predetermined response factors. The mass of butene was calculated by subtracting the masses of the other oligomers from the total mass of ethylene consumed.

Figure 2.27. GC-MS of Oligomers Formed by **7** (Table 1, entry 1) (Impurities from the toluene solvent are labelled by *)

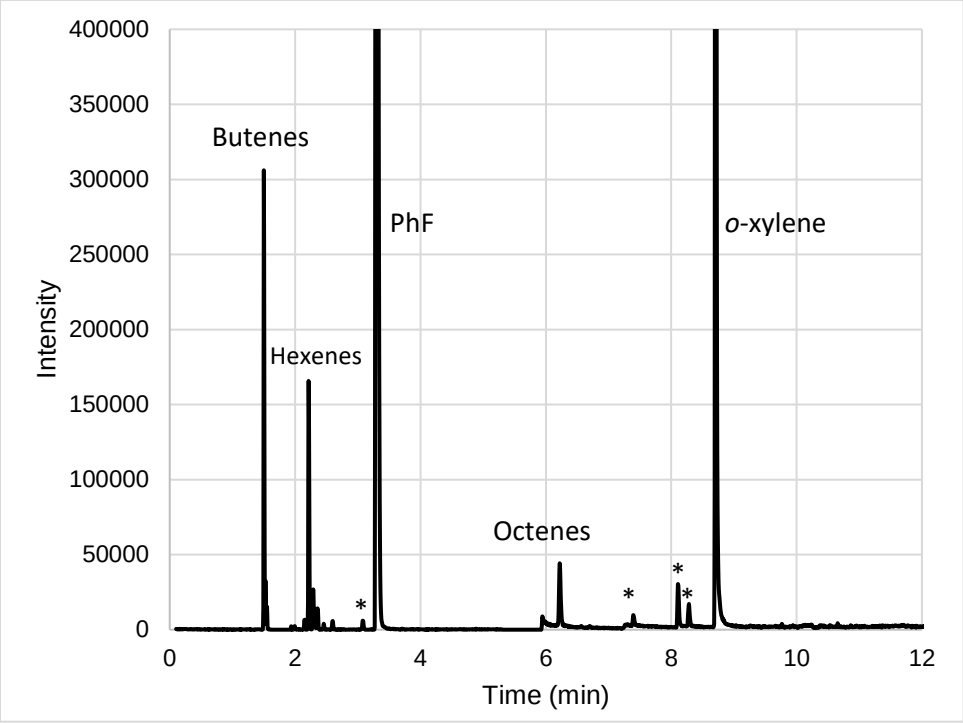

Figure 2.28. GC-MS of Oligomers Formed by **8** (Table 1, entry 4) (Impurities from the toluene solvent are labelled by *)

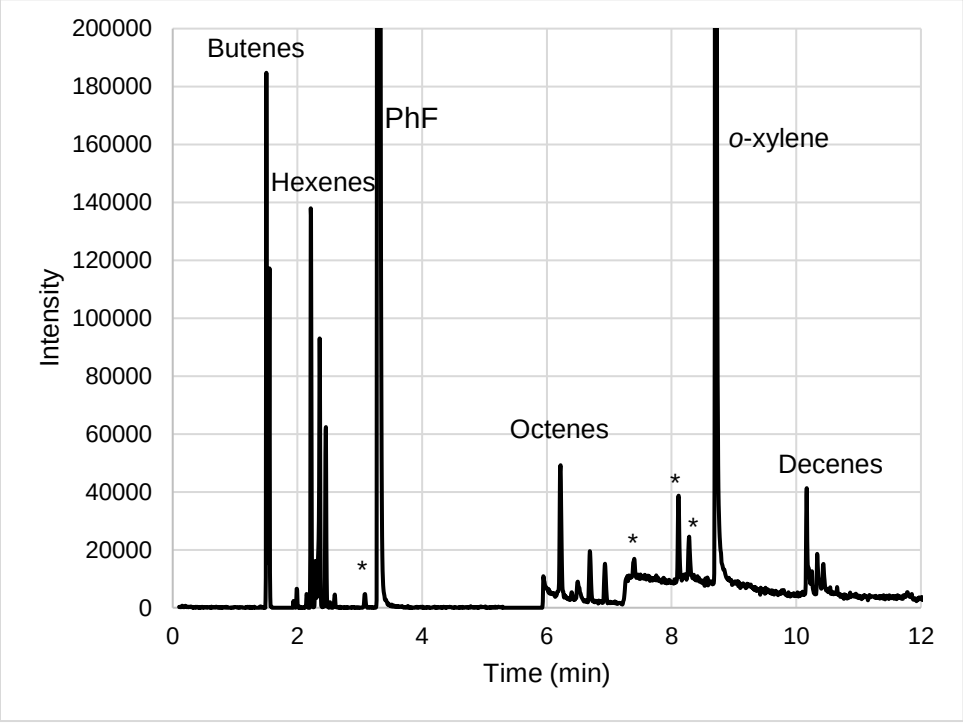

Figure 2.29. Schulz-Flory Plot of Oligomers Formed by **7** (Table 1, Entry 3).

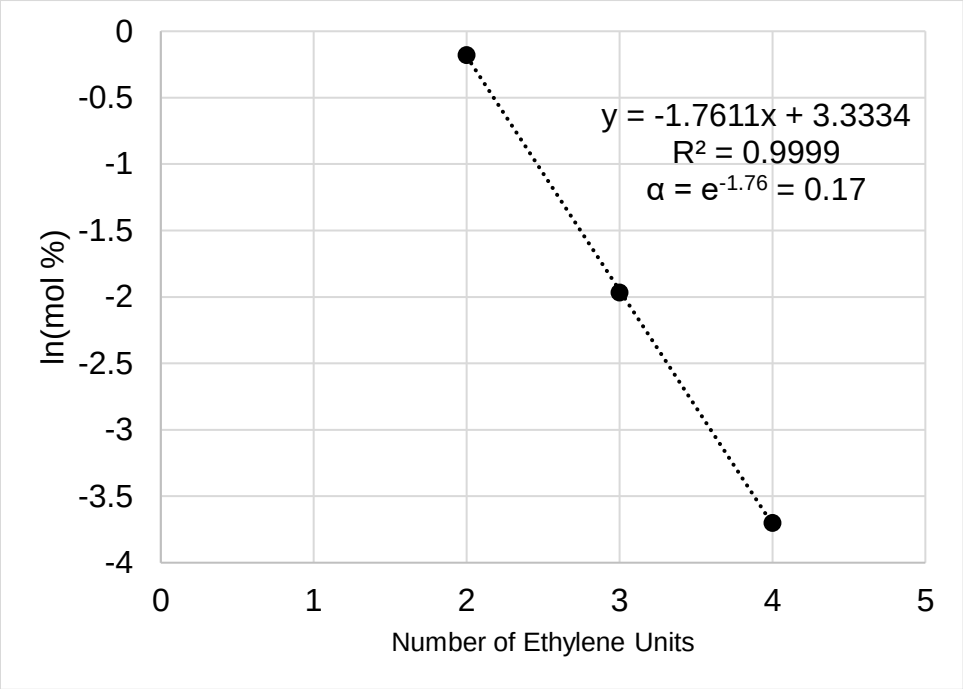

Figure 2.30. Schulz-Flory Plot of Oligomers Formed by **8** (Table 1, Entry 6).

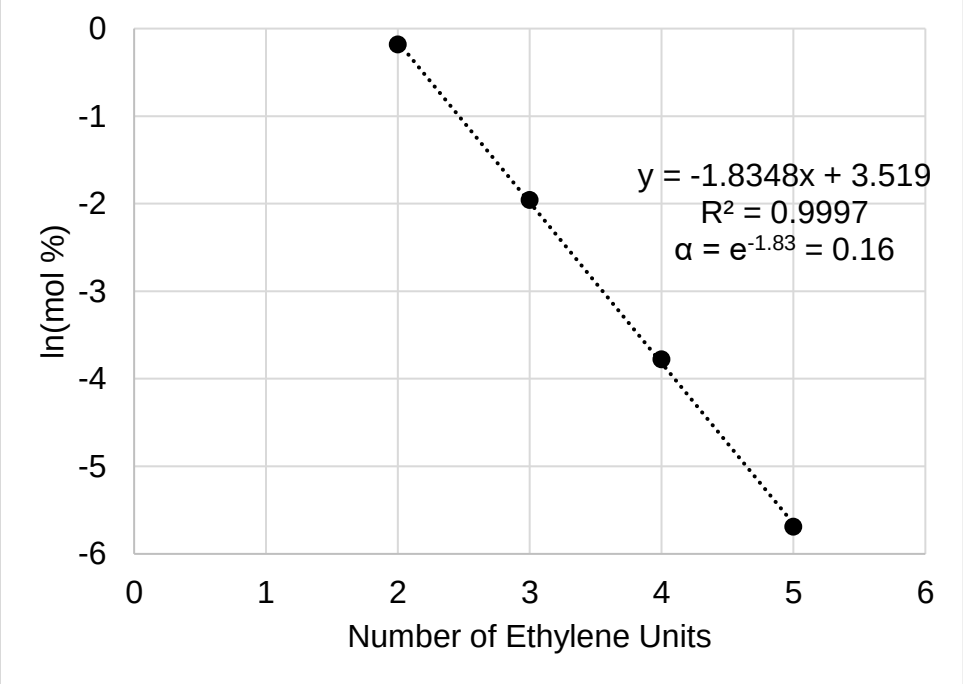

For catalyst **9**, after the ethylene line was closed and the Fisher-Porter bottle was vented, methanol (50 mL) was added to precipitate the polymer. The polymer was collected by filtration, washed with methanol (50 mL), and dried for 2 d at 70 ºC in a vacuum oven.

High pressure ethylene polymerization reactions. Ethylene polymerizations at 54 atm were performed using a stainless-steel Parr 300 mL autoclave, which was equipped with a magnetically-driven 1.5-inch diameter four-blade propeller stirrer, thermocouple, water cooling loop, and a Parr 4842 controller. In a N_2 glovebox, a 200 mL glass autoclave liner was charged with toluene (49 mL) and a stock solution of the catalyst in PhF (1 mL) and placed in the autoclave. The autoclave was sealed, removed from the glovebox, and attached to the ethylene line. The mixture was stirred (270 rpm) at 23ºC for 15 min and then pressurized to 54 atm of ethylene. The ethylene pressure was kept constant by feeding ethylene on demand. After 2 h the ethylene line was closed and the autoclave was vented. Methanol (50 mL) was added to precipitate the polymer, which was characterized as described above.

DSC measurements were performed on a TA Instruments 2920 differential scanning calorimeter. Samples (5 mg) were annealed by heating to 170 ºC at 15 C/min, cooled to 0 ºC at 10 °C/min, and analyzed by heating to 170 °C at 15 °C/min. ^{1}H and $^{13}C\{^{1}H\}$ NMR spectra of PE samples were obtained at 100 ºC in dry degassed $CDCl_2CDCl_2$ solvent using a Bruker Advance 500 NMR instrument. Gel permeation chromatography (GPC) was performed on a Polymer Laboratories PL−GPC 200 instrument at 150 °C with 1,2,4-trichlorobenzene (stabilized with 125 ppm BHT) as the mobile phase. Three PLgel 10 μm Mixed-B LS columns were used. The molecular weights were calibrated using narrow polystyrene standards with a 10-point calibration of M_n from 570 Da to 5670 kDa, and are corrected for linear polyethylene by universal calibration

by using the following Mark−Houwink parameters: polystyrene, K = 1.75 × 10−2 $cm^3\ g^{-1}$, α = 0.67; polyethylene, K = 5.90 × 10^{-2} $cm^3\ g^{-1}$, α = 0.69.[64]

Figure 2.31. NMR Spectra of the Polyethylene Formed by **9**.

(a) $^{13}C\{^1H\}$ NMR of Aliphatic Region of Polyethylene Formed by **9** (Table 2, entry 1) ($CDCl_2CDCl_2$, 126 MHz, 100 ºC)

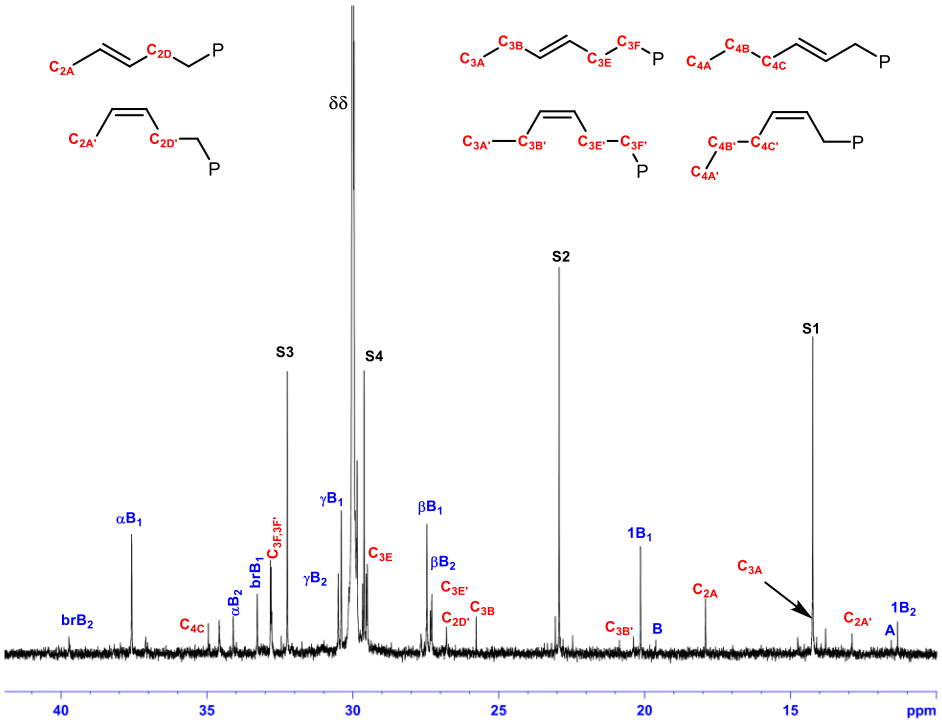

Figure 2.31, continued.

(b) HMBC of Polyethylene Formed by **9** (Table 2, entry 1) ($CDCl_2CDCl_2$, 500 MHz, 100 ºC)

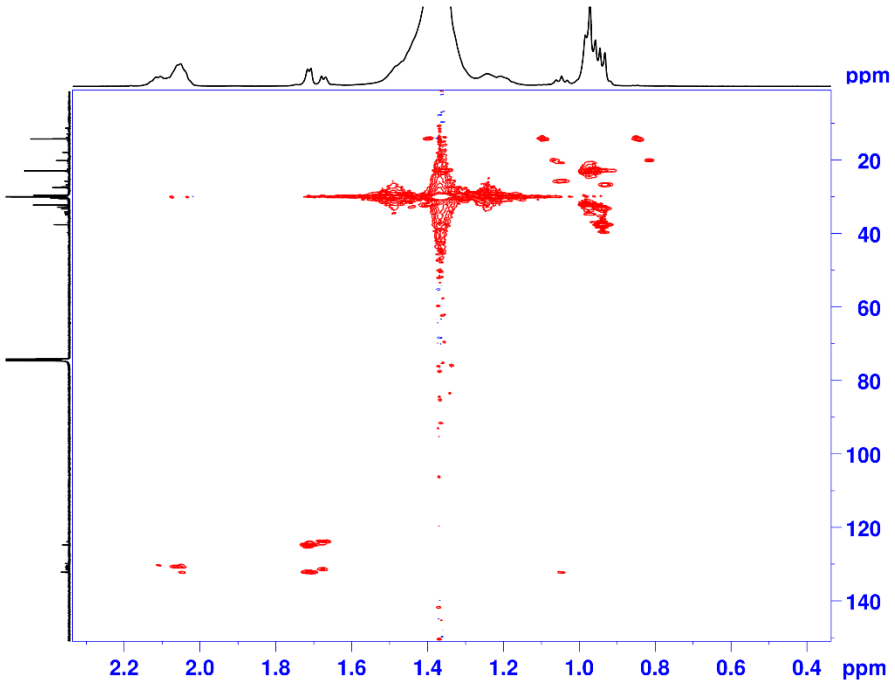

(c) Expansion of HMBC ((1.15 – 0.85 ppm), (30 – 12 ppm)) of Polyethylene Formed by **9** (Table 2, entry 1) ($CDCl_2CDCl_2$, 500 MHz, 100 ºC)

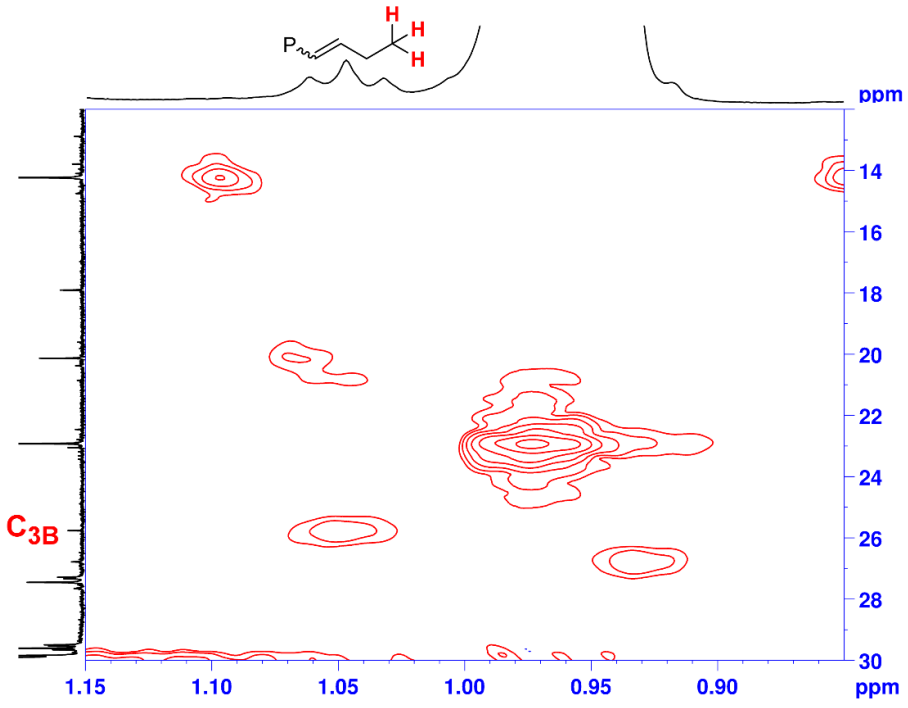

Figure 2.31, continued.

(d) Expansion of HMBC ((1.15 – 0.85 ppm), (135 – 130 ppm)) of Polyethylene Formed by **9** (Table 2, entry 1) ($CDCl_2CDCl_2$, 500 MHz, 100 ºC)

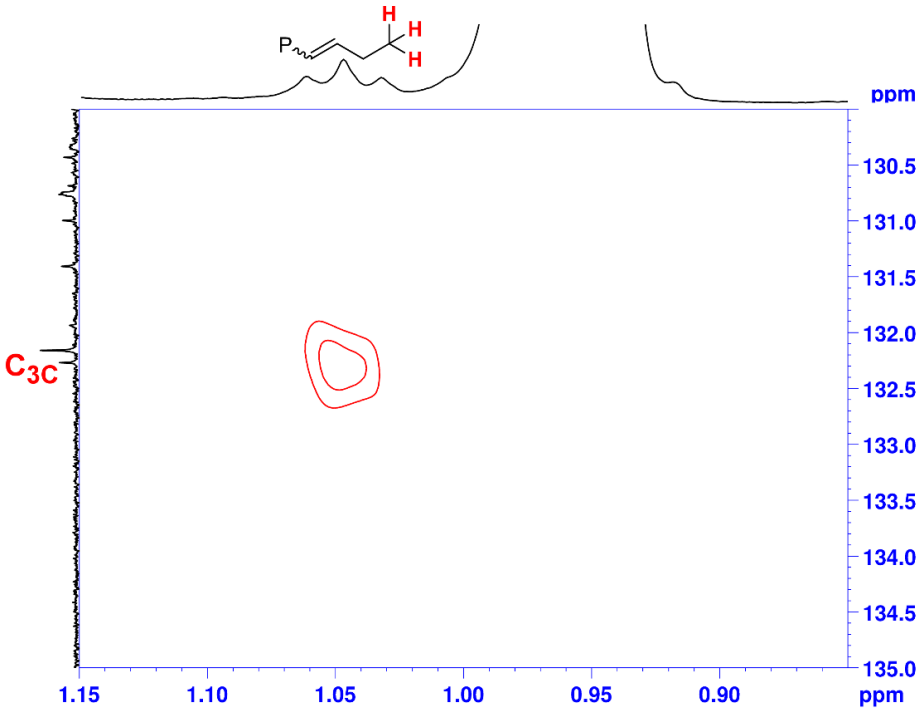

(e) HSQC of the Polyethylene Formed by **9** (Table 2, entry 1) ($CDCl_2CDCl_2$, 500 MHz, 100 ºC)

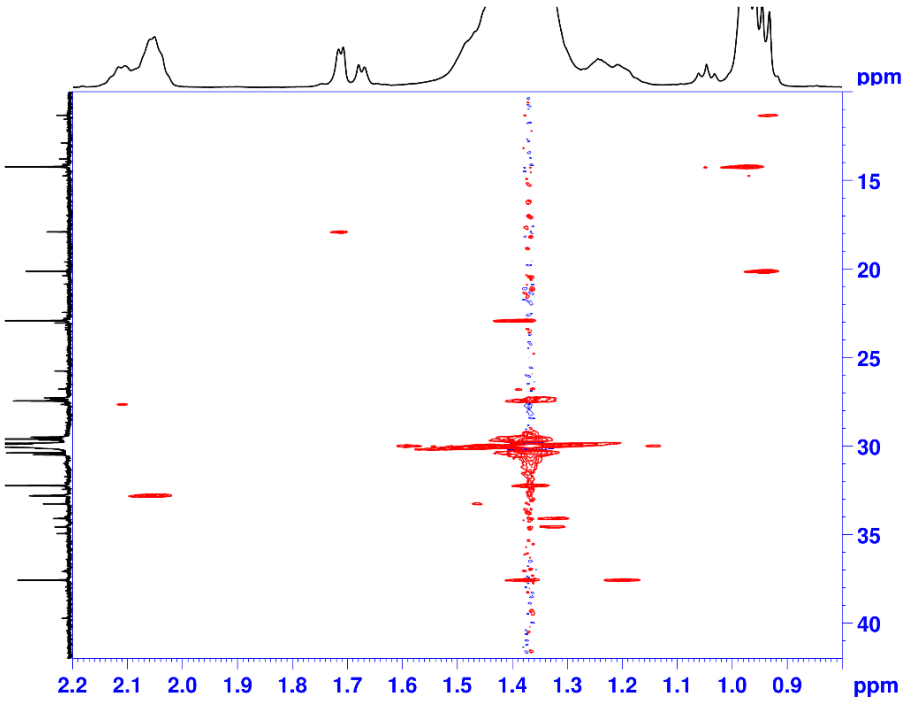

Figure 2.31, continued.

(f) Expansion of HSQC ((1.50 – 0.70 ppm), (40 – 35 ppm)) of Polyethylene Formed by **9** (Table 2, entry 1) ($CDCl_2CDCl_2$, 500 MHz, 100 ºC)

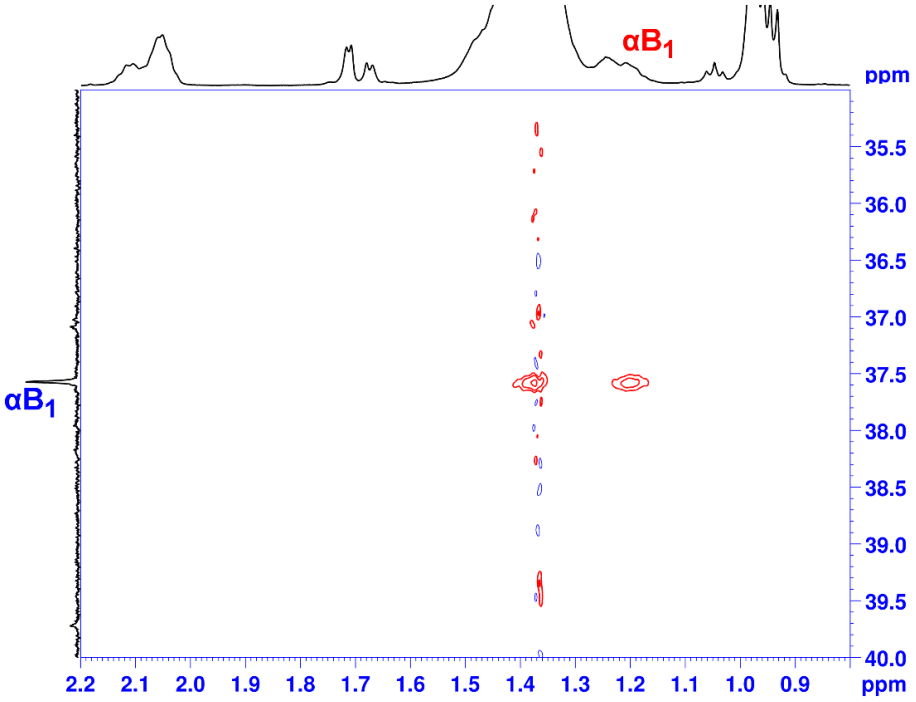

X-ray Crystallography. Data for **7-CH_3CN**, **8**, **9** were collected at 100 K on a Bruker APEX2 platform-CCD X-ray diffractometer system (fine focus Mo-radiation, λ = 0.71073 Å, 50KV/30mA power). Data for $[Li(THF)_3]$[**5**] were collected at 100 K on a Bruker D8 VENTURE with PHOTON 100 CMOS detector system equipped with a Mo-target micro-focus X-ray tube (λ = 0.71073 Å). Direct methods were used to locate many atoms from the E-map. Repeated difference Fourier maps enabled location of all expected non-hydrogen atoms. Following anisotropic refinement of all non-H atoms, ideal H atom positions were calculated. Final refinement was anisotropic for all non-H atoms and isotropic-riding for H atoms.

Specific Refinement Details for 7-CH_3CN. There is one molecule of $C_{10}H_{20}B_9Cl_9NPPd$ and one partially occupied C_6H_5F solvent molecule (89% occupied) present in the asymmetric unit

of the unit cell. One of the two isopropyl-groups of $C_{10}H_{20}B_9Cl_9NPPd$ was modeled with disorder (disordered site occupancy factor ratio was 81%/19%).

Specific Refinement Details for 8. There was one whole molecule disorder of $C_{18}H_{21}B_9Cl_9OPPd$ present in the asymmetric unit of the unit cell. (disordered site occupancy ratio was 90%/10%).

Specific Refinement Details for 9. There was one molecule of $C_{20}H_{25}B_8Cl_9O_3PPd$ (where the THF was modeled with 50%/50% disorder), one disordered solvent molecule of CH_2Cl_2 (disordered site occupancy ratio was 57%/43%), partially occupied disordered solvents of C_5H_{12}/CH_2Cl_2 (disordered site occupancy ratio was 50%/4%) present in the asymmetric unit of the unit cell. The partially occupied disordered solvents of C_5H_{12}/CH_2Cl_2 molecules were located at the 2-fold rotation axis parallel to the b-axis.

Table 2.3 X-ray crystallographic parameters

Identification code	[Li(THF)$_3$][**5**]	**7**–**CH$_3$CN**•(PhF)$_{0.89}$	**8**	**9**•(CH$_2$Cl$_2$)$_{1.037}$(C$_5$H$_{12}$)$_{0.5}$
Empirical formula	$C_{47.07}H_{66.15}B_{18}Cl_{22.15}O_6P_2Pd_2$	$C_{15.36}H_{24.47}B_9Cl_9F_{0.89}NPPd$	$C_{18}H_{21}B_9Cl_9OPPd$	$C_{23.54}H_{33.07}B_9Cl_{11.07}O_3PPd$
Formula weight	1982.62	793.81	807.06	991.19
Temperature	100(2) K	100(2) K	100(2) K	100(2) K
Wavelength (Å)	0.71073	0.71073	0.71073	0.71073
Crystal system	Triclinic	Monoclinic	Monoclinic	Monoclinic
Space group	P-1	P21/n	P21/c	C2/c
Unit cell dimensions	a = 11.3936(9) Å, α = 112.058(2)°	a = 9.4242(3) Å α = 90°	a = 11.3882(4) Å, α = 90°	a = 35.4349(15), α = 90
	b = 18.2924(15) Å, β = 90.830(2)°	b = 19.9211(6) Å, β = 100.0240(5)°	b = 15.4099(5) Å, β = 104.5787(5)°	b = 10.7750(5), β = 98.2521(6)
	c = 18.3437(15) Å, γ = 106.104(2)°	c = 17.3641(5) Å, γ = 90°	c = 18.1835(6) Å, γ = 90°	c = 21.1647(9), γ = 90
Volume Å^3	3373.9(5)	3210.18(17)	3088.30(18) Å^3	7997.3
Z	2	4	4	8
Density (g/cm3)	1.723	1.642	1.736	1.647
Absorption coefficient (mm^{-1})	1.376	1.394	1.449	1.273
F(000)	1740	1563	1584	3940.4
Crystal size (mm^3)	0.327 × 0.311 × 0.271	0.475 x 0.207 x 0.143	0.437 x 0.272 x 0.103	0.545 x 0.485 x 0.211
Theta range for data collection	4.186 to 57.522	2.045 to 30.508°.	1.757 to 30.505°.	
Index ranges	-15 ≤ h ≤ 15, -24 ≤ k ≤ 24, -23 ≤ l ≤ 24	-13<=h<=13, -28<=k<=28, -24<=l<=24	-16<=h<=16, -22<=k<=22, -25<=l<=25	
Reflections collected	135782	76394	72659	93649
Independent reflections	17269 [R_{int} = 0.0358, R_{sigma} = 0.0244]	9810 [R_{int} = 0.0232]	9403 [R_{int} = 0.0282]	11349 [R_{int} = 0.0195]
Absorption correction	SADABS based on redundant diffractions	Semi-empirical from equivalents	Semi-empirical from equivalents	SADABS based on redundant diffractions
Refinement method	Full-matrix least-squares on F2	Full-matrix least-squares on F2	Full-matrix least-squares on F2	Full-matrix least-squares on F2
Data / restraints / parameters	17269/0/768	9810/24/358	9403/570/670	
Goodness-of-fit on F2	1.04	1.225	1.192	1.073
Final R indices [I>2sigma(I)]	R_1 = 0.0306, wR_2 = 0.0745	R_1 = 0.0335, wR_2 = 0.0859	R_1 = 0.0286, wR_2 = 0.0597	R_1 = 0.0212, wR_2 = 0.0553
R indices (all data)	R_1 = 0.0399, wR_2 =0.0783	R_1 = 0.0358, wR_2 = 0.0869	R_1 = 0.0318, wR_2 = 0.0607	R_1= 0.0212, wR_2 = 0.0566
Largest diff. peak and hole (eÅ^3)	0.66/-0.65	1.206/-0.725	0.611/-0.781	0.590/-0.444

2.5 References and Notes

(1) Nakamura, A.; Anselment, T. M. J.; Claverie, J.; Goodall, B.; Jordan, R. F.; Mecking, S.; Rieger, B.; Sen, A.; van Leeuwen, P. W. N. M.; Nozaki, K. *Acc. Chem. Res.* **2013**, *46*, 1438–1449.

(2) Ito, S.; Nozaki, K. *Chem. Rec.* **2010**, *10*, 315–325.

(3) Nakamura, A.; Ito, S.; Nozaki, K. *Chem. Rev.* **2009**, *109*, 5215–5244.

(4) Sui, X.; Dai, S.; Chen, C. *ACS Catal.* **2015**, *5*, 5932–5937.

(5) Zhang, Y.; Cao, Y.; Leng, X.; Chen, C.; Huang, Z. *Organometallics* **2014**, *33*, 3738–3745.

(6) Mitsushige, Y.; Carrow, B. P.; Ito, S.; Nozaki, K. *Chem. Sci.* **2016**, *7*, 737–744.

(7) Noda, S.; Nakamura, A.; Kochi, T.; Chung, L. W.; Morokuma, K.; Nozaki, K. *J. Am. Chem. Soc.* **2009**, *131*, 14088–14100.

(8) Contrella, N. D.; Sampson, J. R.; Jordan, R. F. *Organometallics* **2014**, *33*, 3546–3555.

(9) Kim, Y.; Jordan, R. F. *Organometallics* **2011**, *30*, 4250–4256.

(10) Johnson, A. M.; Contrella, N. D.; Sampson, J. R.; Zheng, M.; Jordan, R. F. *Organometallics* **2017**, *36*, 4990–5002.

(11) Gott, A. L.; Piers, W. E.; Dutton, J. L.; McDonald, R.; Parvez, M. *Organometallics* **2011**, *30*, 4236–4249.

(12) Wucher, P.; Goldbach, V.; Mecking, S. *Organometallics* **2013**, *32*, 4516–4522.

(13) Spokoyny, A. M.; Lewis, C. D.; Teverovskiy, G.; Buchwald, S. L. *Organometallics* **2012**, *31*, 8478–8481.

(14) Estrada, J.; Lugo, C. A.; McArthur, S. G.; Lavallo, V. *Chem. Commun.* **2016**, *52*, 1824–1826.

(15) Fisher, S. P.; El-Hellani, A.; Tham, F. S.; Lavallo, V. *Dalton Trans.* **2016**, *45*, 9762–9765.

(16) Riley, L. E.; Krämer, T.; McMullin, C. L.; Ellis, D.; Rosair, G. M.; Sivaev, I. B.; Welch, A. J. *Dalton Trans.* **2017**, *46*, 5218–5228.

(17) King, A. S.; Ferguson, G.; Britten, J. F.; Valliant, J. F. *Inorg. Chem.* **2004**, *43*, 3507–3513.

(18) Soloway, A. H.; Tjarks, W.; Barnum, B. A.; Rong, F.-G.; Barth, R. F.; Codogni, I. M.; Wilson, J. G. *Chem. Rev.* **1998**, *98*, 1515–1562.

(19) Lavallo, V.; Wright, J. H.; Tham, F. S.; Quinlivan, S. *Angew. Chem. Int. Ed. Engl.* **2013**, *52*, 3172–3176.

(20) Spokoyny, A. M. *Pure Appl. Chem.* **2013**, *85*.

(21) Olid, D.; Núñez, R.; Viñas, C.; Teixidor, F. *Chem. Soc. Rev.* **2013**, *42*, 3318–3336.

(22) Douvris, C.; Michl, J. *Chem. Rev.* **2013**, *113*, PR179–233.

(23) Popescu, A. R.; Teixidor, F.; Viñas, C. *Coord Chem Rev* **2014**, *269*, 54–84.

(24) Scholz, M.; Hey-Hawkins, E. *Chem. Rev.* **2011**, *111*, 7035–7062.

(25) Grimes, R. N. *Dalton Trans.* **2015**, *44*, 5939–5956.

(26) Xie, Z. *Acc. Chem. Res.* **2003**, *36*, 1–9.

(27) Yao, Z.-J.; Jin, G.-X. *Coord Chem Rev* **2013**, *257*, 2522–2535.

(28) (a) Hosmane, N. *Boron science: new technologies and applications*; Hosmane, N., Ed.; 1st ed.; CRC Press, 2011. (b) Hosmane, N. S. *Handbook of Boron Chemistry in Organometallics, Catalysis, Materials and Medicine*; Eagling, R., Ed.; 1st ed.; Imperial College Press/World Scientific Publishing (UK) Ltd., 2018.

(29) Grimes, R. N. *Carboranes*; 3rd ed.; Elsevier, 2016.

(30) (a) Dodge, T.; Curtis, M. A.; Russell, J. M.; Sabat, M.; Finn, M. G.; Grimes, R. N. *J. Am. Chem. Soc.* **2000**, *122*, 10573–10580. (b) Boring, E.; Sabat, M.; Finn, M. G.; Grimes, R. N. *Organometallics* **1998**, *17*, 3865–3874. (c) Yinghuai, Z.; Hosmane, N. S. *J. Organomet. Chem.* **2013**, *747*, 25–29. (d) Yinghuai, Z.; Nong, L. C.; Zhao, L. C.; Widjaja, E.; Hwei, C. S.; Cun, W.; Tan, J.; Meurs, M. V.; Hosmane, N. S.; Maguire, J. A. S *Organometallics* **2009**, *28*, 60–64. (e) Yinghuai, Z.; Yulin, Z.; Carpenter, K.; Maguire, J. A.; Hosmane, N. S. *J. Organomet. Chem.* **2005**, *690*, 2802–2808. (f) Paxson, T. E.; Hawthorne, M. F. *J. Am. Chem. Soc.* **1974**, *96*, 4674–4676. (g) Hewes, J. D.; Kreimendahl, C. W.; Marder, T. B.; Hawthorne, M. F. *J. Am. Chem. Soc.* **1984**, *106*, 5757–5759. (h) Long, J. A.; Marder, T. B.; Behnken, P. E.; Hawthorne, M. F. *J. Am. Chem. Soc.* **1984**, *106*, 2979–2989. (i) Zhu, Y.; Carpenter, K.; Ching, C. B.; Bahnmueller, S.; Chan, P. K.; Srid, V. S.; Leong, W. K.; Hawthorne, M. F. *Angew. Chem. Int. Ed. Engl.* **2003**, *42*, 3792–3795. (j) Behnken, P. E.; Busby, D. C.; Delaney, M. S.; King, R. E.; Kreimendahl, C. W.; Marder, T. B.; Wilczynski, J. J.; Hawthorne, M. F. *J. Am. Chem. Soc.* **1984**, *106*, 7444–7450. (k) Crowther, D. J.; Baenziger, N. C.; Jordan, R. F. *J. Am. Chem. Soc.* **1991**, *113*, 1455–1457. (l) Kreuder, C.; Jordan, R. F.; Zhang, H. Early Metal *Organometallics* **1995**, *14*, 2993–3001. (m) Yoshida, M.; Jordan, R. F. *Organometallics* **1997**, *16*, 4508–4510.

(31) Reed, C. A. *Chem. Commun.* **2005**, 1669–1677.

(32) Reed, C. A. *Acc. Chem. Res.* **1998**, *31*, 133–139.

(33) Grimes, R. N. In *Carboranes*; Elsevier, 2016; pp. 929–944.

(34) Estrada, J.; Woen, D. H.; Tham, F. S.; Miyake, G. M.; Lavallo, V. *Inorg. Chem.* **2015**, *54*, 5142–5144.

(35) Piche, L.; Daigle, J. C.; Rehse, G.; Claverie, J. P. *Chem. Eur. J.* **2012**, *18*, 3277–3285.

(36) Britovsek, G. J. P.; Malinowski, R.; McGuinness, D. S.; Nobbs, J. D.; Tomov, A. K.; Wadsley, A. W.; Young, C. T. *ACS Catal.* **2015**, *5*, 6922–6925.

(37) Ittel, S. D.; Johnson, L. K.; Brookhart, M. *Chem. Rev.* **2000**, *100*, 1169–1204.

(38) Seger, M. R.; Maciel, G. E. *Anal. Chem.* **2004**, *76*, 5734–5747.

(39) Wiedemann, T.; Voit, G.; Tchernook, A.; Roesle, P.; Göttker-Schnetmann, I.; Mecking, S. *J. Am. Chem. Soc.* **2014**, *136*, 2078–2085.

(40) Azoulay, J. D.; Bazan, G. C.; Galland, G. B. *Macromolecules* **2010**, *43*, 2794–2800.

(41) Liu, W.; Rinaldi, P. L.; McIntosh, L. H.; Quirk, R. P. *Macromolecules* **2001**, *34*, 4757–4767.

(42) Hansen, E. W.; Blom, R.; Bade, O. M. *Polymer* **1997**, *38*, 4295–4304.

(43) Zhou, X.; Bontemps, S.; Jordan, R. F. *Organometallics* **2008**, *27*, 4821–4824.

(44) Kolbert, A. C.; Didier, J. G.; Xu, L. *Macromolecules* **1996**, *29*, 8591–8598.

(45) Prasad, A.; Mandelkern, L. *Macromolecules* **1989**, *22*, 914–920.

(46) Kanazawa, M.; Ito, S.; Nozaki, K. *Organometallics* **2011**, *30*, 6049–6052.

(47) Anselment, T. M. J.; Wichmann, C.; Anderson, C. E.; Herdtweck, E.; Rieger, B. *Organometallics* **2011**, *30*, 6602–6611.

(48) Skupov, K. M.; Piche, L.; Claverie, J. P. *Macromolecules* **2008**, *41*, 2309–2310.

(49) Reynhardt, E. C. *J. Phys. D, Appl. Phys.* **1986**, *19*, 1925–1938.

(50) Ciesińska, W.; Liszyńska, B.; Zieliński, J. *J Therm Anal Calorim* **2016**, *125*, 1439–1443.

(51) Hato, M. J.; Luyt, A. S. *J. Appl. Polym. Sci.* **2007**, *104*, 2225–2236.

(52) Mpanza, H.; Luyt, A. *S. Afr. J. Chem* **2006**, *59*, 48–54.

(53) Retief, J. J.; le Roux, J. H. *S. Afr. J. Sci.* **1983**, *79*, 234–239.

(54) Möller, M.; Cantow, H.; Drotloff, H.; Emeis, D.; Lee, K.; Wegner, G. *Die Makromolekulare Chemie* **1986**, *5*, 1237–1252.

(55) Luyt, A. S.; Krupa, I. *Thermochim. Acta* **2008**, *467*, 117–120.

(56) Mandelkern, L.; Price, J. M.; Gopalan, M.; Fatou, J. G. *J. Polym. Sci. A-2 Polym. Phys.* **1966**, *4*, 385–400.

(57) Guo, X.; Pethica, B. A.; Huang, J. S.; Prud'homme, R. K. *Macromolecules* **2004**, *37*, 5638–5645.

(58) Benn, R. *Org. Magn. Reson.* **1983**, *21*, 723–726.

(59) The Pd-Me and the polymer chain methyl resonances are included in this calculation because they cannot be resolved from the the other Pd-R' resonances that are growing in. Assuming that the Pd-Me and Pd-R' species have similar insertion rate constants, only the y-intercept

of the plots of X_n versus time are affected as the total number of of total methyl groups, from Pd-Me and the polymer chain methyls, is constant.

(60) Gu, W.; McCulloch, B. J.; Reibenspies, J. H.; Ozerov, O. V. *Chem. Commun.* **2010**, *46*, 2820–2822.

(61) Santos, L. S.; Metzger, J. O. *Rapid Commun. Mass Spectrom.* **2008**, *22*, 898–904.

(62) The batch of **9** used for the low temperature experiments contained 15% of the corresponding CH_3CN complex. .

(63) Lynden-Bell, R. M.; Sheppard, N. *Proceedings of the Royal Society A: Mathematical, Physical and Engineering Sciences* **1962**, *269*, 385–403.

(64) Grinshpun, V.; Rudin, A. *Makromol. Chem., Rapid. Commun.* **1985**, *6*, 219–223.

Chapter Three

Template-free Synthesis of Macrocyclic Bis(pyridine-diimine) and Bis(pyridine-dienamido) Ligands and Complexes

3.1 Introduction

Transition metal complexes supported by redox-active pyridine-diimine (PDI) ligands are useful catalysts for a wide range of reactions.[1–9] Multinuclear transition-metal complexes supported by multinucleating bis- or multi-PDI ligands are of interest because long range metal-metal cooperativity effects may engender new reactivity. Linear multinuclear PDI complexes have been shown to have improved catalytic performance in ethylene homopolymerization.[5,10–13] However, due to the conformational flexibility and geometry of these compounds, it is difficult to explain the origin of the enhanced performance. It would be ideal to incorporate two or more PDI active sites into a rigid macrocyclic ring to enable exploration of potential metal-metal cooperativity effects.

There have been several reports of multinuclear complexes supported by macrocyclic multi-PDI ligands. Dinuclear complexes (**A**)M_2Cl_4 and (**B**)M_2Cl_4 (M = Fe, CO) and trinuclear complex (**C**)Fe_3Cl_6 (Chart 3.1) were synthesized by direct imine condensation of 2,6-diacetylpyridine and the respective dianiline to generate ligands **A-C,** followed by reaction of the ligands with the respective MCl_2 salt in THF.[14–16] (**A**)M_2Cl_4 and (**C**)Fe_3Cl_6 when activated by MMAO-12 and MAO respectively, exhibit increased catalyst lifetimes and activities in ethylene homopolymerization compared to analogous mononuclear PDI catalysts. (**B**)M_2Cl_4 ($R^1 = R^2 = Me$) when activated by MMAO-12 or $AlMe_3$ produces polyethylene that contains primarily ethyl and propyl branches, which is in contrast to the analogous mononuclear PDI catalyst, which produces highly linear polyethylene.

Chart 3.1. Multinuclear Complexes of Macrocyclic PDI Ligands Synthesized by Direct Imine Condensation Reactions.

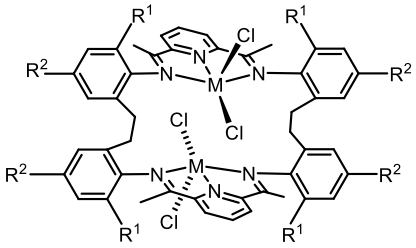

(**A**)M_2Cl_4 (M = Fe, Co) (R^1 = R^2 = H; R^1 = R^2 = Me; R^1 = ^{i}Pr, R^2 = H)

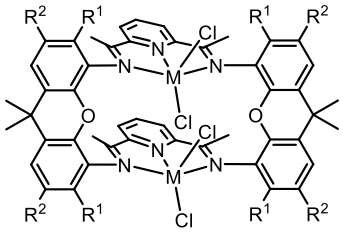

(**B**)M_2Cl_4 (M = Fe, Co) (R^1 = R^2 = Me; R^1 = H, R^2 = ^{t}Bu)

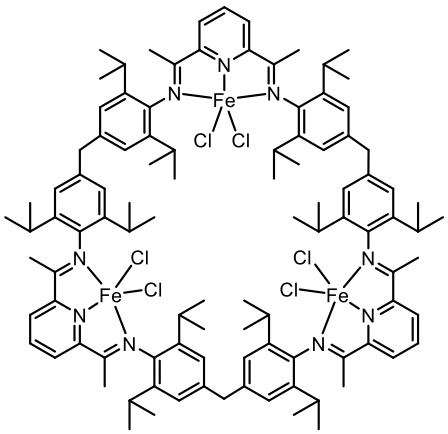

(**C**)Fe_3Cl_6

While ligands **A**–**C** can be synthesized under standard imine condensation conditions, attempts to synthesize other macrocyclic multi-PDI ligands by direct imine condensation typically results in intractable condensation polymers. A general strategy for avoiding this problem is to use metal-based templates to overcome the enthalpic and/or entropic macrocyclization penalties.[17–25] The function of the templates can be explained by examining the conformations of the PDI and pyridine-diketone (PDK) units. These moieties can exist in two different conformers: (s-*cis*)$_2$ or (s-*trans*)$_2$ (Figure 3.1). In the (s-*cis*)$_2$ conformer, the lone pairs of both C=X (X = O or NR) moieties and the pyridine lone pair are directed towards each other, while in the (s-*trans*)$_2$ conformer these lone pairs point away from each other. While the (s-*cis*)$_2$ conformer is observed in (PDI)M complexes, the (s-*trans*)$_2$ conformer is invariably observed in the solid-state structures of free PDI

ligands because in this conformation the lone-pair repulsion that is present in the (s-*cis*)$_2$ conformation is relieved.[14,26–31] These conformational considerations are important in the synthesis of *n*-PDI macrocycles, where *n* PDK molecules condense with *n* diamine molecules. The final intermediate in this reaction is a species that has 1 pyridine-imine-ketone moiety and *n*-1 PDI units terminated with the last unreacted amine group (Figure 3.2a). In the *n* (s-*cis*)$_2$ conformer, where the PDIs and pyridine-imine-ketone moieties are all in the (s-*cis*)$_2$ conformation, the distance between the reactive ketone and amine groups is minimized, promoting macrocyclization. However, in the ground-state *n* (*s-trans*)$_2$ conformer, this distance is maximized, therefore favoring the formation of condensation polymer.

Figure 3.1. Conformations of PDI, PDK, and pyridine-imine-ketone compounds.

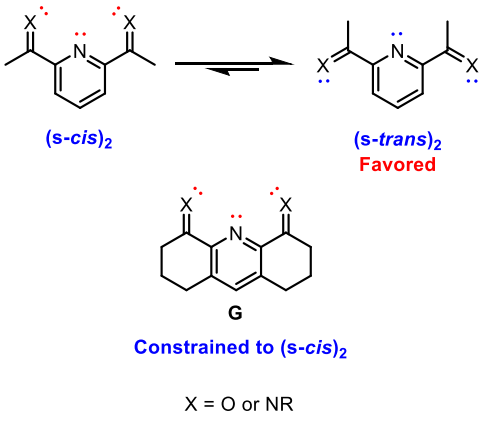

Figure 3.2. a) Conformers of the final intermediate in the formation of macrocyclic *n*-PDI compounds. b) Structure of the final intermediate during the macrocyclization of **A** (R^1 = R^2 = H).

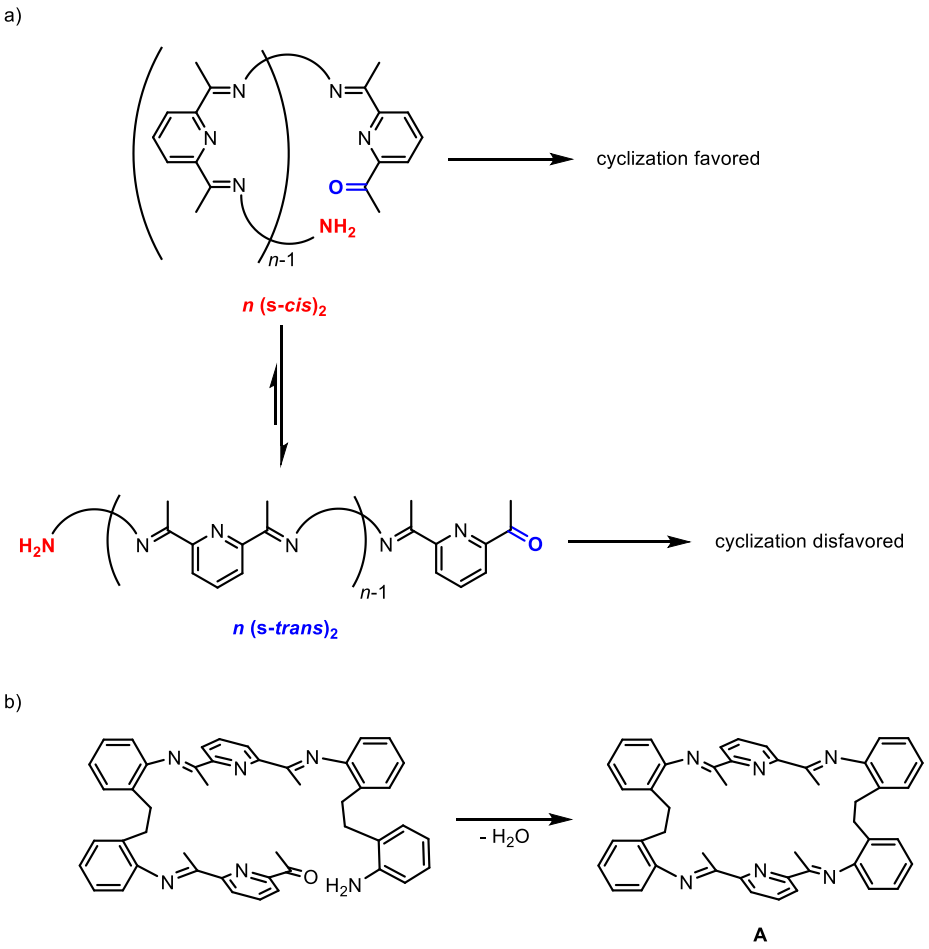

With the use of metal-based templates however, the desired (s-*cis*)$_2$ conformation is trapped by coordination of the C=X moieties binding to the metal ion, preorganizing them for macrocyclization. Several bis-PDI complexes have been synthesized using specially designed binucleating templates comprising two metal ions connected by a bridging anionic unit (Chart 3.2). The bridging unit fixes the two metal centers spatially, lowering the entropic costs of macrocyclization. One of the first bis-PDI complexes of this type, [(**D**)Cu_2Im][CF_3SO_3]$_3$, was reported by Burrows as a urea hydrolyase active site analogue.[32–35] This complex was synthesized

by reacting CuOTf and imidazole to form a putative $[Cu\text{-}Im\text{-}Cu]^{3+}$ complex, which was then added to a solution of 2,6-diacetylpyridine and *m*-xylylenediamine. Groysman has recently shown that an analogous zinc complex $[(\mathbf{D})Zn_2ox][CF_3SO_3]_3$ is formed using dizinc oxalate as the binucleating template.[36] The Zn_2ox template was shown to be more general as it can also be used with 2,6-formylpyridine and *p*-xylylenediamine to produce $[(\mathbf{E})Zn_2ox][CF_3SO_3]_3$. It should be emphasized that the binucleating template is critical for macrocyclization in the synthesis of $[(\mathbf{D})Cu_2Im][CF_3SO_3]_3$ and $[(\mathbf{D})Zn_2ox][CF_3SO_3]_3$. Attempted synthesis of these complexes in the absence of imidazole or oxalate results in intractable condensation polymer, suggesting that the presence of metals alone is insufficient for macrocyclization and that the bridging unit helps to pay the enthalpic penalty of having two cationic metal centers close in space. Nitschke generated $[(\mathbf{F})Pd_2(CH_3CN)_2][BF_4]_4$ using 2,6-diformylpyridine, 3-aminophenyl sulfone, and $[Pd(CH_3CN)_4][BF_4]_2$.[37] The X-ray structure of $[(\mathbf{F})Pd_2(CH_3CN)_2][BF_4]_4$ shows that a tetrafluoroborate molecule is electrostatically interacting with the two Pd centers in the intermetallic cavity. It was suggested that the BF_4^- functions as a template for this macrocyclic complex.[38,39]

Chart 3.2. Bis-PDI complexes Synthesized Using Binucleating Templates.

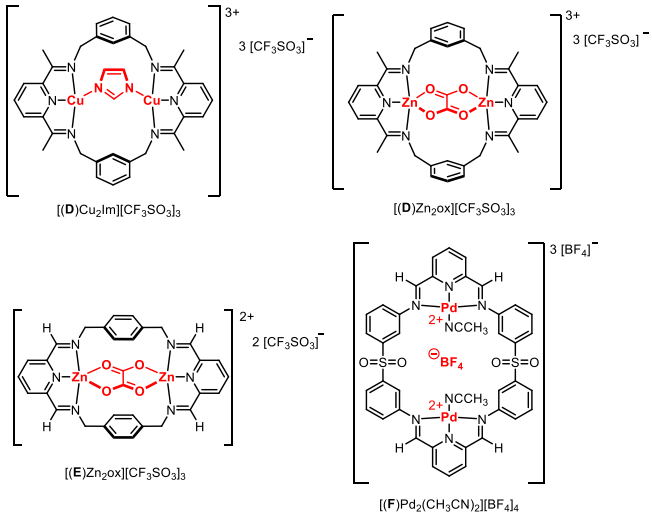

The observed template-free synthesis of **A-C** can be understood using the conformational considerations discussed above. These bis-PDI macrocyclic ligands are formed in the 2 (s-*trans*)$_2$ conformation, as confirmed for **A** by X-ray diffraction. The dianilines used in the synthesis of **A** and **B** force the PDI moieties to be stacked on top of each other. This geometry minimizes the distance between the final ketone and free amine groups in the 2 (s-*trans*)$_2$ conformer of the final PDI-pyridine-ketone-imine intermediate, favoring cyclization (Figure 3.2b). **C** is synthesized under dilute conditions (4 mM total) over the course of 1 week, helping to favor macrocyclization.[4,40] Additionally, the large Ar–CH_2–Ar angle of the dianiline may help to form the tris-PDI macrocycle in this case, however it is unknown if the bis-PDI macrocycle is formed as a side product in this reaction.

There are two major challenges associated with using binucleating templates. The first is that they are difficult to design *a priori*, especially using metals with fluxional coordination geometries that result in difficult-to-predict dynamic processes for the intermediates in the condensation process. The second problem is that once the templated complex is made, the

templates are often difficult to remove without destroying the ligand in the process. For example, Burrows found that attempted demetalation of [(**D**)Cu_2Im][CF_3SO_3]$_3$ with benzene/Na_4EDTA(aq) is inefficient due to the poor solubility of the complex in organic solvents, a slow demetallation rate (even at elevated temperatures), and a moderate hydrolysis rate of free ligand **D**. Additionally, Groysman screened various demetalation procedures and found that the removal of the zinc oxalate unit of [(**E**)Zn_2ox][CF_3SO_3]$_3$ requires the use of strong aqueous acid, hydrolyzing **E** in the process. Finally, while not reported by Nitschke, in our hands attempting to demetalate [(**E**)$Pd_2(CH_3CN)_2$][BF_4]$_4$ with Na_4EDTA results in decomposition.

The objective of this work is to develop a non-templated synthesis of a variant of ligand **D** in order to enable the synthesis of a wide range of dinuclear bis-PDI complexes. This goal was accomplished by use of 9-butyl-octahydroacridinediketone (**1**, Scheme 3.1). [41–43] The annulated octrahydroacridine backbone (**G**, Figure 3.1) structurally constrains the C=X moieties in the desired (s-*cis*)$_2$ conformation, which favors the formation of a macrocyclic bis-PDI ligand (as the enamine tautomer **2**' in Scheme 1) in a condensation reaction with *m*-xylylenediamine without the use of a template.

3.2 Results and Discussion

Compound **1** was prepared using the procedures reported by Bell and Thummel for similar compounds.[41,44–46] The condensation of **1** and *m*-xylylenediamine in butanol in the presence of *p*-toluenesulfonic acid yields bis-(pyridine-dienamine) compound **2'**, a tautomer of target bis-PDI **2** in 88 % yield. This condensation-macrocyclization reaction is done at total concentration of 415 mM, 2.3 times more concentrated than the templated synthesis of [(**D**)Cu_2Im][CF_3SO_3]$_3$ (concentration of 2,6-diacteylpyridine + *m*-xylylenediamine = 180 mM), demonstrating the advantage of preorganizing the PDI moieties in the (s-*trans*)$_2$ conformation. This is a rare example

of of a pyridine-diketone reacting with amines to produce the pyridine-dienamine product, with the only other report by Thummel where condensation of non-butylated **1** with HN^iPr_2 results results in the pyridine-dienamine product.[47] The IR spectrum of **2'** contains a characteristic N–H stretching band at 3400 cm^{-1}. The ^1H NMR spectrum of **2'** contains broad triplet at δ 5.11, indicative of the N–H moiety being coupled to the benzylic hydrogens at δ 4.11, and a sharp vinylic triplet at δ 4.87, consistent with coupling to one of the methylene groups on the octahydroacridine backbone. The $^{13}C\{^1H\}$ NMR spectrum of **2'** contains resonances at δ 126.7 and 98.7, which are characteristic of the vinylic carbons of an enamine. In contrast, the tetraimine tautomer of **2** is expected to exhibit no IR bands above 3000 cm^{-1}, no ^1H NMR resonances in the vinylic region, no ^{13}C NMR resonances between δ 120 and δ 50 and a ^{13}C NMR resonance at ca. δ 170 for the imine carbon.

Scheme 3.1. Synthesis of Proligand **2'**.

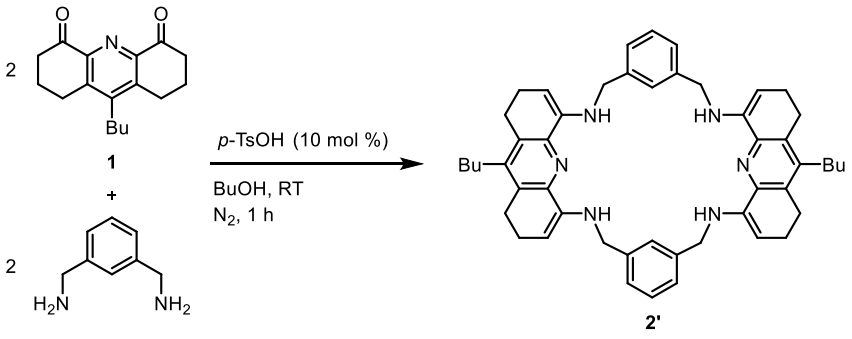

Synthesis of Metal Complexes of 2. The direct template-free synthesis and high-yield isolation of free proligand **2'** without the use of a template provides an opportunity to synthesize a wide array of dinuclear metal complexes. The reaction of **2'** and 2 equiv. of $ZnCl_2$ in butanol at 110 ºC for 16 h, filtration, and heating the crude solid in CH_2Cl_2 for 2d at 35 ºC generates the bis-

PDI dinuclear complex (**2**)Zn_2Cl_4 in 60% yield (Scheme 3.2 a). The use of hot protic solvent is important as metalation is sluggish otherwise; presumably the butanol facilitates the tautomerization of **2'** to the bis-PDI tautomer **2** prior to metalation. X-ray diffraction analysis shows that the 24-membered macrocyclic ring in (**2**)Zn_2Cl_4 adopts a chair conformation. The molecular symmetry is C_i and the Zn–Zn distance is 5.515(1) Å (Figure 3.3 and Figure 3.4). This Zn–Zn distance is significantly shorter than the Cu–Cu distance of 5.9181(9) Å determined for [(**D**)Cu_2Im][CF_3SO_3]$_3$. From a side-on view perpendicular to the Cl–Zn–Cl planes, the structure resembles the "double decker" structure determined for (**A**)Co_2Cl_4 (Chart 3.3a).[14] Both Zn centers have trigonal-bipyramidal coordination geometries and the metrical parameters are consistent with those observed for mononuclear (PDI)$ZnCl_2$ complexes.[48,49] $^{13}C\{^1H\}$ NMR confirms that (**2**)Zn_2Cl_4 exist as the tetraimine tautomer by the absence of the vinylic carbon resonances observed for **2'** and the presence of a characteristic imine carbon resonance at δ 166.3.

Scheme 3.2. Synthesis of Bis-PDI (**2**)M_2Cl_4 (M = Zn, Co, Fe) Complexes.

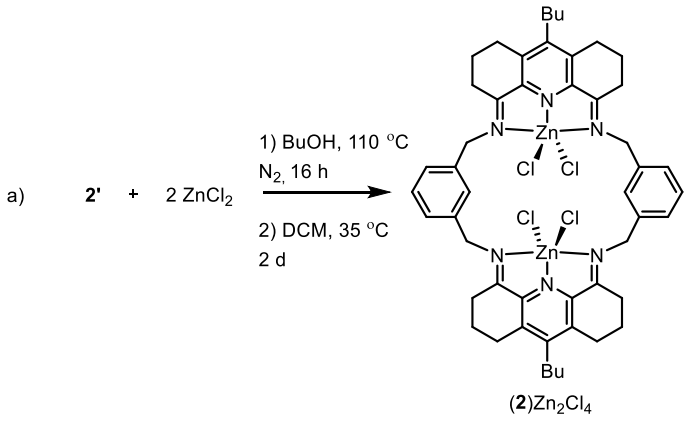

Figure 3.3. Molecular Structure of (**2**)Zn_2Cl_4•$3CH_2Cl_2$. H atoms and CH_2Cl_2 solvent molecules are omitted. Key bond and atom distances (Å): N1–C1 1.284(7), N2–C2 1.308(7), Zn1–N3 2.073(4), Zn1–Cl1 2.244(1), Zn1–Cl2 2.259(1), Zn1–Zn2 5.515(1). Key bond angles (º): N1–Zn1–N2 146.9(2), N1–Zn1–N3 73.5(2), N2–Zn1–N3 74.6(2), N2–Zn1–Cl1 135.9(1), N2–Zn1–Cl2 110.9(1). Color key: C gray, N light blue, Zn light gray, Cl green. Thermal ellipsoids are drawn at 50%.

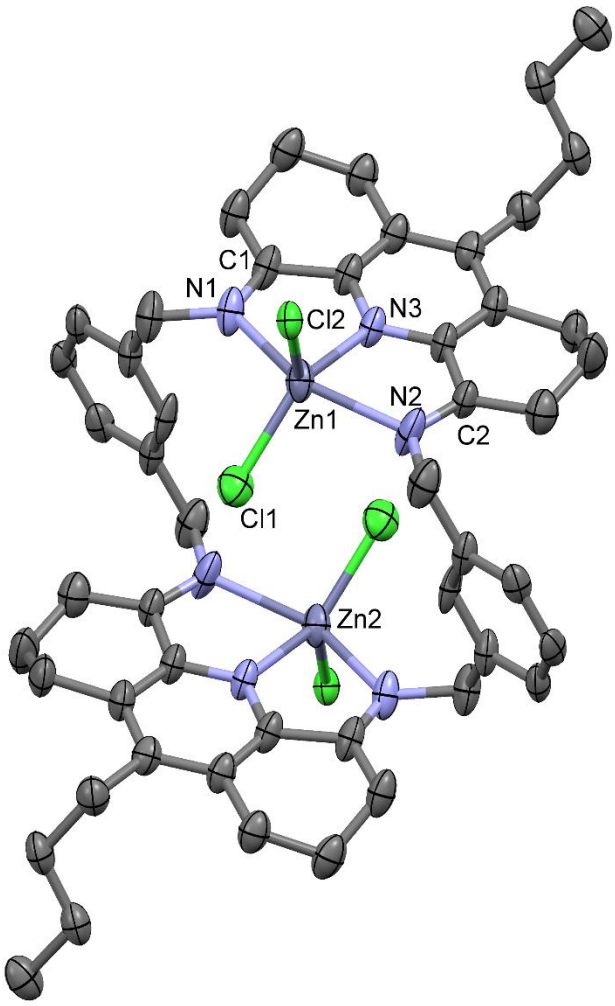

Figure 3.4. View of the molecular structure of (**2**)Zn_2Cl_4 looking down the pyridine planes. Color key: C gray, N light blue, Zn light gray, Cl green.

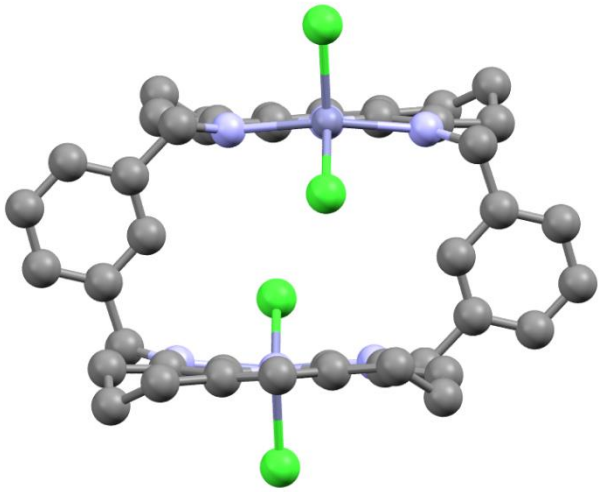

The ^{1}H NMR spectrum of (**2**)Zn_2Cl_4 contains a broad AA' spin pattern at δ 5.45 and 4.35 at 295 K for the benzylic hydrogens, which broadens s the temperature is increased and coalesces to a broad singlet at δ 4.98 at 390 K (Figure 3.5), indicative of fluxional behavior. VT-NMR and lineshape analysis using gNMR 5 of (**2**)Zn_2Cl_4 in $CDCl_2CDCl_2$ from 295 K to 390 K was performed to determine rate constants for the exchange of the benzylic hydrogens (Figure 3.5). The activation parameters determined by an Eyring analysis are $\Delta H^{\neq}$ = 9.5(3) kcal/mol and $\Delta S^{\neq}$ = -20.5(7) eu. The free energy barrier ($\Delta G^{\neq}$) is 15.5(3) kcal/mol at 295 K and 17.3(3) kcal/mol at 380 K.

Figure 3.5. Left: VT NMR behavior of the benzylic resonances of (**2**)Zn_2Cl_4. Right: Lineshape analysis of the benzylic resonances of (**2**)Zn_2Cl_4. (NMR conditions: 500 MHz, $CDCl_2CDCl_2$, 295 K to 390 K) (The singlet at ca. δ 5.7 is one of the ^{13}C satellites from the $CDCl_2CDCl_2$ solvent resonance).

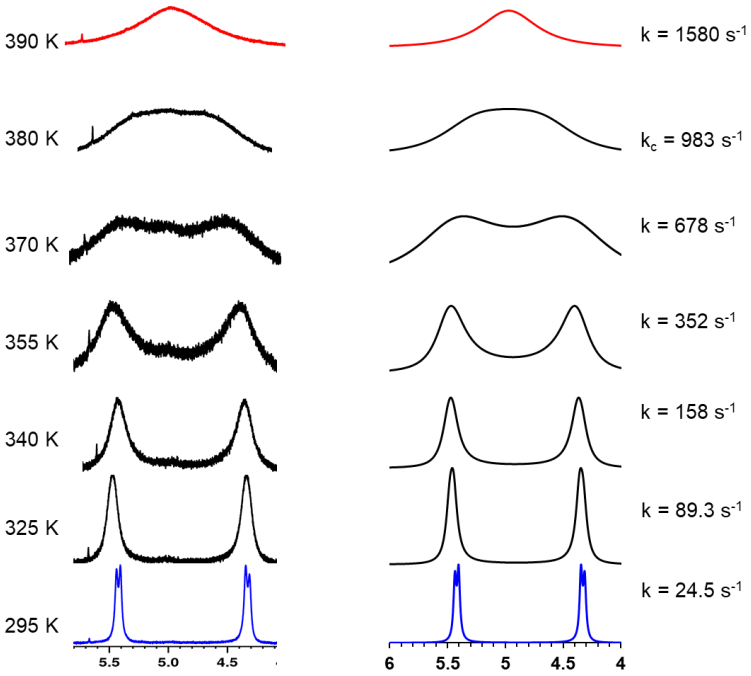

Additionally, the resonances that correspond to the octahydroacridine backbone exhibit temperature-dependent behavior. At 295 K, the methylene hydrogens of the octahydroacridine backbone appear as two broad resonances at δ 2.75 and 1.90 (Figure 3.6). As the temperature is raised, these resonances sharpen. The imine α-hydrogens (H_j and H_k) resonances coalesce at approximately 366 K (500 Mhz), with an estimated k_c of 666 s^{-1} to a broad singlet at δ 2.37. The imine γ-hydrogens (H_f and H_g), the imine β-hydrogens (H_h and H_i) sharpen to a triplet at δ 2.81 and quintet at δ 1.64 respectively. The estimated $\Delta G^{\neq}$ of 16.8 kcal/mol at 366 K agrees very well with the calculated barrier of 17.0(3) kcal/mol calculated from the activation parameters determined from the Eyring analysis of the benzylic resonances. These results indicate that the

same dynamic process is exchanging the benzylic, imine α-hydrogens, and the other acridine backbone resonances.

Figure 3.6. Left: VT-NMR behavior of the octahydroacridine resonances of (**2**)Zn_2Cl_4. (NMR conditions: 500 MHz, $CDCl_2CDCl_2$, 295 K to 390 K). Right: labelling scheme for the octahydroacridine hydrogens of (**2**)Zn_2Cl_4.

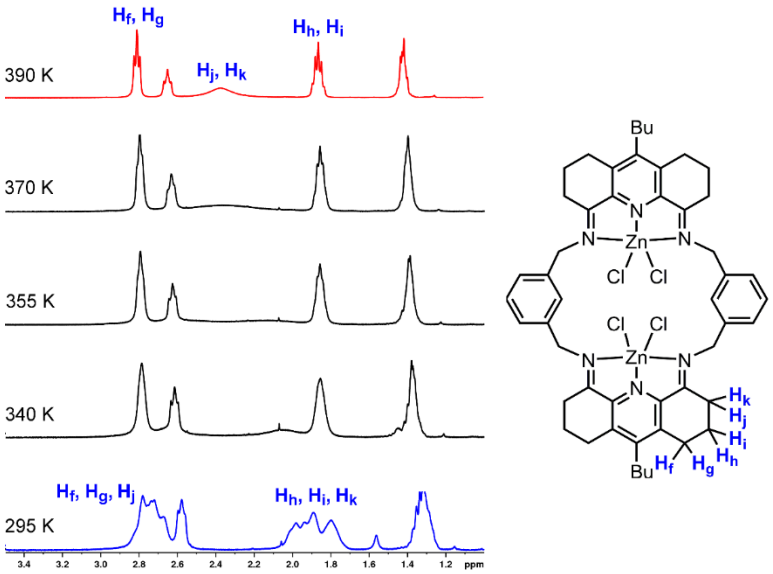

In order for the benzylic hydrogens to be exchanged, the 24-membered macrocyclic ring has to invert, i.e. the *endo* benzylic hydrogens have to become *exo* and vice versa (Figure 3.7). This process likely involves a series of correlated C_{xylyl}–$C_{benzylic}$ and $C_{benzylic}$–N_{imine} bond rotations and the simultaneous isomerism of the two 5-coordinate Zn centers between trigonal bipyramidal and square pyramidal geometries. The large and negative $\Delta S^{\neq}$ value suggests a highly ordered transition state for this process, which results from the macrocyclic structure of the complex. Similar large and negative activation entropies have observed for other compounds that undergo macrocyclic ring inversion.[50–53]

Figure 3.7. Macrocyclic ring inversion of (**2**)Zn_2Cl_4. The *exo* benzylic hydrogens are colored red, the *endo* benzylic hydrogens are colored blue in the structure on the left and vice versa in the structure on the right.

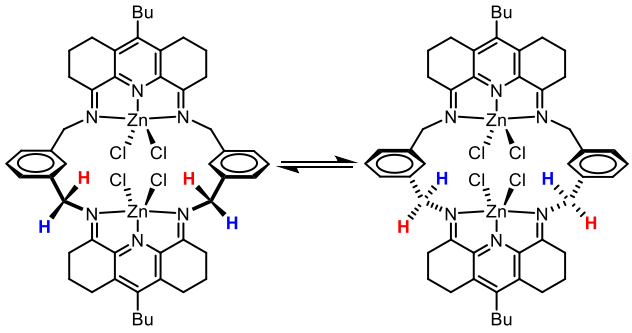

Similar to (**2**)Zn_2Cl_4, (**2**)Co_2Cl_4 is readily prepared from **2'** and 2 equiv. of $CoCl_2$ in butanol at 110 ºC and was isolated in 80% yield (Scheme 3.2 b). The solid-state structure of (**2**)Co_2Cl_4 resembles that of (**2**)Zn_2Cl_4, with both Co centers having distorted trigonal-bipyramidal geometry and Co–Co distance of 5.501(1) Å. This distance is considerably shorter than the Co–Co distance of 7.731(2) Å observed in (**A**)Co_2Cl_4, which is due to a smaller macrocyclic ring size in (**2**)Co_2Cl_4. The μ_{eff} value determined by the Evans method is be 6.3 BM, which is consistent with two independent high-spin (S = 3/2) Co^{2+} centers. This result is consistent with previous results for mononuclear (PDI)CoX_2 (X = Cl, Br) compounds.[3] The ^{1}H NMR spectrum contains both broad and sharp paramagnetically-shifted resonances. The sharp resonances are assigned to the butyl group and the *m*-xylylenediamine linker hydrogens due to their large distance from the Co centers. Fluxional behavior for this complex is observed in solution: 14 resonances (one pair of acridine resonances are coalesced based on integration) are observed at room temperature indicating that the ring inversion for (**2**)Co_2Cl_4 is slow. 15 resonances would be expected in the ^{1}H NMR spectrum of (**2**)Co_2Cl_4 if the macrocyclic ring inversion is slow and 11 are expected if the inversion is fast.

Figure 3.8. Molecular structure of 3(**2**)Co_2Cl_4•$4CH_2Cl_2$. H atoms and CH_2Cl_2 molecules are omitted. Key bond and atom distances (Å): C1–N1 1.282(4), C2–N2 1.281(4), Co1–N3 2.037(3), Co1–N1 2.145(3), Co1–N2 2.189(2), Co1–Cl1 2.249(1), Co1–Cl2 2.320(1), Co1–Co2 5.501(1). Key bond angles (º): N1–Co1–N2 148.8(1), N1–Co1–N3 75.6(1), Cl1–Co1–Cl2 114.44(4), N3–Co1–Cl1 149.55(8), N3–Co1–Cl2 95.91(8). Color key: C gray, N light blue, Co blue, Cl green. Thermal ellipsoids are drawn at 50%.

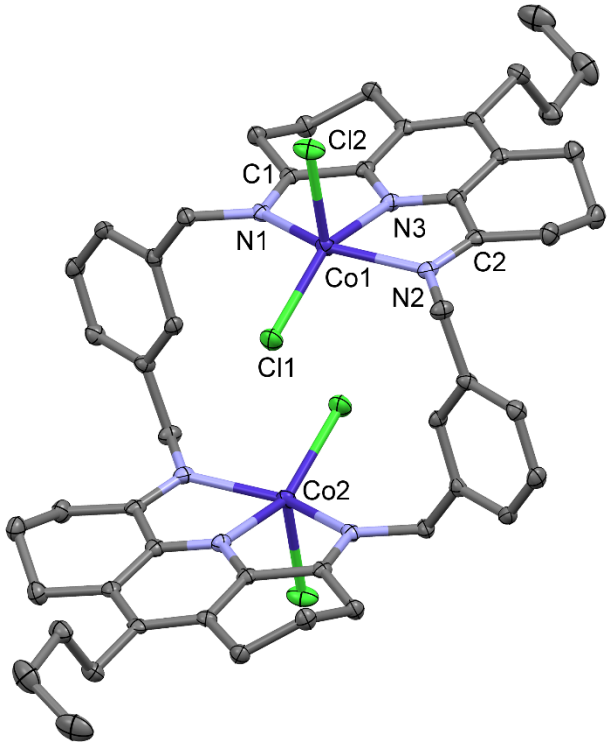

(**2**)Fe_2Cl_4 is easily prepared from 2 equiv. of $FeCl_2$ in butanol at 110 ºC and was isolated in 88% yield (Scheme 3.2 b). The μ_{eff} value determined by the Evans method is ca. 6.7 BM, which is consistent with two independent high-spin (S = 2) Fe^{2+} centers and in line with what is reported for other (PDI)FeX_2 (X = Cl, Br) complexes.[3] 13 resonances are observed in ^{1}H NMR, intermediate between the 15 expected for slow ring inversion and 11 expected for fast inversion. Due to their close proximity to the Fe^{2+} centers it is likely that the 2 expected benzylic resonances are broadened into the baseline and are therefore not observed. With this in mind, the macrocyclic ring flip of (**2**)Fe_2Cl_4 is most likely slow on the NMR timescale.

A dinuclear square-planar Pd complex was also synthesized. Reaction of **2'** with 4 equiv. of $PdBr_2$ in CH_3CN yields a brown precipitate, tentatively assigned as [(**2**)Pd_2Br_2][Pd_2Br_6]. It has been reported that the reaction of PDI^{Ph} (*N*,*N*'-(2,6-pyridinediyldiethylidyne)bis-benzenamine) and two equiv. of $PdCl_2$ yields [(PDI^{Ph})PdCl][$PdCl_3$].[54–57] A similar reaction is expected to occur with $PdBr_2$. Crystallographic evidence shows that the $PdBr_3^-$ unit exists as the $Pd_2Br_6^{2-}$ dimer.[58–60] The above reports support the tentative assignment of the composition of [(**2**)Pd_2Br_2][Pd_2Br_6]. Anion exchange using $NaBAr^F_4$ (BAr^{F-} = $B(3,5\text{-}(CF_3)_2\text{-}Ph)_4^-$) in CH_2Cl_2 followed by trituration with Et_2O yields [(**2**)Pd_2Br_2][BAr^F_4]$_2$ as a brown powder in 63 % overall yield (Scheme 3.3). The X-ray structure of [(**2**)Pd_2Br_2][BAr^F_4]$_2$ shows that the conformation of the **2** ligand is similar to that in (**2**)Zn_2Cl_4 and (**2**)Co_2Cl_4 (Figure 3.9). The Pd-Pd distance is 4.9402(4) Å, shorter than the M-M distances observed for (**2**)Zn_2Cl_4 and (**2**)Co_2Cl_4. This is likely because the PDI moieties in [(**2**)Pd_2Br_2][BAr^F_4]$_2$ are canted down into the intermetallic cavity compared to (**2**)Zn_2Cl_4 and (**2**)Co_2Cl_4 (Chart 3.3a). Both palladium centers are square planar with the bromine atoms directly over the axial site of the distal palladium center. The Br and distal Pd atoms are 4.0336(4) Å apart, larger than the sum of Van der Waals radii (sum of Pd and Br radii = 3.48 Å) and while no significant bonding interaction is expected, the contracted N3-Pd1-Br angle (174.71(6)º) suggests a weak electrostatic interaction is present. In the ^1H NMR spectrum, broad signals are observed for both the inequivalent benzylic resonances and octahydroacridine backbone methylene hydrogen resonances, suggesting that a similar ring inversion process to what is observed for (**2**)M_2Cl_4 is occurring. However, [(**2**)Pd_2Br_2][BAr^F_4]$_2$ is not thermally stable above room temperature therefore VT NMR analysis was not possible.

Scheme 3.3. Synthesis of [(**2**)Pd_2Br_2][$BAr^F{}_4$]$_2$.

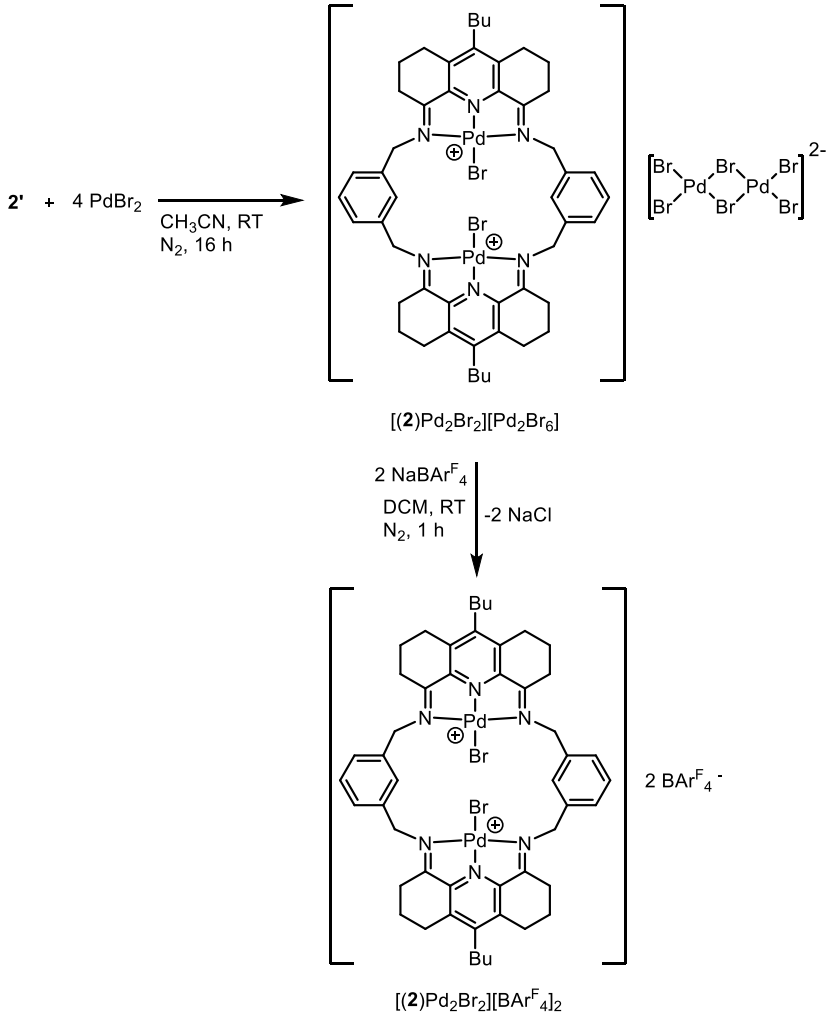

Figure 3.9. Molecular structure of [(**2**)Pd_2Br_2][$BAr^F{}_4$]$_2$. H atoms and $BAr^F{}_4^-$ molecules are omitted. Key bond and atom distances (Å): N1–C1 1.334(4), N2–C2 1.299(4), Pd1–N1 2.061(2), Pd1–N2 2.054(2), Pd1–N3 1.929(2), Pd1–Br1 2.4009(4), Pd1–Pd2 4.9402(4), Pd2–Br1 4.0336(4). Key bond angles (º): N1–Pd1–N2 80.07(9) N2–Pd1–N3 79.48(9), N1–Pd1–N3 159.14(9), N1–Pd1–Br1 99.15(7), N3–Pd1–Br1 174.71(6). $\tau_4 = 0.19$, $\tau_4' = 0.13$. Color key: C gray, N light blue, Pd teal, Br orange. Thermal ellipsoids are drawn at 50%.

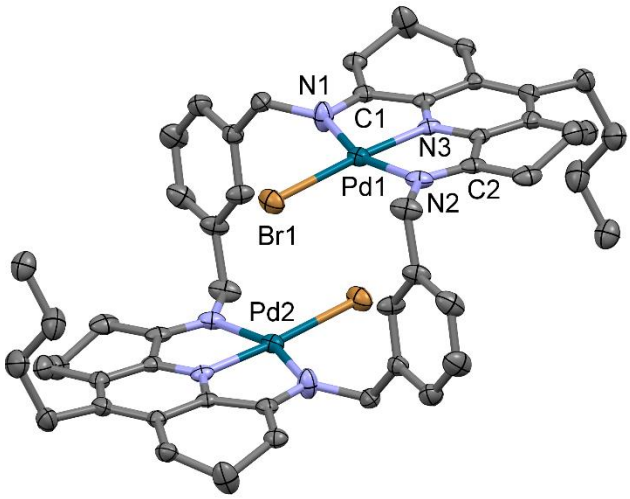

Synthesis of the Bis-PDE Complexes of 2'. The bis-(pyridine-dienamine) tautomer form of **2'** allows for the facile synthesis of bis-(pyridine-dienamido) (bis-PDE) complexes by deprotonation-metalation with metal sources containing basic ligands. Reaction of **2'** with 2 equiv. of $Zr(NMe_2)_4$ in PhCl readily generates (**2'**–4H)$Zr_2(NMe_2)_4$ in 79 %.yield *via* amine elimination (Scheme 4). The ^{1}H NMR spectrum of (**2'**–4H)$Zr_2(NMe_2)_4$ shows that the benzylic hydrogens are inequivalent, similar to what is observed for (**2**)Zn_2Cl_4. However, the benzylic resonances are not broadened due to exchange, indicative of a static structure on the NMR timescale. The vinylic resonances observed at δ 4.67 and δ 98.4 observed in ^{1}H and ^{13}C{^{1}H} NMR spectra respectively confirm the bis-PDE form of the ligand.

Scheme 3.4. Synthesis of (**2'**–4H)$Zr_2(NMe_2)_4$.

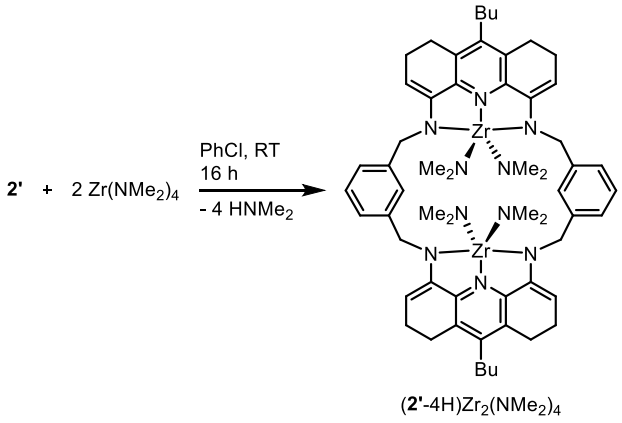

Alkylation reactions of (**2'**–4H)$Zr_2(NMe_2)_4$ were explored in an effort to prepare crystalline analogue for structural analysis. (**2'**–4H)$Zr_2(NMe_2)_4$ reacts with excess $AlMe_3$ to generate (**2'**-4H)Zr_2Me_4 in 67 % yield (Scheme 5 a), whereas reaction with the bulkier $Al(CH_2SiMe_3)_3$ produces (**2'**–4H)$Zr_2(CH_2SiMe_3)_2(NMe_2)_2$ in 74 % yield (Scheme 5 b). Similar to what is observed for (**2'**–4H)$Zr_2(NMe_2)_4$, vinylic resonances at ca. δ 4.8 and ca δ 98 are observed in ^{1}H NMR and ^{13}C{^{1}H} NMR respectively for both (**2'**–4H)Zr_2Me_4 and (**2'**–4H)$Zr_2(CH_2SiMe_3)_2(NMe_2)_2$, consistent with the bis-PDE form of the ligand. Additionally, the benzylic hydrogens are inequivalent and appear as two sharp doublets, indicating that the structure is static in solution. Specifically, the ^{1}H NMR spectrum of (**2'**–4H)$Zr_2(CH_2SiMe_3)_2(NMe_2)_2$ does not broaden as the temperature is increased and no EXSY correlations between the benzylic resonances are observed in the ^{1}H-^{1}H NOESY spectrum.

XRD analysis shows that (**2'**–4H)$Zr_2(CH_2SiMe_3)_2(NMe_2)_2$ adopts a similar conformation to that of (**2**)Zn_2Cl_4, (**2**)Co_2Cl_4, and [(**2**)Pd_2Br_2][$BAr^F{}_4$]$_2$ (Figure 3.10 and Chart 3.3). Both Zr centers are distorted square pyramidal with the bulky -CH_2SiMe_3 groups in the more sterically-accessible axial sites, and the smaller -NMe_2 groups in the equatorial sites perpendicular to the

PDE planes. Compared to (**2**)Zn_2Cl_4 and (**2**)Co_2Cl_4, the metal-metal distance in (**2'**–4H)$Zr_2(CH_2SiMe_3)_2(NMe_2)_2$ is elongated to 6.1273(7) Å. The N1-C1 bond distance in the bis-PDE complex (**2'**–4H)$Zr_2(CH_2SiMe_3)_2(NMe_2)_2$. is 1.391(4) Å, ca. 0.15 Å longer than the N1-C1 bond distances observed for PDI complexes and consistent with results for previously reported PDE complexes.[61–63]

Scheme 3.5. Synthesis of (**2'**–4H)Zr_2Me_4 and (**2'**–4H)$Zr_2(CH_2SiMe_3)_2(NMe_2)_2$.

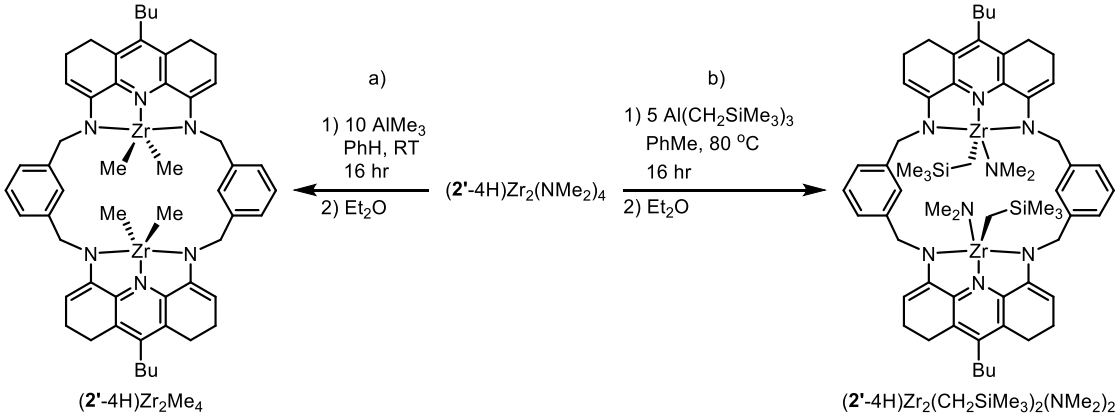

Figure 3.10. Molecular structure of (**2'**−4H)$Zr_2(CH_2SiMe_3)_2(NMe_2)_2$. H atoms are omitted. Key bond and atom distances (Å): N1–C1 1.391(4), N1–Zr1 2.151(2), N3–Zr2 2.248(2), N2–C2 1.390(3), N2–Zr1 2.149(2), C3–Zr1 2.240(3), N4–Zr1 2.050(2), Zr1–Zr2 6.1273(7). Key bond angles (º): N1–Zr1–N3 70.25(9), N2–Zr1–N3 69.97(9), N1–Zr1–N2 136.13(9), N3–Zr1–C3 101.4(1), N3–Zr1–N4 143.83(9), N1–Zr1–N4 98.38(9). Color key: C gray, N light blue, Zr cyan, Si tan. Thermal ellipsoids are drawn at 75%.

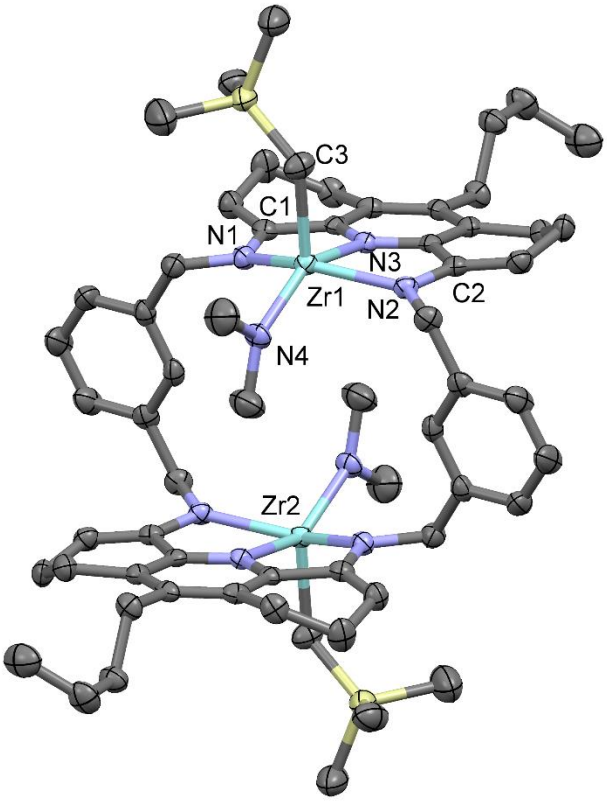

As noted above, the Pd-Pd distance in [(**2**)Pd_2Br_2][$BAr^F{}_4$]$_2$ (4.9402(4) Å) and the Zr-Zr distance in (**2'**−4H)$Zr_2(CH_2SiMe_3)_2(NMe_2)_2$ (6.1273(7) Å) are shorter and longer respectively compared the Zn-Zn distance (5.515(1) Å) in (**2**)Zn_2Cl_4. These differences can be explained by examining side-on views and views down the pyridine rings of these structures, which are shown in Chart 3.3. The four-coordinate square-planar Pd sites in [(**2**)Pd_2Br_2][$BAr^F{}_4$]$_2$ do not have a ligand pointing towards the distal binding site, in contrast to what is observed in the solid-state structure of trigonal-bipyramidal (**2**)Zn_2Cl_4. The resulting lower degree of steric crowding in

[(**2**)Pd_2Br_2][$BAr^F{}_4$]$_2$ allows for the macrocyclic ligand to adopt a conformation in which the PDI moieties are slid parallel away from each other and towards the center of the intermetallic cavity compared to the conformation observed for (**2**)Zn_2Cl_4. Additionally, both Pd centers are displaced 0.091 Å out of the PDI planes toward the intermetallic cavity. These conformational differences result in the shortening of the Pd-Pd distance. In contrast, to accommodate the bulky NMe_2 ligands in (**2'–**4H)$Zr_2(CH_2SiMe_3)_2(NMe_2)_2$, the two binding sites are forced to move away from each other which results in less canting of the xylylene linker rings ((**2**)Zn_2Cl_4: C1–C2–C3 168.85º; (**2'–**4H)$Zr_2(CH_2SiMe_3)_2(NMe_2)_2$: C1–C2–C3 174.81º). In addition, both of the Zr centers lie 0.442 Å out of the PDE plane away from the intermetallic cavity. Both of these factors elongate the Zr-Zr distance.

Chart 3.3. a) Side-on Views of the Molecular Structures of (Left to Right) (**2**)Zn_2Cl_4, (**2**)Co_2Cl_4, [(**2**)Pd_2Br_2][$BAr^F{}_4$]$_2$, and (**2'**–4H)$Zr_2(CH_2SiMe_3)_2(NMe_2)_2$, (**A**)$Co_2Cl_4$. The Front-Facing Xylylene Linker, Butyl Groups, and Hydrogens Are Omitted. b) Views of the Molecular Structures of (Left to Right) (**2**)Zn_2Cl_4, [(**2**)Pd_2Br_2][$BAr^F{}_4$]$_2$, (**2'**–4H)$Zr_2(CH_2SiMe_3)_2(NMe_2)_2$ Down the Pyridine Rings. The Bottom Pyridine Rings of the Structures are Aligned. Butyl Groups, Hydrogens, and $BAr^F{}_4^-$ Molecules Are Omitted.

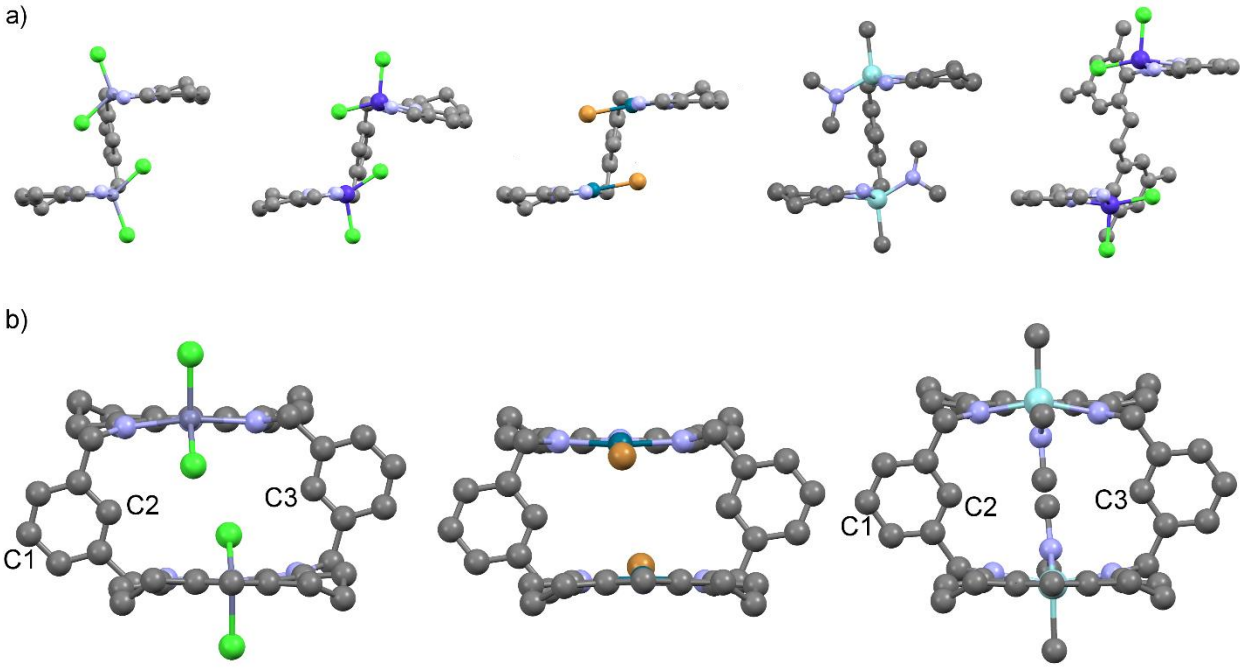

Ethylene Polymerization Results. Attempting to use MAO or MMAO-12 as activators in ethylene homopolymerization with (**2**)Co_2Cl_4 and (**2**)Fe_2Cl_4 results in partial decomposition and no observed formation of oligo- or polyethylene. However, the reaction of (**2**)Fe_2Cl_4 and 1000 equiv. of Al^iBu_3 under 400 psi of ethylene pressure at 25°C results in the production of C_4 – C_{10} α-olefins with an activity of 240 kg $mmol_{Fe}^{-1}$ h^{-1} and a Schulz-Flory propagation coefficient of 0.10. Under the same polymerization conditions, (**2**)Co_2Cl_4 produces traces of 1-butene and 1-hexene. The poor polymerization performance likely due to the lack of steric pressure from *m*-xylylenediamine linker. Attempted activation of (**2'**–4H)Zr_2Me_4 with MAO or [CPh_3][$B(Ar^F{}_4)_4$]/Al^tBu_3 results in decomposition.

3.3 Conclusion

This chapter describes the synthesis of a bis-(pyridine-dienamine) proligand **2'**, a variant of **D**, using octrahydroacridine as a ligand backbone that preorganizes the system for macrocyclization. The template-free synthesis of **2'** allows for facile syntheses of a wide array of bis-PDI and bis-PDE metal complexes. Five-coordinate dinculear bis-PDI (**2**)M_2Cl_4 (M = Zn, Co, Fe) complexes were synthesized. These complexes exhibit macrocyclic ring inversion on the NMR timescale. This process was explored for (**2**)Zn_2Cl_4 by VT NMR and lineshape analysis. Eyring analysis determined $\Delta G^{\neq}$ to be 15.5(3) kcal/mol at 295 K and 17.3(3) kcal/mol at the coalescance temperature of 380 K for the benzylic hydrogens. A square-planar dinuclear bis-PDI Pd complex, [(**2**)Pd_2Br_2][$BAr^F{}_4$]$_2$, was synthesized and shows similar solution behavior and solid-state structure to that of (**2**)M_2Cl_4 (M = Zn, Co). Deprotonation-metalation of bis-(pyridine-dienamine) proligand **2**' with $Zr(NMe_2)_4$ results in formation of bis-PDE (**2'**)$Zr_2(NMe_2)_4$, which was subsequently alkylated with $AlMe_3$ and $Al(CH_2SiMe_3)_3$ to generate (**2'**–4H)Zr_2Me_4 and (**2'**–4H)$Zr_2(CH_2SiMe_3)_2(NMe_2)_2$ respectively, the latter of which was characterized in the solid-state.

3.4 Experimental Section

General Procedures. All experiments were performed using drybox or Schlenk techniques under a nitrogen atmosphere unless noted otherwise. Nitrogen was purified by passage through Q-5 oxygen scavenger and activated molecular sieves. CH_2Cl_2, Et_2O, THF were dried by passage through activated alumina. Hexanes and pentanes were purified by passage through BASF R3−11 oxygen scavenger and activated alumina. 1,2-dichloroethane was dried over magnesium sulfate for 24 h and then distilled over calcium hydride and stored under nitrogen. $CDCl_3$, CD_2Cl_2, $CDCl_2CDCl_2$, and C_6D_5Cl were distilled from and stored over activated 3 Å molecular sieves.

C_6D_6 and $C_6D_5CD_3$ were distilled from purple Na/benzophenone solutions. Anhydrous metal salts were purchased from Strem Chemical, Inc. and used without further purification. Acetic acid, benzaldehyde, anhydrous acetonitrile, and anhydrous n-butanol, MAO, MMAO-12, and Al^tBu_3 were purchased from Sigma-Aldrich and used without further purification. *m*-Xylylenediamine was purchased from Sigma-Aldrich, distilled, and stored under nitrogen. $NaBAr^F_4$ was donated by Boulder Scientific and used as received. Combustion analyses were performed by Midwest Microlab. 9-butyl-1,2,3,4,5,6,7,8-octahydroacridine was synthesized using the procedure reported by Bell.[44,45] $Al(CH_2SiMe_3)_3$ was synthesized from literature procedures.[64]

NMR spectra were recorded on a Bruker ADVANCE II+ 500 or DRX 400 spectrometer. ^1H and $^{13}C\{^1H\}$ chemical shifts are reported relative to $SiMe_4$ and internally referenced to residual ^1H and $^{13}C\{^1H\}$ solvent resonances. $^{11}B\{^1H\}$ and $^{19}F\{^1H\}$ chemical shifts were externally referenced to BF_3OEt_2 (δ 0.0 for ^{11}B and δ −153.0 for ^{19}F).

Electrospray mass spectra (ESI-MS) were recorded on a 6130 LCMS (low resolution) instrument High-resolution accurate mass spectra (HRA-MS) were recorded using Agilent 6224 TOF−MS instrument in mixed mode. MALDI-TOF-TOF-MS spectra were collected on a Bruker Ultraflextreme instrument using dithranol as the matrix. The observed isotope patterns closely matched isotope patterns calculated using envipat 2.2 Web,[65] which are reported in the SI for each metal complex. The reported m/z value corresponds to the most intense peak in the isotope pattern.

X-ray quality crystals of (**2**)Zn_2Cl_4, (**2**)Co_2Cl_4, and [(**2**)Pd_2Br_2][BAr^F_4]$_2$ were grown from layering a 1,2-dichloroethane solution of each compound with hexanes (1/1) at room temperature over 2 days. X-ray quality crystals of (**2'**–4H)$Zr_2(CH_2SiMe_3)_2(NMe_2)_2$ were grown from layering a saturated PhMe solution with hexane (1/15) at room temperature over 3 days.

9-butyl-1,2,3,4,5,6,7,8-octahydro-4,5-bis(phenylmethylene)-acridine. 9-butyl-1,2,3,4,5,6,7,8-octahydroacridine (39.2 g, 0.16 mol) and acetic anhydride (120 mL, 1.27 mol) were added to a round bottom flask. Benzaldehyde (145 mL, 1.43 mmol) was added using an addition funnel. The orange solution was refluxed for 16 h, during which time the solution turned a dark red color. The flask was then submerged in an ice bath until a yellow crystalline solid began to form and then the flask was transferred to a -15 ºC freezer and left to stand for 6 h. The resulting yellow crystalline solid was collected and washed with ethanol (3 x 150 mL). The solid dried overnight under vacuum to yield 9-butyl-1,2,3,4,5,6,7,8-octahydro-4,5-bis(phenylmethylene)-acridine as a red-yellow crystalline powder. Yield: 54.0 g, 83 %. By ^{1}H NMR, the major impurities are benzaldehyde, acetic acid, and acetic anhydride. ^{1}H NMR ($CDCl_3$, 500 MHz): δ 8.11 (s, 2H, Ph*H*C=C), 7.42 (d, $^{3}J_{HH}$ = 10 Hz, 4H, *o*-Ar), 7.35 (t, $^{3}J_{HH}$ = 10 Hz, 4H, *m*-Ar), 7.22 (t, $^{3}J_{HH}$ = 10 Hz, 2H, *p*-ArH), 2.83 (m, 8H, C=CC*H*$_2$CH$_2$C*H*$_2$), 2.59 (t, $^{3}J_{HH}$ = 10 Hz, 2H, C*H*$_2$CH$_2$CH$_2$CH$_3$), 1.84 (quintet, $^{3}J_{HH}$ = 5 Hz, 4H, C=CCH$_2$C*H*$_2$CH$_2$), 1.44 (m, 4H, CH$_2$C*H*$_2$C*H*$_2$CH$_3$), 0.97 (t, $^{3}J_{HH}$ = 9 Hz, 3H, CH$_2$CH$_2$CH$_2$C*H*$_3$). ^{13}C{^{1}H} NMR ($CDCl_3$, 500 MHz): δ 149.6, 148.4, 138.6, 136.8, 129.8, 129.6, 128.1, 126.5, 126.3, 30.7, 28.2, 27.8, 26.4, 23.5, 23.2, 14.0. ESI-MS m/z: 420.3 $[M+H]^+$. ESI/APCI-TOF HR-MS (m/z): $[M+H]^+$. Calcd for $C_{31}H_{33}N$ 420.2691; Found 420.2684.

Scheme 3.6. Synthesis of 9-butyl-1,2,3,4,5,6,7,8-octahydro-4,5-bis(phenylmethylene)-acridine.

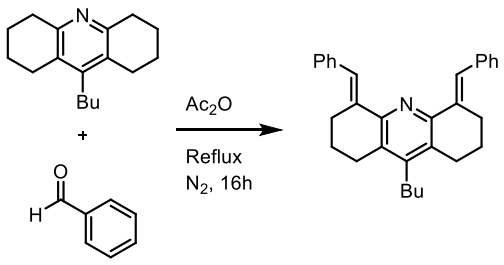

Figure 3.11. NMR Spectra for 9-butyl-1,2,3,4,5,6,7,8-octahydro-4,5-bis(phenylmethylene)-acridine.

(a) ^{1}H NMR ($CDCl_3$, 500 MHz, 23 ºC)

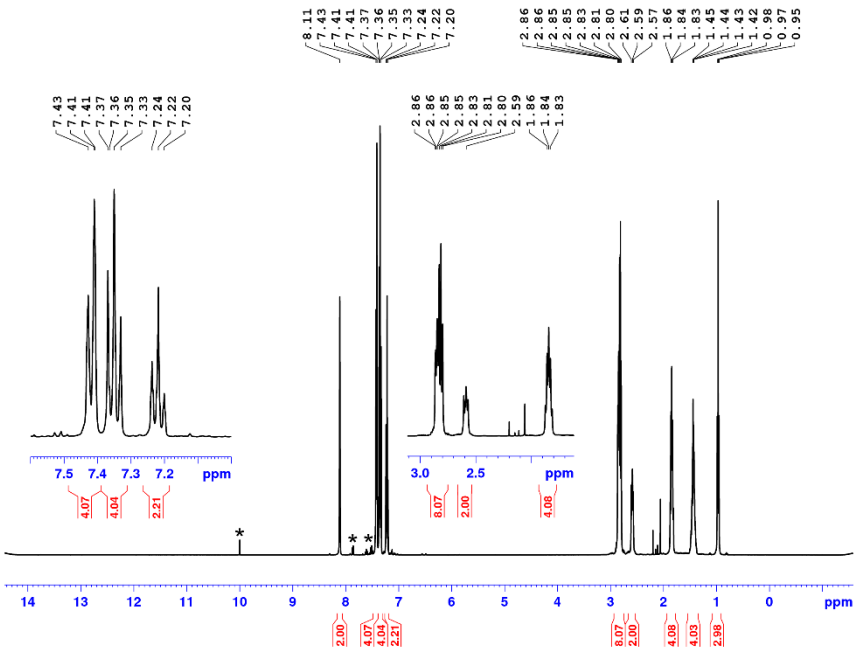

(b) $^{13}C\{^{1}H\}$ NMR ($CDCl_3$, 126 MHz, 23 ºC)

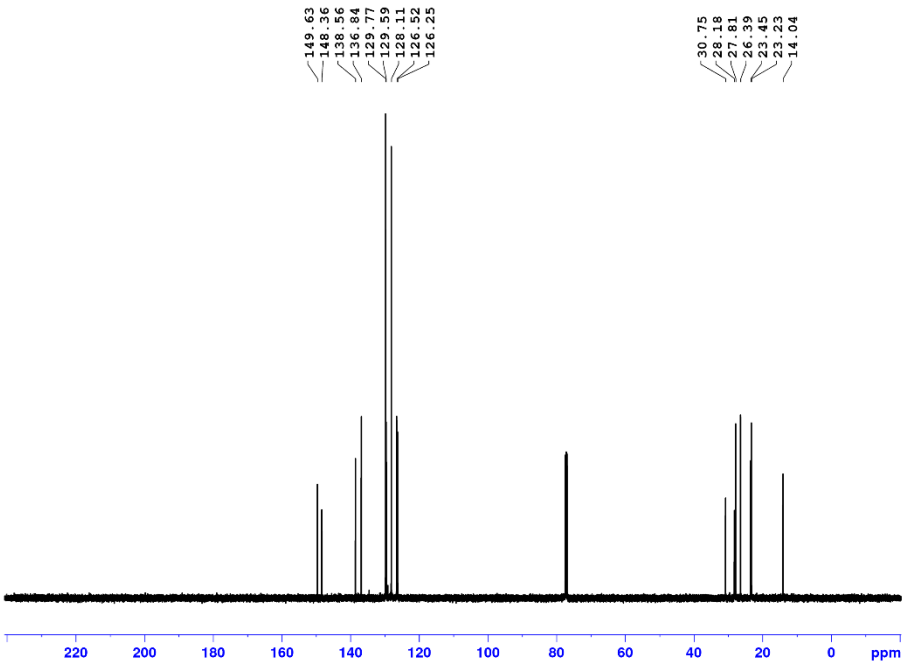

9-butyl-2,3,7,8-tetrahydro-4,5(1*H*,6*H*)-acridinedione (1). A three-neck 500 ML round bottom flask was charged with 9-butyl-1,2,3,4,5,6,7,8-octahydro-4,5-bis(phenylmethylene)-acridine (11.2 g, 26.74 mmol), CH_2Cl_2 (300 mL), and methanol (100 mL). The solution was cooled to -78 ºC while O_2 was bubbled through the solution. The reaction flask was connected to a bubbler containing a 10% potassium iodide in 1/1 water/acetic acid indicator solution, which turns brown in the presence of O_3. After sparging the solution for 15 minutes, the ozone generator was turned on. After 30 to 45 min, the solution became a persistent blue color. The generator was then turned off and the solution purged with O_2 for 15 min, resulting in a colorless solution. Dimethyl sulfide (9 mL, 0.12 mol) was added dropwise. The resulting pale-yellow solution was left to stir for 16 h at room temperature. The resulting bright yellow solution was concentrated to a yellow oil and washed with hot hexane (2 x 40 mL). The oil was dissolved in CH_2Cl_2 (100 mL), then subsequently washed with water (40 mL), 15 % aqueous sodium bisulfite (50 mL), and water (40 mL). The organic layer was dried with magnesium sulfate and concentrated on a rotary evaporator. The resulting yellow oil was then triturated with Et_2O (100 mL) and vigorous stirred to yield a bright yellow-orange solid, which was collected and washed with Et_2O (2 x 25 mL). The solid was ground in a mortar and pestle and placed in a vacuum oven at 70 ºC overnight, to yield **1** as a yellow solid. Yield: 4.7 g, 72 %. ^{1}H NMR: ($CDCl_3$, 500 MHz, 23 ºC): δ 3.02 (t, $^3J_{HH}$ = 8 Hz, 4H, O=C$CH_2CH_2CH_2$), 2.77 (t, $^3J_{HH}$ = 8 Hz, 4H, O=C$CH_2CH_2CH_2$), 2.72 (t, $^3J_{HH}$ = 9.5 Hz, 2H, $CH_2CH_2CH_2CH_3$), 2.18 (quintet, $^3J_{HH}$ = 8.5 Hz, 4H, O=C$CH_2CH_2CH_2$), 1.48 (m, 4H, $CH_2CH_2CH_2CH_3$), 0.99 (t, $^3J_{HH}$ = 9 Hz, 3H, $CH_2CH_2CH_2CH_3$). ^{13}C{^{1}H} NMR ($CDCl_3$, 125 MHz, 23 ºC): δ 196.1, 150.7, 147.1, 141.5, 39.2, 30.5, 28.5, 26.2, 23.2, 21.9, 13.8. ESI-MS (m/z): 272.2 $[M+H]^+$. ESI/APCI-TOF HR-MS (m/z): $[M+H]^+$. Calcd for $C_{17}H_{21}NO_2$ 272.1651; Found 272.1645.

Scheme 3.7. Synthesis of 9-butyl-2,3,7,8-tetrahydro-4,5(1*H*,6*H*)-acridinedione.

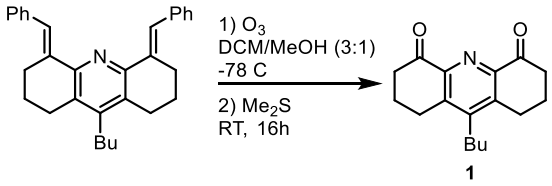

1

Figure 3.12. NMR spectra of **1**.
(a) ^{1}H NMR ($CDCl_3$, 500 MHz, 23 ºC)

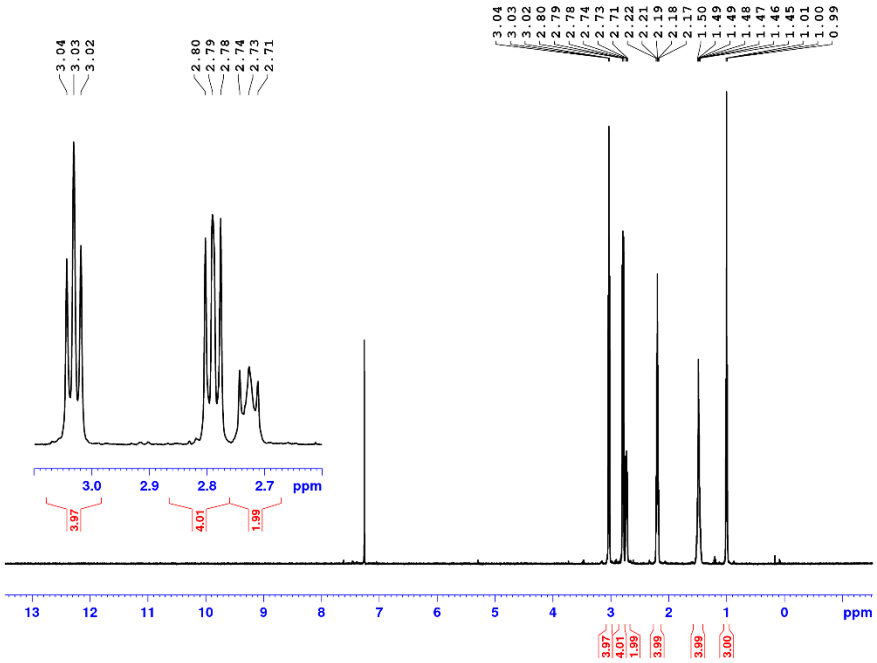

Figure 3.12, continued.

(b) $^{13}C\{^{1}H\}$ NMR ($CDCl_3$, 126 MHz, 23 ºC)

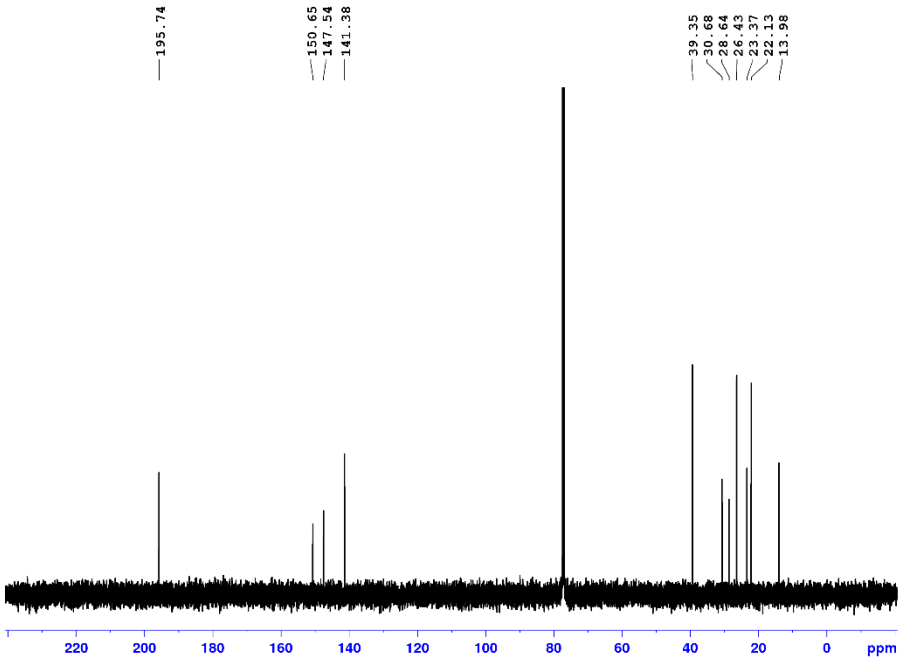

2'. **1** (1.69 g, 6.23 mmol) and *p*-toluenesulfonic acid hydrate (59 mg, 0.6 mmol) were added to n-butanol (30 mL) and stirred until homogeneous. *m*-Xylylenediamine (848 µL, 6.23 mmol) was then added via syringe. Within 5 min, a beige precipitate began to form. The dark red reaction mixture was left to stir for 1 h. The resulting beige precipitate was then collected and washed with ethanol (125 mL) under air and dried under vacuum overnight to yield **2'** as a beige solid Yield: 1.90 g, 82 %. The labelling scheme for **2'** is shown in Figure 3.13. ^{1}H NMR (CD_2Cl_2, 500 MHz, 23 ºC): δ: 7.30 (m, 8H, H_c, H_d, H_e), 5.12 (br t, $^{3}J_{HH}$ = 4H, H_j), 4.87 (t, $^{3}J_{HH}$ = 4.5 Hz, 4H, H_k), 4.11 (d, $^{3}J_{HH}$ = 4 Hz, 8H, H_a,H_b), 2.79 (t, $^{3}J_{HH}$ = 8 Hz, 8 H, H_f,H_g), 2.65 (t, $^{3}J_{HH}$ = 7.5 Hz, 4H, H_l), 2.34 (q, $^{3}J_{HH}$ = 4.5 Hz, 8H, H_h,H_i), 1.43 (m, 8H, H_m, H_n), 0.95 (t, $^{3}J_{HH}$ = 6 Hz, 6H, H_o). $^{13}C\{^{1}H\}$ NMR ($CDCl_3$, 125 MHz, 23 ºC): δ 145.8 (*o*-py), 145.4 (*m*-py), 141.2 (*p*-py), 139.9 (C_{xylyl}-$C_{benzylic}$), 129.3 (*C*-H_k), 129.2 (*C*-H_c, *C*-H_d, or *C*-H_e), 128.6 (*C*-H_c, *C*-H_d, or *C*-H_e), 126.7 (*C*-H_c, *C*-H_d, or *C*-H_e),

94.8 (*C*-H_k), 48.8 (*C*-H_a,H_b), 31.8 (*C*-H_m), 28.3 (*C*-H_l), 24.5 (*C*-H_f, H_g), 23.1 (*C*-H_n), 21.9 (*C*-H_h,H_i), 14.12 (*C*-H_o). IR (KBr Disk): ν(cm^{-1}) 3400.2 (N–H), 3049.4, 2955.0, 2874.0, 2854.1, 2812.2, 1641.6, 1560.2, 1488.5, 1464.5, 1427.8, 1403.6, 1384.8, 1357.7, 1291.3, 1211.5, 1163.5, 1099.4, 1018.5, 978.3, 909.1, 201.5, 755.1, 703.9. ESI-MS (m/z): 743.6 $[M+H]^+$, 798.3 $[M+Na]^+$. ESI/APCI-TOF HRA-MS (m/z): $[M+H]^+$.Calcd for $C_{50}H_{59}N_6$ 743.4801; Found 743.4782.

Figure 3.13. Labelling scheme for **2'**.

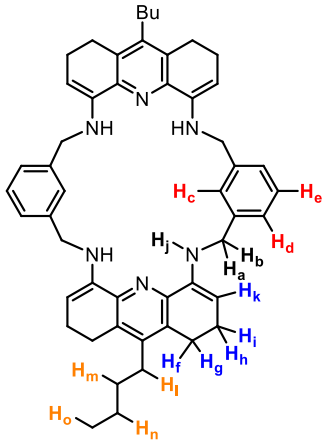

Figure 3.14. NMR Spectra for **2'**.
(a) ^{1}H NMR of **2'** ($CDCl_3$, 500 MHz, 23 ºC)

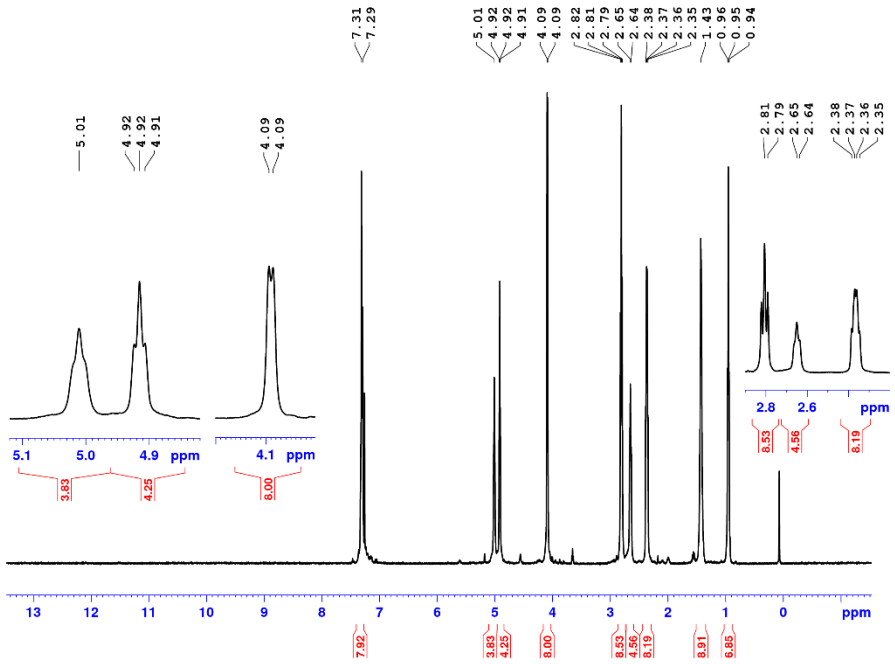

(b) $^{13}C\{^{1}H\}$ NMR of **2'** ($CDCl_3$, 126 MHz, 23 ºC)

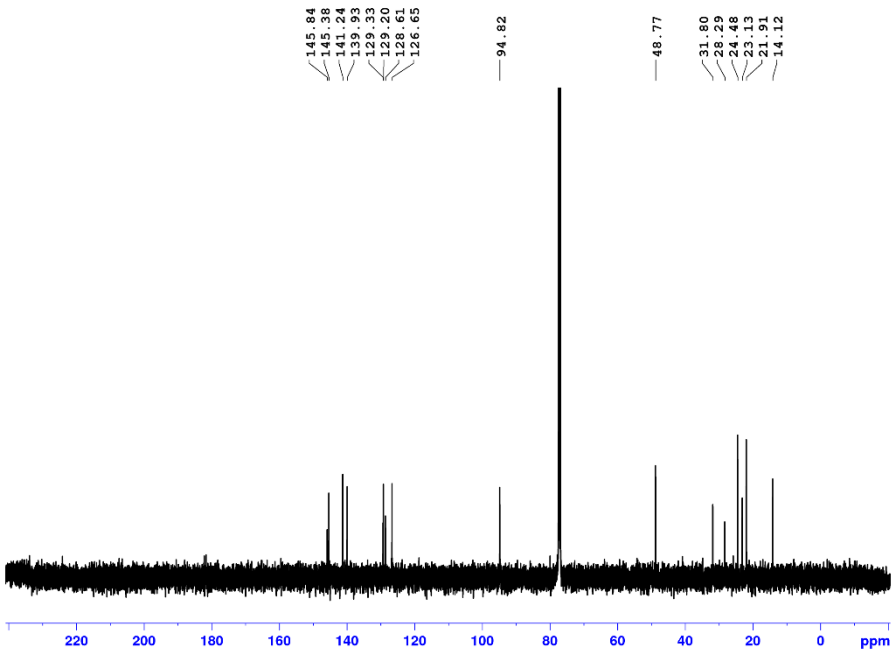

Figure 3.14, continued.

(c) COSY of **2'** ($CDCl_3$, 500 MHz, 23 ºC)

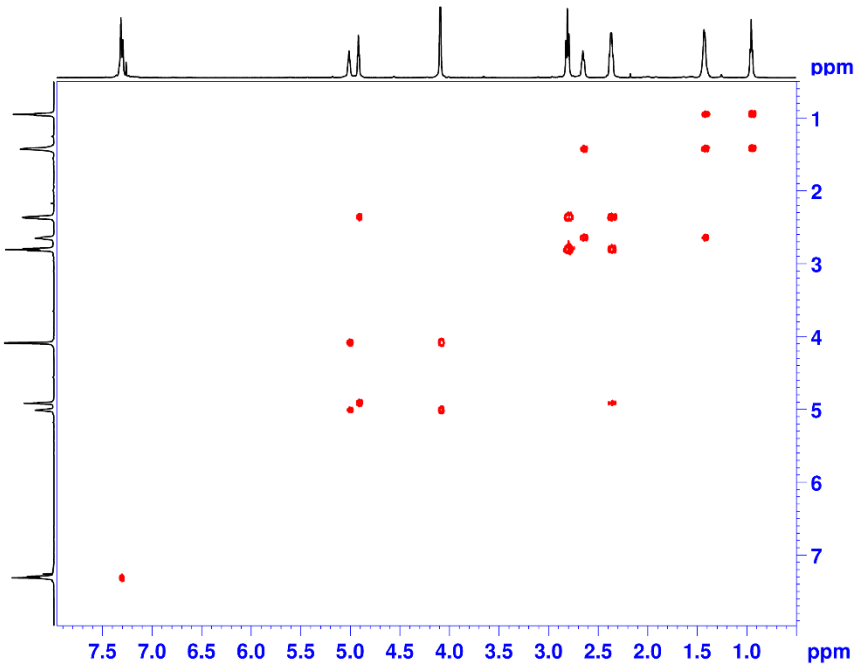

(d) ^{1}H-^{13}C HMQC ($CDCl_3$, 500 MHz, 23 ºC)

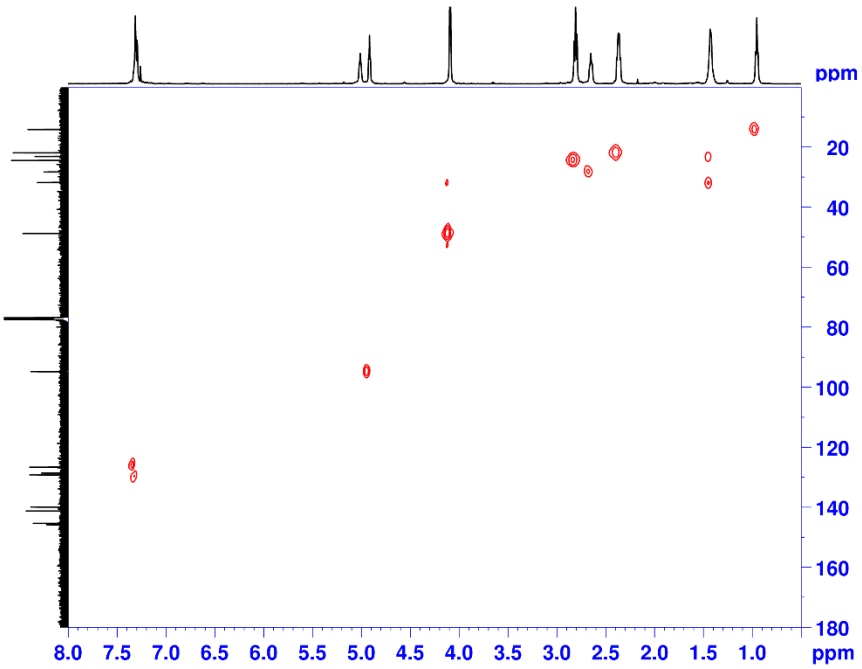

Figure 3.14, continued.

(e) ^{1}H-^{13}C HMBC of **2'** ($CDCl_3$, 500 MHz, 23 ºC)

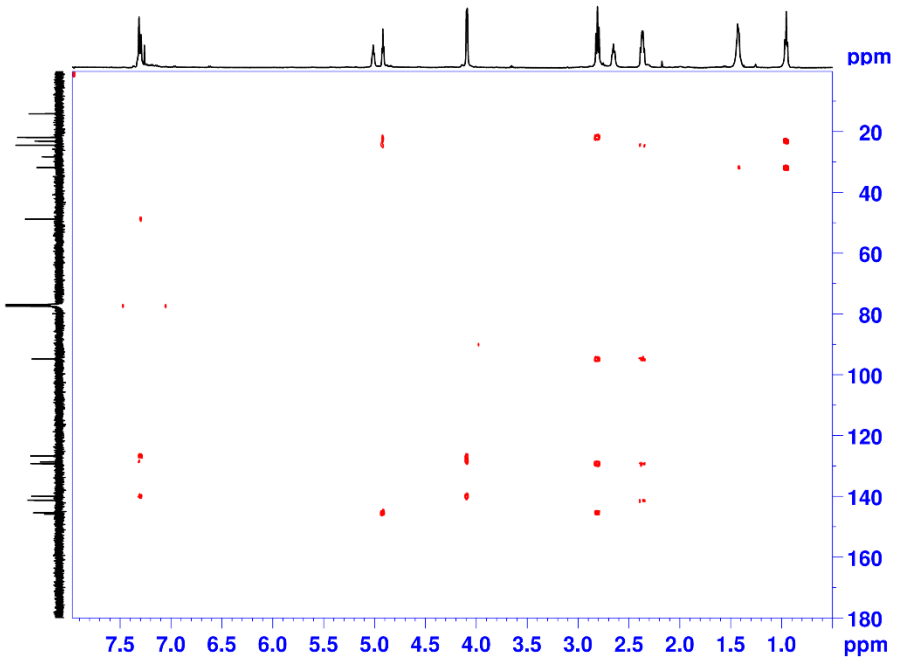

(2)Zn_2Cl_4. $ZnCl_2$ (146 mg, 1.08 mmol) and **1'** (400 mg, 0.538 mmol) were suspended in n-butanol (40 mL). The bright yellow suspension was heated to 110 ºC and stirred for 16 h. The yellow solid was collected and then dissolved in anhydrous CH_2Cl_2 (25 mL) and heated at 40 ºC for 2 d. The CH_2Cl_2 was layered with hexane (25 mL) to yield (**2**)Zn_2Cl_4 as a white solid. Yield: 340 mg, 62%. The labelling scheme for (**2**)Zn_2Cl_4 is shown in Figure 3.15. ^{1}H NMR (CD_2Cl_2, 500 MHz, 23 ºC): δ 8.07 (s, 2H, H_c), 7.22 (m, 6H, H_d,H_e), 5.45 (br d, $^{2}J_{HH}$ = 9 Hz, 4H, H_a), 4.35 (br d, $^{2}J_{HH}$ = 9 Hz, 4H, H_b), 2.84 (m, 12H, H_f, H_g, H_k), 2.67 (t, $^{3}J_{HH}$ = 7 Hz, 4H, H_l), 1.99 (m, 12H, H_h, H_i, H_j), 1.44 (m, 8H, H_m, H_n), 0.96 (t, $^{3}J_{HH}$ = 7 Hz, 6H, H_o). ^{1}H NMR ($CDCl_2CDCl_2$, 400 MHz, 23 ºC): δ 7.99 (s, 2H), 7.15 (m, 6H), 5.42 (br d, $^{2}J_{HH}$ = 12 Hz, 4H), 4.33 (br d, $^{2}J_{HH}$ = 12 Hz, 4H), 2.78 (m, 12H), 2.58 (t, $^{3}J_{HH}$ = 8 Hz, 4H), 1.89 (m, 12H), 1.32 (m, 8H), 0.86 (t, $^{3}J_{HH}$ = 7 Hz, 6H) ^{13}C{^{1}H} NMR (CD_2Cl_2, 125 MHz, 23 ºC): δ 166.3 (*C*=N), 154.6 (*p*–py), 142.6 (*o*–py), 140.0 (C_{xylyl}-

$C_{benzylic}$), 137.8 (*m*–py), 130.3 (*C*–H_c), 127.5 (*C*–H_d or *C*–H_e), 127.3 (*C*–H_d or *C*–H_e), 53.3 (*C*–H_a,H_b), 30.6 (*C*–H_m), 29.0 (*C*-H_l), 28.9 (*C*–H_k,H_j), 25.0 (*C*–H_f,H_g), 23.6 (*C*–H_n), 21.2 (*C*–H_h,H_i), 13.9 (*C*-H_o). IR (KBr Disk): ν(cm^{-1}) 3043.8, 2952.2, 2868.0, 1645.6, 1606.6, 1606.8, 1574.5, 1507.2, 1487.2, 1453.4, 1423.3, 1320.7, 1267.6, 1234.7, 1145.9, 1104.0, 1078.5, 1040.6, 999.78, 967.1, 935.6, 904.1, 875.6, 850.8, 784.9, 710.2. MALDI-TOF-TOF (Dithranol) (m/z): 1129.4 [M – 3Cl + Dithranol – 2H]$^+$, 979.24 [M – Cl]$^+$, 945.26 [M – 2Cl]$^+$, 841.37 [M – Zn – 3Cl]$^+$. ESI/APCI-TOF HRA-MS (m/z): [M-Cl]$^+$ Calcd for $C_{50}H_{58}N_6Zn_2Cl_3$ 975.2371; Found 975.2388.

Figure 3.15. Labelling scheme for (**2**)Zn_2Cl_4.

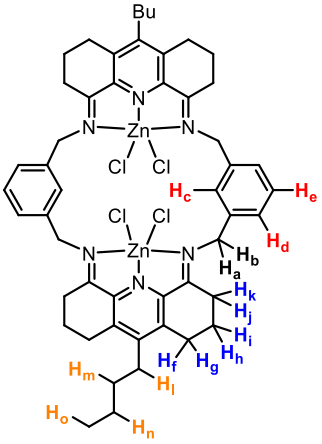

Figure 3.16. NMR Spectra of (**2**)Zn_2Cl_4.
(a) ^1H NMR (CD_2Cl_2, 500 MHz, 23 ºC)

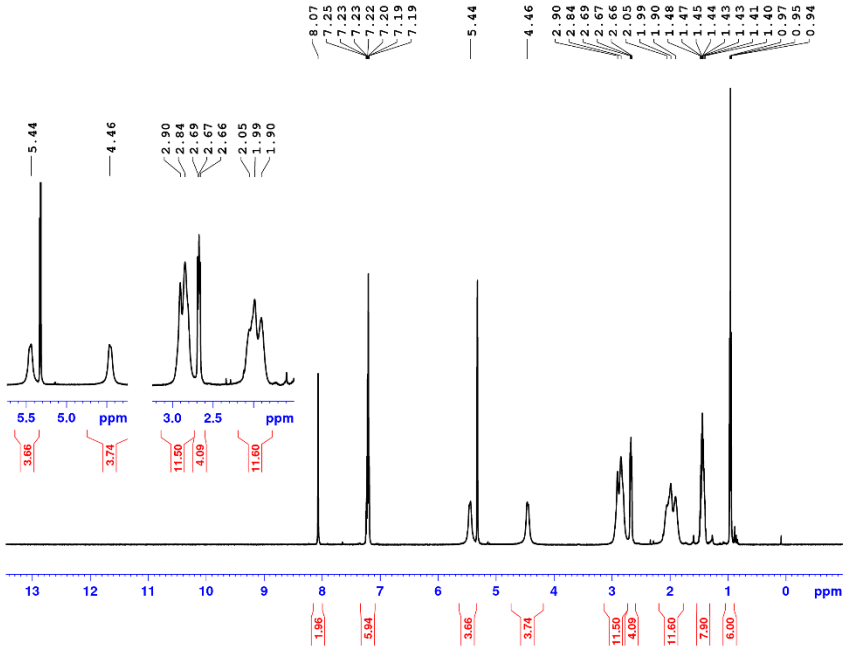

(b) $^{13}C\{^1H\}$ NMR (CD_2Cl_2, 500 MHz)

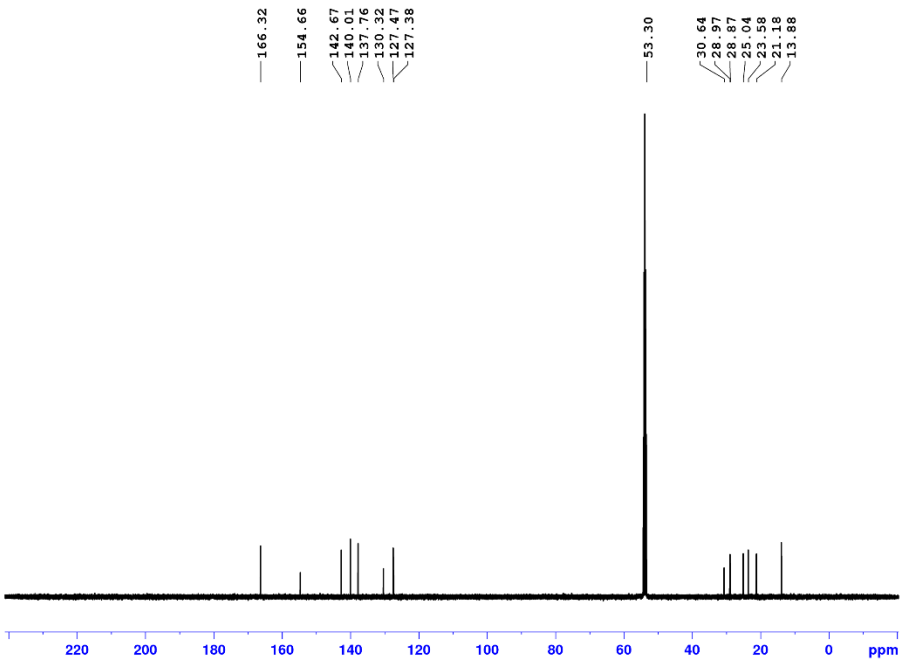

Figure 3.16, continued.

(c) ^{1}H COSY (CD_2Cl_2, 500 MHz)

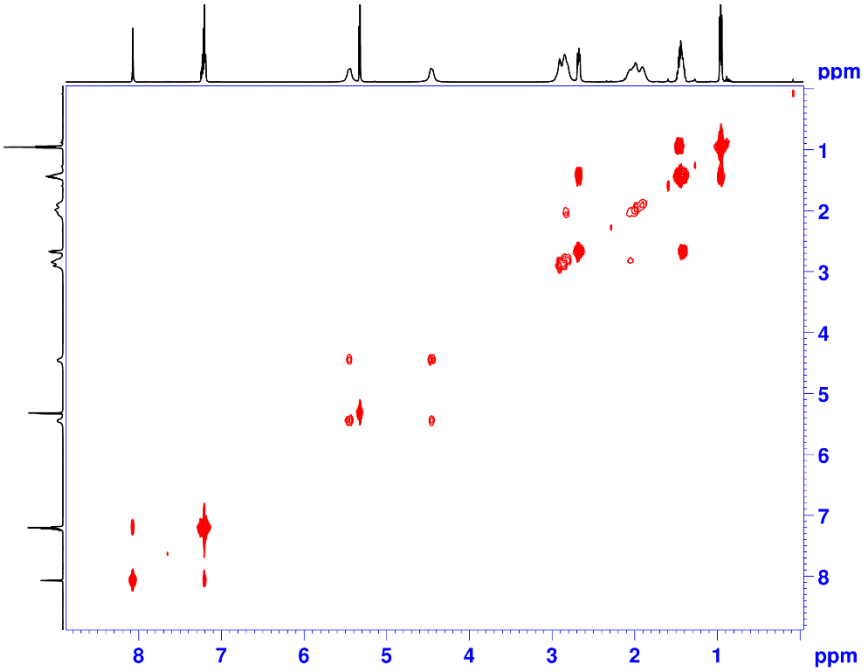

(d) ^{1}H-^{1}H NOESY (CD_2Cl_2, 500 MHz, 23 ºC)

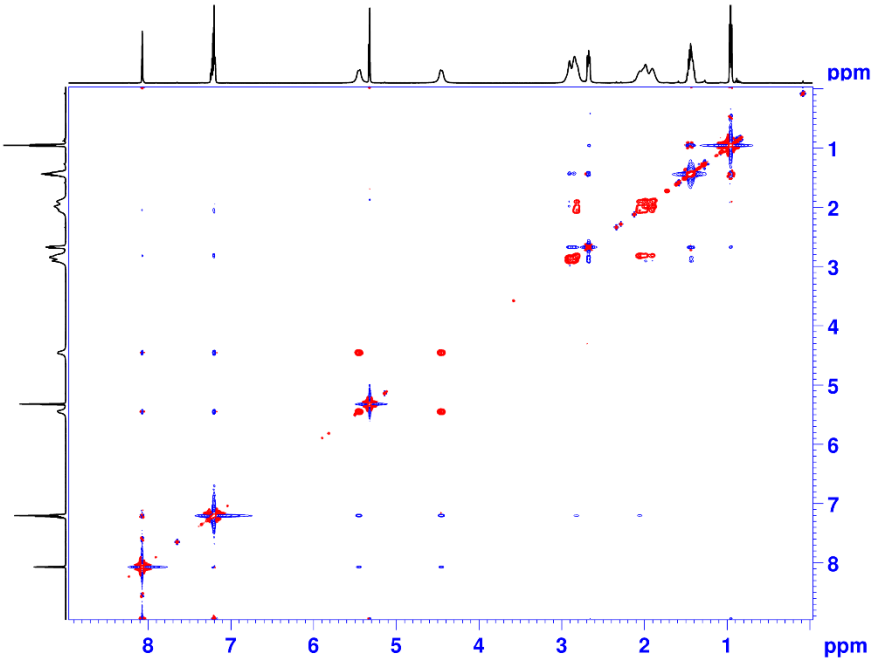

Figure 3.16, continued.

(e) Expansion of ^{1}H-^{1}H NOESY of (CD_2Cl_2, 500 MHz, 23 ºC) (δ 3.0 – 1.0)

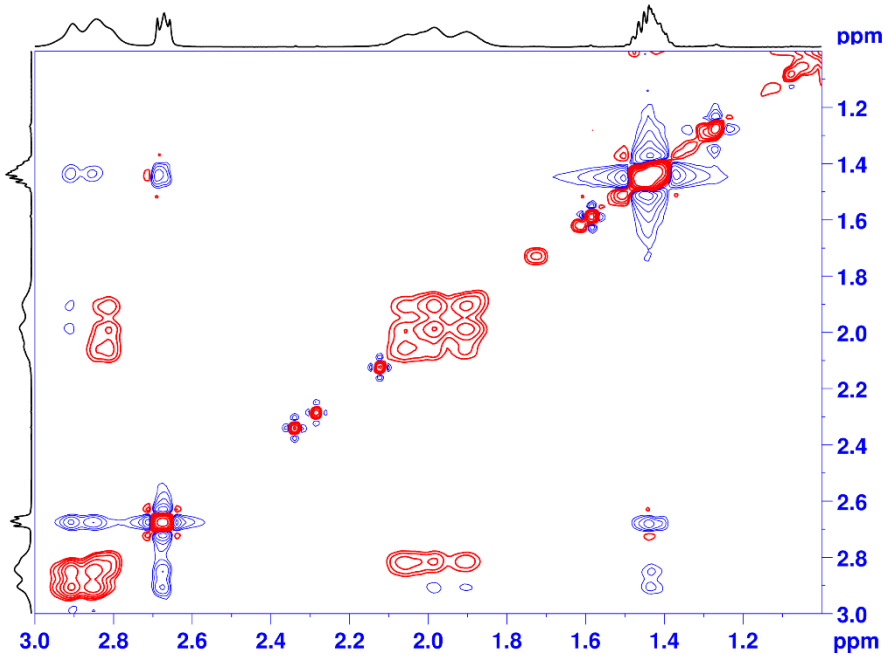

(f) ^{1}H-^{13}C HSQC (CD_2Cl_2, 500 MHz, 23 ºC)

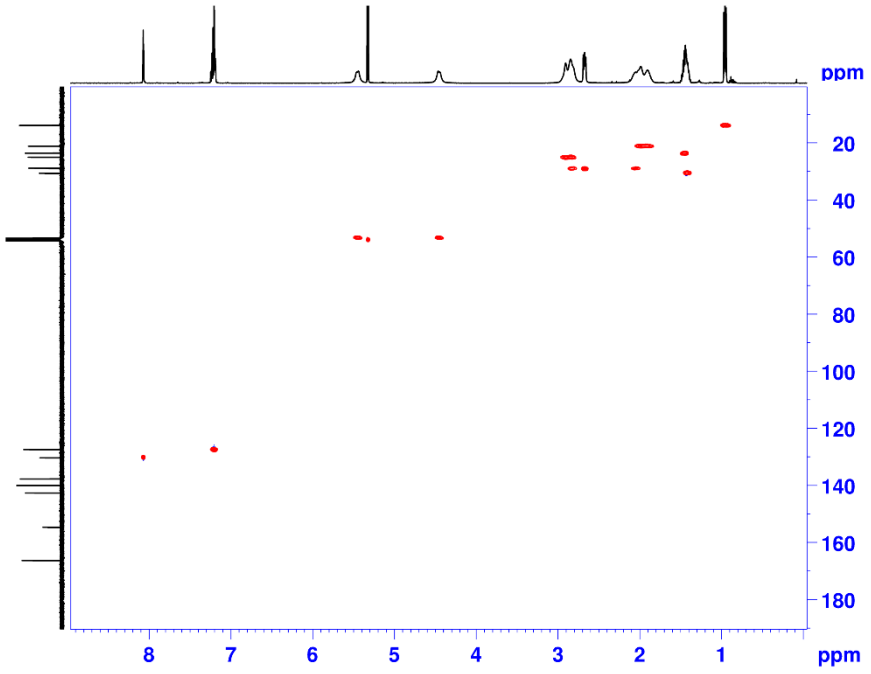

Figure 3.16, continued.

(g) Expansion of ^{1}H-^{13}C HSQC (CD_2Cl_2, 500 MHz, 23 ºC) (δ 6.0 – 3.5, δ 56 – 50)

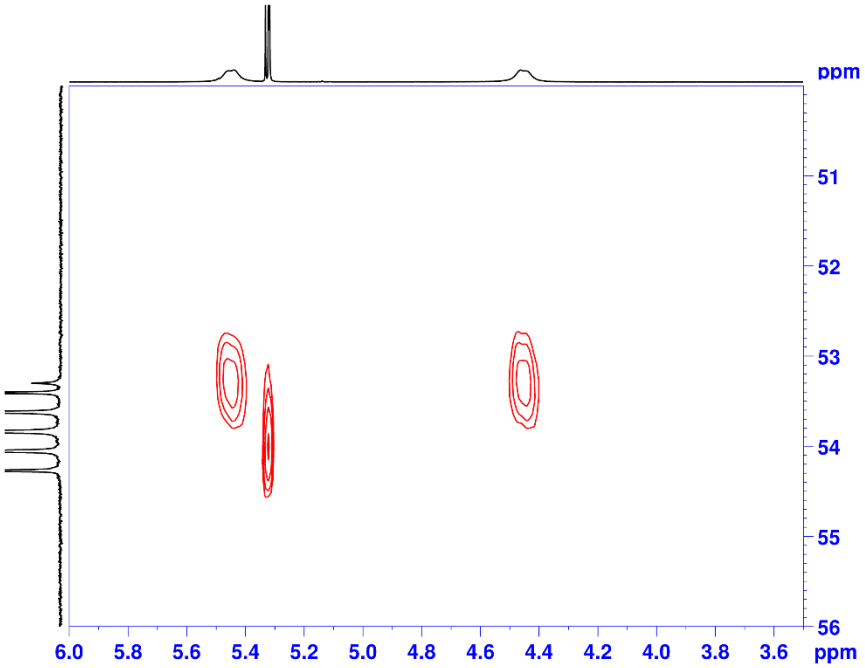

(h) Expansion of ^{1}H-^{13}C HSQC (CD_2Cl_2, 500 MHz, 23 ºC) (δ 3.2 – 1.7, δ 32 – 20)

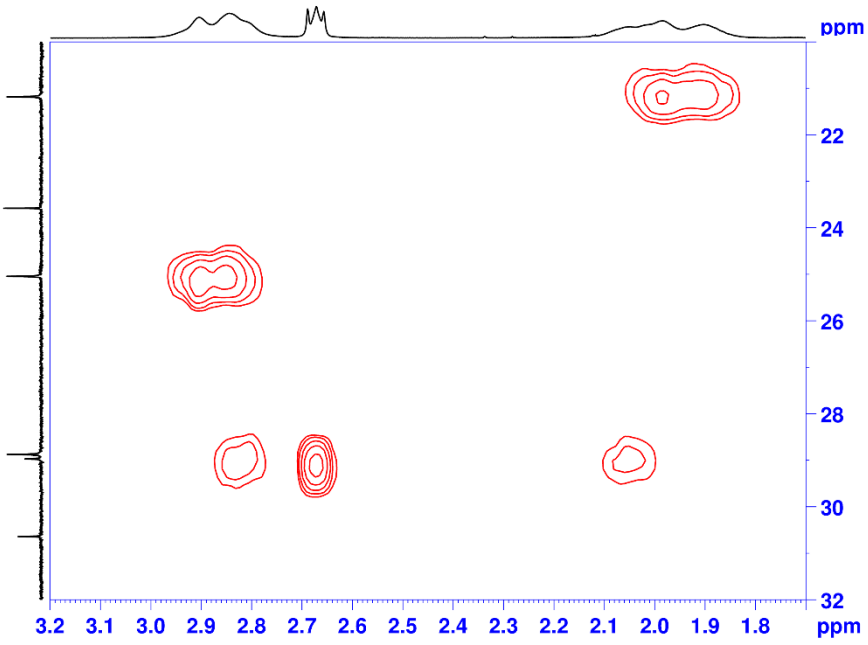

Figure 3.16, continued.

(i) ^{1}H-^{13}C HMBC (CD_2Cl_2, 500 MHz, 23 ºC)

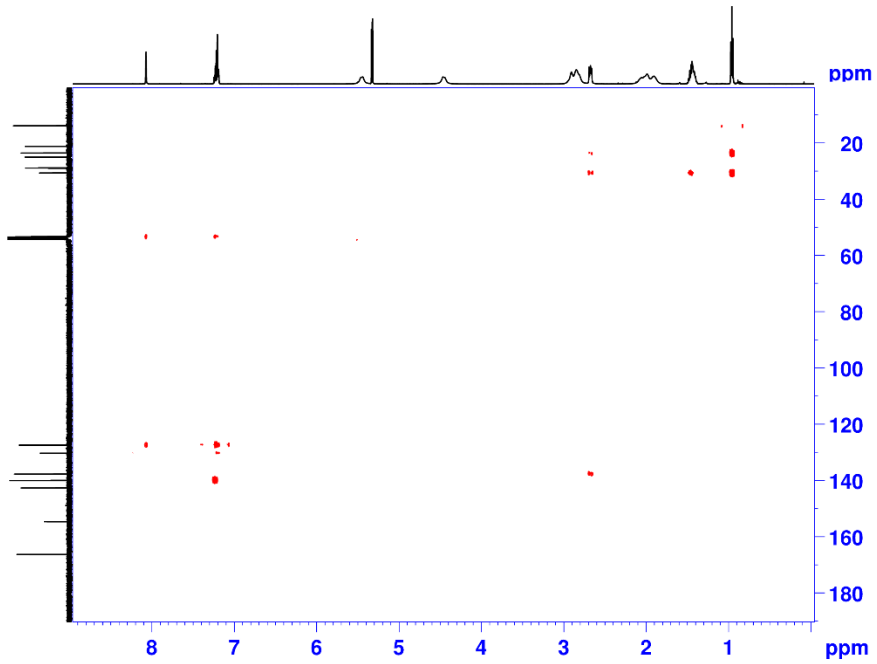

(j) VT NMR ($CDCl_2CDCl_2$, 400 MHz, 295 K to 390 K)

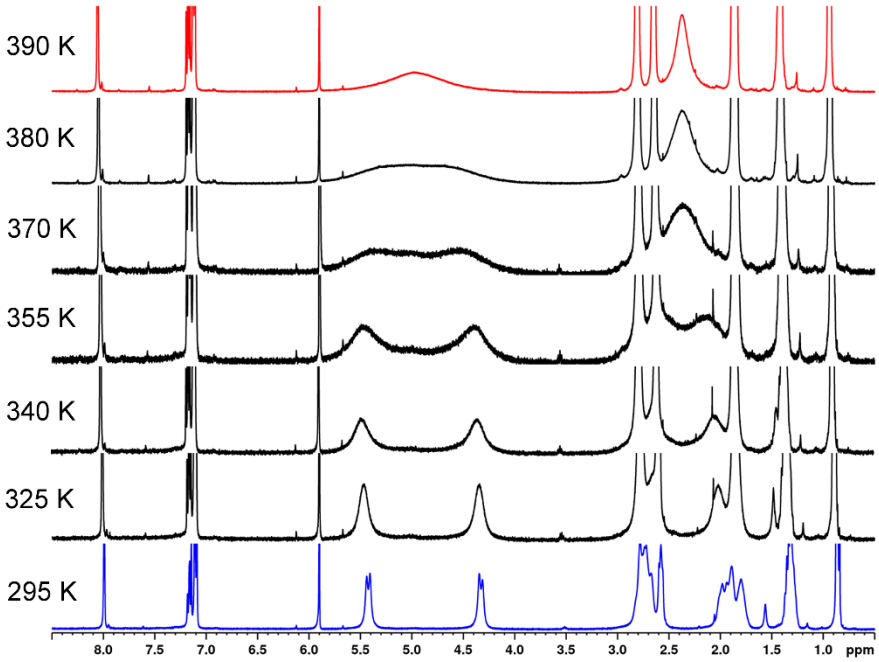

NMR Assignment Rationale for (2)Zn_2Cl_4. Based on the X-ray structure and the COSY spectrum, there are four independent *J*-coupled systems: the aromatic hydrogens of the *m*-xylylene linker (H_c, H_d, H_e), the benzylic hydrogens (H_a, H_b), the three methylene groups of the octrahydroacridine backbone (H_e, H_g, H_h, H_i, H_j, H_k), and the butyl tail (H_l, H_m, H_n, H_o).

*Butyl Tail***:** The assignments for the butyl tail are straight-forward based on chemical shifts and multiplicities.

H_l: δ 2.67

H_m : δ 1.44

H_n: δ 1.44

H_o : δ 0.96

m-Xylylene linker Hydrogens: In proligand **2'**, all of the *m*-xylylene resonances overlap to give a multiplet at δ 7.25. In (**2**)Zn_2Cl_4, 4 of those 6 resonances overlapped at δ 7.22, and singlet with an integral of 2H appears at δ 8.07. H_c is expected to give rise to a singlet, as *meta* and *para* couplings are small.

H_b δ: 8.07

H_c, H_d δ: 7.22

Benzylic Hydrogens: Two broad doublets are seen with a total integration of 8H. Therefore, the benzylic hydrogens are inequivalent on the NMR time scale, resulting in a AB spin system. In $CDCl_2CDCl_2$, the doublet peaks are well resolved but still broad with a coupling of $^2J_{HH}$ = 12 Hz.

H_a, H_b δ: 5.43, 4.33

Octahydroacridine Backbone Hydrogens: Based on the X-ray structure, the protons in each

methylene group of the octahydroacridine backbone are inequivalent. Two broad signals at δ 2.84 and δ 1.98, each with an integral of 12H, are observed. HSQC shows that the protons at δ 2.84 are correlated to the carbon signals at δ 25.0 and δ 28.8. The protons at δ 1.98 are correlated to the carbon signals at δ 21.2 and δ 28.8. This suggests that the H_k and H_j are inequivalent and overlap with the resonances that correspond to H_f and H_g, and H_h and H_i. In the ^1H-^1H NOESY spectra there is a correlation between H_l, which are attached to the carbon bonded to the pyridine ring, and the broad signal at δ 2.84: therefore, it is H_f, H_g. Only H_j and H_k are within NOE contact with H_c, H_c, and H_d as the other two methylene groups are too far away to be in NOE contact (>5 Å).

H_e, H_e',H_g' δ: 2.84

H_f, H_f',H_g δ: 1.98

VT NMR Analysis of (2)Zn_2Cl_4. Spectra of a 32 mM solution of (**2**)Zn_2Cl_4 in dry degassed $CDCl_2CDCl_2$ in a J. Young tube were recorded on a Bruker Advance 400 MHz NMR over the temperature range of 295 K to 390 K. The sample was equilibrated at each temperature for 15 minutes prior to data collection. As the temperature increases, the benzylic resonances δ 5.45 and 4.34 broaden and coalesce. The estimated rate constant at coalescence for the benzylic resonances was calculated to be 970 s^{-1} using $k_c = 2.22\sqrt{(\nu_a - \nu_b)^2 + 4J_{ab}{}^2}$. Rate constants at all temperatures were determined using iterative line fitting *via* the Exchange routine of gNMR5.0. The benzylic proton resonance at room temperature are broadened due to exchange, and therefore the natural linewidth in the absence of exchange was assumed to be that for the non-exchanging resonance at δ 8.07.

As the temperature is increased, H_f, H_g' sharpen to a broad triplet, the signal at δ 1.98 becomes a broad quintet, H_f, H_f' sharpen to a broad quintet, and a broad signal appears at δ 2.45. These multiplicities were confirmed using resolution enhancement of the proton spectrum at 370 K, confirming the assignments for these resonances made previously. Therefore, the broad resonance at δ 2.45 that appears at 370 K is due to the coalescence of H_g and H_g'. The coalescence temperature of H_g and H_g' was estimated to be 366 K with an estimated rate constant at coalescence of 666 s^{-1}.

Table 3.1. Calculated Rate Constants from Lineshape Analysis of (**2**)Zn_2Cl_4

Temperature (K)	**Calculated Rate Constant (s^{-1})**	**Uncertainty**
295	24.5	1.3
310	43.6	1.1
325	83.9	1.1
340	158	1.1
355	352	1.2
370	678	5
375	742	1
377	802	1
378	838	1
379	888	1
380	983	1
385	1210	1
390	1580	17

Figure 3.17. Eyring analysis of the benzylic hydrogen exchange in (**2**)Zn_2Cl_4.

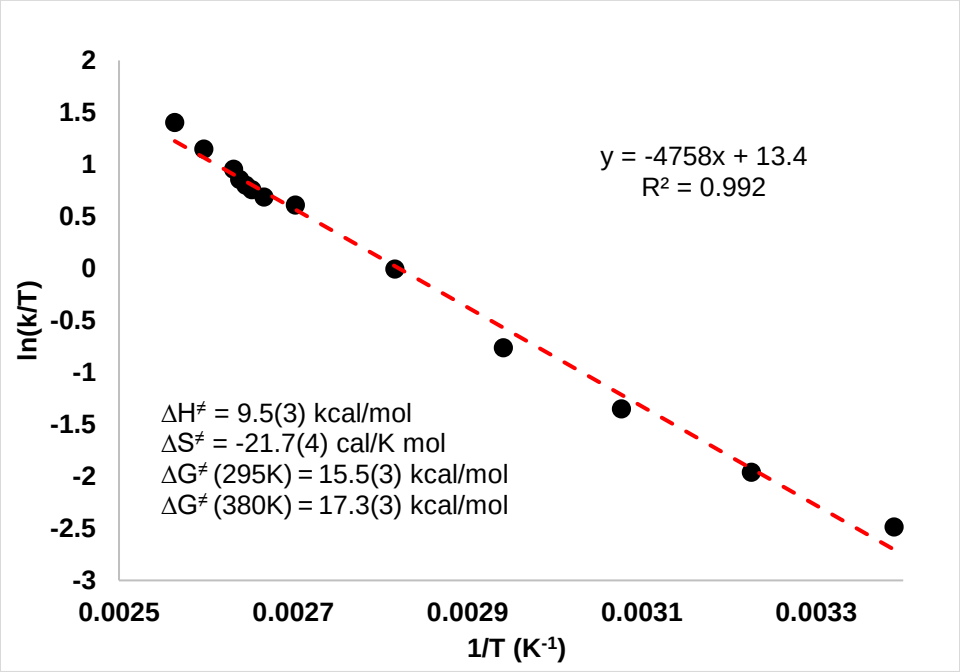

Figure 3.18. High temperature ^{1}H NMR spectra of (**2**)Zn_2Cl_4 ($CDCl_2CDCl_2$, 400 MHz, 370 K).

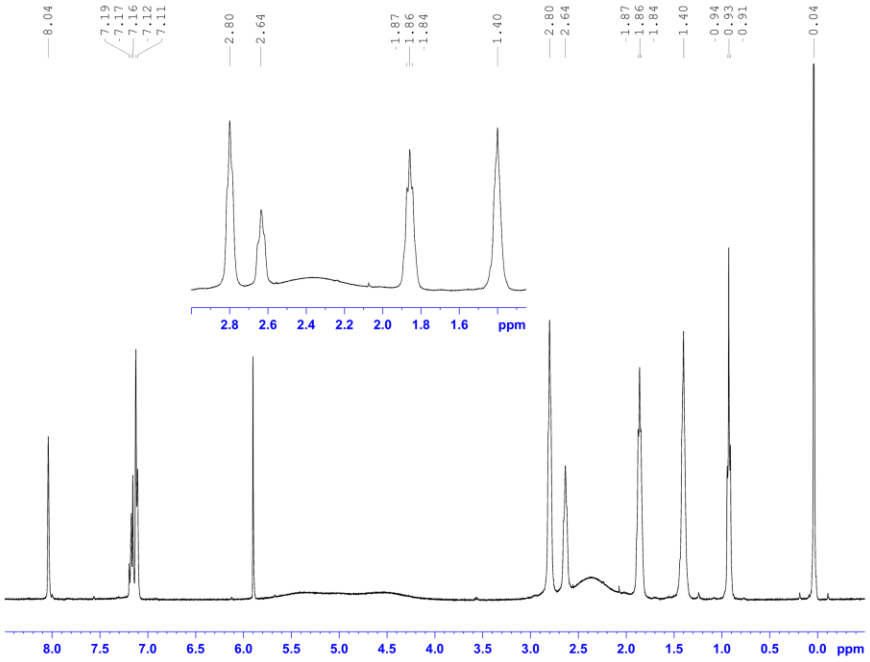

Figure 3.19. Resolution Enhanced high temperature ^{1}H NMR spectrum of (**2**)Zn_2Cl_4 ($CDCl_2CDCl_2$, 400 MHz, 370 K).

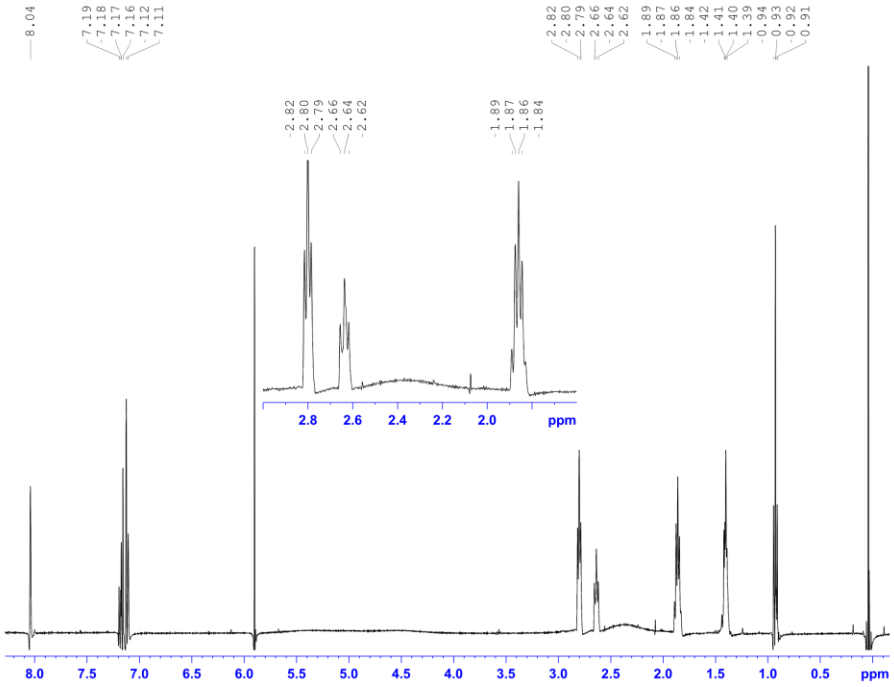

Figure 3.20. Mass spectra for (**2**)Zn_2Cl_4
(a) MALDI-TOF-TOF Spectrum for $C_{50}H_{58}N_6Zn_2Cl_3$ $[M\text{-}Cl]^+$

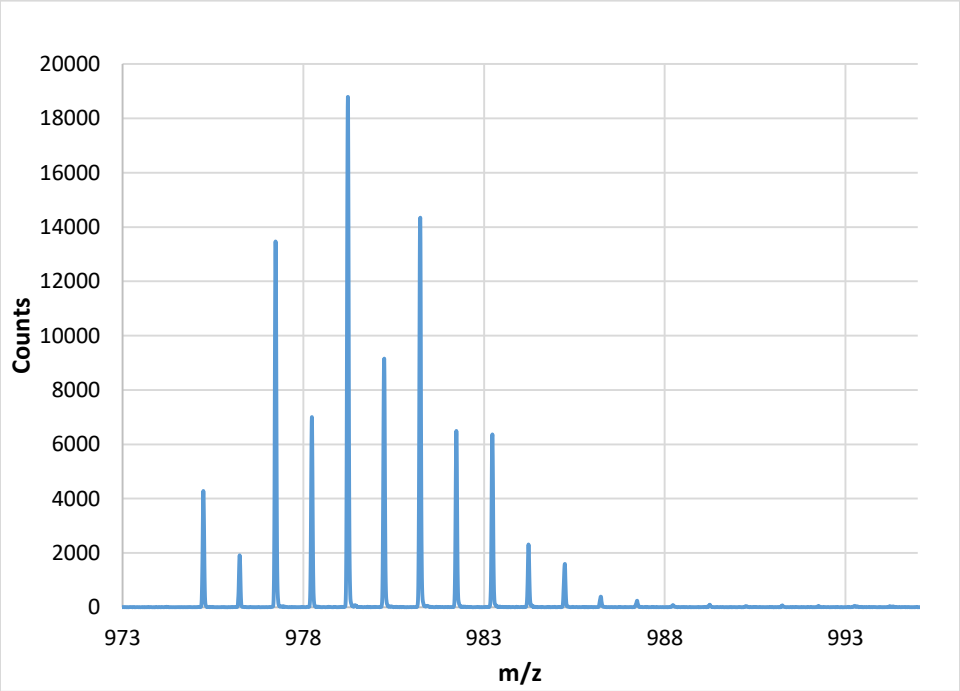

(b) HRA-MS

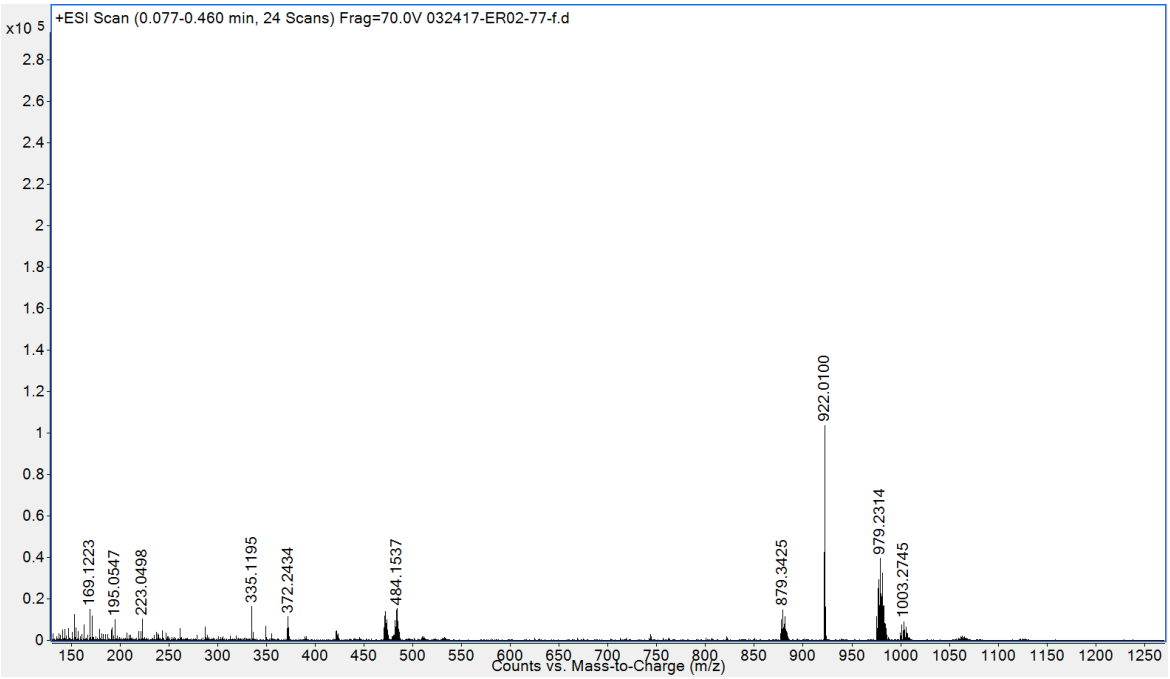

Figure 3.20, continued.

(c) Expansion of HRA-MS to show $C_{50}H_{58}N_6Zn_2Cl_3$ $[M\text{-}Cl]^+$

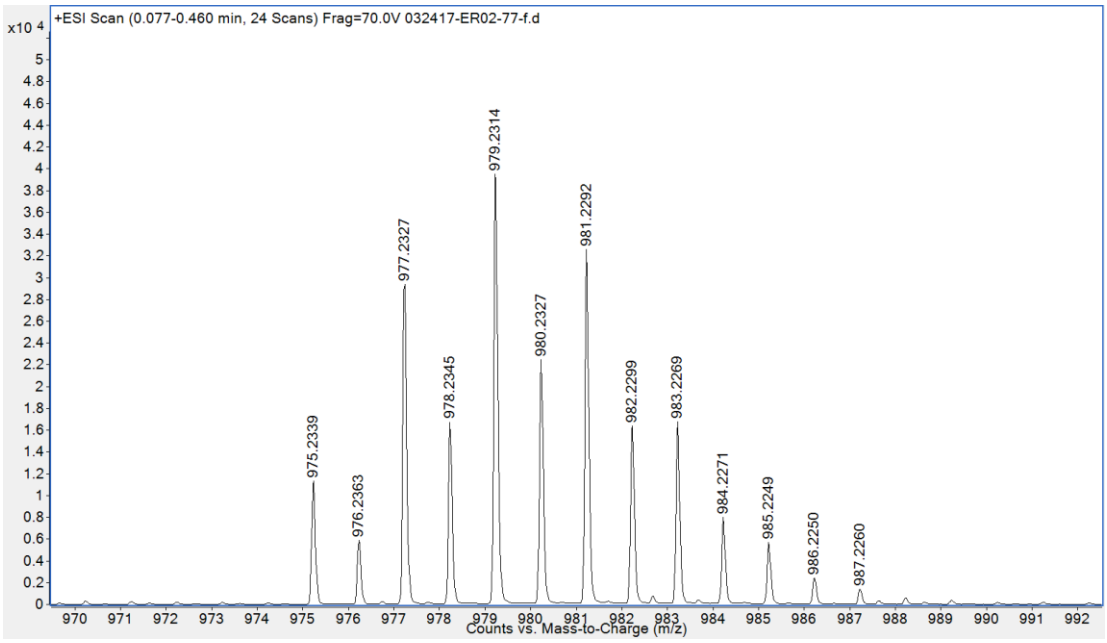

(d) Calculated Isotope Pattern for $C_{50}H_{58}N_6Zn_2Cl_3$ $[M\text{-}Cl]^+$

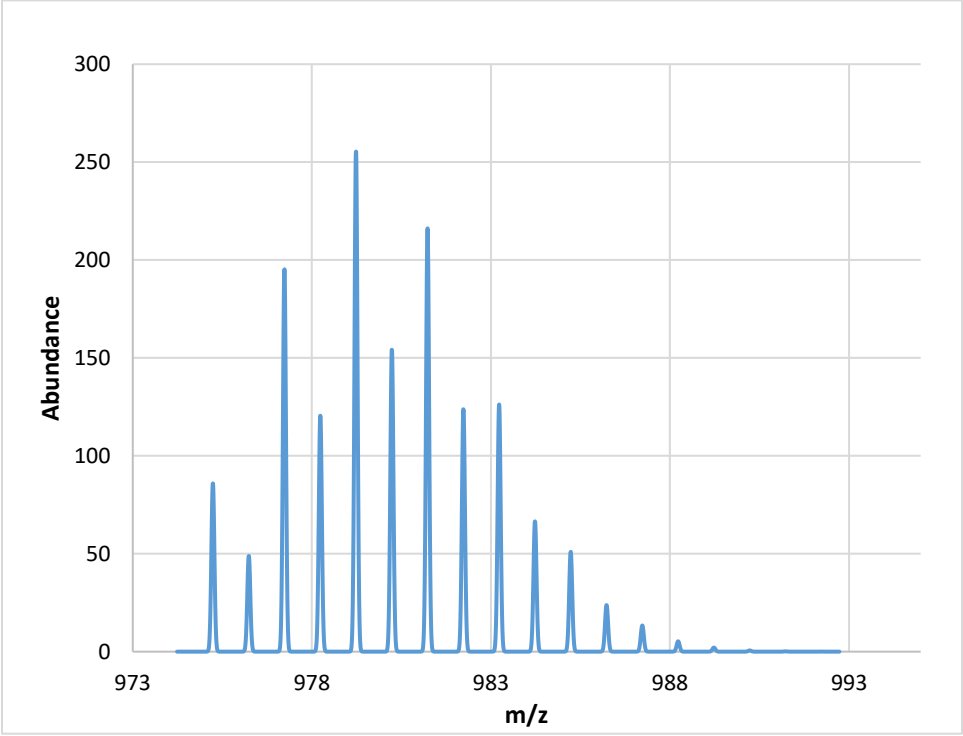

(2)Co_2Cl_4. $CoCl_2$ (140 mg, 1.08 mmol) and **2'** (400 mg, 0.538 mmol) were suspended in n-butanol (40 mL). The blue suspension was heated to 110 ºC and stirred for 16 h, resulting in a brown solution. The solvent was evaporated, the crude solid then collected and washed with THF (25 mL), and dried under vacuum to afford (**2**)Co_2Cl_4 as a light-brown solid. Yield: 400 mg, 80%. The labelling scheme for (**2**)Co_2Cl_4 is shown in Figure 3.21. ^{1}H NMR (CD_2Cl_2, 500 MHz, 23 ºC): δ 62.71 ($\nu_{1/2}$ = 700 Hz), 49.39 ($\nu_{1/2}$ = 240 Hz), 40.40 ($\nu_{1/2}$ = 180 Hz), 37.96 (s, 4H, $\nu_{1/2}$ = 37 Hz, H_l), 29.08 (s, 4H, $\nu_{1/2}$ = 40 Hz, H_m), 28.65 ($\nu_{1/2}$ = 250 Hz), 22.36 ($\nu_{1/2}$ = 120 Hz), 18.22 (s, 4H, $\nu_{1/2}$ = 24 Hz, H_m), 13.31 (s, 6H, $\nu_{1/2}$ = 17 Hz, H_o), -7.04 (s, 2H, $\nu_{1/2}$ = 20 Hz, H_e), -8.52 ($\nu_{1/2}$ = 430) Hz, -15.04 (s, 4H, $\nu_{1/2}$ = 24 Hz, H_d), -28.17 ($\nu_{1/2}$ = 120 Hz), -81.20 ($\nu_{1/2}$ = 340 Hz). IR (KBr Disk): ν(cm^{-1}) 3044.8, 2925.9, 2869.21, 1630.6, 1574.1, 1487.5, 1451.8, 1319.3, 1267.8, 1235.7, 1104.0, 1077.9, 1039.4, 1001.1, 936.5, 910.6, 848.6, 787.5, 726.9, 710.7. UV-Vis (nm, CH_2Cl_2): 664.1, 395.9. MALDI-TOF-TOF (Dithranol) (m/z): 1119.4 $[M - 3Cl + Dithranol - 2H]^+$, 965.24 $[M - Cl]^+$, 930.28 $[M - 2Cl]^+$. ESI/APCI-TOF HRA-MS (m/z): $[M\text{-}Cl]^+$ Calcd for $C_{50}H_{58}N_6Co_2Cl_3$ 965.2447; Found 965.2437. μ_{eff} (Evans Method): 6.3.

Figure 3.21. Labelling scheme for (**2**)Co_2Cl_4.

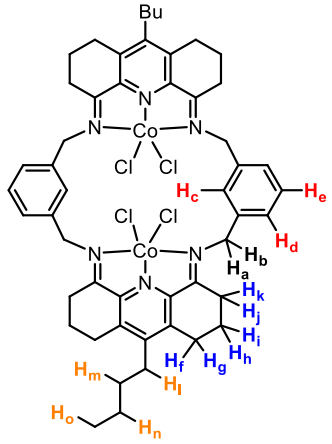

Figure 3.22. ^{1}H NMR spectrum of (**2**)Co_2Cl_4 (CD_2Cl_2, 500 MHz, 23 ºC).

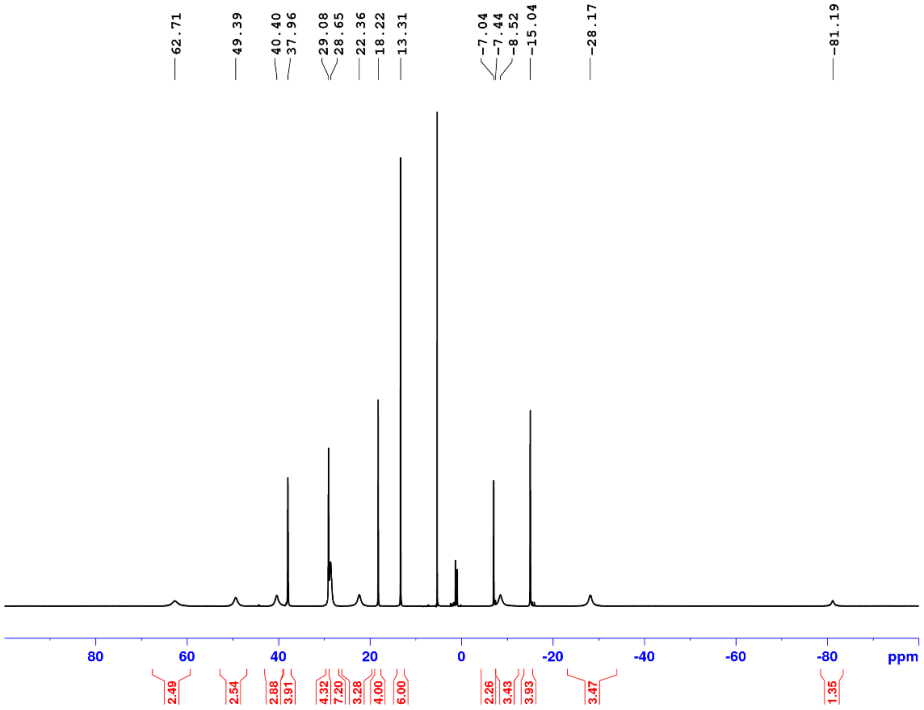

Figure 3.23. Mass spectra of (**2**)Co_2Cl_4.
(a) MALDI-TOF-TOF Spectrum for $C_{50}H_{58}N_6Co_2Cl_3$ $[M\text{-}Cl]^+$

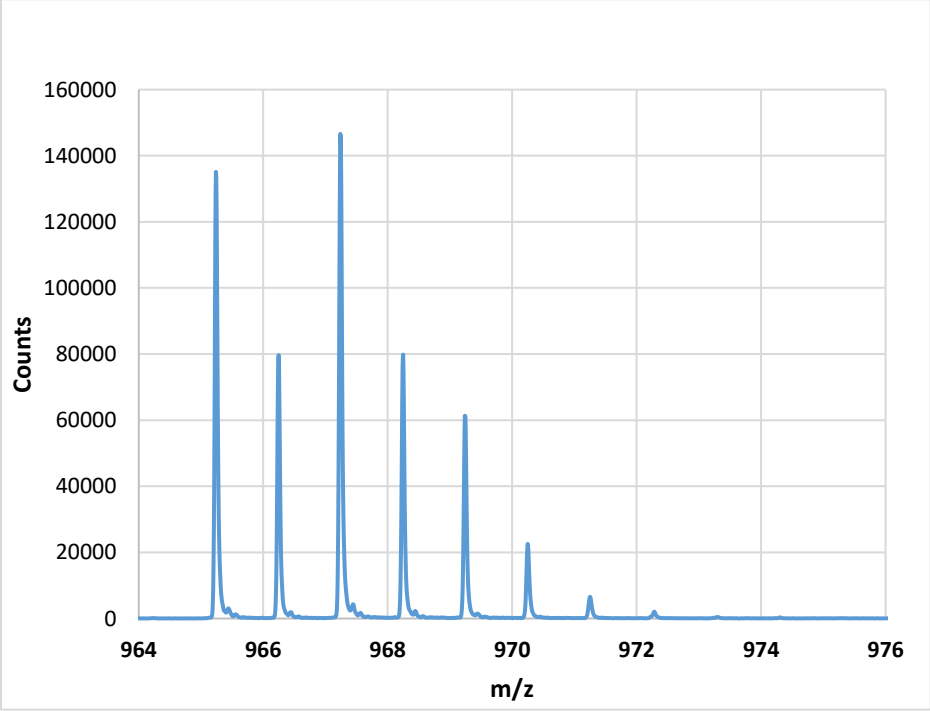

Figure 3.23, continued.

(b) HRA-MS

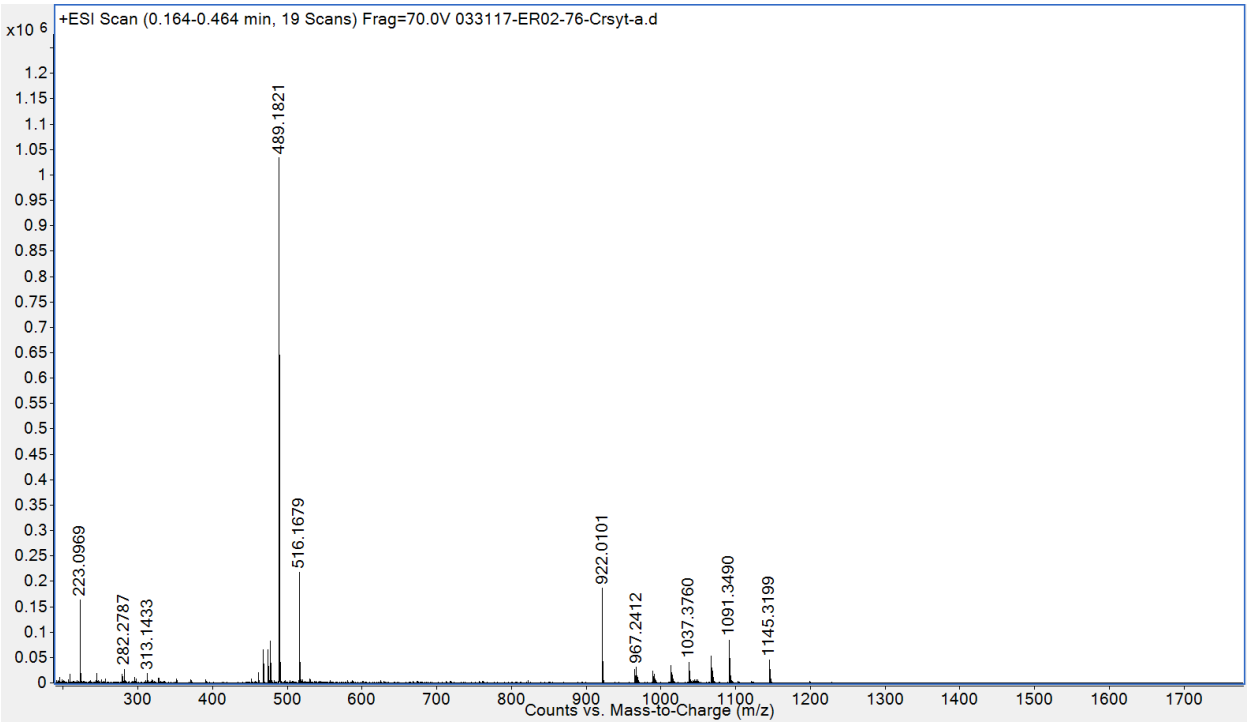

(c) Expansion of HRA-MS to show $C_{50}H_{58}N_6Co_2Cl_3$ $[M\text{-}Cl]^+$

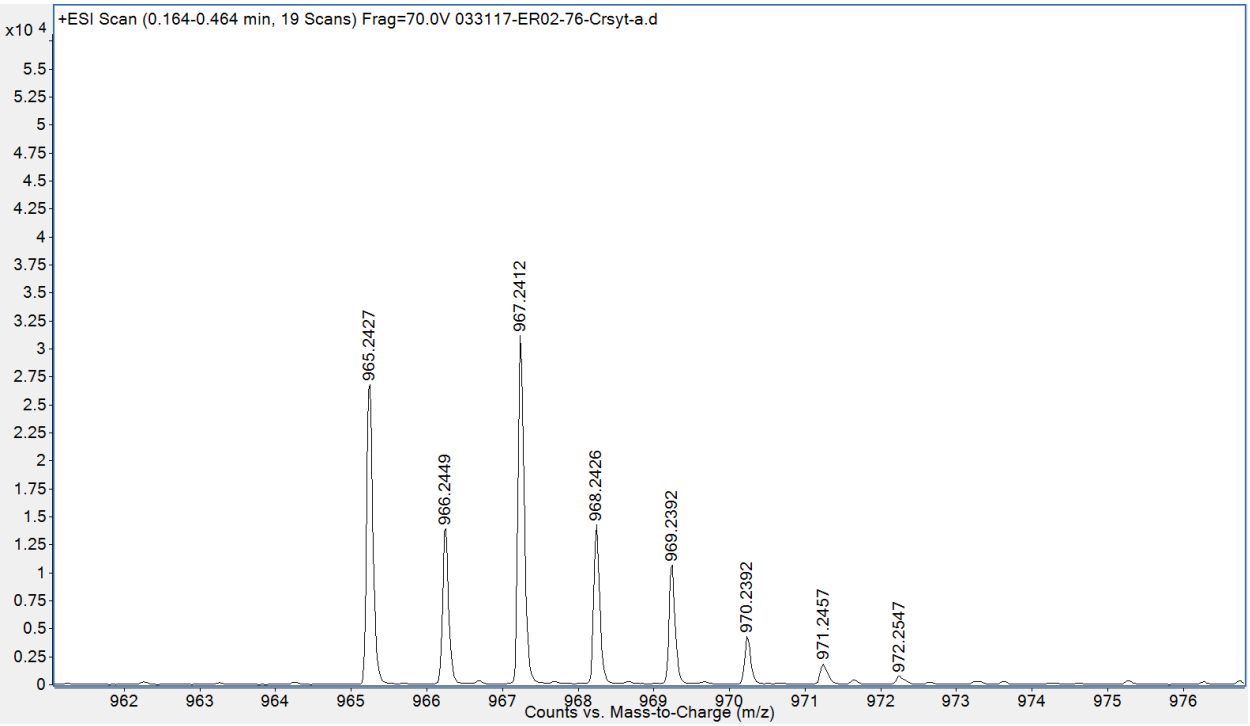

Figure 3.23, continued.

(d) Calculated Isotope Pattern for $C_{50}H_{58}N_6Co_2Cl_3$ $[M\text{-}Cl]^+$

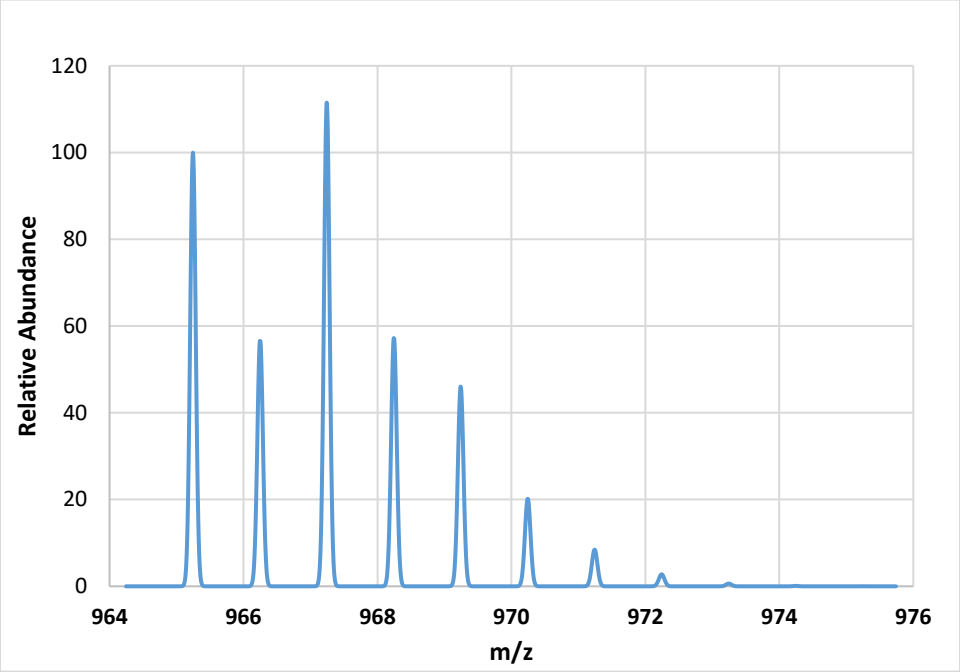

(2)Fe_2Cl_4. $FeCl_2$ (137 mg, 1.08 mmol) and **1'** (400.0 mg, 0.538 mmol) were suspended in n-butanol (40 mL). The purple suspension was heated to 110 ºC and stirred for 16 h, resulting in a dark blue solution. The solvent was evaporated, the crude solid then collected and washed with THF (25 mL), and dried under vacuum to afford (**2**)Fe_2Cl_4 as a dark purple solid. Yield: 474 mg, 88%. The labelling scheme for (**2**)Fe_2Cl_4 is shown in Figure 3.24. The benzylic hydrogens are not observed due to presumed paramagnetic broadening. ^{1}H NMR (CD_2Cl_2, 500 MHz, 23 ºC): δ 21.0 (br s, 2H, $\nu_{1/2}$ = 180 Hz, H_c), 16.6 (s, 4H, $\nu_{1/2}$ = 55 Hz), 12.1 (s, 4H, $\nu_{1/2}$ = 19 Hz, H_l), 9.5 (s, 4H, $\nu_{1/2}$ = 42 Hz), 6.7 (s, 2 H, $\nu_{1/2}$ = 12 Hz, H_e), 6.4 (s, 4H, $\nu_{1/2}$ = 19 Hz, H_m), 2.1 (s, 4H, $\nu_{1/2}$ = 18 Hz, H_n), 1.7 (s, 6H, $\nu_{1/2}$ = 12 Hz, H_o), 1.5 (s, 4H, $\nu_{1/2}$ = 22 Hz, H_d), -4.9 (s, 4H, $\nu_{1/2}$ = 27 Hz), -20.6 (s, 4H, $\nu_{1/2}$ = 20 Hz), -24.1 (s, 4H, $\nu_{1/2}$ = 70 Hz), -55.0 (s, 4H, $\nu_{1/2}$ = 110 Hz). IR (KBr Disk): ν(cm^{-1}) 3048.8, 2953.2, 2930.2, 2868.6, 1625.8, 1572.8, 1487.3, 1452.8, 1426.1, 1377.1, 1320.4, 1283.9,

1270.2, 1236.5, 1199.3, 1149.3, 1102.4, 1076.9, 1039.7, 1001.8, 967.6, 929.5, 912.3, 876.3, 849.3, 786.5, 728.9, 708.8, 650.6, 622.7, 598.7. UV-Vis (nm, CH_2Cl_2): 612.1, 330.0. MALDI-TOF-TOF (Dithranol) (m/z): 1119.4 $[M - 3Cl + Dithranol - 2H]^+$, 965.24 $[M - Cl]^+$, 930.28 $[M - 2Cl]^+$. ESI/APCI-TOF HRA-MS (m/z): $[M\text{-}Cl]^+$ Calcd for $C_{50}H_{58}N_6Fe_2Cl_3$ 995.2580; Found: 995.2550. μ_{eff} (Evans Method): 6.7.

Figure 3.24. Labelling scheme for (**2**)Fe_2Cl_4.

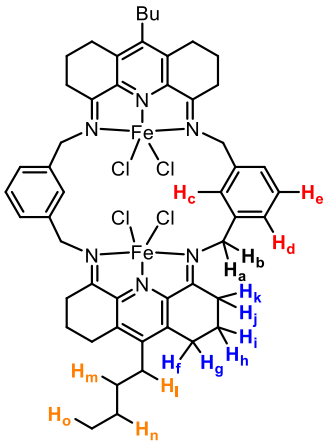

Figure 3.25. ^{1}H NMR spectrum of (**2**)Fe_2Cl_4 (CD_2Cl_2, 500 MHz, 23 ºC).

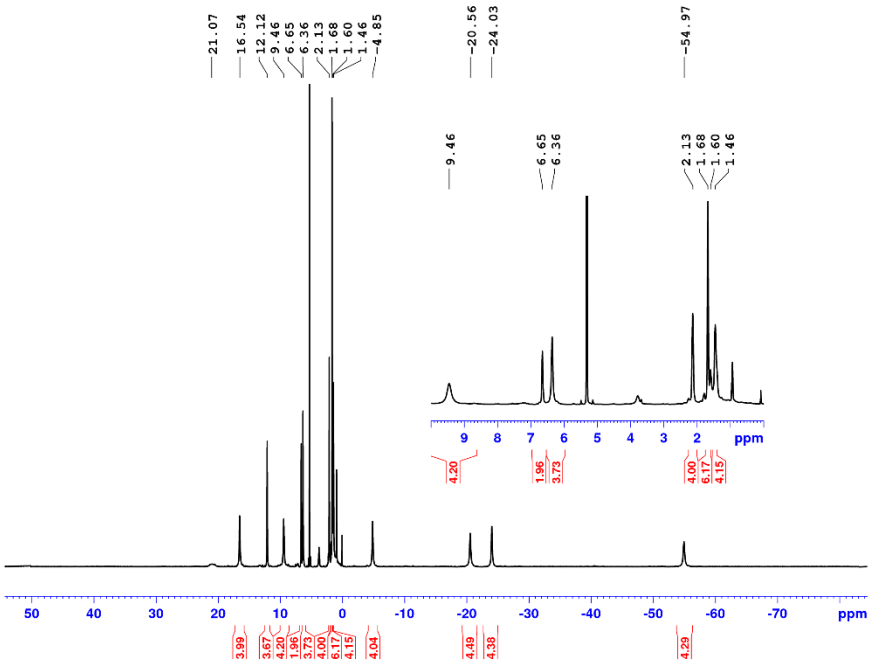

Figure 3.26. Mass spectra of (**2**)Fe_2Cl_4.
(a) MALDI-TOF-TOF Spectrum for $C_{50}H_{58}N_6Fe_2Cl_3$ $[M\text{-}Cl]^+$

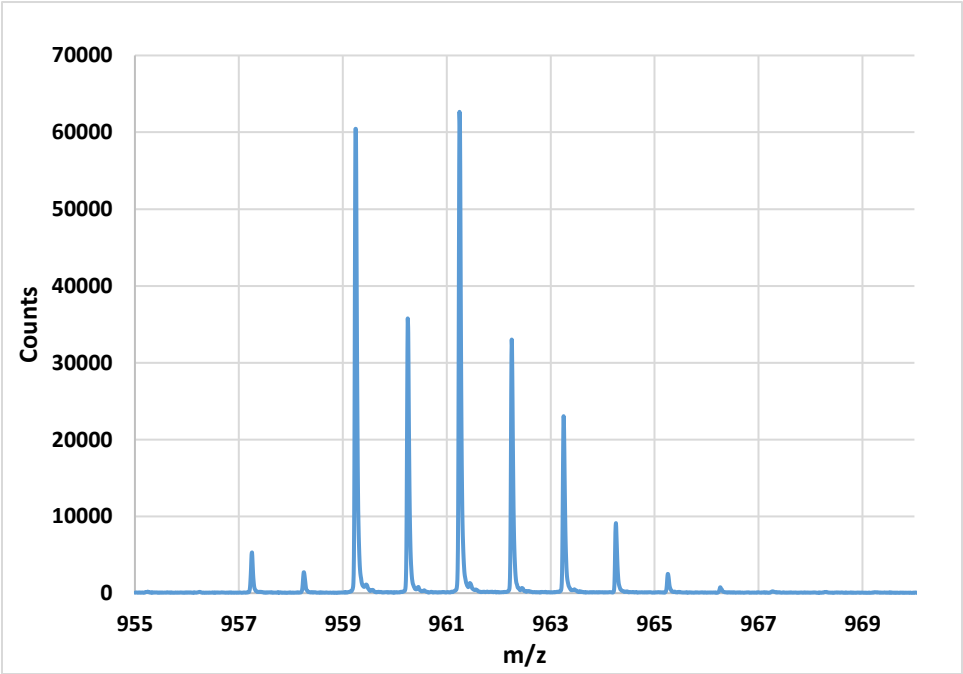

Figure 3.26, continued.

(b) HRA-MS

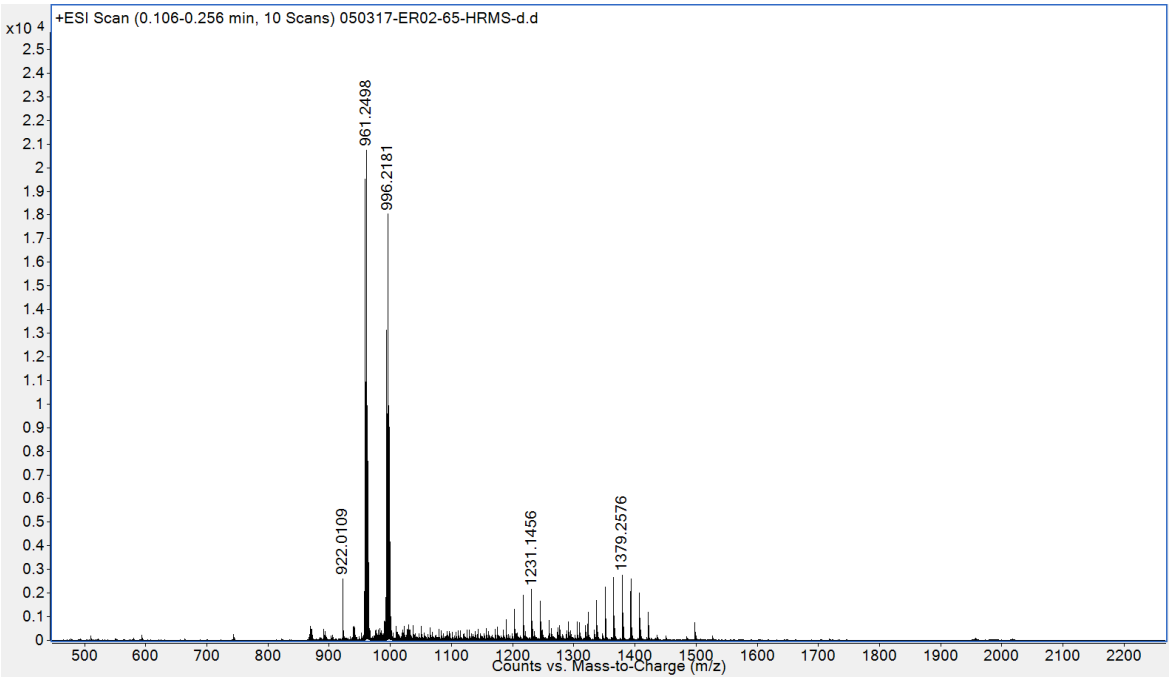

(c) Expansion of HRA-MS to show $C_{50}H_{58}N_6Fe_2Cl_3$ $[M\text{-}Cl]^+$

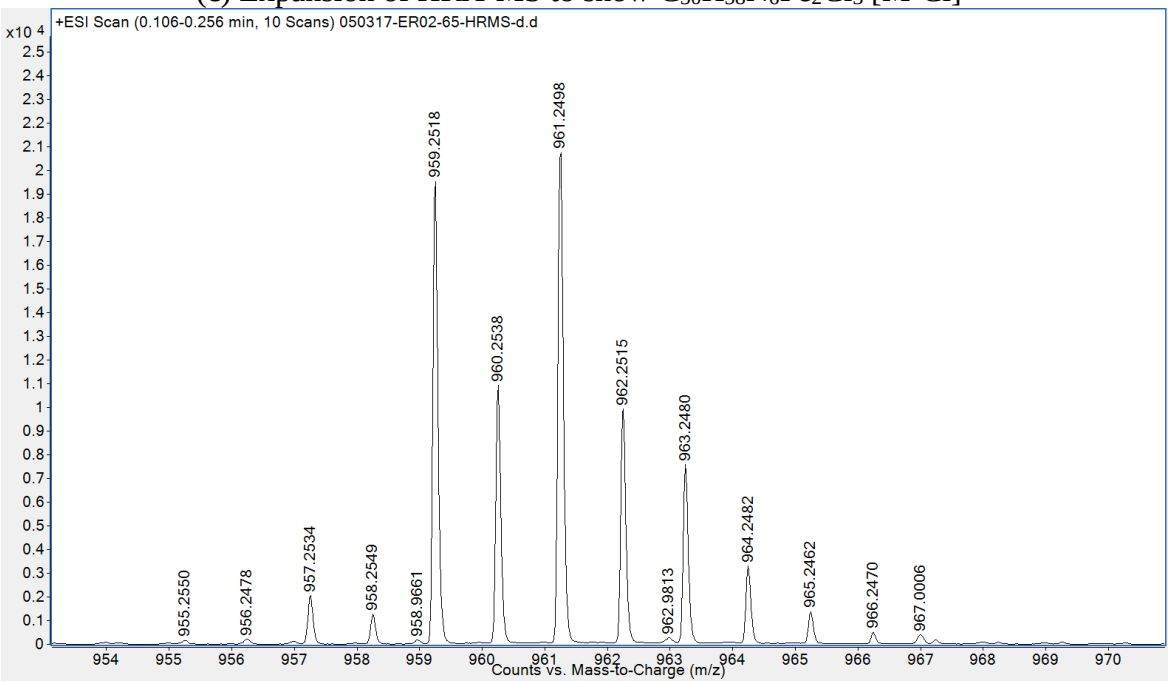

Figure 3.26, continued.

(d) Calculated Isotope Pattern for $C_{50}H_{58}N_6Fe_2Cl_3$ $[M\text{-}Cl]^+$

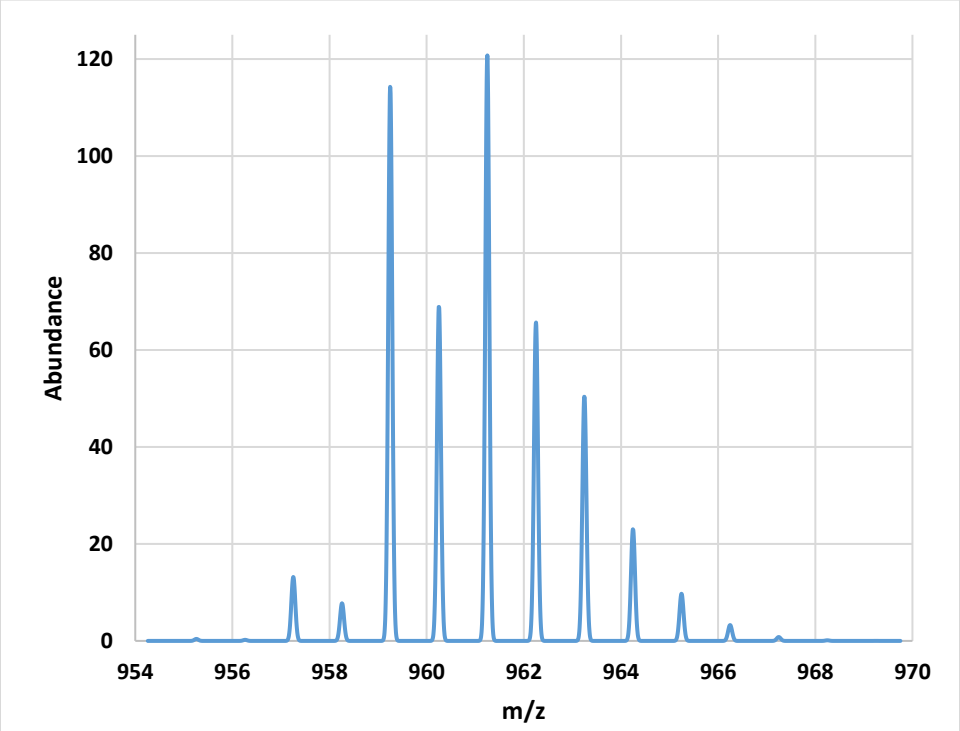

[(2)Pd_2Br_2][$BAr^F{}_4$]$_2$. $PdBr_2$ (447.4 mg, 1.76 mmol) and **2'** (333.2 mg, 0.44 mmol) was suspended in acetonitrile (40 mL). The orange suspension was left to stir for 16 h. The resulting brown solid was collected and washed with 40 mL of acetonitrile. This solid was assumed to be [(**2**)Pd_2Br_2][Pd_2Br_6]$_2$. Yield: 700 mg, 88%. [(**2**)Pd_2Br_2][Pd_2Br_6]$_2$ (100 mg, 0.55 mmol) was then suspended in CH_2Cl_2 (15 mL) and stirred rapidly. Na[$BAr^F{}_4$] (98.0 mg, 0.11 mmol) was added in one portion and the suspension was left to stir for 1 h. The resulting suspension was filtered through celite and concentrated to ca. 5 mL. The concentrate was then filtered through a 0.2 μm syringe filter and concentrated to a dark brown solid which was dried overnight under vacuum. The crude solid was triturated with Et_2O (15 mL) and the resulting light brown solid collected and dried under vacuum to yield [(**2**)Pd_2Br_2][$BAr^F{}_4$]$_2$. Yield: 80 mg, 51 %. The labelling scheme for [(**2**)Pd_2Br_2][$BAr^F{}_4$]$_2$ is shown in Figure 3.27. ^{1}H NMR (CD_2Cl_2, 500 MHz, 23 ºC): δ 8.18 (s, 2H,

H_c), 7.72 (br s, 16H, H_q), 7.56 (br s, 8H, H_p), 7.36 (t, $^3J_{HH}$ = 5 Hz, 2H, H_e), 7.22 (d, $^3J_{HH}$ = 5 Hz, 4H, H_d), 5.54 (br s, 4H, H_a), 4.69 (br s, 4H, H_b), 3.00 (br s, 4H, H_k), 2.87 (br s, 8H, H_f, H_g), 2.71 (br t, 4H, H_l), 2.60 (br s, 4H, H_j), 2.07 (br s, 8H, H_h, H_i), 1.42 (br s, 8H, H_m,H_n), 0.93 (br t, 6H, H_o). $^{13}C\{^1H\}$ NMR (CD_2Cl_2, 125 MHz): δ 184.7 (*C*=N), 162.1 (q, $^1J_{CB}$= 50 Hz, *C*-B), 156.4 (*p*-py), 149.6 (*m*-py), 143.9 (*o*-py), 135.9 (C_{xylyl}-$C_{benzylic}$), 135.2 (*C*-H_q), 129.8 (*C*-H_c), 129.2 (qq, $^2J_{CF}$ = 31 Hz, $^3J_{CB}$ = 3 Hz, *C*-CF_3), 129.0 (*C*-H_e), 125.0 (q, $^1J_{CF}$ = 270 Hz, -*C*F_3), 128.2 (*C*-H_d), 117.9 (m, *C*-H_p), 59.2 (*C*-H_a,H_b), 30.8 (*C*-H_k,H_j), 30.6 (*C*-H_m), 29.4 (*C*-H_l), 24.6 (*C*-H_f,H_g), 23.3 (*C*-H_n), 21.9 (*C*-H_h,H_i), 13.7 (*C*-H_o). $^{19}F\{^1H\}$ NMR (CD_2Cl_2, 470 MHz, 23 ºC): δ -63.3. $^{11}B\{^1H\}$ NMR (CD_2Cl_2, 400 MHz, 23 ºC): δ -6.6. IR (KBr, Disk): ν(cm^{-1}) 2965.1, 2879.0, 1653.4, 1610.2, 1569.4, 1457.2, 1355.23, 1278.4, 1121.1, 1001.1, 936.6, 886.8, 838.9, 785.7, 744.7, 712.15. ESI/APCI-TOF HRA-MS (m/z): $[M\text{-}BAr^F{}_4]^+$ Calcd for $C_{82}H_{70}BBr_2F_{24}N_6Pd_2$ 1979.1833; Found 1979.1816.

Figure 3.27. Labelling scheme for [(**2**)Pd_2Br_2][$BAr^F{}_4$]$_2$.

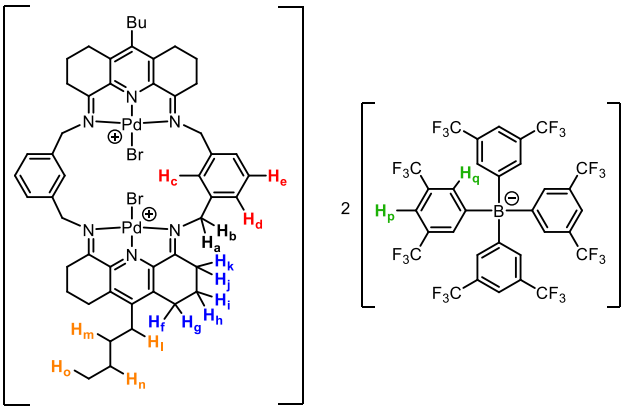

Figure 3.28. NMR spectra of [(**2**)Pd_2Br_2][$BAr^F{}_4$]$_2$.

(a) ^{1}H NMR (CD_2Cl_2, 500 MHz, 23 ºC)

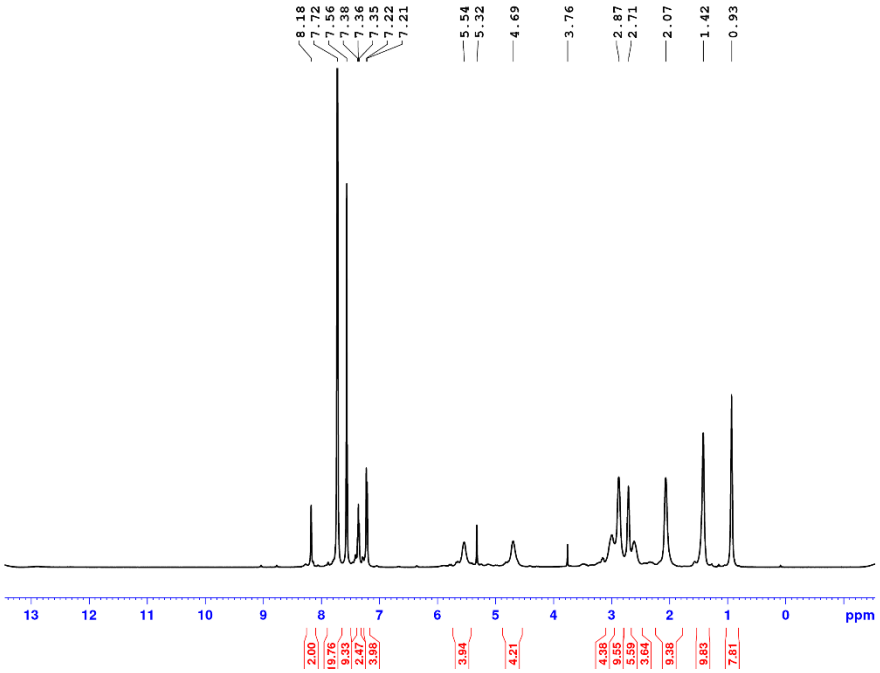

(b) ^{13}C{^{1}H} NMR (CD_2Cl_2, 126 MHz, 23 ºC)

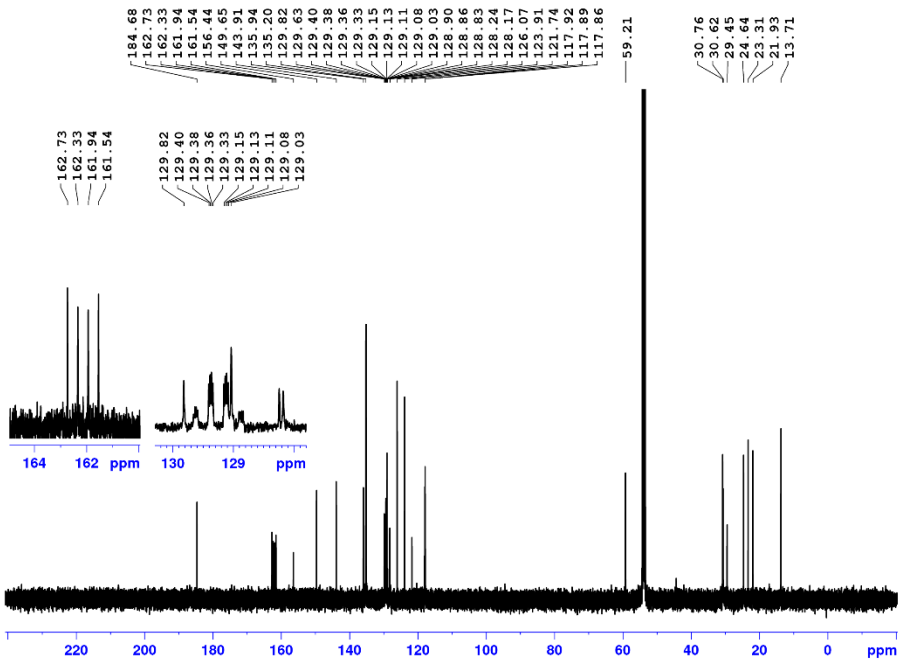

Figure 3.28, continued.

(c) $^{19}F\{^{1}H\}$ NMR (CD_2Cl_2, 470 MHz, 23 ºC)

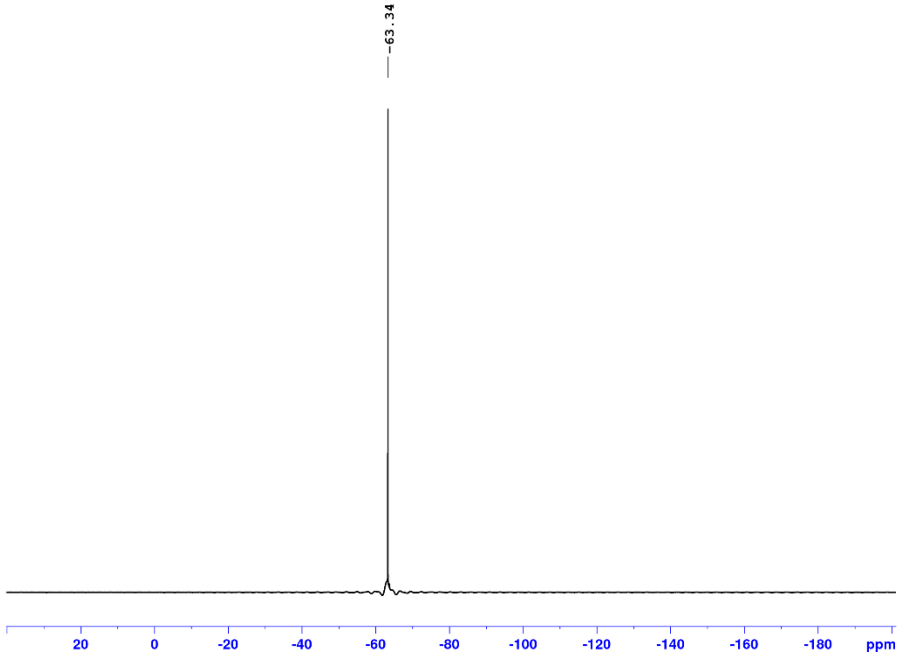

(d) $^{11}B\{^{1}H\}$ NMR (CD_2Cl_2, 160 MHz, 23 ºC)

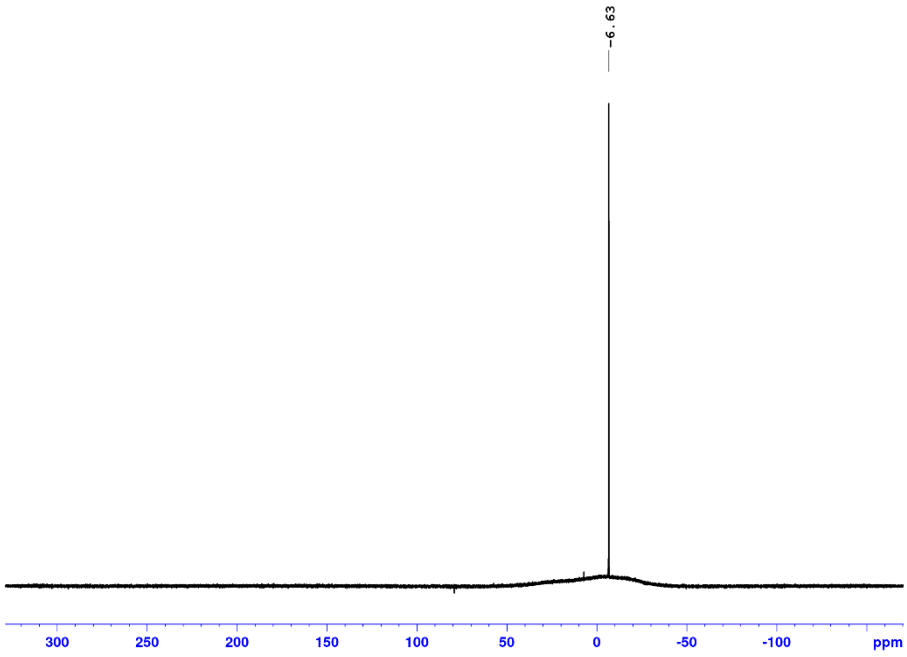

Figure 3.28, continued.

(e) ^{1}H-^{1}H COSY (CD_2Cl_2, 500 MHz, 23 ºC)

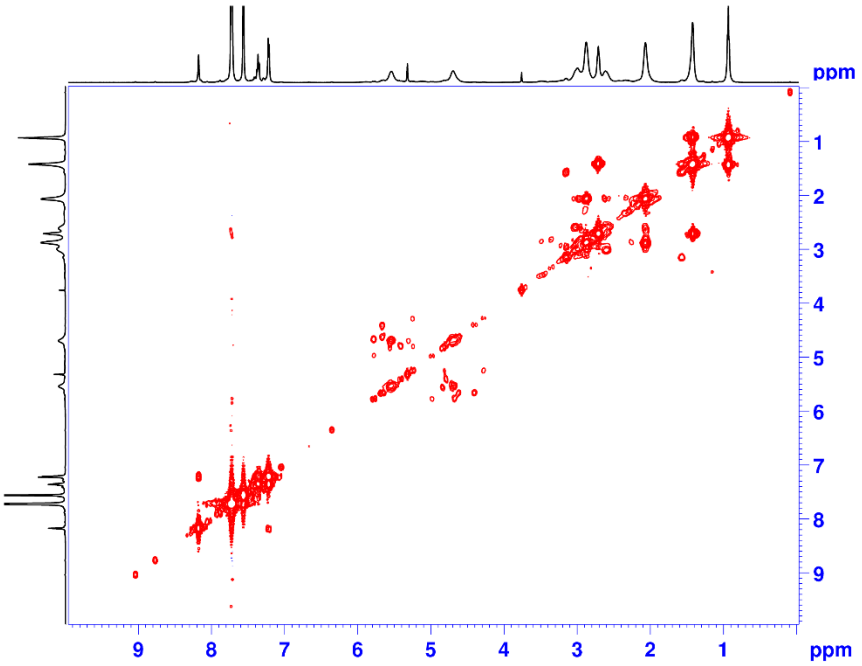

(f) ^{1}H-^{1}H NOESY of [(**2**)Pd_2Br_2][BAr^{F}_4]$_2$ (CD_2Cl_2, 500 MHz, 23 ºC)

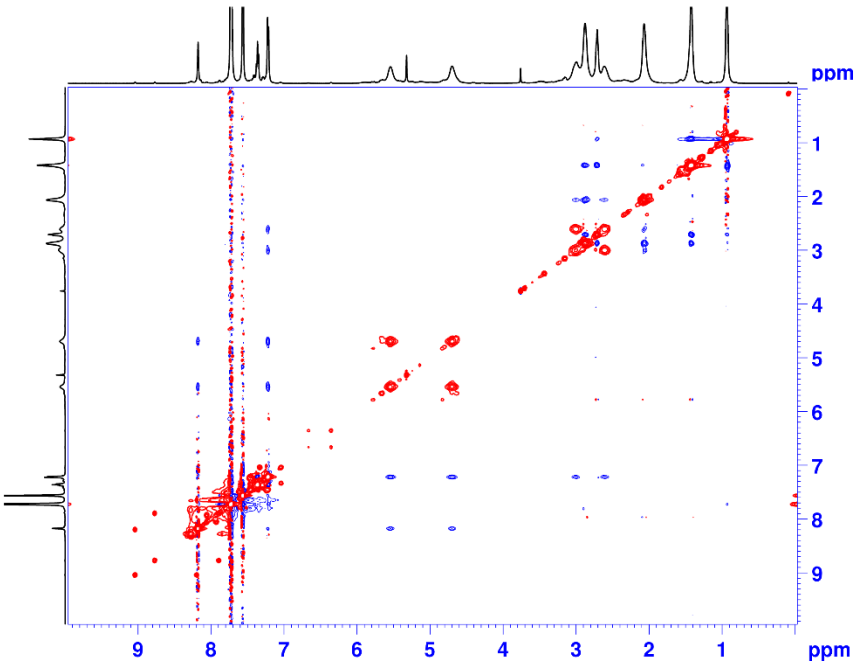

Figure 3.28, continued.

(g) ^{1}H-^{13}C HSQC (CD_2Cl_2, 500 MHz, 23 ºC)

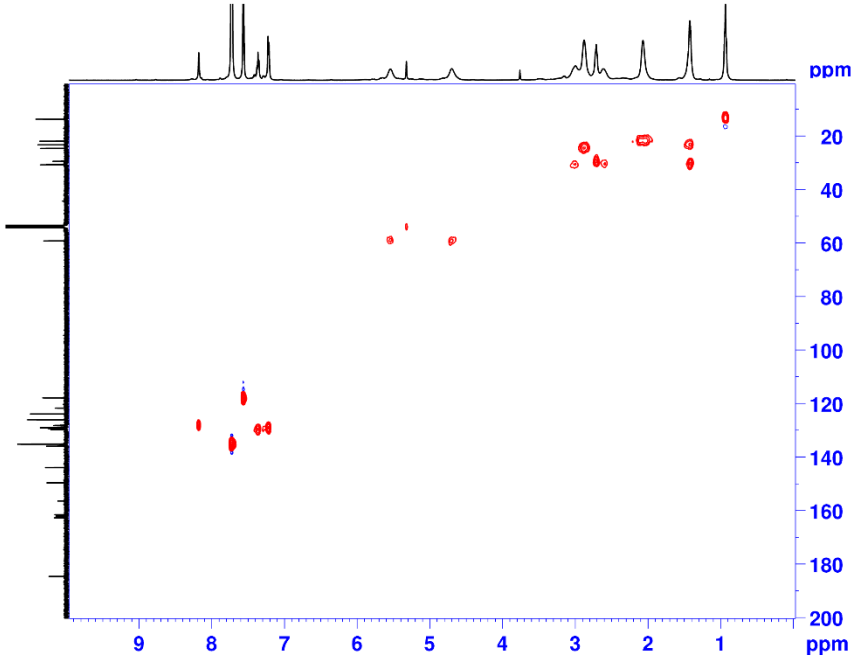

Figure 3.29. Mass spectra of [(**2**)Pd_2Br_2][$BAr^F{}_4$]$_2$
(a) HRA-MS

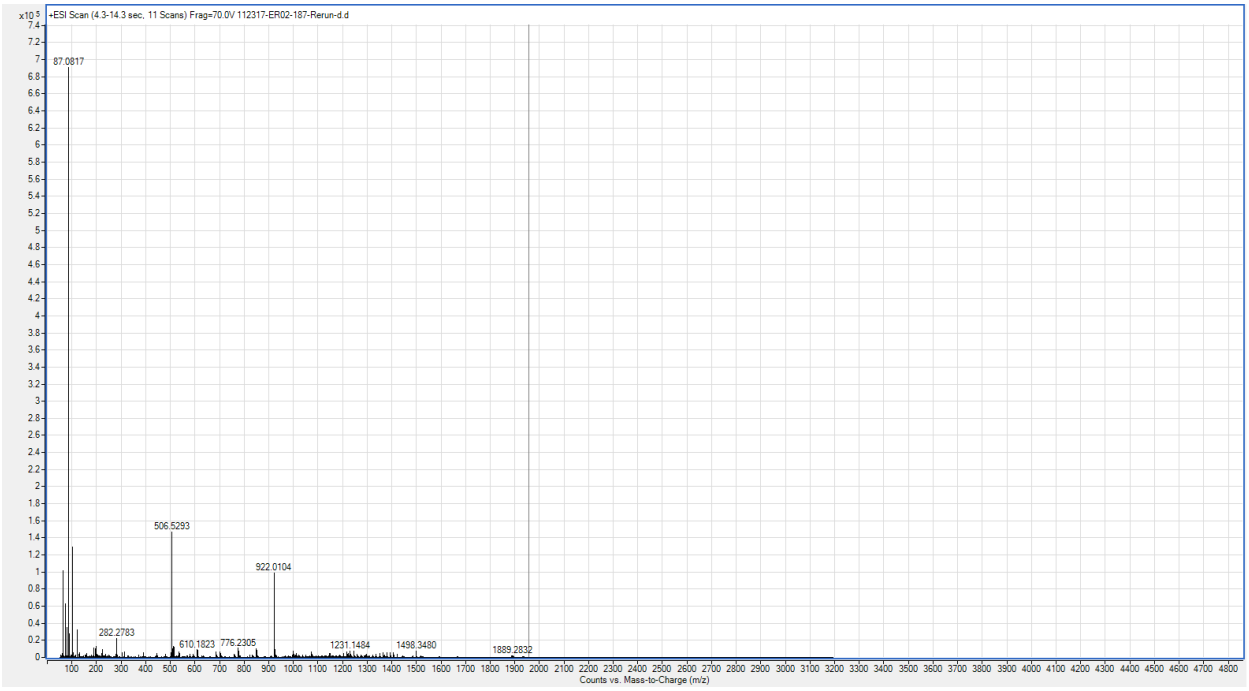

Figure 3.29, continued.

(b) Expansion of HRA-MS (m/z 1830 – 2060)

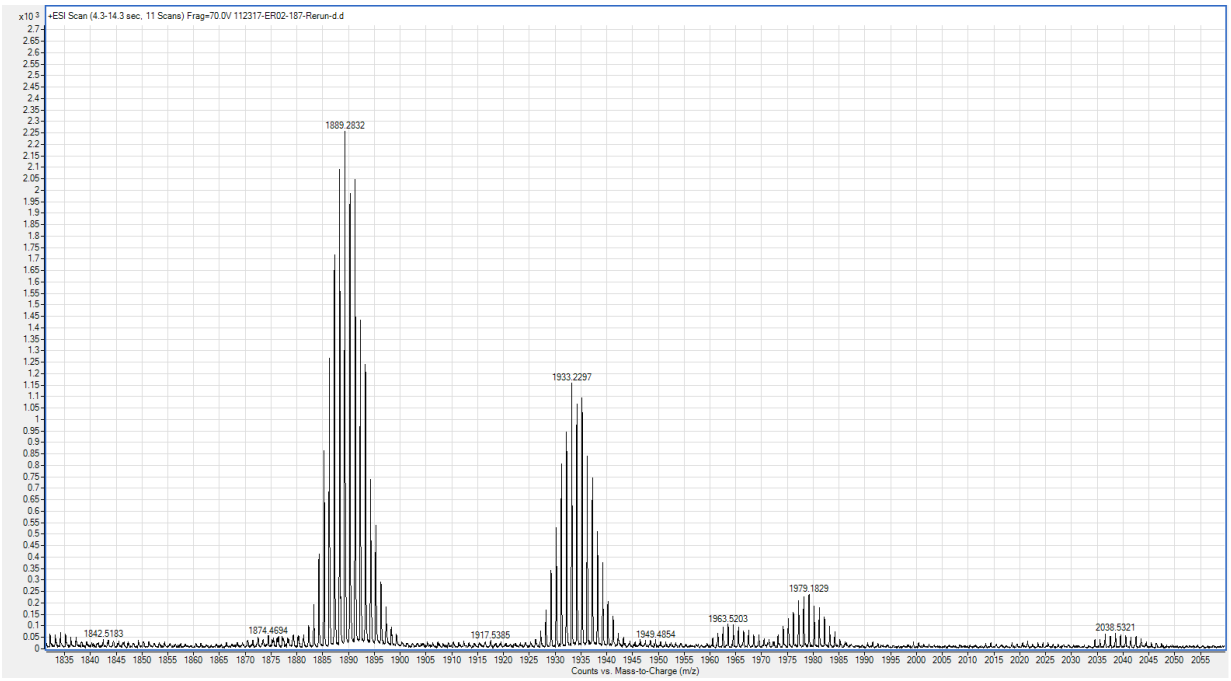

(c) Expansion of HRA-MS to show $C_{82}H_{70}BBr_2F_{24}N_6Pd_2$ $[M\text{-}BAr^F{}_4]^+$

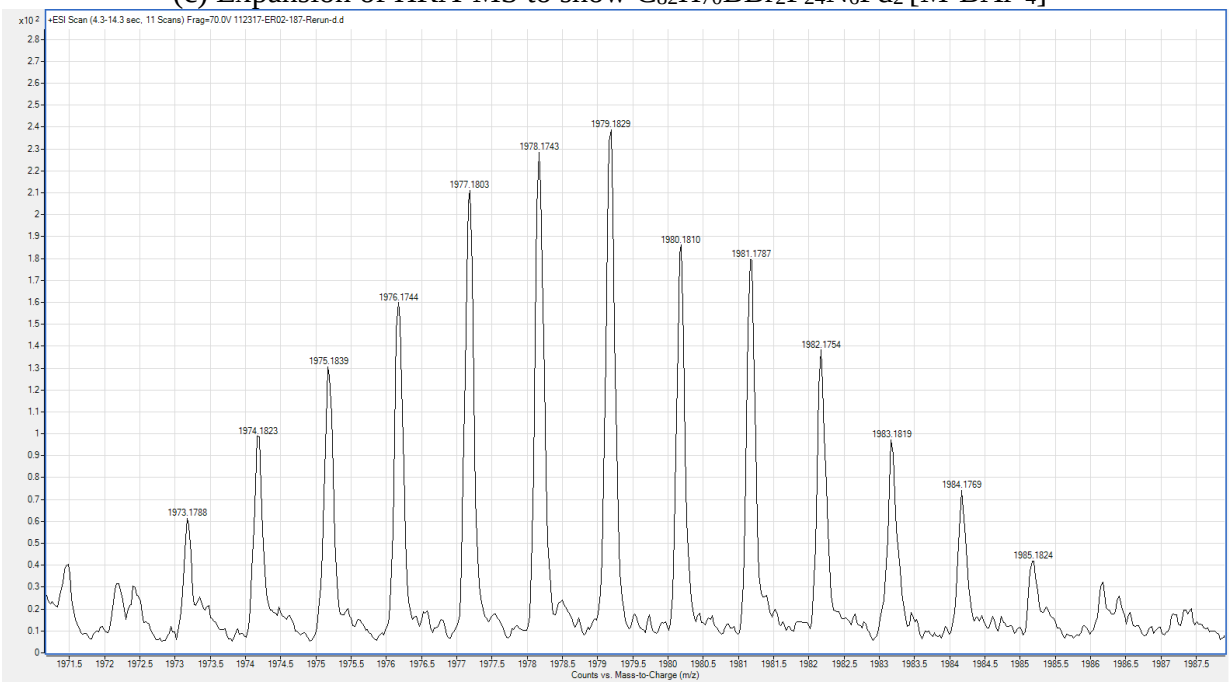

Figure 3.29, continued.

(d) Calculated Isotope Pattern for $C_{82}H_{70}BBr_2F_{24}N_6Pd_2$ $[M\text{-}BAr^F{}_4]^+$

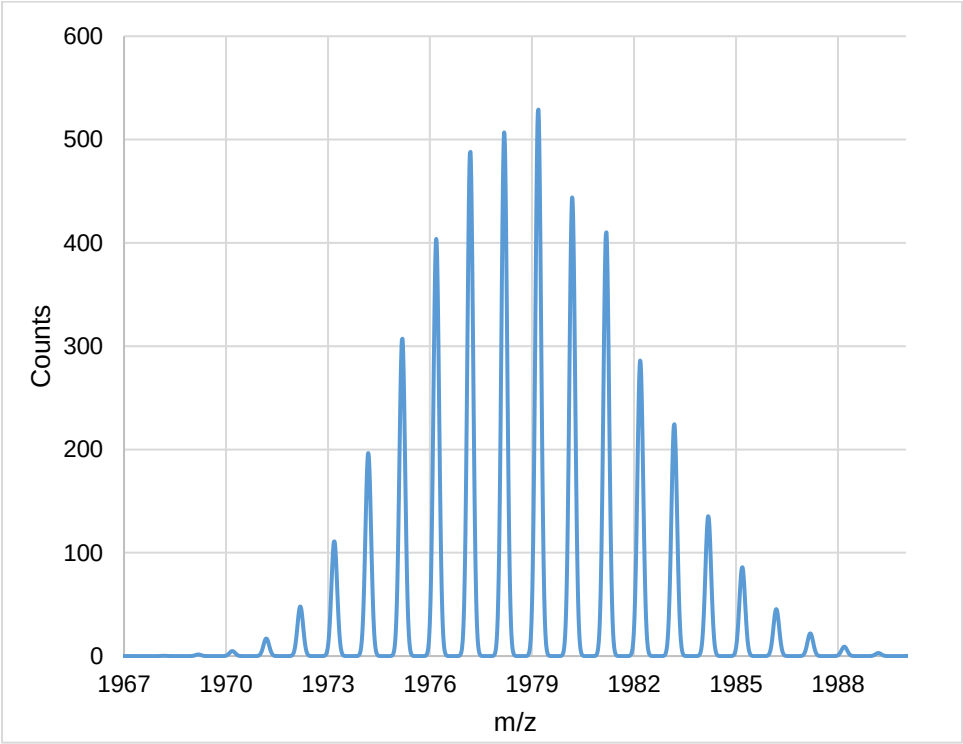

(2'–4H)$Zr_2(NMe_2)_4$. $Zr(NMe_2)_4$ (222.1 mg, 0.830 mmol) and **2'** (308.4 mg, 0.415 mmol) were suspended in PhCl (10 mL). The yellow suspension was left to stir for 5 h. Hexane (10 mL) was added and yellow-orange suspension was stirred with purging N_2. The resulting bright yellow solid was collected and washed with hexane (2 x 25 mL) and dried under vacuum overnight to yield (**2'**–4H)$Zr_2(NMe_2)_4$. Yield: 360 mg, 79%. The labelling scheme for (**2'**–4H)$Zr_2(NMe_2)_4$ is shown in Figure 3.30. ^{1}H NMR (C_6D_6, 500 MHz, 23 ºC): δ 8.11 (s, 2H, H_c), 7.27 (m, 6H, H_d, H_e), 5.40 (d, $^2J_{HH}$ = 15 Hz, 4H, H_a), 4.67 (dd, $^3J_{HH}$ = 5 Hz, $^3J_{HH}$ = 8 Hz, 4H, H_j) 4.55 (d, $^2J_{HH}$ = 15 Hz, 4H, H_b), 3.03 (s, 12H, H_a), 2.95 (s, 12H, H_b), 2.21 (m, 20 H, H_f, H_g, H_h, H_i, H_k), 1.05 (m, 8H, H_l,H_m), 0.81 (t, $^3J_{HH}$ = 8.5 Hz, 6H, H_n). $^{13}C\{^1H\}$ NMR (C_6D_5Cl, 126 MHz): δ 151.2 (py-*o*), 148.6 (py-*p*), 148.4 (C_{xylyl}-$C_{benzylic}$), 143.6 (py-*m*), 127.2 (*C*-H_d), 126.7 (obscured by solvent resonances,

from HSQC, *C*-H_e), 125.9 (obscured by solvent resonances, from HSQC, *C*-H_c), 98.4 (*C*-H_j), 53.6 (*C*-H_a,H_b), 43.3 (N-*C*H_3), 42.1 (N-*C*H_3), 30.9 (*C*-H_l or *C*-H_m), 27.8 (*C*-H_k), 23.5 (*C*-H_h,H_i), 23.0 (*C*-H_f,H_g), 22.9 (*C*-H_l or *C*-H_m), 14.1 (*C*-H_n), the N-*C*=C resonance is obscured by solvent resonances. Anal. Calcd for $C_{58}H_{78}N_{10}Zr_2$: C, 63.46; H, 7.16; N, 12.76. Found: C, 63.22; H, 7.35; N, 12.42.

Figure 3.30. Labelling scheme for (**2'**–4H)$Zr_2(NMe_2)_4$.

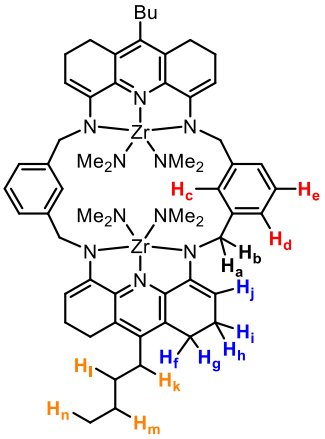

Figure 3.31. NMR spectra of (**2'**–4H)$Zr_2(NMe_2)_4$.
(a) ^{1}H NMR (C_6D_6, 500 MHz, 23 ºC)

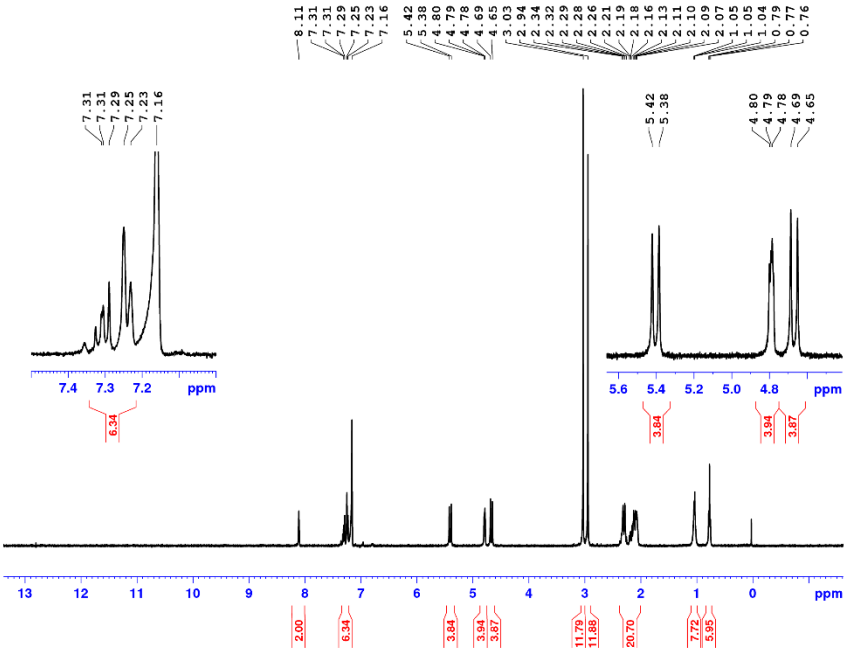

(b) ^{1}H NMR (C_6D_5Cl, 500 MHz, 23 ºC) (* denotes $HNMe_2$ impurity from hydrolysis)

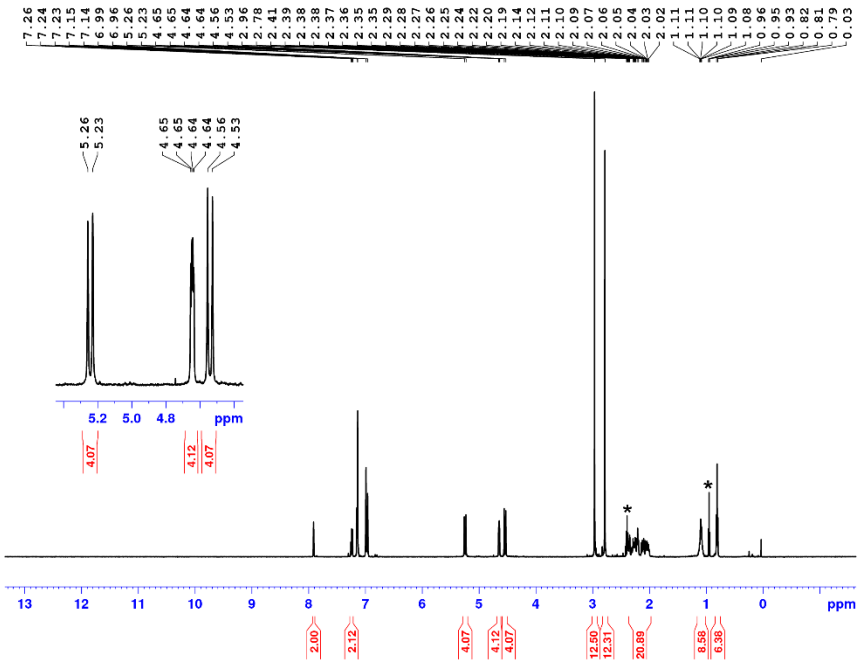

Figure 3.31, continued.

(c) ^{13}C NMR (C_6D_5Cl, 126 MHz, 23 ºC)

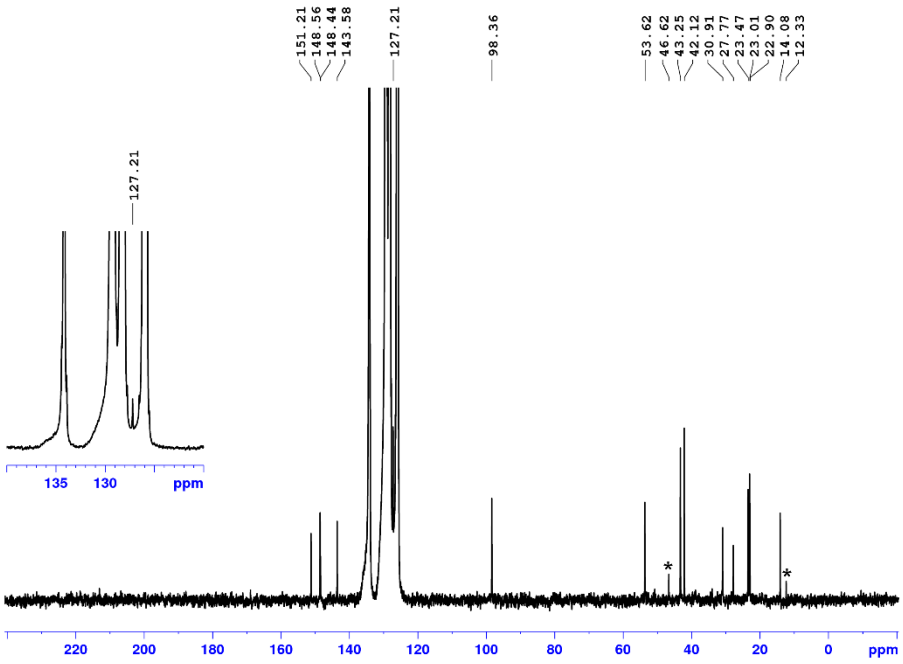

(d) ^{1}H COSY (C_6D_5Cl, 500 MHz, 23 ºC)

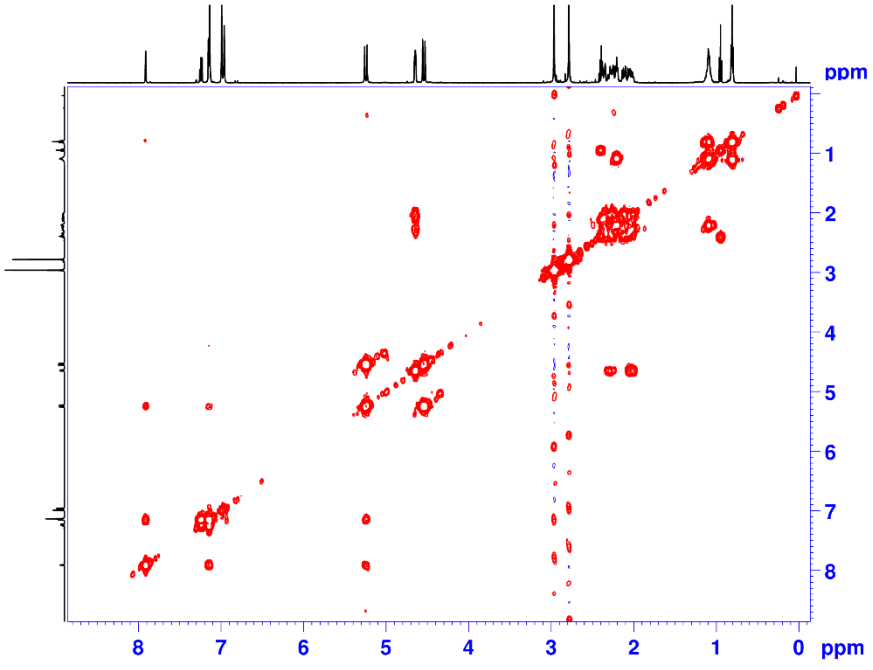

Figure 3.31, continued.

Figure 3.31, continued.

(e) ^{1}H-^{13}C HSQC (C_6D_5Cl, 500 MHz, 23 ºC)

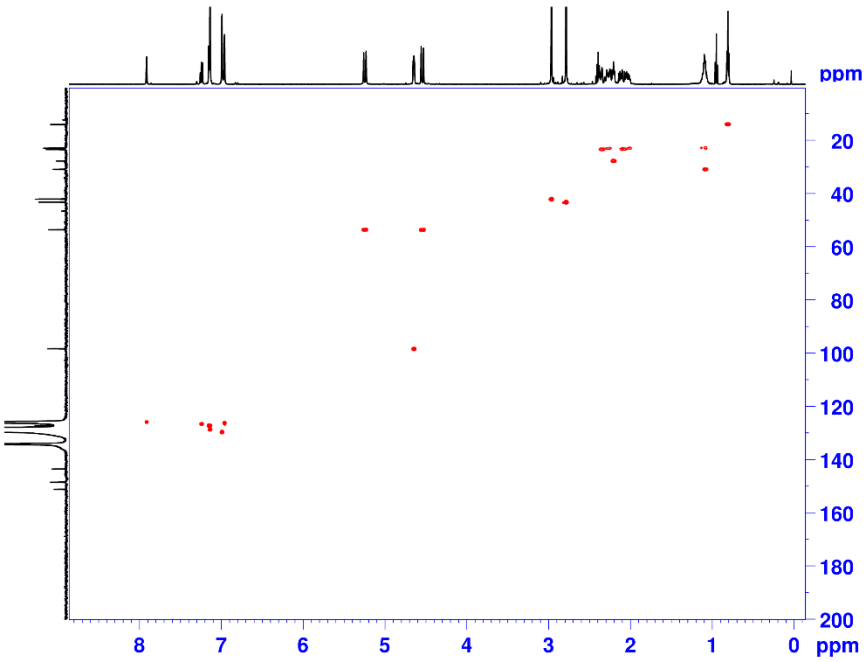

(f) Expansion of ^{1}H-^{13}C HSQC (C_6D_5Cl, 500 MHz, 23 ºC) (δ 8.0 – 6.8, δ 140 – 120)

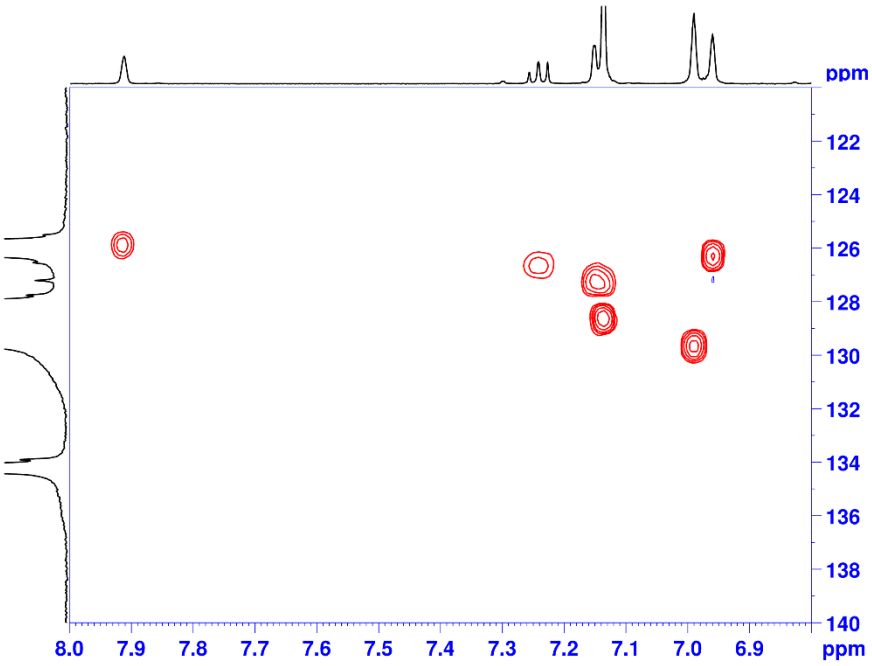

(2'–4H)Zr_2Me_4. (**2'–**4H)$Zr_2(NMe_2)_4$ (300 mg, 0.273 mmol) was suspended in PhH (30 mL). $AlMe_3$ (393 mg, 2.73 mmol) was added dropwise with stirring. The reaction mixture was left to stir for 16 hr. Hexane (30 mL) was added to the suspension and the suspension filtered. The resulting solid was subsequently washed with hexane (15 mL), Et_2O (2 x 10 mL), and hexane (15 mL) and left to dry overnight to yield (**2'–**4H)Zr_2Me_4 as a bright yellow solid which contains 10 % Et_2O. Yield 180.3 mg, 67 %. The labelling scheme for (**2'**–4H)Zr_2Me_4 is shown in Figure 3.32. ^{1}H NMR (C_6D_6, 500 MHz, 23 ºC): δ 8.45 (s, 2H, H_c), 7.33 (t, $^3J_{HH}$ = 7.5 Hz, 2H, H_e), 7.25 (d, $^3J_{HH}$ = 7.5 Hz, 2H, H_d), 5.59 (d, $^2J_{HH}$ = 15 Hz, 4H, H_a), 4.82 (t, $^3J_{HH}$ = 4 Hz, 4H, H_j) 4.61 (d, $^2J_{HH}$ = 15 Hz, 4H, H_b), 2.2 (s, 12H, H_f, H_g, H_h, H_i), 2.03 (t, 4H, H_k), 1.06 (m, 20 H, H_l, H_m), 0.76 (t, $^3J_{HH}$ = 7 Hz, 6H, H_n), 0.57 (s, 6H, Zr-Me^1), 0.55 (s, 6H, Zr-Me^2).. Anal. Calcd for $C_{54}H_{66}N_6Zr_2$: C, 66.07; H, 6.78; N, 8.56. Found: C, 65.56; H, 7.18; N, 9.34. The slight deviation in the amount of C is most likely due to formation of Zr-C during combustion. This compound decomposes instantly upon exposure to chlorinated solvents and is not soluble enough in C_6D_6 or $C_6D_5CD_3$ for a $^{13}C\{^1H\}$ to be collected.

Figure 3.32. Labelling scheme for (**2'**–4H)Zr_2Me_4.

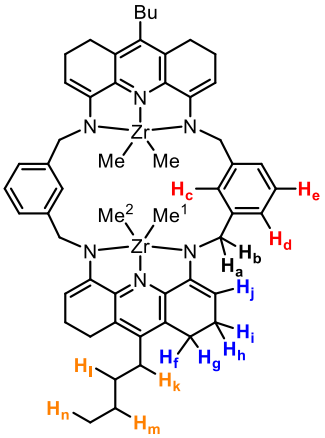

Figure 3.33. ^{1}H NMR spectrum for (**2'**–4H)Zr_2Me_4 (C_6D_6, 500 MHz, 23 ºC).

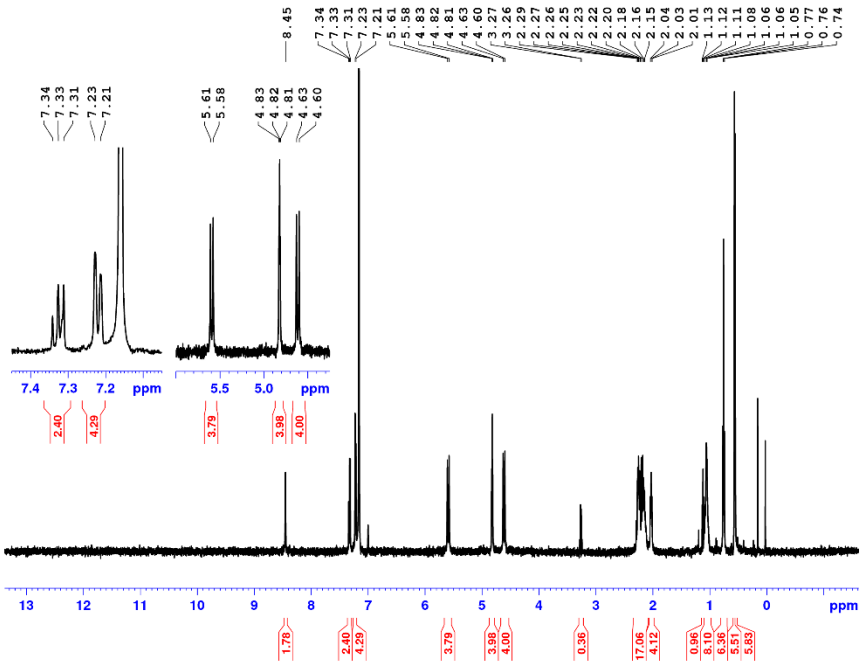

(2'–4H)$Zr_2(CH_2SiMe_3)_2(NMe_2)_2$: (**2'**–4H)$Zr_2(NMe_2)_4$ (300.0 mg, 0.285 mmol) was suspended in PhMe (15 mL) and $Al(CH_2SiMe_3)_3$ (411.2mg, 1.425) was added in one portion. The mixture was then heated at 80 ºC and stirred for 16 hr. The solvent was removed under reduced pressure. The resulting dark yellow solid was suspended in Et_2O (15 mL) and stirred for 5 min. Pentane (15 mL) was added and the suspension was filtered and the solid washed with pentane (2 x15 mL) and dried under vacuum overnight to yield (**2'–**4H)$Zr_2(CH_2SiMe_3)_2(NMe_2)_2$ as a dark yellow solid. Yield: 250.0 mg, 74 %. The labelling scheme for (**2'**–4H)$Zr_2(CH_2SiMe_3)_2(NMe_2)_2$ is shown in Figure 3.34. ^{1}H NMR (C_6D_6, 500 MHz, 23 ºC): δ 7.88 (s, 2H, H_c), 7.24 (t, J_{HH} = 7.5 Hz, 2H, H_e), 7.17 (d, J_{HH} = 7.5 Hz, H_d, overlapped with solvent peak) 5.37 (t, $^{2}J_{HH}$ = 15 Hz, 4H, H_a), 4.83 (br dd, 4H, H_j), 4.69 (d, $^{2}J_{HH}$ = 15 Hz, 4H, H_b), 2.79 (s, 12H, -N(CH_3)$_2$), 2.35 (m, 8 H, H_f, H_g), 2.13 (m, 12H, H_h, H_i, H_k), 1.07 (m, 8H, H_l, H_m), 0.78 (t, 6H, H_n, $^{3}J_{HH}$ = 6 Hz), 0.72 (s, 4H, -

C*H*$_2$Si(CH$_3$)$_3$), 0.02 (s, 18H, -CH$_2$Si(C*H*$_3$)$_3$).^{13}C{^{1}H} NMR (C$_6$D$_6$, 126 MHz, 23 ºC): δ 151.3 (*o*-py), 149.2 (*p*-py), 148.7 (*C*$_{xylyl}$-C$_{benzylic}$), 143.56 (*m*-py), 127.6 (*C*-H$_d$), 126.9 (*C*-H$_e$), 126.0 (*C*-H$_c$), 99.7 (*C*-H$_j$), 53.7 (*C*-H$_a$,H$_b$), 51.1 (-C*H*$_2$Si(CH$_3$)$_3$), 41.1 (-N(*C*H$_3$)$_2$), 31.0 (*C*-H$_l$), 27.9 (*C*-H$_k$), 23.6 (*C*-H$_h$,H$_i$), 23.3 (*C*-H$_f$,H$_g$), 22.9 (*C*-H$_m$), 14.1 (*C*-H$_n$), 2.5 (-CH$_2$Si(*C*H$_3$)$_3$). Anal. Calcd for C$_{62}$H$_{88}$N$_8$Si$_2$Zr$_2$: C, 62.89; H, 7.49; N, 9.46. Found: C, 62.61; H, 7.50; N, 9.47.

Figure 3.34. Labelling scheme for (**2'**–4H)Zr$_2$(CH$_2$SiMe$_3$)$_2$(NMe$_2$)$_2$.

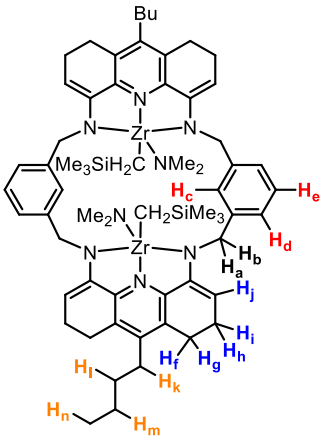

Figure 3.35. NMR spectra of (**2'**–4H)$Zr_2(CH_2SiMe_3)_2(NMe_2)_2$.
(a) ^1H NMR (C_6D_6, 500 MHz, 23 ºC)

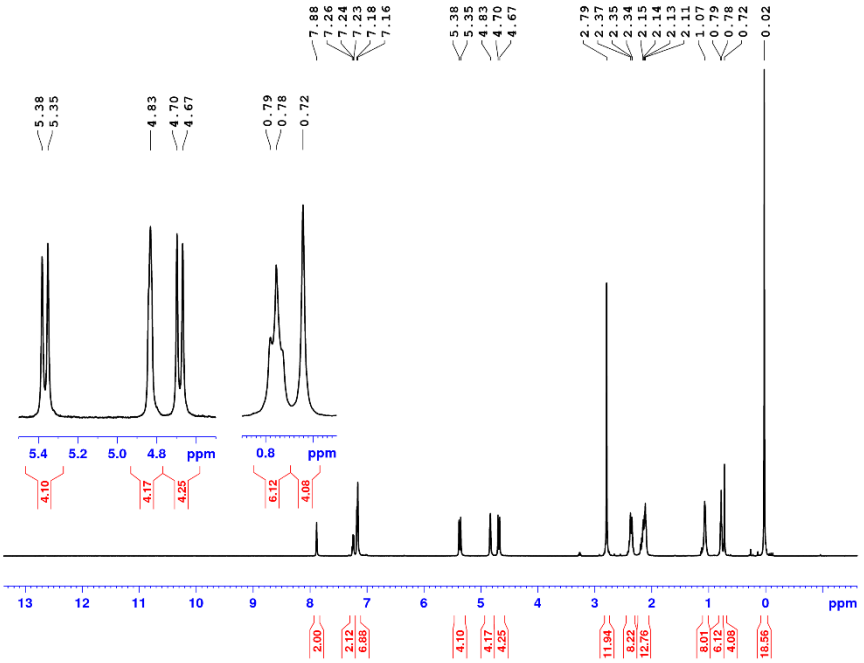

(b) $^{13}C\{^1H\}$ NMR (C_6D_6, 126 MHz, 23 ºC)

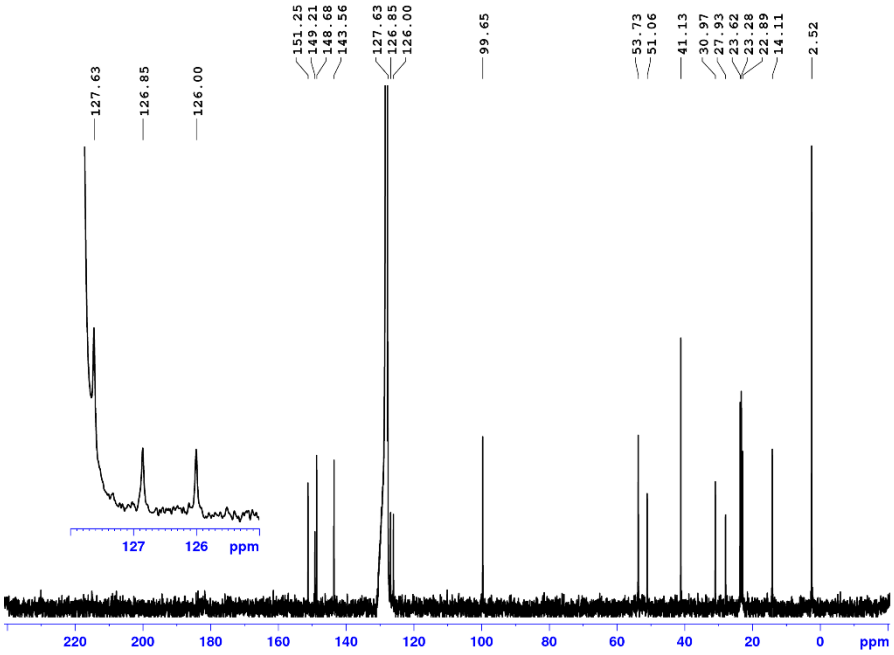

Figure 3.35, continued.

(c) ^{1}H COSY (C_6D_6, 500 MHz, 23 ºC)

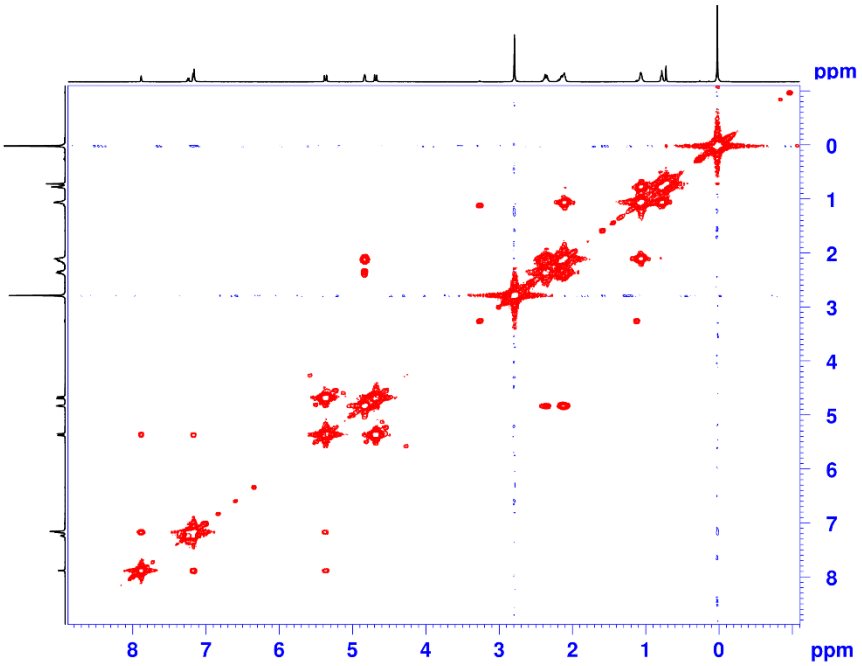

(d) ^{1}H-^{1}H (C_6D_6, 500 MHz, 23 ºC)

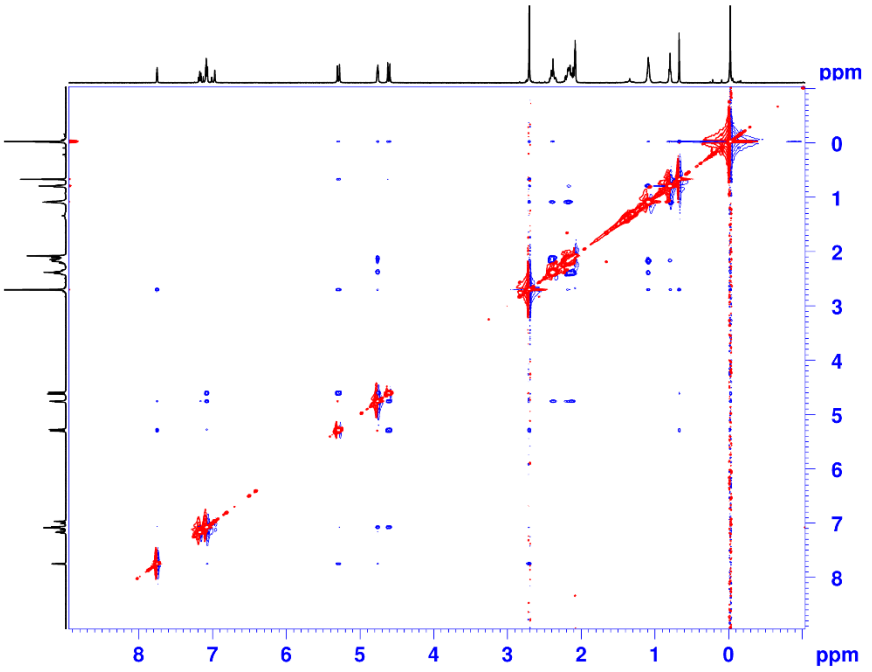

Figure 3.35, continued.
(e) ^{1}H-^{13}C HSQC (C_6D_6, 500 MHz, 23 ºC)

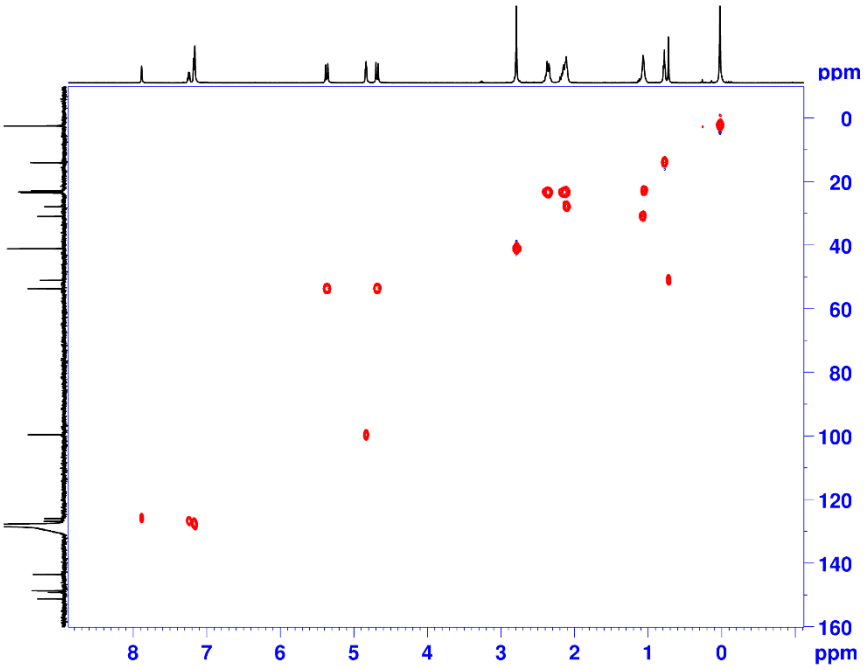

(f) ^{1}H NMR ($C_6D_5CD_3$, 500 MHz, 23 ºC)

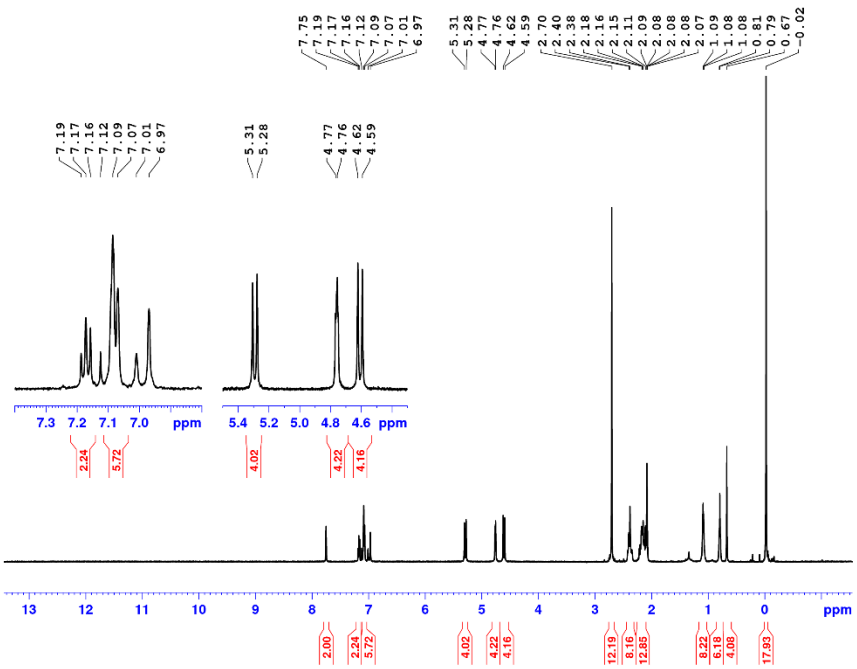

Figure 3.35, continued.

(g) ^{1}H NMR ($C_6D_5CD_3$, 500 MHz, 80 ºC)

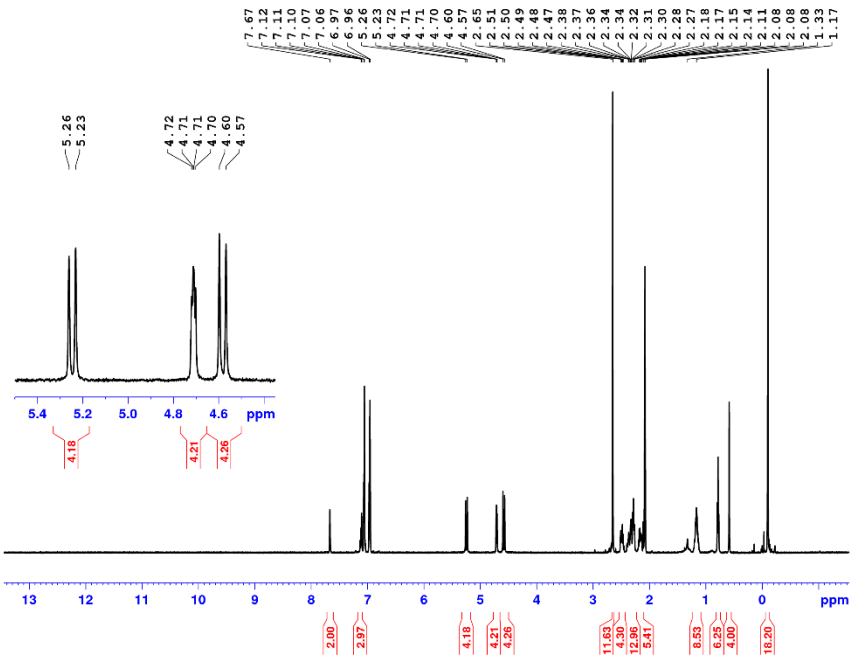

Ethylene Oligomerization For (2)Co_2Cl_4 and (2)Fe_2Cl_4 Ethylene polymerizations at 400 psi were performed using a stainless-steel Parr 300 mL autoclave, which was equipped with a magnetically-driven 1.5-inch diameter four-blade propeller stirrer, an injection line, thermocouple, water cooling loop, and a Parr 4842 controller. In a N_2 glovebox, a 200 mL glass autoclave liner was charged with a stock solution of the metal complex in CH_2Cl_2 (1 mL) and a stock solution of the catalyst in PhF (1 mL) and placed in the autoclave. The autoclave was sealed and CH_2Cl_2 removed under vacuum in the glovebox. The autoclave was then opened and toluene (45 mL) added. A stock solution of Al^iBu_3, MAO, or MMAO-12 (5 mL) was added to the injection line. Removed from the glovebox, attached to the ethylene line, and pressurized to 350 psi. After equilibrating for 15 min, the activator solution was added using 400 psi of ethylene pressure. The

ethylene pressure was kept constant by feeding ethylene on demand. After 30 min the ethylene line was closed and the autoclave was vented. Methanol (50 mL) was added to quench the excess activator. *o*-Xylene (100 μL) was added as an internal standard, and the solution was analyzed by GC-MS using an Aglient 6890/5973N GC-MS instrument. The masses of hexene, octene, and decene were determined by GC-MS using predetermined response factors. The mass of butene was calculated by extrapolation of the Schulz-Flory fit from the higher mass oligomers.

Figure 3.36. Schulz-Flory plot of oligomers formed by (**2**)Fe_2Cl_4 (1000 equiv. Al^{t}Bu$_3$, 400 psi, 30 min)

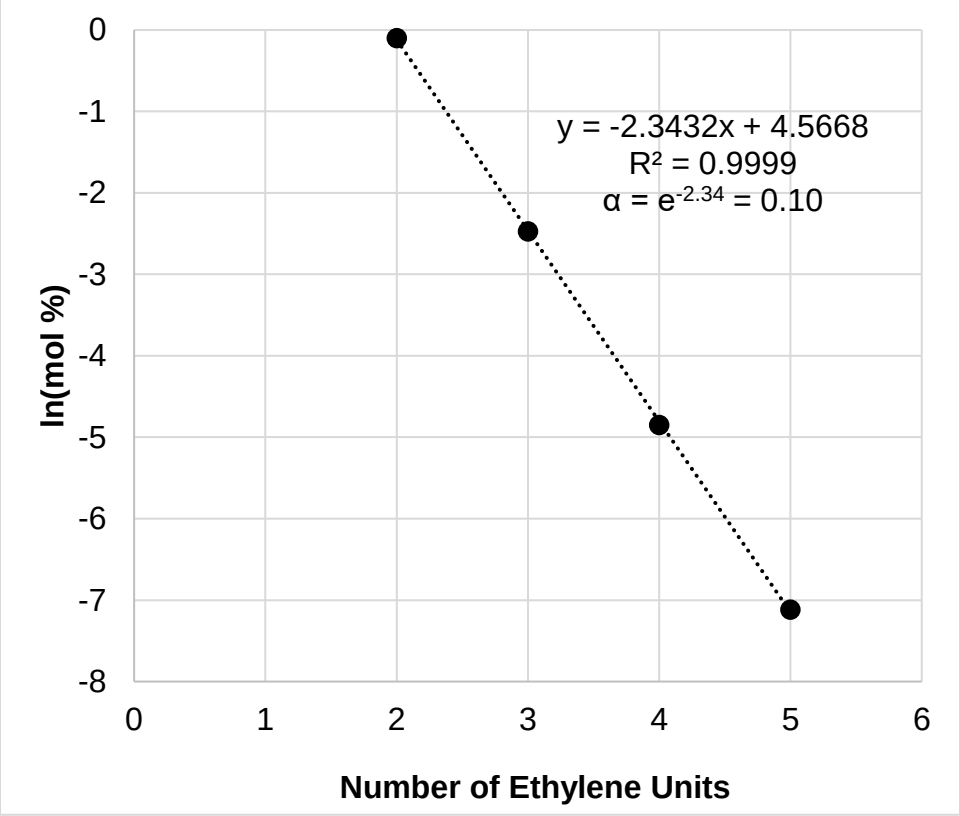

X-ray Crystallography. Data were measured at 100 K on a Bruker D8 VENTURE with PHOTON 100 CMOS detector system equipped with a Mo-target X-ray tube (λ = 0.71073 Å). Data reduction and integration were performed with the Bruker APEX3 software package (Bruker AXS, version 2015.5-2, 2015). Data were scaled and corrected for absorption effects using the multi-scan procedure as implemented in SADABS (Bruker AXS, version 2014/5, 2015, part of Bruker APEX3 software package). The structures were solved by SHELXT and refined by a full-matrix least-squares procedure using OLEX2.

Specific Refinement Details For (2)Zn_2Cl_4. All atoms were refined with anisotropic thermal parameters. A dangling n-Bu group was disordered over two positions. One of the $C_2H_4Cl_2$ solvent molecules showed disorder of the C-atoms. Hydrogen atoms were included in idealized positions for structure factor calculations.

Specific Refinement Details For (2)Co_2Cl_4. All elements were refined with anisotropic thermal parameters. Hydrogen atoms were included in idealized positions for structure factor calculations. Notably, the dangling side *n-Bu* chains are well resolved. 2 out of 3.5 independent 1,2-dichloroethane (DCE) molecules were found to be disordered. Each disorder was individually modelled. In one, the separation of a single Cl into two positions was satisfactory, while the second DCE required a whole-body disorder modelling. The ratios of major/minor parts refined to *ca*. 0.6 in both cases. Geometric and thermal parameters restraints were utilized to facilitate disorder modelling

Specific Refinement Details For [(2)Pd_2Br_4][BAr^F_4]. All elements were refined with anisotropic thermal parameters. Hydrogen atoms were included in idealized positions for structure factor calculations. Notably, the dangling side *n-Bu* chains and all -CF_3 groups are well resolved.

Specific Refinement Details For (2'–4H)$Zr_2(CH_2SiMe_3)_2(NMe_2)_2$. The structure was solved and refined with HKLF 4 file format. All elements were refined with anisotropic thermal parameters. Hydrogen atoms were included in idealized positions for structure factor calculations.

Table 3.2. X-ray Crystallographic Parameters for (**2**)Zn_2Cl_4.

Empirical formula	$C_{56}H_{70}Cl_{10}N_6Zn_2$
Formula weight	1312.42
Temperature/K	100(2)
Crystal system	monoclinic
Space group	C2/c
a/Å	29.591(4)
b/Å	10.4524(14)
c/Å	20.211(3)
α/°	90
β/°	110.024(6)
γ/°	90
Volume/Å^3	5873.2(14)
Z	4
ρ_{calc}g/cm^3	1.484
μ/mm^{-1}	1.315
F(000)	2712.0
Crystal size/mm^3	0.29 × 0.21 × 0.13
Radiation	MoKα (λ = 0.71073)
2Θ range for data collection/°	4.448 to 51.53
Index ranges	$-36 \leq h \leq 36$, $-12 \leq k \leq 12$, $-23 \leq l \leq 24$
Reflections collected	44059
Independent reflections	5617 [R_{int} = 0.0641, R_{sigma} = 0.0399]
Data/restraints/parameters	5617/19/368
Goodness-of-fit on F^2	1.083
Final R indexes [I>=2σ (I)]	R_1 = 0.0582, wR_2 = 0.1265
Final R indexes [all data]	R_1 = 0.0931, wR_2 = 0.1442
Largest diff. peak/hole / e Å^{-3}	0.80/-0.69

Table 3.3. X-ray Crystallographic Parameters for (**2**)Co_2Cl_4.

Empirical formula	$C_{164}H_{202}Cl_{26}Co_6N_{18}$
Formula weight	3700.70
Temperature/K	100(2)
Crystal system	triclinic
Space group	P-1
a/Å	13.957(3)
b/Å	16.187(4)
c/Å	19.592(4)
α/°	72.718(7)
β/°	85.142(7)
γ/°	86.999(7)
Volume/Å^3	4209.5(16)
Z	1
ρ_{calc}g/cm^3	1.460
μ/mm^{-1}	1.047
F(000)	1916.0
Crystal size/mm^3	0.27 × 0.09 × 0.08
Radiation	MoKα (λ = 0.71073)
2Θ range for data collection/°	4.276 to 57.644
Index ranges	$-18 \leq h \leq 18$, $-21 \leq k \leq 21$, $-26 \leq l \leq 26$
Reflections collected	116174
Independent reflections	21916 [R_{int} = 0.0579, R_{sigma} = 0.0571]
Data/restraints/parameters	21916/31/996
Goodness-of-fit on F^2	1.052
Final R indexes [I>=2σ (I)]	R_1 = 0.0558, wR_2 = 0.1204
Final R indexes [all data]	R_1 = 0.0901, wR_2 = 0.1328
Largest diff. peak/hole / e Å^{-3}	1.45/-1.46

Table 3.4. X-ray Crystallographic Parameters fo [(**2**)Pd_2Br_2][$BAr^F{}_4$]$_2$.

Empirical formula	$C_{114}H_{82}B_2Br_2F_{48}N_6Pd_2$
Formula weight	2842.09
Temperature/K	100(2)
Crystal system	triclinic
Space group	P-1
a/Å	13.4066(7)
b/Å	13.5948(7)
c/Å	15.2126(8)
α/°	90.758(2)
β/°	90.910(2)
γ/°	95.475(2)
Volume/Å^3	2759.3(2)
Z	1
ρ_{calc}g/cm^3	1.710
μ/mm^{-1}	1.185
F(000)	1412.0
Crystal size/mm^3	0.22 × 0.14 × 0.08
Radiation	MoKα (λ = 0.71073)
2Θ range for data collection/°	4.488 to 55.942
Index ranges	$-17 \leq h \leq 17$, $-17 \leq k \leq 17$, $-19 \leq l \leq 19$
Reflections collected	89678
Independent reflections	13023 [R_{int} = 0.0433, R_{sigma} = 0.0402]
Data/restraints/parameters	13023/0/785
Goodness-of-fit on F^2	1.035
Final R indexes [I>=2σ (I)]	R_1 = 0.0396, wR_2 = 0.0834
Final R indexes [all data]	R_1 = 0.0655, wR_2 = 0.0918
Largest diff. peak/hole / e Å^{-3}	0.84/-0.97

Table 3.5. X-ray Crystallographic Parameters (**2'**–4H)$Zr_2(CH_2SiMe_3)_2(NMe_2)_2$.

Empirical formula	$C_{62}H_{88}N_8Si_2Zr_2$
Formula weight	1184.02
Temperature/K	100(2)
Crystal system	triclinic
Space group	P-1
a/Å	14.6548(10)
b/Å	14.8581(10)
c/Å	17.1701(16)
α/°	94.675(2)
β/°	109.060(2)
γ/°	119.188(2)
Volume/$Å^3$	2950.8(4)
Z	2
$\rho_{calc}g/cm^3$	1.333
μ/mm^{-1}	0.440
F(000)	1248.0
Crystal size/mm^3	0.381 × 0.243 × 0.238
Radiation	MoKα (λ = 0.71073)
2Θ range for data collection/°	4.764 to 56.002
Reflections collected	14241
Independent reflections	14241 [R_{int} = 0.0563, R_{sigma} = 0.0307]
Data/restraints/parameters	14241/0/679
Goodness-of-fit on F^2	1.083
Final R indexes [I>=2σ (I)]	R_1 = 0.0446, wR_2 = 0.0864
Final R indexes [all data]	R_1 = 0.0609, wR_2 = 0.0921
Largest diff. peak/hole / e $Å^{-3}$	0.75/-0.45

3.5 References and Notes

(1) Small, B. L.; Brookhart, M.; Bennett, A. M. A. *J. Am. Chem. Soc.* **1998**, *120*, 4049.

(2) Small, B. L. *Acc. Chem. Res.* **2015**, *48*, 2599.

(3) Britovsek, G. J. P.; Bruce, M.; Gibson, V. C.; Kimberley, B. S.; Maddox, P. J.; Mastroianni, S.; McTavish, S. J.; Redshaw, C.; Solan, G. A.; Strömberg, S.; White, A. J. P.; Williams, D. J. *J. Am. Chem. Soc.* **1999**, *121*, 8728.

(4) Gibson, V. C.; Redshaw, C.; Solan, G. A. *Chem. Rev.* **2007**, *107*, 1745.

(5) Flisak, Z.; Sun, W.-H. *ACS Catal.* **2015**, *5*, 4713.

(6) Biernesser, A. B.; Li, B.; Byers, J. A. *J. Am. Chem. Soc.* **2013**, *135*, 16553.

(7) Qi, M.; Dong, Q.; Wang, D.; Byers, J. A. *J. Am. Chem. Soc.* **2018**, *140*, 5686.

(8) Schmidt, V. A.; Hoyt, J. M.; Margulieux, G. W.; Chirik, P. J. *J. Am. Chem. Soc.* **2015**, *137*, 7903.

(9) Hoyt, J. M.; Schmidt, V. A.; Tondreau, A. M.; Chirik, P. J. *Science* **2015**, *349*, 960.

(10) Wang, L.; Sun, J. *Inorg. Chim. Acta* **2008**, *361*, 1843.

(11) Suo, H.; Solan, G. A.; Ma, Y.; Sun, W.-H. *Coord Chem Rev* **2018**, *372*, 101.

(12) Xing, Q.; Zhao, T.; Qiao, Y.; Wang, L.; Redshaw, C.; Sun, W.-H. *RSC Adv.* **2013**, *3*, 26184.

(13) Xing, Q.; Zhao, T.; Du, S.; Yang, W.; Liang, T.; Redshaw, C.; Sun, W.-H. *Organometallics* **2014**, *33*, 1382.

(14) Takeuchi, D.; Takano, S.; Takeuchi, Y.; Osakada, K. *Organometallics* **2014**, *33*, 5316.

(15) Takano, S.; Takeuchi, Y.; Takeuchi, D.; Osakada, K. *Chem. Lett.* **2014**, *43*, 465.

(16) Liu, J.; Li, Y.; Liu, J.; Li, Z. *Macromolecules* **2005**, *38*, 2559.

(17) Rezaeivala, M.; Keypour, H. *Coord Chem Rev* **2014**, *280*, 203.

(18) Healy, M. D. S.; Rest, A. J. Advances in inorganic chemistry and radiochemistry; Elsevier, 1978; Vol. 21, pp. 1–40.

(19) Cabbiness, D. K.; Margerum, D. W. *J. Am. Chem. Soc.* **1969**, *91*, 6540.

(20) Izatt, R. M.; Christensen, J. J. *Synthesis of Macrocycles: The Design of Selective Complexing Agents (Progress in Macrocyclic Chemistry) (v. 3)*; 1st ed.; Wiley, 1987.

(21) *Synthetic multidentate macrocyclic compounds*; Elsevier, 1978.

(22) Busch, D. H.; Stephenson, N. A. *Coord Chem Rev* **1990**, *100*, 119.

(23) Curtis, N. F. *Coord Chem Rev* **1968**, *3*, 3.

(24) Costisor, O.; Linert, W. *Metal mediated template synthesis of ligands*; WORLD SCIENTIFIC, 2004.

(25) Thompson, M. C.; Busch, D. H. *J. Am. Chem. Soc.* **1964**, *86*, 213.

(26) Dammann, W.; Buban, T.; Schiller, C.; Burger, P. *Dalton Trans.* **2018**, *47*, 12105.

(27) Huang, F.; Xing, Q.; Liang, T.; Flisak, Z.; Ye, B.; Hu, X.; Yang, W.; Sun, W.-H. *Dalton Trans.* **2014**, *43*, 16818.

(28) Agrifoglio, G.; Reyes, J.; Atencio, R.; Briceño, A. *Acta Crystallogr. Sect. E, Struct. Rep. Online* **2007**, *64*, o28.

(29) Wallenhorst, C.; Kehr, G.; Luftmann, H.; Fröhlich, R.; Erker, G. *Organometallics* **2008**, *27*, 6547.

(30) Ionkin, A. S.; Marshall, W. J.; Adelman, D. J.; Fones, B. B.; Fish, B. M.; Schiffhauer, M. F.; Soper, P. D.; Waterland, R. L.; Spence, R. E.; Xie, T. *J. Polym. Sci. A Polym. Chem.* **2008**, *46*, 585.

(31) Pelascini, F.; Wesolek, M.; Peruch, F.; Lutz, P. J. *Eur J Inorg Chem* **2006**, *2006*, 4309.

(32) Salata, C. A.; Youinou, M. T.; Burrows, C. J. *J. Am. Chem. Soc.* **1989**, *111*, 9278.

(33) Salata, C. A.; Youinou, M. T.; Burrows, C. J. *Inorg. Chem.* **1991**, *30*, 3454.

(34) Nelson, S. M.; Knox, C. V.; McCann, M.; Drew, M. G. B. *J. Chem. Soc., Dalton Trans.* **1981**, 1669.

(35) Drew, M. G. B.; Cairns, C.; Lavery, A.; Nelson, S. M. *J. Chem. Soc., Chem. Commun.* **1980**, 1122.

(36) Beattie, J. W.; SantaLucia, D. J.; White, D. S.; Groysman, S. *Inorg. Chim. Acta* **2017**, *460*, 8.

(37) Browne, C.; Ronson, T. K.; Nitschke, J. R. *Angew. Chem. Int. Ed. Engl.* **2014**, *53*, 10701.

(38) Alfonso, I.; Bolte, M.; Bru, M.; Burguete, M. I.; Luis, S. V.; Rubio, J. *J. Am. Chem. Soc.* **2008**, *130*, 6137.

(39) Borisova, N. E.; Reshetova, M. D.; Ustynyuk, Y. A. *Chem. Rev.* **2007**, *107*, 46.

(40) Gibson, V. C.; McTavish, S.; Redshaw, C.; Solan, G. A.; White, A. J. P.; Williams, D. J. *Dalton Trans.* **2003**, 221.

(41) Thummel, R. P.; Jahng, Y. *J. Org. Chem.* **1985**, *50*, 2407.

(42) Appukuttan, V. K.; Liu, Y.; Son, B. C.; Ha, C.-S.; Suh, H.; Kim, I. *Organometallics* **2011**, *30*, 2285.

(43) Hanton, M. J.; Tenza, K. *Organometallics* **2008**, *27*, 5712.

(44) Bell, T. W.; Rothenberger, S. D. *Tetrahedron Lett.* **1987**, *28*, 4817.

(45) Bell, T. W.; Cho, Y.-M.; Firestone, A.; Karin, H.; Liu, J.; Ludwig, R.; Rothenberger, S. D. *Org. Synth.* **1990**, *69*, 226.

(46) Pilato, M. L.; Catalano, V. J.; Bell, T. W. *J. Org. Chem.* **2001**, *66*, 1525.

(47) Groen, J. H.; Annemieke, de Z.; Vlaar, Mark J. M.; Ernsting, J. M.; van Leeuwen, Piet W. N. M.; Vrieze, K.; Kooijman, H.; Smeets, Wilberth J. J.; Spek, A. L.; Budzelaar, Peter H. M.; Xiang, Q.; Thummel, R. P. *European Journal of Inorganic Chemistry* **1998**.

(48) Li, X.; Zhu, D.; Gao, W.; Zhang, Y.; Mu, Y. *J. Chem. Res. (S)* **2006**, *2006*, 371.

(49) Fan, R.; Zhu, D.; Ding, H.; Mu, Y.; Su, Q.; Xia, H. *Synth Met* **2005**, *149*, 135.

(50) Munch, J. H. *Die Makromolekulare Chemie* **1977**.

(51) Blahut, J.; Hermann, P.; Tošner, Z.; Platas-Iglesias, C. *Phys. Chem. Chem. Phys.* **2017**, *19*, 26662.

(52) Klawitter, I.; Anneser, M. R.; Dechert, S.; Meyer, S.; Demeshko, S.; Haslinger, S.; Pöthig, A.; Kühn, F. E.; Meyer, F. *Organometallics* **2015**, *34*, 2819.

(53) Bogdan, A. R.; Jerome, S. V.; Houk, K. N.; James, K. *J. Am. Chem. Soc.* **2012**, *134*, 2127.

(54) *Synthesis and Reactivity in Inorganic, Metal-Organic, and Nano-Metal Chemistry*.

(55) Liu, P.; Zhou, L.; Li, X.; He, R. *J Organomet Chem* **2009**, *694*, 2290.

(56) Jurca, T.; Hiscock, L. K.; Korobkov, I.; Rowley, C. N.; Richeson, D. S. *Dalton Trans.* **2014**, *43*, 690.

(57) Singh, A. P.; Roesky, H. W.; Carl, E.; Stalke, D.; Demers, J.-P.; Lange, A. *J. Am. Chem. Soc.* **2012**, *134*, 4998.

(58) Tušek-Božić, L.; Matijašić, I.; Bocelli, G.; Sgarabotto, P.; Furlani, A.; Scarcia, V.; Papaioannou, A. *Inorg. Chim. Acta* **1991**, *185*, 229.

(59) Moreno-Vida, M. I.; Colacio-Rodriguez, E.; Moreno-Carretero, M. N.; Salas-Peregrin, J. M.; Simard, M.; Beauchamp, A. L. *Inorg. Chim. Acta* **1989**, *157*, 201.

(60) Naghipour, A.; Ghorbani-Choghamarani, A.; Heidarizadi, F.; Notash, B. *Polyhedron* **2016**, *105*, 18.

(61) Reardon, D.; Aharonian, G.; Gambarotta, S.; Yap, G. P. A. *Organometallics* **2002**, *21*, 786.

(62) Sugiyama, H.; Korobkov, I.; Gambarotta, S.; Möller, A.; Budzelaar, P. H. M. *Inorg. Chem.* **2004**, *43*, 5771.

(63) Bouwkamp, M. W.; Lobkovsky, E.; Chirik, P. J. *Inorg. Chem.* **2006**, *45*, 2.

(64) Beachley, O. T.; Tessier-Youngs, C.; Simmons, R. G.; Hallock, R. B. *Inorg. Chem.* **1982**, *21*, 1970.

(65) Loos, M.; Gerber, C.; Corona, F.; Hollender, J.; Singer, H. *Anal. Chem.* **2015**, *87*, 5738.